



HAL
open science

Explicit and implicit large eddy simulation of turbulent combustion with multi-scale forcing

Song Zhao

► **To cite this version:**

Song Zhao. Explicit and implicit large eddy simulation of turbulent combustion with multi-scale forcing. Other. Université d'Orléans, 2016. English. NNT : 2016ORLE2023 . tel-01412627

HAL Id: tel-01412627

<https://theses.hal.science/tel-01412627>

Submitted on 8 Dec 2016

HAL is a multi-disciplinary open access archive for the deposit and dissemination of scientific research documents, whether they are published or not. The documents may come from teaching and research institutions in France or abroad, or from public or private research centers.

L'archive ouverte pluridisciplinaire **HAL**, est destinée au dépôt et à la diffusion de documents scientifiques de niveau recherche, publiés ou non, émanant des établissements d'enseignement et de recherche français ou étrangers, des laboratoires publics ou privés.

ÉCOLE DOCTORALE
ÉNERGIE, MATÉRIAUX, SCIENCES DE LA TERRE ET DE L'UNIVERS
Institut de Combustion Aérodynamique Réactivité et Environnement,
CNRS Orléans

THÈSE présentée par : **Song ZHAO**
soutenue le : **3 mai 2016**

pour obtenir le grade de : **Docteur de l'université d'Orléans**
Discipline : **Physique**

**Explicit and Implicit Large Eddy Simulation of Turbulent
Combustion with Multi-Scale Forcing**

THÈSE dirigée par :

Ivan FEDIOUN Maître de conférences (HDR), Université d'Orléans
Iskender GÖKALP Directeur de Recherches, CNRS, ICARE, Co-directeur

RAPPORTEURS :

Benoît FIORINA Professeur, École Centrale Paris, CNRS, EM2C
Arnaud MURA Directeur de Recherche, CNRS, Institut P'

JURY :

Ivan FEDIOUN Maître de conférences (HDR), Université d'Orléans
Benoît FIORINA Professeur, École Centrale Paris, CNRS, EM2C
Iskender GÖKALP Directeur de Recherches, CNRS, ICARE
Nicolas LARDJANE Chercheur, CEA-DAM-IDF
Vincent MOUREAU Chargé de Recherche, CNRS, CORIA
Arnaud MURA Directeur de Recherche, CNRS, Institut P'
Vladimir SABELNIKOV Directeur de Recherche, ONERA

Acknowledgments

I would like to thank my supervisors, Dr. Ivan FEDIOUN and Dr. Iskender Gökalp for their patient guidance, encouragements and advises. I am lucky to have a research group that cares me so much. I would like to thank our group members Mehmet KARACA, Evgeniy ORLIK and Thierry ANDRE for their help during my stay both in my research and daily life in Orléans.

I would like to thank the French Government's Investissement d'Avenir program: Laboratoire d'Excellence CAPRYSESSES (Grant No. ANR-11-LABX-0006-01) to provide me my fellowship. I would like to appreciate the HPC resource provided by IDRIS and ARTEMIS (PHOEBUS). This work was granted access to the HPC resources of IDRIS under the allocations 201X-2b0913 made by GENCI (Grand Equipement National de Calcul Intensif).

Finally, I would like to thank my family for their support.

Contents

1	Introduction	9
1.1	Context and objectives	12
1.2	Outline of this thesis	13
1.3	Experimental setup	15
1.3.1	The multi-scale injection	15
1.3.2	Non-reactive experiments	16
1.3.3	Reactive experiments	17
2	Governing equations for turbulent combustion	19
2.1	Navier-Stokes equations in conservation form	19
2.1.1	The equation of state	20
2.1.2	The species equations	21
2.1.3	The momentum equation	23
2.1.4	The energy equation	23
2.1.5	N-S equations in vector form	24
2.2	Large-Eddy Simulations	25
2.2.1	Filtered Navier-Stokes Equations for LES	25
2.2.2	LES subgrid modeling	28
2.3	Turbulent premixed combustion	31
2.3.1	Laminar premixed flame	31
2.3.2	Turbulent premixed flame	32
2.3.3	Turbulent flame models for LES	33
2.3.4	ATF model in turbulent combustion	33
3	Numerics	36
3.1	Overview	37
3.2	Inviscid flux calculation	38
3.2.1	Numerical schemes for spatial derivatives	38
3.2.2	Comparison of different schemes in the context of LES	44
3.3	Low Mach modifications for time step enlarging	54
3.3.1	Artificial reduction of the speed of sound	54
3.3.2	The ASR implementation for 3D multi-species N-S equations	56
3.3.3	Test-cases for ASR method	61
3.4	Boundary conditions for “synthetic” HIT injection	65
3.4.1	HIT field built from experimental measurements	65
3.4.2	Characteristic boundary conditions for HIT injection	68
4	Academic test-cases	70
4.1	One dimensional laminar premixed flame	71
4.1.1	ILES of 1D laminar premixed flame	71
4.1.2	1D premixed laminar flame with ATF model	76
4.2	HIT decaying	78

4.2.1	Initial field generation	78
4.2.2	Comparison of different LES strategies	79
4.3	Two dimensional turbulent flame	83
4.3.1	Comparison between different LES strategies	83
4.3.2	Discussion and improvements	88
5	Three dimensional multi-scale forcing turbulent premixed combustion	94
5.1	Non-reactive simulation	94
5.1.1	Numerical setup	94
5.1.2	Results and discussions	96
5.2	Simulations of 3D reactive cases	102
5.2.1	Numerical setup	102
5.2.2	Results and discussions	102
6	Conclusions and perspectives	107
	Appendices	109
A	Chemical Schemes	110
A.1	One step CH ₄ /Air chemical schemes	110
A.2	9 species 28 reactions H ₂ -Air chemical schemes	111
B	Numerical Details	112
B.1	The WENO coefficients	112
B.2	Diagonalization of Jacobian Matrix	115
B.3	MAXIMA code for diagonalization and NSCBC	122
B.4	Computational cost for Taylor-Green and Double-Mach test cases	125
B.5	Stream function with a given spectrum	126
C	(I)LES nomenclature	127

List of symbols

$[A]$	Molar concentration of species A
δ	Diffusive flame thickness
δ_L^0	Thermal flame thickness
δ_{ij}	Kronecker delta
$\dot{\omega}_\alpha$	Chemical source term of species α
ϵ_{ijk}	Levi-Civita symbol
η	Kolmogorov scale
γ	Specific heat ratio
λ	Thermal conductivity
$\langle \cdot \rangle$	Ensemble average
\mathcal{C}	Courant number
$D_{\alpha\beta}$	Inter-diffusion matrix of species α and β in the mixture
$\mathcal{O}(\Delta x^i)$	A value of order Δx^i
\mathcal{R}	The universal gas constant
D_a	Damköhler number
K_a	Karlovitz number
Sc	Schmidt number
μ	Dynamic viscosity
μ_α	Dynamic viscosity of species α
μ_{sgs}^t	Subgrid eddy viscosity
ν	Kinematic viscosity
∂	Partial derivative
ϕ	Equivalence ratio
ρ	Mass density
ρ_α	Mass density of species α
τ_{ij}	Viscous stress tensor

ε	Kinetic energy dissipation rate
$\tilde{\cdot}$	Favre filtered variable
Ξ	Subgrid scale flame wrinkling factor
C_p	Specific heat at constant pressure
C_v	Specific heat at constant volume
$C_{p\alpha}$	Specific heat at constant pressure for species α
$C_{v\alpha}$	Specific heat at constant volume for species α
E	Total energy
$E(K)$	3D turbulent energy spectrum
$E_{ij}(\vec{K})$	3D energy spectrum tensor
$f_{,j}$	Derivative of f on j direction
$F_{11}(K)$	1D energy spectrum
g	The gravity of Earth
j_c	Imaginary unit
$J_{\alpha j}$	Species mass flux for species α in j direction
L_{11}	Integral scale
N_{sp}	Number of species
p	Pressure
q_j	Heat flux on j direction
$Q_{ij}(\vec{\xi})$	Space correlation tensor
S_L^0	Laminar flame speed
$V_{\alpha j}$	Species diffusion velocity for species α in j direction
W	Molecular weight of the mixture
W_α	Molecular weight of species α
X_α	Mole fraction of species α
Y_α	Mass fraction of species α

Chapter 1

Introduction

Contexte et objectifs

Le cadre général de cette étude est la production d'énergie propre à partir de turbines à gaz brûlant du syngaz : un mélange de CO, H₂ et d'autres espèces. La composition du syngaz n'est pas toujours bien connue, car il provient de la biomasse, de la gazéification du charbon ou de divers déchets organiques. Si la diversité de la matière première est un atout intéressant pour cette technologie, l'incertitude quant à la composition du gaz pose problème pour une combustion complète, efficace et sûre.

Une façon d'optimiser la combustion prémélangée de syngaz est d'augmenter les interactions flamme/turbulence, i.e. la densité de surface de flamme. Pour cela, on peut augmenter le taux de turbulence du jet prémélangé comme l'ont montré Yuen & Gülder [1]. Cependant, un générateur de turbulence à simple grille ne produit guère plus que 3~4% d'intensité turbulente. Une précédente étude expérimentale par Mazellier *et al.* [2] a montré qu'un système de grilles décalées avec différents diamètres de perçage et rapports d'obstruction était capable de générer une turbulence homogène et isotrope ayant jusqu'à 15% d'intensité. Cela a conduit à construire un brûleur expérimental de type bec Bunsen au laboratoire français ICARE. Les flammes prémélangées à haute intensité turbulente ainsi générées y ont été étudiées analytiquement et expérimentalement [3, 4, 5].

La motivation initiale de ce travail de thèse était de simuler numériquement ces flammes prémélangées pour compléter les données expérimentales, et pour une meilleure compréhension des phénomènes physiques sous-jacents. Cela suppose que les méthodes numériques retenues soient capables de décrire avec suffisamment de précision les phénomènes physiques complexes mis en jeu dans les flammes turbulentes de prémélange. L'idéal serait de recourir à la Simulation Numérique Directe (SND) associée à une cinétique chimique détaillée, mais on considère en général que les SND sont trop coûteuses [6], bien que ce soit aujourd'hui possible pour un brûleur de laboratoire, étant entrés dans l'ère du calcul péta, voire exafloppique. Un tel exemple de simulation d'avant-garde est la base de données de Hawkes *et al.* [7]. A l'opposé, les méthodes statistiques en moyenne de Reynolds, dites "Reynolds Averaged Navier-Stokes" (RANS) peuvent s'exécuter sur un ordinateur de bureau moderne, mais reposent entièrement sur des modélisations physiques [8] qui ont montré leurs limites pour les configurations complexes [6, 9]. L'approche RANS reste néanmoins très utile, et est en fait la méthode pratiquement applicable en configuration industrielle. De complexité intermédiaire entre les SND et l'approche RANS, la Simulation des Grandes Echelles (SGE, ou LES en anglais pour "Large Eddy Simulation") est aujourd'hui couramment employée grâce à l'extraordinaire augmentation de la puissance des ordinateurs. Dans les SGE, les "grandes" échelles de l'écoulement turbulent sont simulées explicitement tandis que les "petites" sont modélisées. La définition des grandes et petites échelles dépend du choix d'un filtre dont la largeur n'est pas toujours bien caractérisée. Le maillage produit un premier filtrage à la fréquence de Nyquist, qui élimine les échelles dites "sous-maille". Un second filtrage peut être explicitement appliqué aux variables de l'écoulement, ou imposé implicitement par le schéma numérique. On doit plutôt parler alors d'échelles "sous-filtre". La dif-

ficulté majeure dans la SGE d'écoulements réactifs est que la flamme, c'est à dire la région où les réactions chimiques ont lieu, est généralement plus mince que la taille des mailles [10], donc typiquement à l'échelle sous-maille et *doit* être modélisée. Lors des deux dernières décénies, de nombreuses approches et de nombreux modèles ont été proposés pour décrire la structure de la flamme et ses interactions avec la turbulence [11]. La table 1 dans [12] en donne un aperçu synthétique.

Un aspect important des simulations numériques directes et des grandes échelles est que les erreurs (dispersives et surtout dissipatives) introduites par les schémas de résolution numérique de l'écoulement ont un bien plus grand impact sur la solution qu'en RANS, puisqu'une large plage d'échelles doit être fidèlement représentée [13]. Il est nécessaire d'employer des schémas à haut pouvoir de résolution, mais possédant tout de même une certaine quantité de dissipation numérique pour assurer la stabilité du calcul. Une technique de SGE alternative est l'approche dite d'Intégration Monotone (MILES), ou plus généralement des SGE Implicites (ILES) qui prétendent "capturer la physique par le numérique" [14, 15]. Cette approche, également désignée par "numerical LES" par Pope [16], repose entièrement sur les propriétés des schémas numériques pour éliminer et modéliser les petites échelles de l'écoulement simulé, au lieu d'appliquer un modèle sous-maille explicite. L'approche ILES est très controversée dans la communauté de la combustion, et dans le cadre d'écoulements réactifs, elle peut être combinée à un modèle de combustion sous-maille, ou utilisée dans l'approche quasi-laminaire, i.e. sans modèle de combustion. Il y a donc quatre stratégies possibles pour la SGE d'écoulements réactifs :

1. SGE explicite (LES) pour l'écoulement avec modèle de combustion
2. SGE explicite (LES) pour l'écoulement sans modèle de combustion
3. SGE implicite (ILES) pour l'écoulement avec modèle de combustion
4. SGE implicite (ILES) pour l'écoulement sans modèle de combustion

La première est l'approche standard, très courante dans la littérature. La seconde est moins répandue et on peut citer les travaux de Duwig *et al.* [17, 18] en combustion turbulente prémélangée, et ceux de Duwig & Fuchs [19] en combustion non-prémélangée. Les troisième et quatrième approches sont encore plus rares.

En fait, notre équipe a déjà acquis une certaine expérience dans la simulation d'écoulements turbulents réactifs à grande vitesse en configuration non-prémélangée (flammes de diffusion). Les SGE explicite et implicite d'un jet supersonique (Mach 2) air/H₂ non-prémélangé réactif [20] ont été réalisées en approche quasi-laminaire [21, 22, 23], et les SGE implicites à l'aide de schémas à capture de choc d'ordre élevé ont produit des résultats très satisfaisants. Par conséquent, il a été décidé d'extrapoler ces méthodes numériques aux présentes expériences d'écoulement prémélangé basse-vitesse. A cette fin, les points d'évolution nécessaires suivants ont été identifiés :

1. Modifier le code compressible pour traiter efficacement les écoulements à bas Mach.
2. Définir une méthodologie pour reproduire numériquement l'écoulement turbulent multi-échelles expérimental en entrée.
3. Evaluer l'approche ILES pour la combustion prémélangée sans aucun modèle de combustion.
4. Eventuellement, si besoin, implémenter un modèle sous-maille de combustion prémélangée.

Ce document décrit les différentes étapes de cette aventure. En fait, il a rapidement été constaté que les interactions complexes entre les méthodes numériques mises en œuvre et la physique simulée sont bien plus significatives pour les flammes prémélangées que pour les flammes de diffusion : les vitesses de flamme laminaire ou turbulente sont difficiles à reproduire sur des maillages grossiers. Par conséquent, l'objectif initial (la simulation de l'expérience...) s'est déplacé vers une problématique plus fondamentale : comprendre l'impact des erreurs numériques sur les résultats de (I)LES. Par

exemple, est-il nécessaire d'épaissir artificiellement le front de flamme lorsqu'on utilise un schéma dissipatif ? Le filtre implicite associé et le modèle sous-maille qui en découle sont-ils capables de simuler le plissement turbulent de la flamme ? Quelle est la résolution nécessaire pour qu'un schéma à capture de choc produise la bonne vitesse de flamme laminaire ? Dans ce but, une série d'expériences numériques a été mise en place pour traiter des cas-test académiques. Différents schémas numériques et différentes stratégies de modélisation ont été évalués, afin de tirer des conclusions aussi claires que possible.

Plan de la thèse

Ce manuscrit est organisé de la façon suivante : l'expérience à simuler est d'abord décrite à la section 1.3. Ensuite, le chapitre 2 résume les équations pour un écoulement turbulent réactif, et on y présente un nouveau modèle de combustion prémélangée récemment développé à ICARE [24]. Le chapitre 3 donne une description et une analyse approfondie des méthodes numériques employées. On y examine le pouvoir de résolution et le filtrage implicite des schémas, dans le contexte des simulations des grandes échelles. Certains points particuliers comme la formulation bas-Mach des équations ou la génération des conditions aux limites turbulentes en entrée y sont également détaillés. Le chapitre 4 est consacré aux cas-test académiques, indispensables pour définir une stratégie fiable pour les simulations de l'expérience en configurations non-réactive et réactive, détaillées au chapitre 5.

Remarque: Dans ce document, on a testé de nombreuses stratégies (I)LES, dont on donne ici une nomenclature pour une bonne lisibilité. La table 1.1 aidera le lecteur à repérer rapidement les différentes stratégies numériques tout au long du document. Elles seront détaillées au chapitre 3. Cette table se trouve également en annexe C.

1.1 Context and objectives

The framework of this study is the production of clean energy from gas turbines burning syngas: a mixture of CO, H₂ and other species. The syngas can not always be well characterized, since it may come from biomass, coal gasification or various organic wastes. If the diversity of the raw material is very attractive for these technologies, the uncertainty in the gas composition is a challenging problem for complete, efficient and safe combustion.

One way to optimize the premixed combustion of syngas is to improve the flame/turbulence interactions, i.e. the flame surface density. To that end, one can increase the turbulence intensity of the premixed jet as shown in [1]. However, simple grid turbulence generators hardly allow for more than 3~4% of turbulence intensity. A previous experimental study by Mazellier *et al.* [2] has shown that a system of shifted grids with different hole sizes and blockage ratios was able to generate a homogeneous and isotropic turbulence with intensity as high as 15%. This has led to design an experimental Bunsen burner at our laboratory ICARE, France. The resulting premixed flames with high turbulence intensity have been studied analytically and experimentally in [3, 4, 5].

The initial motivation for this work was the numerical simulation of this experimental premixed flame to supplement experimental data, and also for a better understanding of the underlying physics. This supposes that the envisaged numerical methodology should be able to describe with sufficient accuracy the complicated physics embedded in such a turbulent premixed flame. Ideally, one would like to resort to Direct Numerical Simulation together with detailed chemistry, but it is generally acknowledged that DNS is prohibitively expensive [6], although it might be feasible today for a burner at the laboratory scale, since we are now at the peta or even exascale era. Such an example of cutting-edge simulation is the database of Hawkes *et al.* [7]. At the opposite, statistical methods known as Reynolds Averaged Navier-Stokes simulations (RANS) can run on a (modern) desktop computer, but rely entirely on modeling considerations [8] that have proven their limits in complex situations [6, 9]. The RANS approach is however still very useful, and in fact the standard practical technique for industrial applications. Intermediate between DNS and RANS is the Large Eddy Simulation (LES), now routinely used thanks to the tremendous increase in computational power. In LES, the "large" turbulent scales of the flow are explicitly simulated whereas the "small" ones are modeled. The definition of large and small scales depends on the choice of a filter width, not always clearly defined. One filter is produced by the grid, which segregates the "subgrid scales" at the Nyquist frequency, the other one may be explicitly applied to the flow variables or embedded in the numerics. One should then rather speak of "subfilter scales". The central difficulty in the LES of reacting flows is that the flame, i.e. the region where chemical reactions take place, is usually thinner than the grid size [10], hence at the subgrid scale and *should* be modeled. In the last two decades, many approaches and models have been proposed to describe the flame structure and its interactions with turbulence [11]. Table 1 in [12] gives a synthetic overview of them.

An important feature of direct and large eddy simulations, is that numerical errors (dispersive, and mostly dissipative) introduced by flow solvers have a much greater impact on the solution than in RANS, since a broad range of scales has to be properly represented [13]. High-resolution schemes are required, but still featuring some amount of numerical dissipation for stability. An alternative LES technique is the Monotone Integrated LES (MILES) or more generally the Implicit LES (ILES) whose claim is "capturing physics with numerics" [14, 15]. This approach, also called *numerical LES* by Pope [16], relies entirely on numerics to remove and model the small scales from the simulated flow field, instead of applying an explicit model. ILES is quite controversial in the combustion community, and in the context of reacting flows, it may be combined with subgrid combustion models or used in the quasi-laminar, or "no-model" approach. Hence, there are four possible strategies for the LES of reacting flows:

1. Flow explicit LES with a combustion model
2. Flow explicit LES without combustion model
3. Flow ILES with a combustion model
4. Flow ILES without combustion model

The first one is the standard one, abundant in the literature. The second one is less common and examples are given by Duwig *et al.* [17, 18] in turbulent premixed combustion and by Duwig & Fuchs [19] in non-premixed combustion. The third and fourth ones are even more scarce in the literature.

In fact, our team has already gained some experience in the numerical simulation of reacting turbulent flows in high-speed non-premixed (diffusion flame) flow configurations. The implicit and explicit flow LES of a supersonic (Mach 2) diffusion air/H₂ reacting jet [20] have been performed in [21, 22, 23] in the quasi-laminar approach, and implicit LES with higher order shock-capturing methods performed quite well. Hence, the idea was to extrapolate these numerical methods to the present low-speed premixed experiment. To that end, the following obvious targets have been identified:

1. Modify the fully compressible solver to handle efficiently low-Mach flows.
2. Define a methodology to reproduce numerically the multi-scale experimental turbulent inflow.
3. Assess the ILES approach to premixed combustion without any combustion model.
4. Eventually, if needed, implement a subgrid scale premixed combustion model.

This document summarizes the different steps of this venture. In fact, it has been rapidly identified that intricate interactions between numerics and the simulated physics were much more significant for premixed than for non-premixed combustion: both laminar and turbulent premixed flame speeds are difficult to catch on coarse grids. As a consequence, the initial motivation (simulate the experiment...) has moved to a more fundamental investigation: understand the impact of numerics on (I)LES results. For instance, is it necessary to artificially thicken the flame front when dissipative numerics are used? Does the built-in numerical filters and associated implicit subgrid model mimic properly the turbulent flame wrinkling? What is the resolution needed for a shock capturing scheme to catch the correct laminar flame speed? To that end, a series of numerical experiments have been set up and applied to academic test-cases. Different numerical schemes and modeling strategies have been assessed, in order to draw conclusions as clear as possible.

1.2 Outline of this thesis

This manuscript is organized as follows: The experiment to be simulated is first described in the introduction section 1.3. Then, chapter 2 gives an overview of the governing equations in numerical

combustion, and a premixed combustion model newly derived at ICARE [24] will be presented. Chapter 3 provides thorough description and analysis of the numerical methods. The implicit filtering and resolving efficiency of different numerical schemes are scrutinized, in the context of large eddy simulations. Some specific points like the low-Mach formulation or the turbulent inflow boundary conditions are also addressed. Chapter 4 is devoted to academic test-cases, mandatory to set up reliable strategies for the final simulation of the actual experiment, both in non-reacting and reacting configurations, detailed in chapter 5.

Remark: In this document, varieties of (I)LES strategies are tested, so a nomenclature is listed here for legibility. Table 1.1 will help the reader all along the document to have a quick reference to the numerical strategy. They will be detailed in chapter 3. This table can also be found in appendix C.

Table 1.1: Nomenclature of different flow and combustion (I)LES strategies.

		Combustion	Non-reacting	Combustion ILES (Quasi-Laminar)	Combustion LES	
					Flow	Thickened flame ($\mathcal{F} = n$)
Flow ILES		4th Central+SM	4C-SM-NR			
		4th Central+SSF	4C-SSF-NR			
Flow ILES		$(1 - \alpha)$ 4th Central + α 5th Upwind	HYB$_{\alpha}$-NR			HYB$_{\alpha}$-TF$_n$-WF
		5th Upwind	UP5-NR	UP5-QL	UP5-TF$_n$	UP5-TF$_n$-WF
		WENO-JS5	JS5-NR	JS5-QL		
		WENO-M5	M5-NR			
		WENO-Z5	Z5-NR			
		WENO-MZ5	MZ5-NR	MZ5-QL		
		WENO-JS7	JS7-NR			

1.3 Experimental setup

1.3.1 The multi-scale injection

The objective of the multi-scale, multi-grid turbulence generator is to achieve a high-intensity, nearly homogeneous and isotropic turbulence (HIT). Compared to 3~4% with a single-grid generator, the multi-grid generator can lead to a HIT with turbulence intensity as high as 15% [4]. The length scales characterizing the multi-scale generated turbulence are also smaller, while the turbulent kinetic energy produced is evidently larger, especially in the small scales [2, 3].

This idea has been applied to design a Bunsen type experimental burner as sketched in figure 1.1. This burner is equipped with a multi-scale turbulence generator constituted by 3 perforated plates. The holes diameter, mesh size, blockage ratio and pressure drop coefficient of each plate are listed in table 1.2. The last grid is located 60.5mm upstream the burner exit. The burner's inner diameter is $D = 25$ mm and the bulk velocity is $U_D = 3.5$ m/s. The jet exits into a vessel in which the pressure can be varied from 0.1 to 1 MPa, matching gas turbine combustion chambers conditions. A photo of the pressurized combustion chamber and the burner can be found in figure 1.2. Results of this experiment confirm that the multi-scale turbulence generator enhances the turbulent premixed combustion by increasing the flame surface density [4, 5]. In this section, some non-reactive air/air and reactive CH_4/air experimental data will be outlined.

Table 1.2: Geometrical characteristics of the multi-scale grid where d_j , M_j , σ_j and K_j stand for the hole diameter, the mesh size, the blockage ratio and the pressure drop coefficient of the j -th perforated plate [4].

Grid	d_j (mm)	M_j (mm)	σ_j	K_j
1	1.55	2	0.46	2.43
2	3.44	5	0.57	4.41
3	7.50	12.5	0.67	8.18

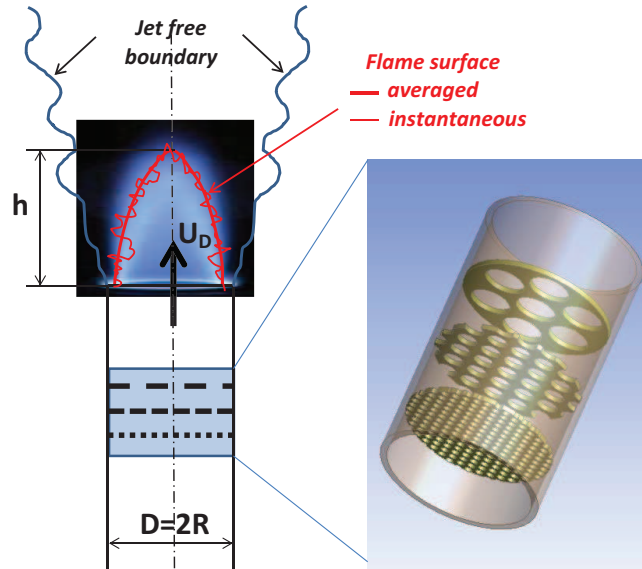


Figure 1.1: Schematic of the turbulent Bunsen burner with multi-scale forcing.

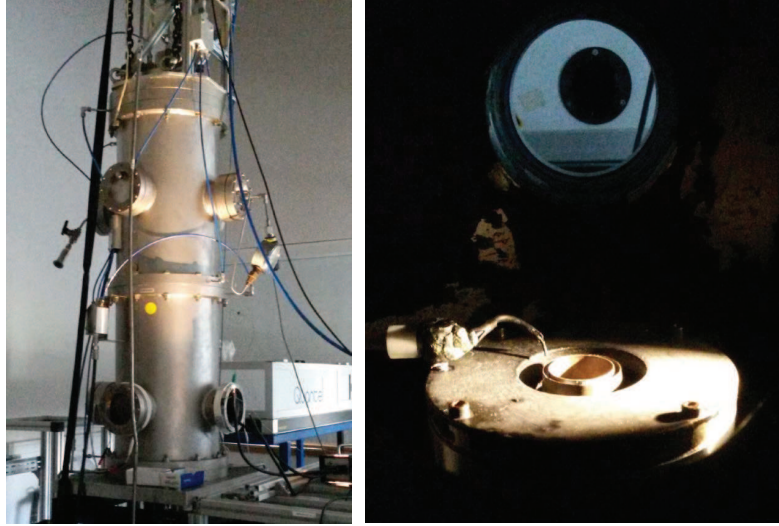


Figure 1.2: Photos of the pressurized combustion chamber (left) and the burner (right).

1.3.2 Non-reactive experiments

Non-reactive experiments are performed to obtain the flow parameters with pure air. A single hot-wire was used to measure the longitudinal velocity component $u(x)$ along the burner axis. The sensing part of the probe is $5\ \mu\text{m}$ in diameter and $1.25\ \text{mm}$ in length so that the spatial resolution, i.e. the ratio of the probe length to the Kolmogorov scale ranges between 6 and 25 depending on the operating pressure [4]. Besides hot-wire measurements, a two-channel Laser Doppler Velocimetry (LDV) system was used to study the longitudinal and radial velocity components, $u(x)$ and $v(x)$. The variation of the longitudinal velocity along the burner axis, measured by hot-wire, and the evolution of the turbulent kinetic energy along the burner axis near the jet exit measured by LDV can be found in figure 1.3(a) and 1.3(b). These curves will be used as references for the numerical simulation of the experiments. Only the case $P_{int} = 0.1\ \text{Mpa}$ is considered in this work. The main turbulent scales of the multi-scale generated turbulence at the jet exit are listed in table 1.3.

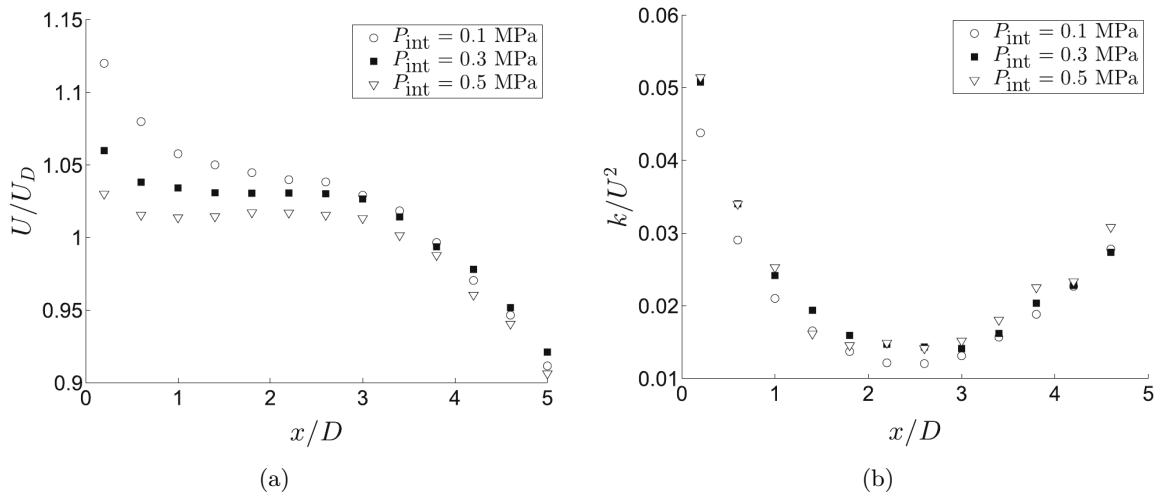


Figure 1.3: (a) Variation of U/U_D along the burner axis (hot-wire measurements); (b) Evolution of the turbulent kinetic energy along the burner axis (LDV measurements) [4].

Table 1.3: Turbulence parameters at the jet exit from non-reactive experiment results [4].

Turbulent kinetic energy(k)	Integral scale(L_{11})	Taylor micro-scale(λ)	Kolmogorov scale(η)
$0.6125 \text{ m}^2/\text{s}^2$	4.25 mm	1.25 mm	0.08 mm

1.3.3 Reactive experiments

In reactive experiments, the flow configuration is identical to the non-reactive cases except a CH_4/air mixture is injected instead of air. The flame measurements are carried out by Mie-scattering tomography at an acquisition rate of $f = 10 \text{ kHz}$. The picture resolution is $0.108 \text{ mm per pixel (mm/px)}$ and the size of the window is $800 \times 384 \text{ px}^2$. The seeding of the flow is made with silicon oil droplets supplied by an atomizer. The typical size of droplets is about $1 \mu\text{m}$. The amount of added oil droplets is assumed to be sufficiently small for not modifying the global flame properties [5]. Figure 1.4 displays a overview of the experiment apparatus, and figure 1.5 shows some example raw tomography images from experimental measurements.

The reactive experiments have been performed under varieties of conditions i.e. different pressure, equivalence ratio and types of fuel. In the current work, only the CH_4/air flame at equivalence ratio $\phi = 0.8$ under $p = 0.1 \text{ MPa}$ is used as reference experiment. The experimental flame is located on the Borghi-Peters diagram [6] as the red dot in figure 1.6 [5]. More details about the reactive experimental setup and results can be found in [3, 4, 5].

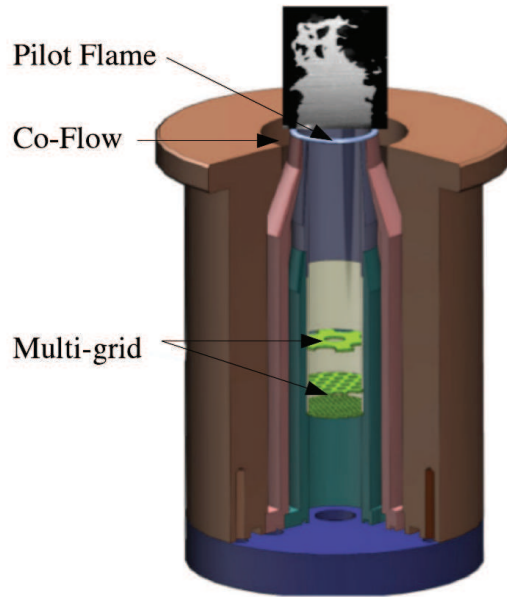


Figure 1.4: High-pressure Bunsen burner with multi-grid injection system used in the experiment [5]

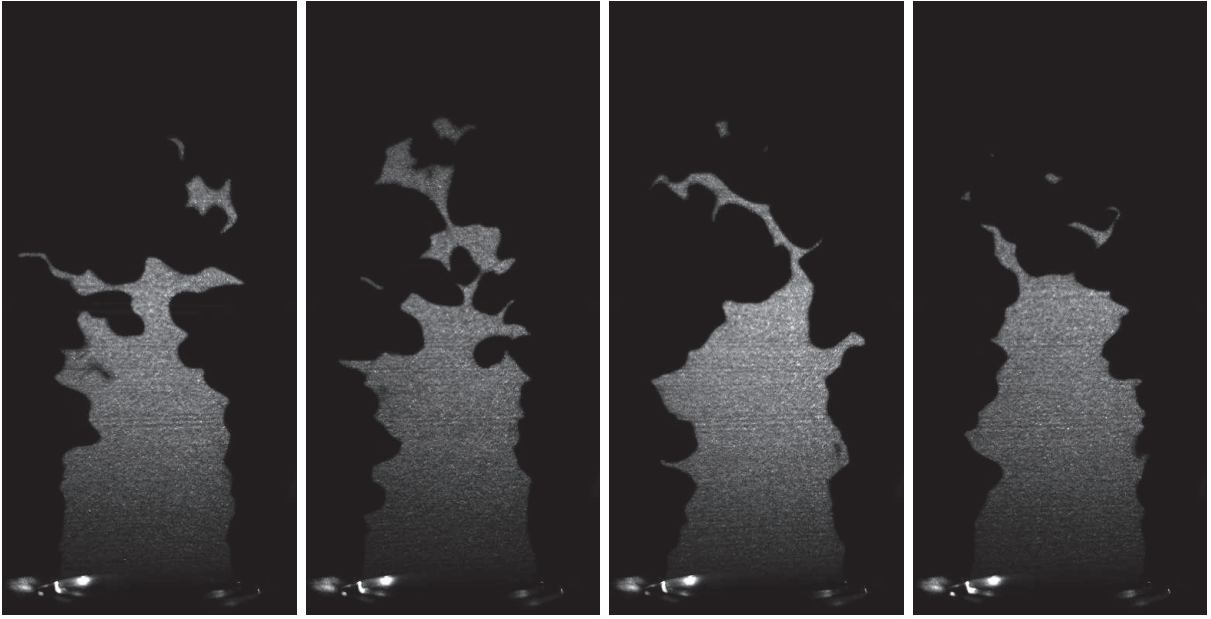


Figure 1.5: Example tomographic photos from reacting experiment. CH_4/Air flame at $\phi = 0.8$, $p = 0.1$ MPa.

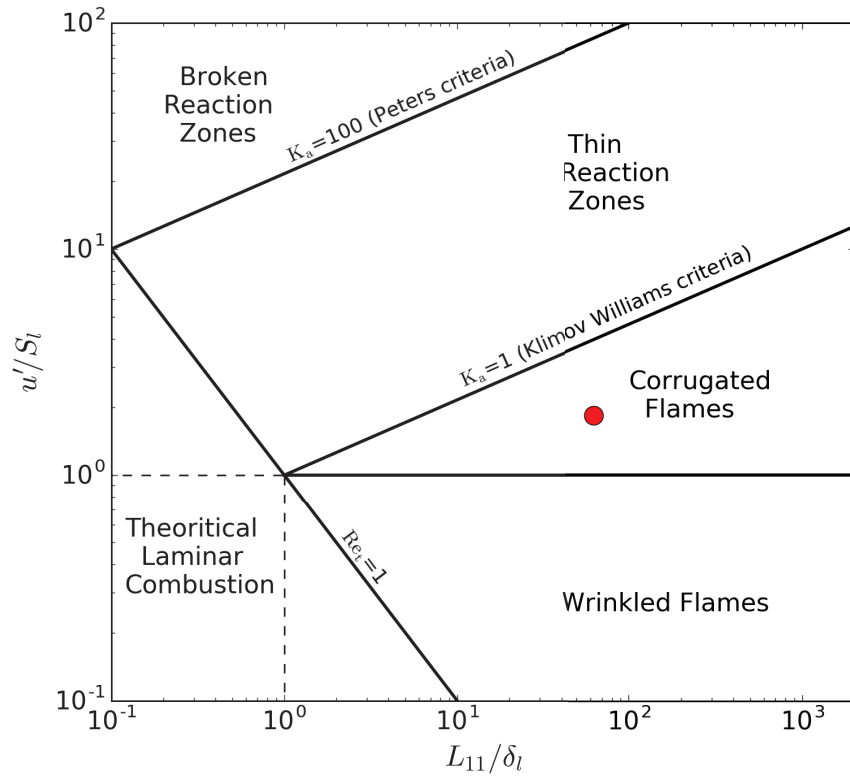


Figure 1.6: The experimental condition overlaid on the turbulent premixed combustion regime diagram [5].

Chapter 2

Governing equations for turbulent combustion

Synopsis

On présente dans ce chapitre les équations générales et les modèles physiques utilisés dans ce travail de thèse. Ce chapitre se compose de trois parties :

- La première section rappelle les équations de Navier-Stokes pour un écoulement de fluide compressible et réactif. Ces équations étant bien connues, la présentation en est volontairement limitée à l'essentiel. L'accent est toutefois mis sur les aspects multi-espèces, la cinétique chimique et les modèles de transport moléculaire.
- La seconde section présente le cadre général des SGE et détaille les équations de Navier-Stokes filtrées, en particulier les différents termes sous-mailles émergeant du filtrage des termes non-linéaires. On y évoque ensuite les différentes approches possibles pour l'écoulement (SGE explicites ou implicites) et les modélisations sous-maille associées.
- La troisième section est consacrée à la simulation de la combustion turbulente prémélangée. Les difficultés qui y sont liées sont illustrées d'abord sur le cas simple de la structure d'une flamme laminaire 1D de prémélange. On rappelle ensuite les différentes stratégies de modélisation de la combustion, puis on présente le modèle de flamme épaissie implémenté dans nos simulations, en association avec le nouveau modèle de plissement sous-maille dont les entrées et la façon de les générer lors du calcul sont finalement détaillées.

The governing equations used in this work will be presented in this chapter. As these mathematical models have already been well detailed in the literature, I would like to just briefly recall them. This chapter will be constituted by three parts: the Navier-Stokes equations will be introduced in the first section, a brief overview of Large-Eddy Simulations will be given after, and this chapter will end by the presentation of the models for premixed turbulent combustion used in this research.

2.1 Navier-Stokes equations in conservation form

The well-known Navier-Stokes (N-S) equations are used in the numerical simulation of turbulent combustion [6]. They describe the conservation laws: mass conservation, Newton's Law of motion, first principle of thermodynamics and balance of species' concentrations. The equation of state and the chemical reaction rates equations are also needed for multi-species reacting flows.

The conservation form of N-S equations for a gas mixture of N_{sp} components without body forces

are recalled here with standard notation and Einstein's convention ($i, j = 1, 2, 3$) as follows:

$$\frac{\partial \rho}{\partial t} + (\rho u_j)_{,j} = 0 \quad (2.1a)$$

$$\frac{\partial \rho u_i}{\partial t} + (\rho u_i u_j + p \delta_{ij})_{,j} = \tau_{ij,j} \quad (2.1b)$$

$$\frac{\partial \rho E}{\partial t} + [(\rho E + p) u_j]_{,j} = (u_i \tau_{ij})_{,j} - q_{j,j} \quad (2.1c)$$

$$\frac{\partial \rho Y_\alpha}{\partial t} + (\rho u_j Y_\alpha)_{,j} = -J_{\alpha j,j} + \dot{\omega}_\alpha \quad \text{for } \alpha = 1, \dots, N_{sp} \quad (2.1d)$$

An equation of state for the gas mixture should be added to close this system. In the following, I would like to briefly discuss these equations one by one. As the description of N-S equations can be easily found in any classical textbook like [6, 25] and the former work of our team on this part has already been presented in [21, 26, 27], I will just focus on the parts which are more relevant to my premixed combustion applications.

2.1.1 The equation of state

The equation of state gives basic thermodynamic properties of the material in the N-S equations. For gases, it is in the form of

$$\mathcal{F}(\rho, p, T) = 0$$

The most widely used model for dilute mono-species gas is the *perfect gas*:

$$p = \rho \frac{\mathcal{R}}{W} T$$

Here $\mathcal{R} = 8.31451 \text{ J.K}^{-1}.\text{mol}^{-1}$ is the universal gas constant; W is the molecular weight of the species. This model can be extended to multi-component cases and be used in combustion simulations. For a mixture, the mass and mole fractions of species α in the mixture should be defined at first:

$$Y_\alpha \equiv \frac{m_\alpha}{\sum_\alpha m_\alpha} = \frac{\rho_\alpha}{\rho}; \quad X_\alpha \equiv \frac{N_\alpha}{\sum_\alpha N_\alpha} = \frac{W}{W_\alpha} Y_\alpha \quad (2.2)$$

in which, m_α/N_α are the mass/moles of species α , and $\sum m/\sum N$ are the total mass/moles of the whole mixture, in a given volume. ρ_α is the partial density or mass concentration of species α ,

$$\rho_\alpha = \rho Y_\alpha$$

One may also calculate the molecular weight of the mixture W by

$$W = \frac{1}{\sum_{\alpha=1}^{N_{sp}} \frac{Y_\alpha}{W_\alpha}} = \sum_{\alpha=1}^{N_{sp}} X_\alpha W_\alpha$$

in which W_α is the molecular weight for species α .

The perfect gas model is extended to a mixture of gas by *Dalton's law*,

$$p = \sum_{\alpha=1}^{N_{sp}} p_\alpha \quad \text{where} \quad p_\alpha = \rho_\alpha \frac{\mathcal{R}}{W_\alpha} T \quad (2.3)$$

Then the equation of state for a perfect gas mixture is

$$p = \rho \frac{\mathcal{R}}{W} T = \rho \mathcal{R} T \sum_{\alpha=1}^{N_{sp}} \frac{Y_\alpha}{W_\alpha} \quad (2.4)$$

It should be noted that the molar concentration of species α , $[A_\alpha]$ is also widely used¹ especially in the context of chemistry

$$[A_\alpha] \equiv \frac{N_\alpha}{V} = \rho \frac{Y_\alpha}{W_\alpha} \quad (2.5)$$

This concentration is always in the unit of mole/m³ and should not be confused with the mole fractions X_α [6].

2.1.2 The species equations

Species mass flux

The species mass flux $J_{\alpha j}$ for species α in j direction in (2.1d) can be expressed using the species diffusion velocity $V_{\alpha j}$ ²

$$J_{\alpha j} \equiv \rho Y_\alpha V_{\alpha j} \quad [\text{kg/m}^2/\text{s}] \quad (2.6)$$

This velocity can be obtained by

$$V_{\alpha j} = - \sum_{\beta=1}^{N_{sp}} \mathcal{D}_{\alpha\beta} d_{\beta j} - D_\alpha^T (\ln T)_{,j} \quad [\text{m/s}] \quad (2.7)$$

in which, in the first term, $\mathcal{D}_{\alpha\beta}$ is the inter-diffusion matrix of species α and β in the mixture, and the diffusion driving force for the species β in the j direction is

$$d_{\beta j} = X_{\beta,j} + (X_\beta - Y_\beta) (\ln P)_{,j} \quad [\text{m}^{-1}] \quad (2.8)$$

The second term in R.H.S of (2.7), $-D_\alpha^T (\ln T)_{,j}$, is to model the thermal diffusion (*Soret effect*) and D_α^T is the thermal diffusion coefficient for species α . In this work, the coefficients in (2.7) are obtained by the EGLIB library³ [28, 29, 30].

Chemical kinetics

For the simulations of combustion, the chemical system should also be modeled for the source terms $\dot{\omega}_\alpha$ in the species equations (2.1d). A chemical reaction system that involves N_{sp} species and N_{reac} reactions reads

$$\sum_{\alpha=1}^{N_{sp}} \nu'_{\alpha j} A_\alpha \rightleftharpoons \sum_{\alpha=1}^{N_{sp}} \nu''_{\alpha j} A_\alpha \quad j = 1, \dots, N_{reac} \quad (2.9)$$

where $\nu'_{\alpha j}$ and $\nu''_{\alpha j}$ are the molar stoichiometric coefficients of species α in reaction j , corresponding to the reactants and products. The total molar coefficients $\nu_{\alpha j}$ can be defined as

$$\nu_{\alpha j} \equiv \nu''_{\alpha j} - \nu'_{\alpha j}$$

As the chemical reaction enforces the mass conservation, we have

$$\sum_{\alpha=1}^{N_{sp}} \nu_{\alpha j} W_\alpha = 0 \quad j = 1, \dots, N_{reac} \quad (2.10)$$

The source term $\dot{\omega}_\alpha$ in the N-S equation (2.1d) is the net production/consumption rate of species α . It can be calculated by the sum of production/consumption rates of species α in each reaction

$$\dot{\omega}_\alpha = \sum_{j=1}^{N_{reac}} \dot{\omega}_{\alpha j} \quad [\text{kg/m}^3/\text{s}]$$

¹where A_α is the chemical symbol of species α

²The unit after is the S.I. unit for any variable.

³In EGLIB, the diffusion velocity is obtained by solving a linear system of size $N_{sp} \times N_{sp}$. This method is accurate but very costly in calculation consumption. In fact, in the context of LES, this accurate method is not really necessary.

The rate $\dot{\omega}_{\alpha j}$ in reaction j can be computed from the rate of progress \mathcal{Q}_j of reaction j by

$$\dot{\omega}_{\alpha j} = W_{\alpha} \nu_{\alpha j} \mathcal{Q}_j \quad [\text{kg/m}^3/\text{s}]$$

The rate of progress \mathcal{Q}_j is evaluated from the rate of progress of the forward and backward reactions for reversible reactions⁴

$$\mathcal{Q}_j = K_{fj} \prod_{\alpha=1}^{N_{sp}} [A_{\alpha}]^{\nu'_{\alpha j}} - K_{rj} \prod_{\alpha=1}^{N_{sp}} [A_{\alpha}]^{\nu''_{\alpha j}} \quad [\text{mol/m}^3/\text{s}]$$

where the molar concentration of components $[A_{\alpha}]$ is evaluated from equation (2.5). K_{fj} and K_{rj} are the forward and reverse reaction rates constants for reaction j .

The modeling of rate constants is the central problem in chemical kinetics [6]. They are usually expressed in the form of Arrhenius laws

$$K_{fj} = A_{fj} T^{\beta_{fj}} \exp\left(-\frac{E_{fj}}{\mathcal{R}T}\right) \quad (2.11)$$

where the A_{fj} is the pre-exponential constant, β_{fj} is the temperature exponent and E_{fj} the activation energy⁵. For the reversible reactions, the reverse coefficients are related by the equilibrium constant K_{ej} of the reaction

$$K_{ej} = \frac{K_{fj}}{K_{rj}} = \left(\frac{P_{atm}}{\mathcal{R}T}\right)^{\sum_{\alpha=1}^{N_{sp}} \nu''_{\alpha j} - \nu'_{\alpha j}} \exp\left(\frac{\Delta S_j^0}{\mathcal{R}} - \frac{\Delta H_j^0}{\mathcal{R}T}\right) \quad (2.12)$$

in which ΔH_j^0 and ΔS_j^0 are respectively enthalpy and entropy changes of reaction j .

Normally, in practice, the constants in Arrhenius law (2.11) are inputs into the numerical combustion codes in CHEMKIN format. A simple one-step methane reaction CHEMKIN input file can be found in appendix A.1 [31]. The pre-exponential constant, the temperature exponent and the activation energy are given in the REACTIONS section of the input file in c.g.s unit system. More information on the CHEMKIN format can be found in [32].

An interesting feature of the species equations is that, if we consider the sum of all N_{sp} species equations,

$$\sum_{\alpha=1}^{N_{sp}} \left\{ \frac{\partial \rho Y_{\alpha}}{\partial t} + (\rho u_j Y_{\alpha})_{,j} = -J_{\alpha j,j} + \dot{\omega}_{\alpha} \right\} \quad (2.13)$$

Using the facts that: i) $\sum_{\alpha=1}^{N_{sp}} Y_{\alpha} = 1$; ii) $\sum_{\alpha=1}^{N_{sp}} V_{\alpha j} Y_{\alpha} = 0$; iii) sum of reaction rates

$$\sum_{\alpha=1}^{N_{sp}} \dot{\omega}_{\alpha} = \sum_{\alpha=1}^{N_{sp}} \sum_{j=1}^{N_{reac}} \dot{\omega}_{\alpha j} = \sum_{\alpha=1}^{N_{sp}} \sum_{j=1}^{N_{reac}} W_{\alpha} \nu_{\alpha j} \mathcal{Q}_j = \sum_{j=1}^{N_{reac}} \mathcal{Q}_j \sum_{\alpha=1}^{N_{sp}} W_{\alpha} \nu_{\alpha j} = 0$$

The equation (2.13) turns into the mass conservation equation (2.1). This means that the multi-species N-S equations (2.1) is over constrained. In fact, some simulations of N-S system are performed without the last species equation, i.e. $N_{sp} + 4$ equations in total, and the mass fraction of the last species is obtained by $Y_{N_{sp}} = 1 - \sum_{\alpha=1}^{N_{sp}-1} Y_{\alpha}$. In the current work, we keep using $N_{sp} + 5$ equations for numerical simplicity [21, 26].

⁴For irreversible reactions, just take the first term

⁵Or in the form of activation temperature $K_{fj} = A_{fj} T^{\beta_{fj}} \exp\left(-\frac{T_{afj}}{T}\right)$ with $T_{afj} \equiv \frac{E_{fj}}{\mathcal{R}}$

2.1.3 The momentum equation

The momentum equation (2.1b), based on Newton's second law, relates the fluid particle acceleration to the surface and body forces [33]. The viscous stress in the RHS of (2.1b), τ_{ij} , describes the viscous force from the neighbor materials. For a newtonian fluid, this term is related to the velocity field in the form:

$$\tau_{ij} = \lambda \delta_{ij} u_{k,k} + 2\mu S_{ij}^* \quad (2.14)$$

with

$$S_{ij}^* = \frac{1}{2} (u_{i,j} + u_{j,i}) \quad (2.15)$$

With the Stokes assumption applied, the viscous stress tensor can be further written as

$$\tau_{ij} = \mu S_{ij} = \mu \left(u_{i,j} + u_{j,i} - \frac{2}{3} u_{k,k} \delta_{ij} \right) \quad (2.16)$$

The transport coefficients μ for a gas mixture can be estimated using Wilke's formula [34], from the viscosity μ_α of each species

$$\mu = \frac{\sum_{\alpha=1}^{N_{sp}} X_\alpha \mu_\alpha}{\sum_{\beta=1}^{N_{sp}} X_\beta \phi_{\alpha\beta}} \quad ; \quad \phi_{\alpha\beta} = \frac{\left(1 + \sqrt{\frac{\mu_\alpha}{\mu_\beta}} \left(\frac{W_\beta}{W_\alpha} \right)^{1/4} \right)^2}{\sqrt{8 \left(1 + \frac{W_\alpha}{W_\beta} \right)}}$$

The viscosity coefficient μ_α of species α can be obtained from a polynomial fit in the temperature range [200K, 3000K] of the CHEMKIN-III model [32]. In the current work, they are calculated directly from the EGLIB library [28].

2.1.4 The energy equation

The energy equation (2.1c) gives the energy balance based on the first principle of thermodynamics. In the conservation form of N-S equations, the total energy per unit mass E ($[m^2/s^2]$) is used in the energy equation. It is the sum of internal and kinetic energy,

$$E \equiv \sum_{\alpha=1}^{N_{sp}} \left(\Delta h_\alpha^0 + \int_{T_0}^T C_{p\alpha}(\theta) d\theta \right) Y_\alpha - rT + \frac{1}{2} u_i u_i \quad (2.17)$$

In this definition of total energy, the formation enthalpy Δh_α^0 is already included. So there is no additional term to represent the heat release by chemical reactions in the energy equation (2.1c) [6].

The specific heat at constant pressure $C_{p\alpha}$ and the formation enthalpy Δh_α^0 at temperature⁶ T_0 of species α in equation (2.17) can be taken from thermodynamic databases like A. Burcat and B. Ruscic polynomial thermodynamic database [35].

The heat flux q_j in R.H.S of (2.1c) can be further detailed into three parts:

$$q_j = \sum_{\alpha=1}^{N_{sp}} h_\alpha J_{\alpha j} - \lambda T_{,j} - p \sum_{\alpha=1}^{N_{sp}} D_\alpha^T d_{\alpha j} \quad (2.18)$$

The meanings of these terms are

$\sum_{\alpha=1}^{N_{sp}} h_\alpha J_{\alpha j}$: The heat flux due to partial enthalpy fluxes of species α

$-\lambda T_{,j}$: Heat transfer by conduction computed by Fourier law, λ here is the thermal conductivity of the mixture.

$-p \sum_{\alpha=1}^{N_{sp}} D_\alpha^T d_{\alpha j}$: Heat transfer induced by concentration gradients, also known as thermal diffusion effect, or *Duffour effect* [28, 30]⁷.

⁶ $T_0 = 298.15K$ for CHEMKIN and $298K$ for Burcat database

⁷In the current work, both *Duffour* and *Soret* effects are neglected in the simulations

2.1.5 N-S equations in vector form

As summary, N-S equations rearranged in vector form read:

$$\frac{\partial \mathbf{U}}{\partial t} + \frac{\partial \mathbf{F}}{\partial x} + \frac{\partial \mathbf{G}}{\partial y} + \frac{\partial \mathbf{H}}{\partial z} = \mathbf{V} + \mathbf{S} \quad (2.19)$$

where \mathbf{U} is the vector of conservative variables

$$\mathbf{U} \equiv \begin{bmatrix} \rho \\ \rho u \\ \rho v \\ \rho w \\ \rho E \\ \rho Y_1 \\ \vdots \\ \rho Y_{N_{sp}} \end{bmatrix} \quad (2.20)$$

\mathbf{F} , \mathbf{G} and \mathbf{H} are the fluxes in x , y and z directions

$$\mathbf{F} \equiv \begin{bmatrix} \rho u \\ \rho u^2 + p \\ \rho uv \\ \rho uw \\ \rho Eu + pu \\ \rho u Y_1 \\ \vdots \\ \rho u Y_{N_{sp}} \end{bmatrix} \quad \mathbf{G} \equiv \begin{bmatrix} \rho v \\ \rho vu \\ \rho v^2 + p \\ \rho vw \\ \rho Ev + pv \\ \rho v Y_1 \\ \vdots \\ \rho v Y_{N_{sp}} \end{bmatrix} \quad \mathbf{H} \equiv \begin{bmatrix} \rho w \\ \rho wu \\ \rho wv \\ \rho w^2 + p \\ \rho Ew + pw \\ \rho w Y_1 \\ \vdots \\ \rho w Y_{N_{sp}} \end{bmatrix} \quad (2.21)$$

\mathbf{V} represents the viscous terms

$$\mathbf{V} \equiv \begin{bmatrix} 0 \\ \tau_{xx,x} + \tau_{xy,y} + \tau_{xz,z} \\ \tau_{yx,x} + \tau_{yy,y} + \tau_{yz,z} \\ \tau_{zx,x} + \tau_{zy,y} + \tau_{zz,z} \\ v_5 \\ -J_{1x,x} - J_{1y,y} - J_{1z,z} \\ \vdots \\ -J_{N_{sp}x,x} - J_{N_{sp}y,y} - J_{N_{sp}z,z} \end{bmatrix} \quad (2.22)$$

with

$$v_5 = (u_i \tau_{ij})_{,j} - q_{j,j} \quad \text{for } i, j = 1, 2, 3$$

And the source term \mathbf{S} is

$$\mathbf{S} \equiv \begin{bmatrix} 0 \\ 0 \\ 0 \\ 0 \\ 0 \\ \dot{\omega}_1 \\ \vdots \\ \dot{\omega}_{N_{sp}} \end{bmatrix} \quad (2.23)$$

2.2 Large-Eddy Simulations

After the governing equations for turbulent combustion presented in the previous section, the methods to numerically solve these PDEs are considered. As evoked in the introduction, three main kinds of numerical approaches are used for simulations based on N-S equations. They are Direct Numerical Simulation (DNS), Reynolds Averaged Navier-Stokes Simulations (RANS) and Large-Eddy Simulations (LES). We recall briefly their respective features:

As the N-S equations describe all the length scales in the turbulent flow, DNS are very costly since no modeling is used for any turbulent scale. Until now, the DNS is still not accessible for most complex flows due to the high consumption of computational resources [33].

At the opposite, Reynolds Averaged Navier-Stokes Simulations are generally much less numerically costly with *all* the turbulent scales modeled. But the nature of *average* indicates the RANS simulations generally lack the ability of analyzing the dynamics of the flow.

Lying between these two approaches, Large-Eddy Simulations (LES) explicitly calculate the large scales (scales typically larger than a given filter width) to obtain the dynamics of the turbulent flow and use models for the small and dissipative scales. This approach is developing fast in the last decades thanks to High Performance Computing [33, 16, 36]. In this section, the basic concepts of LES for premixed turbulent combustion will be illustrated.

2.2.1 Filtered Navier-Stokes Equations for LES

The balance equations applied in LES describe the motion of large scales. Theoretically, they should be obtained by linear low-pass filtering operations on the N-S equations (2.1) [16, 37]. A linear filtering process for a variable $\xi(\vec{x}, t)$ reads

$$\bar{\xi}(\vec{x}, t) \equiv \int \xi(\vec{x}', t) G(\vec{x}' - \vec{x}, t) d\vec{x}' \quad (2.24)$$

where the function G is called the kernel of the filter. Usually the filters used in LES are homogeneous⁸ low-pass filters, like cut-off (low-pass) filters in spectral space, box filters and Gaussian filters in physical space [6, 36].

The output of the process, $\bar{\xi}(\vec{x}, t)$, is the filtered variable. Like in RANS where the variables are separated into averages and fluctuations, after the filtering process in LES, any variable ξ can be expressed as sum of the *filtered variable* and the *residual*:

$$\xi \equiv \bar{\xi} + \xi' \quad (2.25)$$

Theoretically, with low-pass filters, the filtered variable $\bar{\xi}$ can be the large-scale part of the original variable ξ . The equations for these filtered variables are then deduced by applying the filtering process to the N-S equations. This procedure is quite similar to the averaging process for averaged equations in RANS. Take the continuity equation (2.1a) as an example, applying filtering (2.24) to both sides of equation, we have

$$\int \left\{ \frac{\partial \rho}{\partial t} + (\rho u_j)_{,j} \right\} G d\vec{x}' = 0$$

For the homogeneous filter G , the convolution commutes with time and space differential operations [38], then

$$\frac{\partial \bar{\rho}}{\partial t} + (\bar{\rho} \bar{u}_j)_{,j} = 0$$

To avoid sub-filter terms in continuity equation, the mass-weighted Favre filter can be used also in LES filtered equations [36]. Similar to compressible RANS simulations, a Favre filter $\tilde{\cdot}$ can be defined as:

$$\bar{\rho} \tilde{\xi} \equiv \int \rho(\vec{x}', t) \xi(\vec{x}', t) G(\vec{x} - \vec{x}', t) d\vec{x}' \equiv \overline{\rho \xi} \quad (2.26)$$

⁸kernel G is independent of \vec{x} and t

Then the filtered mass conservation equation turns into:

$$\frac{\partial \bar{\rho}}{\partial t} + (\bar{\rho} \tilde{u}_j)_{,j} = 0$$

Applying similar treatments to all the N-S equations gives:

$$\frac{\partial \bar{\rho}}{\partial t} + (\bar{\rho} \tilde{u}_j)_{,j} = 0 \quad (2.27a)$$

$$\frac{\partial \bar{\rho} \tilde{u}_i}{\partial t} + (\bar{\rho} \tilde{u}_i \tilde{u}_j + \hat{p} \delta_{ij})_{,j} = \left(\tilde{\mu} \tilde{S}_{ij} \right)_{,j} + (A_{1ij} + A_{2ij} + A_3 \delta_{ij})_{,j} \quad (2.27b)$$

$$\frac{\partial \bar{\rho} \tilde{E}}{\partial t} + \left[(\bar{\rho} \tilde{E} + \hat{p}) \tilde{u}_j \right]_{,j} = (\tilde{u}_i \hat{\tau}_{ij})_{,j} - \hat{q}_{j,j} + (B_{1j} + B_{2j} + B_{3j} + B_{4j})_{,j} \quad (2.27c)$$

$$\frac{\partial \bar{\rho} \tilde{Y}_\alpha}{\partial t} + (\bar{\rho} \tilde{u}_j \tilde{Y}_\alpha)_{,j} = -\hat{J}_{\alpha j,j} + \hat{\omega}_\alpha + (C_{1\alpha j} + C_{2\alpha j})_{,j} + C_{3\alpha} \quad (2.27d)$$

Three types of variables can be found after filtering in (2.27):

1. Filtered/resolved variables. Like filtered density $\bar{\rho}$, Favre filtered velocity \tilde{u}_i etc. They are denoted by $\bar{\cdot}$ and $\tilde{\cdot}$. They are provided directly by the numerical solution of the LES equations.
2. Variables computed from filtered variables directly. Like \hat{T} , \hat{p} , \hat{q}_j , $\hat{\tau}_{ij}$, $\hat{\omega}_\alpha$ etc. These variables can be computed *directly* from the variables of first type, for example, the resolved temperature \hat{T} is calculated from the resolved total energy and velocity with

$$\tilde{E} = \sum_{\alpha=1}^{N_{sp}} \left(\Delta h_\alpha^0 + \int_{T_0}^{\hat{T}} C_{p\alpha}(\theta) d\theta \right) Y_\alpha - \tilde{r} \hat{T} + \frac{1}{2} \tilde{u}_i \tilde{u}_i \quad (2.28)$$

This set of variables are denoted by $\hat{\cdot}$ in (2.27).

3. Sub-filter scale (SFS) terms. Generally speaking, these sub-filter terms represent the effect of scales smaller than the filter size on large scales. They are also called sub-grid scale (SGS) terms in the literature. Their notations start with A , B and C in (2.27). Their appearance in the filtered N-S equations is mainly due to the non-linear operations in N-S equations that can not commute with the filtering convolution operation. They can be written as⁹:

$$A_{1ij} \equiv -\bar{\rho} (\widetilde{u_i u_j} - \tilde{u}_i \tilde{u}_j) \quad (2.29a)$$

$$A_{2ij} \equiv \overline{\mu S_{ij}} - \tilde{\mu} \tilde{S}_{ij} \quad (2.29b)$$

$$A_3 \equiv \bar{\rho} (\overline{rT} - \tilde{r} \hat{T}) \quad (2.29c)$$

$$B_{1j} \equiv -\bar{\rho} (\overline{E u_j} - \tilde{E} \tilde{u}_j) \quad (2.29d)$$

$$B_{2j} \equiv -(\overline{p u_j} - \hat{p} \tilde{u}_j) \quad (2.29e)$$

$$B_{3j} \equiv \overline{u_i \tau_{ij}} - \tilde{u}_i \hat{\tau}_{ij} \quad (2.29f)$$

$$B_{4j} \equiv (\overline{\lambda T_{,j}} - \tilde{\lambda} \hat{T}_{,j}) - \sum_{\alpha=1}^{N_{sp}} (\overline{h_\alpha J_{\alpha j}} - \hat{h}_\alpha \hat{J}_{\alpha j}) \quad (2.29g)$$

$$C_{1\alpha j} \equiv -\bar{\rho} (\widetilde{u_j Y_\alpha} - \tilde{u}_j \tilde{Y}_\alpha) \quad (2.29h)$$

$$C_{2\alpha j} \equiv -\overline{J_{\alpha j}} + \hat{J}_{\alpha j} \quad (2.29i)$$

$$C_{3\alpha} \equiv \overline{\omega_\alpha} - \hat{\omega}_\alpha \quad (2.29j)$$

⁹The expression of these SFS terms may be different in the literature.

Sorting these balance equations for LES in vector form, one may get:

$$\frac{\partial \hat{\mathbf{U}}}{\partial t} + \frac{\partial \hat{\mathbf{F}}}{\partial x} + \frac{\partial \hat{\mathbf{G}}}{\partial y} + \frac{\partial \hat{\mathbf{H}}}{\partial z} = \hat{\mathbf{V}} + \boldsymbol{\tau} + \hat{\mathbf{S}} \quad (2.30)$$

where $\hat{\mathbf{U}}$ is the vector of primary variables resolved in LES,

$$\hat{\mathbf{U}} \equiv \begin{bmatrix} \bar{\rho} \\ \bar{\rho}\tilde{u} \\ \bar{\rho}\tilde{v} \\ \bar{\rho}\tilde{w} \\ \bar{\rho}\tilde{E} \\ \bar{\rho}\tilde{Y}_1 \\ \vdots \\ \bar{\rho}\tilde{Y}_{N_{sp}} \end{bmatrix} \quad (2.31)$$

$\hat{\mathbf{F}}$, $\hat{\mathbf{G}}$ and $\hat{\mathbf{H}}$ are, respectively, the inviscid or Euler resolved fluxes in x , y and z directions

$$\hat{\mathbf{F}} \equiv \begin{bmatrix} \bar{\rho}\tilde{u} \\ \bar{\rho}\tilde{u}^2 + \hat{p} \\ \bar{\rho}\tilde{u}\tilde{v} \\ \bar{\rho}\tilde{u}\tilde{w} \\ \bar{\rho}\tilde{E}\tilde{u} + \hat{p}\tilde{u} \\ \bar{\rho}\tilde{u}\tilde{Y}_1 \\ \vdots \\ \bar{\rho}\tilde{u}\tilde{Y}_{N_{sp}} \end{bmatrix} \quad \hat{\mathbf{G}} \equiv \begin{bmatrix} \bar{\rho}\tilde{v} \\ \bar{\rho}\tilde{v}\tilde{u} \\ \bar{\rho}\tilde{v}^2 + \hat{p} \\ \bar{\rho}\tilde{v}\tilde{w} \\ \bar{\rho}\tilde{E}\tilde{v} + \hat{p}\tilde{v} \\ \bar{\rho}\tilde{v}\tilde{Y}_1 \\ \vdots \\ \bar{\rho}\tilde{v}\tilde{Y}_{N_{sp}} \end{bmatrix} \quad \hat{\mathbf{H}} \equiv \begin{bmatrix} \bar{\rho}\tilde{w} \\ \bar{\rho}\tilde{w}\tilde{u} \\ \bar{\rho}\tilde{w}\tilde{v} \\ \bar{\rho}\tilde{w}^2 + \hat{p} \\ \bar{\rho}\tilde{E}\tilde{w} + \hat{p}\tilde{w} \\ \bar{\rho}\tilde{w}\tilde{Y}_1 \\ \vdots \\ \bar{\rho}\tilde{w}\tilde{Y}_{N_{sp}} \end{bmatrix} \quad (2.32)$$

$\hat{\mathbf{V}}$ is the vector of viscous fluxes,

$$\hat{\mathbf{V}} \equiv \begin{bmatrix} 0 \\ \hat{\tau}_{xx,x} + \hat{\tau}_{xy,y} + \hat{\tau}_{xz,z} \\ \hat{\tau}_{yx,x} + \hat{\tau}_{yy,y} + \hat{\tau}_{yz,z} \\ \hat{\tau}_{zx,x} + \hat{\tau}_{zy,y} + \hat{\tau}_{zz,z} \\ \hat{v}_5 \\ -\hat{J}_{1x,x} - \hat{J}_{1y,y} - \hat{J}_{1z,z} \\ \vdots \\ -\hat{J}_{N_{sp}x,x} - \hat{J}_{N_{sp}y,y} - \hat{J}_{N_{sp}z,z} \end{bmatrix} \quad (2.33)$$

with

$$\hat{v}_5 = (\tilde{u}_i \hat{\tau}_{ij})_{,j} - \hat{q}_{j,j}$$

$\hat{\mathbf{S}}$ is the vector of chemical source terms,

$$\hat{\mathbf{S}} \equiv \begin{bmatrix} 0 \\ 0 \\ 0 \\ 0 \\ 0 \\ \hat{\omega}_1 \\ \vdots \\ \hat{\omega}_{N_{sp}} \end{bmatrix} \quad (2.34)$$

τ represents the vector of explicit sub-filter terms:

$$\tau \equiv \begin{bmatrix} 0 \\ (A_{11j} + A_{21j} + A_3\delta_{1j}), j \\ (A_{12j} + A_{22j} + A_3\delta_{2j}), j \\ (A_{13j} + A_{23j} + A_3\delta_{3j}), j \\ (B_{1j} + B_{2j} + B_{3j} + B_{4j}), j \\ (C_{11j} + C_{21j}), j + C_{31} \\ \vdots \\ (C_{1N_{sp}j} + C_{2N_{sp}j}), j + C_{3N_{sp}} \end{bmatrix} \quad (2.35)$$

with the SFS terms in equations (2.29a) to (2.29j).

In these equations, the variables \widehat{U} , \widehat{F} , \widehat{G} , \widehat{H} , \widehat{V} and \widehat{S} are available during simulation, meanwhile, the SFS term τ has to be modeled. The closure process for LES equations will be discussed after.

2.2.2 LES subgrid modeling

Formally, the continuous LES equations (2.27) describe scales larger than the filter width Δ , and the SFS terms (2.29) need to be modeled during simulations. When these filtered equations are solved numerically on a grid with spacing h ($h \leq \Delta$), the whole process becomes much more complicated. In numerical simulations, numerical errors are always difficult to be eliminated, especially for the simulations with non-spectral methods. Particularly, in LES, as the subfilter terms (scales from η to Δ) are also relatively small, these numerical errors may even be at the same scale and can mimic the SFS models.

To deal with the influence to the SFS terms by the numerics, three kinds of strategies were proposed. One strategy is to separate the two by minimizing the numerical errors and using well designed physical subgrid models. Normally, this leads to high computational consumption because of fine grids and accurate numerical schemes, like spectral methods in Fourier space, or higher-order centered compact finite difference schemes [39] in physical space for instance. This approach is called (*pure*) *physical LES* by Pope in [16]. Or, one can use less accurate numerical schemes and the subgrid model together, but in this case, both the schemes and subgrid models should be tuned with great care together for reliable results as suggested in [40]; Also, as pointed out by some authors in [15, 33, 41, 37], the numerical errors have similar properties as the subgrid model. This leads to the third way to deal with this issue: one may give up subgrid modeling to fully count on numerical residuals as the subgrid model. At the opposite of pure physical LES, this approach is named as *implicit LES* (ILES) or *numerical LES* [22, 23, 33, 16].

Physical LES

In physical LES, subgrid terms are explicitly modeled from large-scale quantities. From the beginning of LES, the pioneers in this field proposed many SGS models [33, 16, 37, 42, 43]. In this section, two LES models used in the present work are introduced briefly; The modeling for the subgrid source terms ($C_{3\alpha}$ in (2.27d)) in species equations for reacting flows will be discussed later in section 2.3.

Generally speaking, LES subgrid models start with the modeling of the unresolved Reynolds stress terms (A_{1ij} in (2.27b)). At this stage, the Boussinesq assumption is commonly used for the modeling of unresolved momentum fluxes by introducing the subgrid eddy viscosity μ_{sgs}^t as

$$\bar{\rho}(\widetilde{u_i u_j} - \widetilde{u_i} \widetilde{u_j}) - \frac{2}{3} \bar{\rho} k_{sgs} \delta_{ij} = -\mu_{sgs}^t \widetilde{S_{ij}} \quad (2.36)$$

with

$$\widetilde{S_{ij}} = \left(\widetilde{u_{i,j}} + \widetilde{u_{j,i}} - \frac{2}{3} \widetilde{u_{k,k}} \delta_{ij} \right)$$

The two methods of evaluating the subgrid eddy viscosity used in the current study are as follows.

Smagorinsky model Because of its simple formulation, the Smagorinsky subgrid-scale model (SM model) is very popular and can be used as a base model for other LES models [6]. The commonly used form of SM model for variable density flows reads [22, 44, 45]:

$$\begin{aligned}\mu_{sgs}^t &= \bar{\rho} (C_S \Delta)^2 |\widetilde{S}^*| \\ |\widetilde{S}^*| &\equiv \left(2\widetilde{S}_{ij}^* \widetilde{S}_{ij}^* \right)^{\frac{1}{2}} \\ \widetilde{S}_{ij}^* &\equiv \frac{1}{2} \left(\widetilde{u}_{i,j} + \widetilde{u}_{j,i} \right)\end{aligned}\quad (2.37)$$

where C_S is a model constant and Δ is the filter size or turbulence resolution length scale. The isotropic contribution $-\frac{2}{3}\bar{\rho}k_{sgs}\delta_{ij}$ in (2.36) is unknown and is usually absorbed into the filtered pressure \widehat{p} . In compressible LES, this isotropic part is generally modeled using Yoshizawa model [6, 46], but for this study, as we focus on the low speed turbulent combustion applications, this term is neglected.

In practice, the filter width Δ is usually very difficult to predict. In the current work, the term $(C_S \Delta)$ in (2.37) is evaluated as (εh) where $h = (\Delta x_1 \Delta x_2 \Delta x_3)^{1/3}$ and ε is taken as $\varepsilon^2 = 0.02$. Taking the constant $C_S = 0.1$, this may be interpreted as varying the numerical accuracy $\Delta/h = \sqrt{2}$. This is the usual range for physical LES using dissipative numerical schemes (question 7 in [16]). However, for more accurate simulations, the Smagorinsky constant should be adapted to the build-in filter width of the numerical scheme [47], or computed dynamically.

Selective Structure Function The Selective Structure Function (SSF) model also follows Boussinesq assumption (2.36) for the calculation of unresolved Reynolds stress. This closure models the subgrid eddy viscosity by

$$\mu_{sgs}^t = f_{\theta_0}(\theta) C_{SF} \Delta \bar{\rho} [F_2(\vec{x}, \Delta)]^{1/2} \quad (2.38)$$

In the standard formulation of the SF model for a uniform grid $h = \Delta x_i = \text{Const}$, the second order structure function $F_2(\vec{x}, \Delta)$ is computed from differences in the resolved velocity field at neighboring grid points, and $\Delta = h$. In the case of a non-uniform grid, the structure function is computed as an algebraic mean of the 1D structure functions over the three directions of space with unit vector \vec{e}_i

$$F_2(\vec{x}, \Delta) = \frac{1}{6} \sum_{i=1}^3 F_2^{(i)} \left(\frac{\Delta}{\Delta x_i} \right)^{2/3} \quad (2.39)$$

$$\begin{aligned}F_2^{(i)} &= \|\vec{u}(\vec{x}) - \vec{u}(\vec{x} + \Delta x_i \vec{e}_i)\|^2 \\ &+ \|\vec{u}(\vec{x}) - \vec{u}(\vec{x} - \Delta x_i \vec{e}_i)\|^2\end{aligned}\quad (2.40)$$

The SSF model includes a sensor for the three-dimensionality of the vorticity field

$$f_{\theta_0}(\theta) = \begin{cases} 1 & \text{if } \theta \geq \theta_0 = 20^\circ \\ 0 & \text{else} \end{cases} \quad (2.41)$$

where θ is the angle between the local vorticity vector and the average vorticity vector built from the six closest neighboring points. This allows to switch-off the model in regions where sharp gradients are present but where the flow is not three-dimensional enough.

The model constant C_{SF} in this work is taken as

$$C_{SF} = 0.105 C_K^{-3/2} = 0.0634 \quad (2.42)$$

where $C_K = 1.4$ is the Kolmogorov constant. Further discussion on this model can be found in [36, 48].

After the unresolved Reynolds stress are evaluated by any of the above models, SGS terms in the species and energy equations are computed using the unresolved Reynolds stress terms with

dimensionless parameters like the SGS Schmidt number and the SGS Prandtl number [22, 6, 33]. The sum of the two major subgrid terms $B_{1j} + B_{2j}$ in energy equation (2.27c) is modeled as a whole with a gradient assumption, using a constant subgrid Prandtl number

$$B_{1j} + B_{2j} = -\frac{\mu_{sgs}^t C_p}{Pr_{sgs}} \widehat{T}_{,j} = -\lambda_{sgs}^t \widehat{T}_{,j} \quad (2.43)$$

The unresolved scalar fluxes ($C_{1\alpha j}$ terms in (2.27d)) is calculated with Schmidt number Sc_{sgs} as

$$C_{1\alpha j} = -\frac{\mu_{sgs}^t}{Sc_{sgs}} \widetilde{Y}_{\alpha,j} = -\bar{\rho} D_{sgs}^t \widetilde{Y}_{\alpha,j} \quad (2.44)$$

Other SGS terms in (2.27) are generally neglected or considered to be closed together with the modeled SGS terms [22, 36].

After the SGS terms closed with SGS models, the LES equations (2.27) which describe scales of motion larger than the filter width Δ can be solved. But in practice, when the simulation of these continuous LES equations (2.27) is performed numerically on a grid with spacing h , the situation is far more complicated. In practice, one chooses $h \leq \Delta$ and $h \gg \eta$, where η is the Kolmogorov scale typical of the smallest eddies that should be accurately resolved in a DNS. The projective filter at the Nyquist frequency induced by the grid, creates another unknown correlations (or stress tensors), which is in the range $[\eta, \Delta]$ due to subfilter scales (SFS), while the other is due to subgrid scales (SGS) in the range $[\eta, h]$. The effect of unresolved SGS and SFS turbulent scales must be modeled while the SFS in the range $[h, \Delta]$ can be theoretically reconstructed if the filter kernel is known [49]. In practice, the continuous filtering operation may be explicit or implicit.

ILES approach

The implementation of ILES can be written in vector form as

$$\frac{\delta \hat{\mathbf{U}}}{\delta t} + \frac{\delta \hat{\mathbf{F}}}{\delta x} + \frac{\delta \hat{\mathbf{G}}}{\delta y} + \frac{\delta \hat{\mathbf{H}}}{\delta z} = \hat{\mathbf{V}} + \hat{\mathbf{S}} \quad (2.45)$$

Compared to the general LES balance equations (2.30), one may find that the subgrid terms $\tilde{\tau}$ is absent and the operator δ takes the place of partial difference operator ∂ . This operator δ here means numerical differential operations on the variables, and should be chosen carefully to recover the subgrid terms. Practically, the ILES is just a LES strategy that use some specific numerical schemes on a under-resolved grid to simulate the N-S equations without any subgrid model.

As the ILES is less evident in physical meaning, this approach is still quite controversial and not discussed much. Recently, the ILES has proven to be acceptable for high speed non-reactive and reactive flows with WENO schemes [22, 23, 50]. For further assessment of ILES, especially for low speed reacting flows, in this study, this strategy will be applied and compared with the traditional physical LES. As the implicit LES is closely connected to the numerics, it will be illustrated in depth in chapter 3.

2.3 Turbulent premixed combustion

As mentioned in the last section, the SGS combustion source terms in the LES equations (2.27d) should also be modeled. Apparently, this modeling process needs the understanding of the combustion phenomenon. Therefore, in this section, a brief introduction to combustion, especially premixed combustion will be given first with a one-dimensional laminar premixed flame test-case; The basic physics of turbulent combustion will be illustrated after. LES models for turbulent premixed combustion used in this work will be discussed at the end of this section.

2.3.1 Laminar premixed flame

A one-dimensional laminar premixed flame is a good example to illustrate the premixed flame structure. It provides the basic principles of combustion and can be the elementary building block of numerical simulation of turbulent flames [6, 11]. The one-dimensional premixed laminar flame describes a flame propagating from the hot, burnt gas mixture into the fuel/oxidizer mixture, the fresh gas. The mass fractions of species in the fresh gas are always denoted by the *equivalence ratio*, which is defined from the *stoichiometric ratio*. Let denote ν'_F and ν'_O as the coefficients corresponding to fuel and oxidizer, when an overall unique reaction is considered



the ratio of mass fractions of fuel and oxidizer is then the mass stoichiometric ratio s

$$s \equiv \frac{\nu'_O W_O}{\nu'_F W_F} = \left(\frac{Y_O}{Y_F} \right)_{st} \quad (2.47)$$

and the equivalence ratio of a given mixture is then:

$$\phi \equiv s \frac{Y_F}{Y_O} = \left(\frac{Y_F}{Y_O} \right) / \left(\frac{Y_F}{Y_O} \right)_{st} \quad (2.48)$$

The equivalence ratio is a central parameter for premixed gases: rich combustion is obtained for $\phi > 1$ (the fuel is in excess) while lean regimes are achieved when $\phi < 1$ (the oxidizer is in excess).

The flame structure and the laminar flame propagation speed can be studied in 1D premixed laminar flame. For example, figure 2.1 shows a H₂-air 1D premixed combustion under atmospheric pressure and ambient room temperature (300K). The equivalence ratio of this case is $\phi = 0.8$. The chemical mechanism used in this test case is shown in appendix A.2. The normalized fuel (H₂), product (H₂O) and intermediate radicals (H₂O₂) mass fractions are plotted along the calculation 1D domain in figure 2.1(a). The normalized temperature and H₂ reaction rate $\dot{\omega}_{H_2}$ profiles are given in figure 2.1(b).

The flame thickness is a key parameter to describe the flame structure. Among several definitions of flame thickness, the *thermal thickness* is often used in numerical simulations and is a good length scale for premixed flames. It is defined as:

$$\delta_L^0 \equiv \frac{T_b - T_f}{\max \left| \frac{\partial T}{\partial x} \right|} \quad (2.49)$$

in which the T_f and T_b is the temperature in fresh and burnt gas. In this case as shown in figure 2.1, the thermal flame thickness evaluated from this equation is $\delta_L^0 = 0.345\text{mm}$. The diffusive thickness δ is defined as

$$\delta \equiv \frac{\lambda_f}{\rho_f C_{p,f} S_L^0} \quad (2.50)$$

where λ_f , ρ_f and $C_{p,f}$ are evaluated in the fresh gas, and S_L^0 is the laminar flame speed, which will be discussed right after. Generally speaking, the thermal flame thickness is larger than the diffusive thickness and the reaction zone [6].

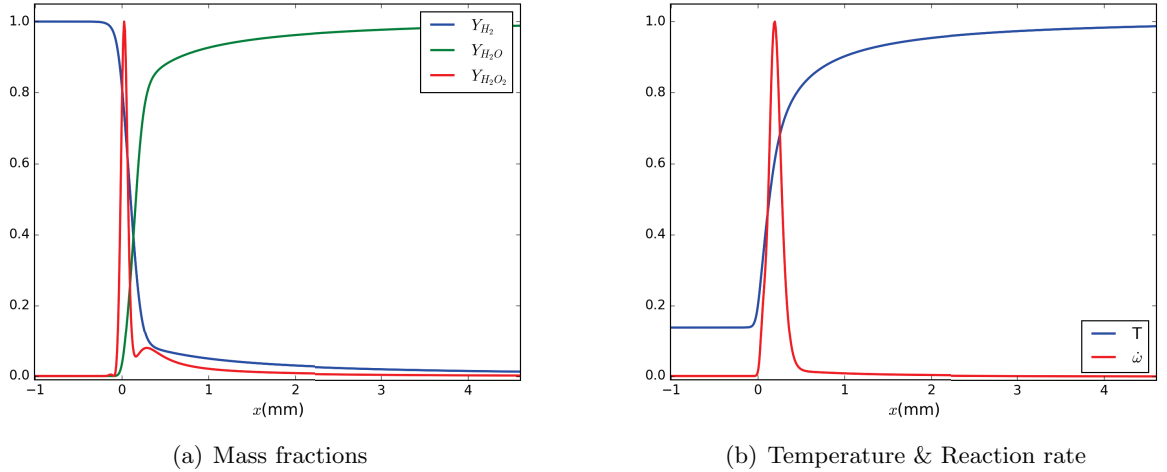


Figure 2.1: Laminar premixed flame structure.

Because there is no flame stretch in this simple 1D case, the laminar flame speed S_L^0 can be obtained simply from the inlet speed when the flame is steady. or can be achieved by the fuel consumption rate, as the integral of the burning rate across the flame front:

$$S_L^0 = -\frac{1}{\rho_f Y_F^f} \int_{-\infty}^{+\infty} \dot{\omega}_F dx \quad (2.51)$$

where the ρ_f and Y_F^f denotes the density and mass fraction of fuel in fresh gas. In this test-case, the flame speed calculated from this equation is $S_L^0 = 1.53\text{m/s}$.

The progress variable of the reaction is defined as the normalized temperature (or other scalar quantities like mass fraction, etc.) as

$$c = \frac{T - T_f}{T_b - T_f} \quad (2.52)$$

and is 0 in the fresh gas and 1 in the burnt gas.

2.3.2 Turbulent premixed flame

A central question in turbulent premixed flame is the interaction between flame and turbulence. With the flame speed and flame thickness introduced before, this interaction can be analyzed parametrically.

To understand how turbulence affects the flame, the time scales of turbulence and flame should be compared. The time scale for combustion can be characterized by the ratio between the flame thickness δ and laminar flame speed S_L^0 . Meanwhile, the time scale of turbulence can be defined either based on the integral scale or the smallest scale. The Damköhler number D_a is defined for the largest eddies and corresponds to the ratio of the integral time scale τ_t to the chemical time scale:

$$D_a \equiv \frac{\tau_t}{\tau_c} = \frac{l_t/u'(l_t)}{\delta/S_L^0} \quad (2.53)$$

in which the l_t denotes the integral turbulent length scale.

The Karlovitz number K_a corresponds to the smallest eddies (Kolmogorov scale) and is the ratio of the chemical time scale to the Kolmogorov time:

$$K_a \equiv \frac{\tau_c}{\tau_k} = \frac{\delta/S_L^0}{\eta_k/u'(\eta_k)} \quad (2.54)$$

and η_k here is the Kolomogorv length scale.

Table 2.1: Classical regimes of turbulent premixed combustion [6].

$K_a < 1$ ($D_a > 1$)	$K_a > 1$ and $D_a > 1$	$D_a \ll 1$
Flamelets	Wrinkled thickened flames	Well stirred reactor
Flame is thinner than all turbulent scales	Small turbulent scales may enter the flame front	All turbulent time scales are smaller than the chemical time scale

According to the ratio between the time scale of combustion to the largest and smallest time scales in turbulence, three different regimes of turbulent premixed combustion can be divided as in table 2.1 from [6]. As seen in this table, for different regimes, the turbulence acts differently on combustion. For the flamelet and wrinkled thickened flames, the most difficult task is to predict the turbulent flame speed.

2.3.3 Turbulent flame models for LES

For different turbulent combustion regimes, different strategies of modeling should be applied [6]. In this research, our flame stays in the flamelet regimes (see figure 1.6 in section 1.3), and the main numerical difficulty is that the flame front is normally too thin to be captured by the grid. Varieties of LES models have been developed for this premixed combustion regime. They can be roughly divided into two categories [12]: those based on the statistical considerations (*pdf* methods), and those, more numerous, based on geometrical considerations. Statistical models, like Filtered Density Function modeling (FDF), or the Conditional Moment Closure (CMC) are mostly applied in non-premixed combustion, but CMC has been extended to premixed combustion [51]. Geometrical models try to deal directly with the problem of capturing the thin flame front on the coarse LES mesh. They can in turn be separated into three categories: (i) level set methods (G equation) either static [52, 53] or dynamic [54] that propagate the thin flame front at the turbulent flame speed, (ii) filtered laminar flames based on the filtered equation for the progress variable, e.g. F-TACLES from EM2C [55] that uses tabulated one-dimensional filtered flames obtained with detailed chemistry, and (iii) artificially thickened flames (ATF) based on the trick proposed by O'Rourke & Bracco [56]. This latter approach is retained in this study for its simplicity, and its possible application with both infinitely fast and detailed chemistry. However, like other geometrical models, ATF requires the evaluation of the SGS wrinkling factor (WF), that can be viewed as the ratio of the turbulent flame speed to the resolved one, related to the flame surface density (FSD). Pioneering works in the field are those of Colin *et al* (TFLES) [57] and Charlette *et al* [58]. Dynamic formulations of the ATF+WF method can be found in [59, 31, 60]. A coupling with tabulated flamelet chemistry has also been proposed by Kuenne *et al* [61].

2.3.4 ATF model in turbulent combustion

The ATF method [56] is a pure mathematical treatment on the species equations (2.1d) without any assumption. Starting with the species equations in fickian approximation:

$$\frac{\partial \rho Y_\alpha}{\partial t} + \frac{\partial}{\partial x_j} (\rho u_j Y_\alpha) = \frac{\partial}{\partial x_j} \left(\rho D_\alpha \frac{\partial Y_\alpha}{\partial x_j} \right) + \dot{\omega}_\alpha$$

a coordinates transformation can be done as:

$$\begin{cases} \xi_i(x_i) & \equiv & \mathcal{F}x_i \\ \tau(t) & \equiv & \mathcal{F}t \end{cases} \quad (2.55)$$

The equation then turns to

$$\frac{\partial \rho Y_\alpha}{\partial \tau} + \frac{\partial}{\partial \xi_j} (\rho u_j Y_\alpha) = \frac{\partial}{\partial \xi_j} \left(\rho \mathcal{F}D_\alpha \frac{\partial Y_\alpha}{\partial \xi_j} \right) + \frac{\dot{\omega}_\alpha}{\mathcal{F}} \quad (2.56)$$

If we solve this equation (2.56) with respect to t and x instead of τ and ξ , Y_α just gets thickened \mathcal{F} times compared to the solution of the original (2.1d) [61]. Other properties of the flame will keep the same. For laminar premixed flame, the flame propagation speed will not change. Figure 2.2 presents the result of the same test case as in figure 2.1 which is done with a ATF method with thickening factor $\mathcal{F} = 2$. One can see that the flame is artificially thickened so that the flame thickness as defined in (2.49) is changed into $\delta_L^0 = 0.691\text{mm}$, which is almost \mathcal{F} times as the original one. But all the other flame characteristics keep unchanged and the flame speed keeps $S_L^0 = 1.58\text{m/s}$ as calculated from equation (2.51).

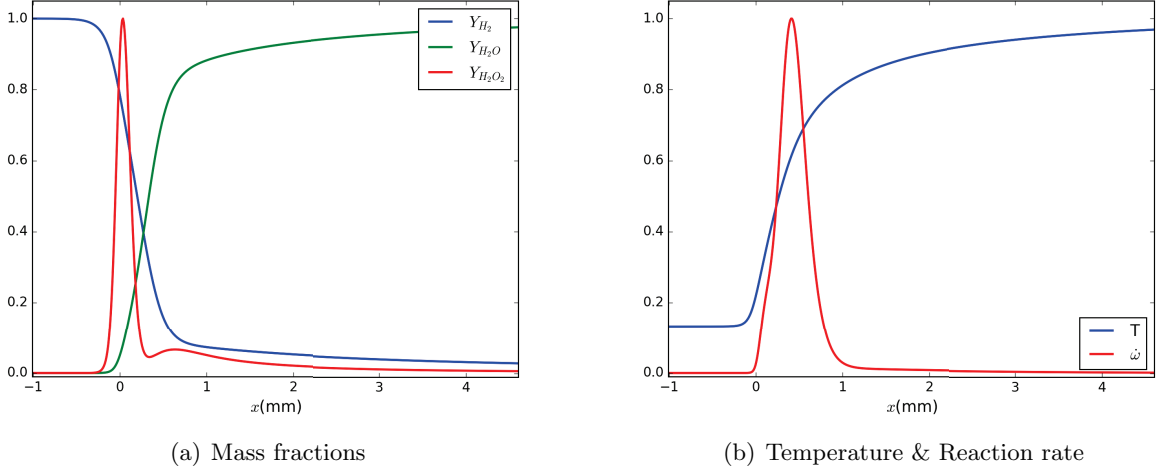


Figure 2.2: Laminar premixed flame structure with thickened flame model at $\mathcal{F} = 2$.

With this artificial thickening treatment of the flame front, the flame is thickened so that it may be resolved on a relatively coarse mesh. This brings us great convenience for numerical simulation. However, for turbulent combustion, the increasing of the flame thickness will affect the flame-turbulence interaction [6]. According to Colin *et al.* [57], after the flame is thickened \mathcal{F} times, compared to the original flame, turbulent eddies smaller than $\mathcal{F}\delta_L^0$ can not interact with the thickened flame any more and their effects have to be incorporated in the modeling as a subgrid scale FSD effect. Also eddies larger than $\mathcal{F}\delta_L^0$ can interact with the flame front but their efficiency may be affected by the increased flame thickness. These effects should be modeled by the subgrid wrinkling factor [57, 58, 59] defined as:

$$\Xi = S_T/S_{T,\text{resolved}} = |\overline{\nabla c}|/|\nabla c| \quad (2.57)$$

where S_T and $S_{T,\text{resolved}}$ are the exact turbulent flame speed and the resolved flame speed, respectively, and c is the progress variable. In the LES formalism, the Favre-filtered species equation reads

$$\frac{\partial \widetilde{\rho Y_\alpha}}{\partial t} + \left(\widetilde{\rho u_j Y_\alpha} \right)_{,j} = - \left(\mathcal{F} \Xi \widetilde{\rho V_{\alpha j}^c Y_\alpha} \right)_{,j} + \frac{\Xi}{\mathcal{F}} \hat{\omega}_\alpha \quad (2.58)$$

where $\hat{\omega}_\alpha = \omega_\alpha(\widetilde{Y}_\alpha, \widetilde{T})$ is the chemical source term in quasi-laminar formulation, i.e. computed with resolved variables. Many models for Ξ have been proposed in the literature, either static [58] or dynamic [31, 59]. Most of them are based on the fractal dimension of the flame surface (e.g. [62]). The assessment of such algebraic flame surface density models has been performed by Chakraborty & Klein [63] and Katragadda *et al* [64].

In the present study, a new SGS model proposed by F. Thiesset *et al.* [5, 65, 24] is implemented. This model, derived from [58], has the form

$$\Xi = \left\{ \left[1 + \left(\frac{\Delta_F}{\eta_i} \right)^\alpha \right] / \left[1 + \left(\frac{\Delta_F}{\eta_o} \right)^\alpha \right] \right\}^{\beta/\alpha} \quad (2.59)$$

where $\alpha = 2$, $\beta = D_f - 2$ as in fractal models, $\Delta_F = \mathcal{F}\delta_L^0$ is the flame filter width, $\eta_o \approx 3L_t$ is the outer length scale (L_t : integral turbulent length scale, input for the model), η_i is the inner cut-off length-scale, related to the local Karlovitz number $K_a = \tau_c/\tau_k$ as in (2.54)

$$\frac{\eta_i}{\delta_L^0} = K_a^{-2} + r_1^* K_a^{-1/2} \quad ; \quad r_1^* = (3C_q)^{3/4} \quad (2.60)$$

with $C_q = \frac{11}{3}C_u$, $C_u \approx 2$ being the ‘‘universal’’ constant in Kolmogorov’s 2/3 law. The first term on the rhs of (2.60) accounts for low Karlovitz numbers, whereas the second one accounts for high K_a . The expression for β in (2.59) slightly differs from the one of [7], and reads

$$3\beta = 1 + \frac{r_1^* K_a^{-1/2}}{K_a^{-2} + r_1^* K_a^{-1/2}} \quad (2.61)$$

The main difficulty is to estimate the local Karlovitz number from the resolved field. Different expressions for K_a are

$$K_a = \text{Sc} \left(\frac{\delta}{\eta} \right)^2 = \text{Sc}^{-1} \left(\frac{u_K}{S_L^0} \right)^2 = \frac{\sqrt{\varepsilon/\nu_u}}{S_L^0/\delta} \quad (2.62)$$

where δ is the diffusive thickness of the flame such that $\text{Re}_f = \delta S_L^0/\nu_u = 1$, u_K is the Kolmogorov velocity scale, and $\text{Sc} = \nu_u/D_{fuel \rightarrow air}$ is the Schmidt number usually assumed close to unity. The last expression for K_a in (2.62) can be used if a value is given to ε . This can be achieved from

$$\varepsilon = C_\varepsilon \frac{k_{sgs}^{3/2}}{\Delta} \approx C_\varepsilon \frac{u_\Delta^3}{\Delta} \quad ; \quad C_\varepsilon = 1.05 \quad (2.63)$$

where Δ and u_Δ are the a length scale and velocity fluctuation at scale Δ , respectively. One possibility is to compute ε from the subgrid scale eddy-viscosity ν_{sgs}^t ¹⁰

$$\varepsilon = \nu_{sgs}^t{}^3 / (C_s \Delta)^4 \quad (2.64)$$

with $C_s = 0.18$ and $\Delta \equiv h = (\Delta x \Delta y \Delta z)^{1/3}$. The subgrid scale eddy-viscosity in (2.64) can be evaluated from flow SGS models, e.g., by the Smagorinsky model in equation (2.37).

Another method to evaluate the turbulent dissipation rate ε is to calculate u_Δ with the operator OP_2 proposed by Colin *et al.* [57]. This operator estimates the turbulent velocity fluctuation u'_Δ at scale $\Delta \approx 10\Delta_x$ where Δ_x is the grid size as

$$u'_\Delta = \|OP_2(\tilde{\mathbf{u}})\| \equiv \|c_2 \Delta_x^3 \nabla \times \nabla_{OP_1}^2(\tilde{\mathbf{u}})\| \quad (2.65)$$

where the $\nabla_{OP_1}^2(\tilde{\mathbf{u}})$ is a numerical Laplacian operator

$$\nabla_{OP_1}^2(\tilde{\mathbf{u}}) \equiv \begin{bmatrix} \frac{\delta^2}{\delta x^2}(\tilde{u}_x) + \frac{\delta^2}{\delta y^2}(\tilde{u}_x) + \frac{\delta^2}{\delta z^2}(\tilde{u}_x) \\ \frac{\delta^2}{\delta x^2}(\tilde{u}_y) + \frac{\delta^2}{\delta y^2}(\tilde{u}_y) + \frac{\delta^2}{\delta z^2}(\tilde{u}_y) \\ \frac{\delta^2}{\delta x^2}(\tilde{u}_z) + \frac{\delta^2}{\delta y^2}(\tilde{u}_z) + \frac{\delta^2}{\delta z^2}(\tilde{u}_z) \end{bmatrix} \quad (2.66)$$

in which the numerical second order derivative calculation operator $\frac{\delta^2}{\delta x^2}(\bullet)$ reads¹¹

$$\frac{\delta^2}{\delta x^2}(\theta) \equiv \frac{\theta_{i+2,jk} - 2\theta_{i,jk} + \theta_{i-2,jk}}{4\Delta_x^2} \quad (2.67)$$

In (2.67), $\theta_{i,jk}$ is the value of θ at grid point x_i, y_j, z_k . The operator OP_2 can remove the dilatation part of the velocity field thanks to the Curl operator $\nabla \times$ in (2.65). Further discussion on the evaluation of SGS flame wrinkling model can be found in chapter 4 with test cases.

In this chapter, the basic governing equations for the LES of turbulent combustion have been introduced. The next chapter will focus on the numerics applied in this research.

¹⁰Simply according to $\nu_{sgs}^t \sim ul$ and $\varepsilon \sim u^3/l$.

¹¹This operator is equivalent to perform a second order center finite difference first order derivative twice.

Chapter 3

Numerics

Synopsis

Ce chapitre, au coeur de ce travail de thèse, décrit les méthodes numériques employées pour les simulations des grandes échelles présentées par la suite.

- La première section donne un aperçu général de ces méthodes : schéma en temps, termes visqueux, et annonce le traitement des flux Euler, des conditions aux limites et de l'approche bas-Mach qui seront développés en détail aux sections suivantes.
- La seconde section est consacrée à la discrétisation des flux Euler, qui est la plus importante source d'erreurs numériques lors des simulations. Ces erreurs sont exploitées dans les SGE implicites, et doivent être caractérisées précisément. On présente d'abord la procédure de reconstruction par schémas linéaires centrés et décentrés en amont, pour la formulation conservative des flux numériques, puis celle par les schémas WENO non-linéaires sous diverses variantes. Le pouvoir de résolution, le filtre implicite et la résolution sous-filtre de ces schémas sont ensuite analysés scrupuleusement. On présente à la suite deux cas-test (tourbillons de Taylor-Green et double réflexion de Mach) illustrant les propriétés dissipatives des divers schémas numériques présentés plus haut.
- La troisième section traite de la formulation et de l'implémentation de la méthode ASR pour les écoulements à faible Mach. Le principe en est illustré sur le système Euler 1D. La formulation conservative de la méthode pour le système Euler 3D, originale, est présentée à la suite avant de donner l'extension de la méthode au cas Navier-Stokes, i.e. avec termes de viscosité. On illustre enfin les performances de la méthode ASR sur trois cas-tests : propagation d'une onde acoustique, écoulement soumis à la gravité, et diffusion d'un pic de température.
- La quatrième section décrit la génération et l'implémentation des conditions aux limites turbulentes en entrée. Un "bloc" de turbulence homogène et isotrope, présentant des propriétés spectrales correspondant au forçage multi-échelles expérimental est d'abord généré à partir des mesures au fil chaud réalisées sur l'axe du jet. Ce bloc de turbulence est ensuite superposé au profil de vitesse moyenne du jet, puis injecté dans le domaine de calcul par une formulation aux caractéristiques des conditions aux limites.

Following the presentation of governing equations, this chapter outlines the numerics for (I)LES. The numerical solution of the filtered, unsteady, fully compressible multi-species Navier-Stokes equations (2.27) is obtained by applying numerical methods to these equations. An overview of the main numerical treatments used in the current work is given in the first section; The inviscid flux evaluation, the low-Mach modifications and the boundary conditions will be then discussed in detail, as they are important for the LES of the low-speed premixed turbulent combustion, especially for the implicit LES applications.

3.1 Overview

The numerical strategies in this study are based on our team's former work in high-speed reactive flows [21, 22, 23, 26, 27]. The main numerical treatments applied in the current work are:

1. Explicit third order TVD Runge-Kutta scheme [66] for time stepping;
2. Finite difference procedures for the inviscid fluxes, like Weighted Essentially Non-Oscillatory (WENO) schemes [66];
3. Fourth order central finite difference for viscous terms;
4. Detailed finite-rate chemistry with Arrhenius laws for chemical source terms;
5. Characteristic-based boundary conditions;
6. Artificial Acoustic Stiffness Reduction (ASR) method [67] for low-Mach simulations.

I would like to briefly illustrate several points of this list in this section. Detailed discussion on other topics can be found in the following sections.

- The time marching strategy is to first discretize the spatial derivatives only and leaving the time continuous (method of lines). The filtered N-S equation (2.30) can then be written as a initial value ODE problem as

$$\frac{\partial u}{\partial t} = \mathcal{NL}(u) \quad (3.1)$$

in which the operator \mathcal{NL} represents all the spatial and local operations including inviscid fluxes (2.32), viscous terms (2.33), source terms (2.34) and SGS terms (2.35). At a given time t , with the value of variables u given at this time which is denoted by u^n , the value of u at the next time step $t + \Delta t$, which is denoted by u^{n+1} , is calculated by the explicit optimal third order TVD Runge-Kutta (R-K) scheme [66]:

$$\begin{aligned} u^{(1)} &= u^n + \Delta t \mathcal{NL}(u^n) \\ u^{(2)} &= \frac{3}{4}u^n + \frac{1}{4}u^{(1)} + \frac{1}{4}\Delta t \mathcal{NL}(u^{(1)}) \\ u^{n+1} &= \frac{1}{3}u^n + \frac{2}{3}u^{(2)} + \frac{2}{3}\Delta t \mathcal{NL}(u^{(2)}) \end{aligned} \quad (3.2)$$

The Butcher array for this R-K scheme can be found in table 3.1.

$$\begin{array}{c|ccc} c_1 & & & 0 \\ c_2 & a_{21} & & 1 \\ c_3 & a_{31} & a_{32} & 1/2 \\ \hline & b_1 & b_2 & b_3 \end{array} = \begin{array}{c|ccc} & & & 1 \\ & & & 1/4 \\ & & & 1/4 \\ \hline & & & 1/6 \\ & & & 1/6 \\ & & & 2/3 \end{array}$$

Table 3.1: Butcher array for the optimal third order TVD Runge-Kutta scheme

- A Finite Difference Method (FDM) framework is applied for the evaluation of spatial derivatives in inviscid fluxes and viscous terms. The inviscid fluxes will be discussed in section 3.2. The evaluation of diffusion terms like

$$\frac{\partial}{\partial x_j} \left(\alpha \frac{\partial f}{\partial x_j} \right)$$

in which α is the diffusion coefficient (like viscosity μ for momentum in (2.27b) or thermal conductivity λ for heat flux (2.27c)), is performed by applying twice a first order derivative with the 4th order accuracy central scheme (3.3).

$$\left. \frac{\partial}{\partial x} f \right|_{x=x_i} = \frac{1}{12\Delta x} (f_{i-2} - 8f_{i-1} + 8f_{i+1} - f_{i+2}) + \mathcal{O}(\Delta x^4) \quad (3.3)$$

3.2 Inviscid flux calculation

The numerical errors brought out by the inviscid flux evaluation are always the main part of all the numerical errors in LES [15, 41, 68]. This makes the choice of flux calculation schemes the central issue in both physical and implicit LES. Especially for ILES, as shown in equation (2.45), this approach relies entirely on the built-in filter of the scheme and its dissipative properties to remove and model small turbulent scales in under-resolved simulations [16, 15, 14]. In this section, the spatial derivation schemes used in this work and their performances in LES will be discussed.

3.2.1 Numerical schemes for spatial derivatives

Flux reconstruction for Finite Difference Methods

The inviscid flux terms are calculated under the finite difference method (FDM) framework in the current study. The basis of FDM will be briefly recalled in this section.

Let us consider the scalar 1D hyperbolic conservation law, with proper initial and boundary conditions,

$$\frac{\partial u}{\partial t} + \frac{\partial f}{\partial x} = 0 \quad ; \quad x, t \in \mathbb{R} \quad (3.4)$$

which admits discontinuous weak solutions as in the conservative form of N-S equations (2.1). The semi-discrete form of (3.4) on a uniform grid $x_i = i\Delta x$, $i = 0, \dots, N$, where $u_i(t)$ is the numerical approximation of $u(x_i, t)$, yields the conservative finite-difference formulation

$$\frac{du_i(t)}{dt} = - \left. \frac{\partial f}{\partial x} \right|_{x=x_i} = - \frac{\hat{f}_{i+1/2} - \hat{f}_{i-1/2}}{\Delta x} \quad (3.5)$$

which is exact, provided the numerical flux $\hat{f}_{i+1/2}$ is equal to $h(x_{i+1/2})$, where the function $h(x)$ is implicitly defined, at a given time t , by

$$f(u(x, t)) = \frac{1}{\Delta x} \int_{x-\Delta x/2}^{x+\Delta x/2} h(\xi) d\xi \quad (3.6)$$

Given the set of node values $f_i \equiv f(u(x_i, t))$ satisfying

$$f_i = \frac{1}{\Delta x} \int_{x_{i-1/2}}^{x_{i+1/2}} h(\xi) d\xi = \bar{h}_i \quad (3.7)$$

the intercell value $h(x_{i\pm 1/2})$ can be approximated at order k with a $(k-1)$ -th order interpolating polynomial $p_r(x)$ built in the stencil $S_r(i)$ of r cells to the left of x_i , s cells to the right and the cell I_i that contains x_i , such that $r + s + 1 = k$:

$$h_{i+1/2}^{(r)} = \sum_{j=0}^{k-1} c_{rj} f_{i-r+j} = h(x_{i+1/2}) + \mathcal{O}(\Delta x^k) \quad r = 0, \dots, k-1$$

$$h_{i-1/2}^{(r)} = \sum_{j=0}^{k-1} c_{r-1,j} f_{i-r+j} = h(x_{i-1/2}) + \mathcal{O}(\Delta x^k) \quad r = 0, \dots, k-1$$

In practice, the left flux $h_{i-1/2}^{(r)}$ is usually calculated as the right boundary flux of the cell I_{i-1} . For example, the 5th order upwind scheme uses a 4th order interpolating polynomial built in the 5-cells stencil $S(i) = \{I_{i-2}, I_{i-1}, I_i, I_{i+1}, I_{i+2}\}$ of 2 cells to the left of x_i and 2 cells to the right to estimate the intercell value $h(x_{i+1/2})$ by [69]

$$h_{i+1/2}^{5\text{-up}}(f) = \frac{1}{60} (2f_{i-2} - 13f_{i-1} + 47f_i + 27f_{i+1} - 3f_{i+2}) = h(x_{i+1/2}) + \mathcal{O}(\Delta x^5) \quad (3.8)$$

and the intercell value $h(x_{i-1/2})$ is interpolated in stencil $S(i-1) = \{I_{i-3}, I_{i-2}, I_{i-1}, I_i, I_{i+1}\}$ of 2 cells to the left of x_{i-1} and 2 cells to the right

$$h_{i-1/2}^{5\text{-up}}(f) = \frac{1}{60} (2f_{i-3} - 13f_{i-2} + 47f_{i-1} + 27f_i - 3f_{i+1}) = h(x_{i-1/2}) + \mathcal{O}(\Delta x^5) \quad (3.9)$$

Using these equations to (3.5), one may obtain the 5th order upwind scheme

$$\left. \frac{\partial f}{\partial x} \right|_{x=x_i}^{5\text{-up}} = \frac{1}{\Delta x} \vec{a} \cdot \vec{f} = \frac{\partial f}{\partial x}(x_i) + \mathcal{O}(\Delta x^5) \quad (3.10)$$

with

$$\vec{a}^{5\text{-up}} = \frac{1}{60} [-2 \quad 15 \quad -60 \quad 20 \quad 30 \quad -3]^T \quad (3.11)$$

and

$$\vec{f} = [f_{i-3} \quad f_{i-2} \quad f_{i-1} \quad f_i \quad f_{i+1} \quad f_{i+2}]^T$$

This scheme is an upwind scheme because it uses 3 cells to the left of $x_{i+1/2}$ and 2 cells to the right. To enforce the stability of the scheme, this scheme should only be applied to a flux $f^{>0}(u)$ for which the *wind* blows from the left to the right

$$\frac{df^{>0}}{du} > 0 \quad (3.12)$$

In this work, the Lax-Friedrichs flux splitting is applied to ensure condition (3.12). The flux $f(u)$ is separated into $f^{>0}$ and $f^{<0}$ as

$$\begin{aligned} f(u) &\equiv f^{>0} + f^{<0} \\ f^{>0} &\equiv \frac{1}{2} (f + \alpha u); \quad f^{<0} \equiv \frac{1}{2} (f - \alpha u) \end{aligned} \quad (3.13)$$

where α is taken as

$$\alpha = \max_u \left| \frac{df(u)}{du} \right| \quad (3.14)$$

over a relevant range of u . During the flux reconstruction step, the reconstruction (3.8) will be performed on $f^{>0}$ in (3.13) instead of f , and the resulting reconstructed value will be denoted as $h_{i+1/2}^-$, where the “-” superscript stands for the left side of intercell $i + 1/2$,

$$h_{i+1/2}^{5\text{-up}^-}(f^{>0}) = \frac{1}{60} (2f_{i-2}^{>0} - 13f_{i-1}^{>0} + 47f_i^{>0} + 27f_{i+1}^{>0} - 3f_{i+2}^{>0}) \quad (3.15)$$

Using the stencil $\{I_{i-1}, I_i, I_{i+1}, I_{i+2}, I_{i+3}\}$, with a symmetry operation of (3.15), the flux reconstruction of $f^{<0}$ is then

$$h_{i+1/2}^{5\text{-up}^+}(f^{<0}) = \frac{1}{60} (2f_{i+3}^{<0} - 13f_{i+2}^{<0} + 47f_{i+1}^{<0} + 27f_i^{<0} - 3f_{i-1}^{<0}) \quad (3.16)$$

and the “+” superscript stands for the right side of intercell $i + 1/2$. The final reconstruction is taken as

$$h_{i+1/2} \equiv h_{i+1/2}^+ + h_{i-1/2}^- \quad (3.17)$$

The same process can be applied for the reconstruction of $h_{i-1/2}$. The derivation of the flux f in (3.4) is obtained by taking the values $h_{i+1/2}$ and $h_{i-1/2}$ as $\hat{f}_{i+1/2}$ and $\hat{f}_{i-1/2}$ in (3.5).

WENO reconstruction

Following this idea of using polynomial interpolation to estimate the intercell values, some modern spatial derivative schemes like WENO are developed to overcome the difficulties brought by discontinuities in the (weak) solutions [66]. It is well known that polynomial interpolation will generate oscillations near discontinuities, which are called Gibbs phenomenon in spectral methods. On the other hand, as we have already seen in the previous section, there exist different estimations of intercell value which can be obtained from different stencils. The main concept of WENO schemes is to use as much as possible stencils in which the solution is smooth in interpolation to minimize the influence of discontinuities.

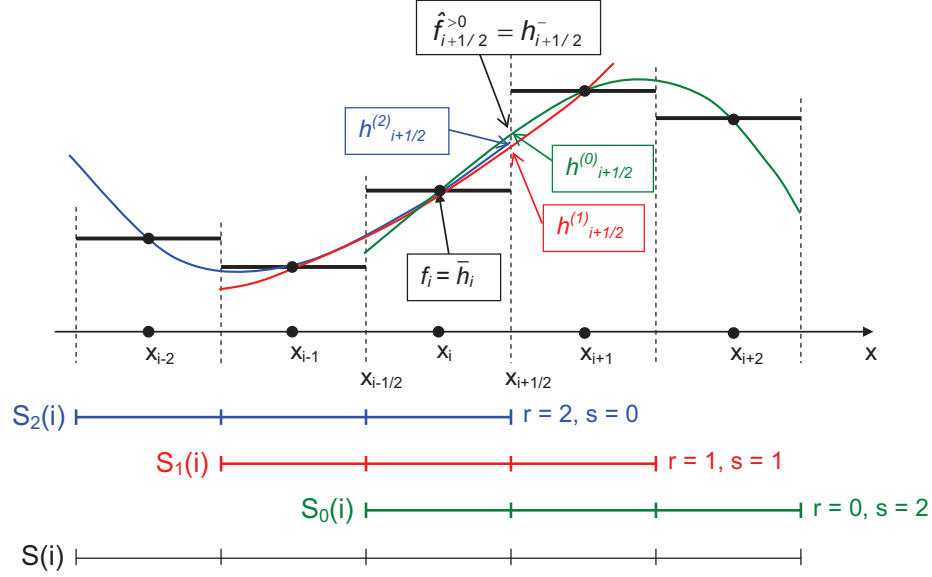


Figure 3.1: Illustration of the WENO method.

Let take 5th order WENO schemes as example. As shown in figure 3.1, for intercell $x_{i+1/2}$, a 5th order WENO scheme will take three 3-cells stencils S_2 , S_1 and S_0 to perform three 2nd order polynomial interpolations. Thus three candidate intercell values $h^{(2)}_{i+1/2}$, $h^{(1)}_{i+1/2}$ and $h^{(0)}_{i+1/2}$ will be obtained [69]:

$$\begin{aligned}
 h^{(2)}_{i+1/2} &= \frac{1}{3}f_{i-2} - \frac{7}{6}f_{i-1} + \frac{11}{6}f_i \\
 h^{(1)}_{i+1/2} &= -\frac{1}{6}f_{i-1} + \frac{5}{6}f_i + \frac{1}{3}f_{i+1} \\
 h^{(0)}_{i+1/2} &= \frac{1}{3}f_i + \frac{5}{6}f_{i+1} - \frac{1}{6}f_{i+2}
 \end{aligned} \tag{3.18}$$

The concept of WENO is to use a weighted average of these 3 candidates to construct the intercell flux $h_{i\pm 1/2}$

$$h_{i+1/2} = \sum_{r=0}^{k-1} \omega_r h_{i+1/2}^{(r)} \tag{3.19}$$

The union of the 3 stencils makes a global stencil $S(i) = \bigcup_r S_r(i)$ of 5 cells centered on x_i , in which there exists a unique polynomial that approximate the intercell flux at fifth order accuracy :

$$h_{i+1/2} = \sum_{r=0}^2 d_r h_{i+1/2}^{(r)} = h(x_{i+1/2}) + \mathcal{O}(\Delta x^5) \tag{3.20}$$

This flux should be identical to (3.8). So d_r can be calculated back from (3.8) as

$$d_0 = \frac{3}{10}, \quad d_1 = \frac{6}{10}, \quad d_2 = \frac{1}{10} \quad (3.21)$$

These weights d_r are called *ideal linear weights*, since they achieve the maximum order of accuracy for the given stencil $S(i)$ and do not depend on node values f_i .

Furthermore, if the function $h(x)$ is not smooth in the stencil $S(i)$, the weights ω_r in (3.19) should be calculated differently. In the case where the function $h(x)$ is not smooth in the stencil $S_r(i)$, the intercell approximate value $h_{i+1/2}^{(r)}$ should be excluded from the linear combination (3.20), or given a much lower weight ω_r instead of the optimal weight d_r , reducing *de facto* locally the accuracy of the scheme. This weighting process, depending on a smoothness indicator, is the core of the WENO method. Several weighting process can be found in the literature:

- **WENO-OPT**

The linear optimum WENO (WENO-OPT) can be constructed by applying the ideal linear weights directly

$$\omega_r^{OP} = d_r \quad ; \quad r = 0, \dots, k-1 \quad (3.22)$$

The resulted WENO-OPT scheme is in fact the upwind 5th order scheme (3.10).

- **WENO-JS**

The JS weights [66, 69, 70] are given by

$$\omega_r^{JS} = \frac{\alpha_r}{\sum_{j=0}^{k-1} \alpha_j} \quad ; \quad \alpha_r = \frac{d_r}{(\epsilon + \beta_r^{JS})^2} \quad ; \quad r = 0, \dots, k-1 \quad (3.23)$$

where ϵ is a small positive constant added to prevent the denominator becoming zero and we take $\epsilon = 10^{-80}$ in our simulations. The smoothness indicator β_r^{JS} here is just a sum of the squares of scaled L^2 norms for all the derivatives of the interpolation polynomial over the interval $(x_{i-1/2}, x_{i+1/2})$

$$\beta_r^{JS} = \sum_{l=1}^{k-1} \int_{x_{i-1/2}}^{x_{i+1/2}} \Delta x^{2l-1} \left(\frac{d^l p_r(x)}{dx^l} \right)^2 d\xi \quad (3.24)$$

The formulations for the evaluation of β_r^{JS} from cell values f_i up to $k = 6$ can be found in appendix B.1.

- **WENO-M**

The method suggested by Henrick *et al.* [71] consists in applying a mapping to the 5th order JS non-linear weights ($k = 3$), to preserve a higher order of accuracy near critical points

$$g_r(\omega) = \frac{\omega (d_r + d_r^2 - 3d_r\omega + \omega^2)}{d_r^2 + \omega(1 - 2d_r)} \quad ; \quad r = 0, 1, 2 \quad (3.25)$$

The new M-weights are

$$\omega_r^M = \frac{\alpha_r^M}{\sum_{j=0}^2 \alpha_j^M} \quad ; \quad \alpha_r^M = g_r(\omega_r^{JS}) \quad ; \quad r = 0, 1, 2 \quad (3.26)$$

- **WENO-Z**

The WENO-Z method [72] is intended to decrease the numerical dissipation and improve the resolving efficiency of the WENO-JS scheme, by designing new stiffness indicators. At 5th order, the WENO-Z weights read

$$\omega_r^Z = \frac{\alpha_r^Z}{\sum_{j=0}^2 \alpha_j^Z} \quad ; \quad \alpha_r^Z = \frac{d_r}{\beta_r^Z} \quad ; \quad r = 0, 1, 2 \quad (3.27)$$

where the stiffness indicators are

$$\frac{1}{\beta_r^Z} = 1 + \left(\frac{\tau_5}{\epsilon + \beta_r^{JS}} \right)^2 \quad ; \quad \tau_5 = |\beta_0^{JS} - \beta_2^{JS}| \quad (3.28)$$

The method has been extended to any order $(2k - 1) > 5$ [73]

$$\omega_r^Z = \frac{\alpha_r^Z}{\sum_{j=0}^{k-1} \alpha_j^Z} \quad ; \quad \alpha_r^Z = \frac{d_r}{\beta_r^Z} \quad ; \quad r = 0, \dots, k-1 \quad (3.29)$$

using the generalized smoothness indicators

$$\frac{1}{\beta_r^Z} = 1 + \left(\frac{\tau_{2k-1}}{\epsilon + \beta_r^{JS}} \right)^p \quad ; \quad \tau_{2k-1} = \begin{cases} |\beta_0^{JS} - \beta_{k-1}^{JS}| & k \text{ odd} \\ |\beta_0^{JS} - \beta_1^{JS} - \beta_{k-2}^{JS} + \beta_{k-1}^{JS}| & k \text{ even} \end{cases} \quad (3.30)$$

• WENO-MZ

A further simple improvement is the combination of WENO-M and WENO-Z, namely WENO-MZ, obtained by mapping the Z weights (3.27) instead of the JS weights in (3.25):

$$\omega_r^{MZ} = \frac{\alpha_r^{MZ}}{\sum_{j=0}^2 \alpha_j^{MZ}} \quad ; \quad \alpha_r^{MZ} = g_r(\omega_r^Z) \quad ; \quad r = 0, 1, 2 \quad (3.31)$$

Apparently, the WENO schemes (except WENO-OPT) are all non-linear schemes as their coefficients for calculating the flux depend also on the local values of the original function.

Flux reconstruction for multi-variables multi-dimensions systems

The N-S system (2.19) is a three dimensional multi-variables system. To apply the FDM framework to the hyperbolic part of this system, especially for the flux splitting, a decoupling of the system should be performed. Let take the flux evaluation on x direction as example. To evaluate $\frac{\partial \mathbf{F}}{\partial x}$, the jacobian matrix

$$A \equiv \frac{\partial \mathbf{F}}{\partial \mathbf{U}} \quad (3.32)$$

should be first diagonalized in order to find the characteristic speeds as

$$A = R \Lambda L \quad (3.33)$$

where R and L are the matrix of right and left eigenvectors of A , such that $RL = LR = I$, and Λ is a diagonal matrix composed by all the eigenvalues λ_i of A

$$\Lambda \equiv \begin{pmatrix} \lambda_1 & & & & \\ & \lambda_2 & & & \\ & & \lambda_3 & & \\ & & & \ddots & \\ & & & & \lambda_{N_{sp}+5} \end{pmatrix} \quad (3.34)$$

A detailed derivation of this eigen decomposition process of N-S equations can be found in appendix B.2.

In the current work, for the reconstruction of $\hat{\mathbf{F}}_{i+1/2}$, the following steps are taken:

1. Calculate the \mathbf{F} field with (2.21).
2. Calculate the average state $\mathbf{U}_{i+1/2} = 1/2(\mathbf{U}_{i+1} + \mathbf{U}_i)$ and use this average state to calculate the matrix of left and right eigen vectors $L_{i+1/2}$ and $R_{i+1/2}$ at $x_{i+1/2}$ as in equation (B.21) and (B.20)

3. Flux splitting. The Lax-Friedrichs flux splitting for a multi-variables system is performed in characteristic space. The split characteristic waves \mathcal{L} on the reconstruction stencil S

$$\begin{aligned}\mathcal{L}_j^{>0} &\equiv \frac{1}{2} (L_{i+1/2} \mathbf{F}_j + \bar{\Lambda} L_{i+1/2} \mathbf{U}_j) \\ \mathcal{L}_j^{<0} &\equiv \frac{1}{2} (L_{i+1/2} \mathbf{F}_j - \bar{\Lambda} L_{i+1/2} \mathbf{U}_j) \text{ for } I_j \in S\end{aligned}\quad (3.35)$$

are taken into the reconstruction process like $f_j^{>0}$ and $f_j^{<0}$ in (3.15) and (3.16) for scalar PDEs. In (3.35), the matrix $\bar{\Lambda}$ is the diagonal matrix of the maximum absolute value of all the eigenvalues over a relevant range

$$\bar{\Lambda} \equiv \begin{pmatrix} \max |\lambda_i| & & & & \\ & \max |\lambda_i| & & & \\ & & \max |\lambda_i| & & \\ & & & \ddots & \\ & & & & \max |\lambda_i| \end{pmatrix}\quad (3.36)$$

4. Reconstruct the intercell value for the characterize waves like in (3.15) and (3.16). For example, the fifth order upwind scheme is then

$$\begin{aligned}\mathbf{h}_{i+1/2}^{5\text{-up}^-}(\mathcal{L}^{>0}) &= \frac{1}{60} \left(2 \underbrace{\left(\frac{1}{2} (L_{i+1/2} \mathbf{F}_{i-2} + \bar{\Lambda} L_{i+1/2} \mathbf{U}_{i-2}) \right)}_{\mathcal{L}_{i-2}^{>0}} - 13 \underbrace{\left(\frac{1}{2} (L_{i+1/2} \mathbf{F}_{i-1} + \bar{\Lambda} L_{i+1/2} \mathbf{U}_{i-1}) \right)}_{\mathcal{L}_{i-1}^{>0}} \right. \\ &\quad + 47 \underbrace{\left(\frac{1}{2} (L_{i+1/2} \mathbf{F}_i + \bar{\Lambda} L_{i+1/2} \mathbf{U}_i) \right)}_{\mathcal{L}_i^{>0}} + 27 \underbrace{\left(\frac{1}{2} (L_{i+1/2} \mathbf{F}_{i+1} + \bar{\Lambda} L_{i+1/2} \mathbf{U}_{i+1}) \right)}_{\mathcal{L}_{i+1}^{>0}} \\ &\quad \left. - 3 \underbrace{\left(\frac{1}{2} (L_{i+1/2} \mathbf{F}_{i+2} + \bar{\Lambda} L_{i+1/2} \mathbf{U}_{i+2}) \right)}_{\mathcal{L}_{i+2}^{>0}} \right)\end{aligned}\quad (3.37)$$

Let denote the resulting constructed value as $\mathbf{h}_{i+1/2}^-(\mathcal{L}^{>0})$ and $\mathbf{h}_{i+1/2}^+(\mathcal{L}^{<0})$, the final reconstructed value $\hat{\mathbf{F}}_{i+1/2}$ reads

$$\hat{\mathbf{F}}_{i+1/2} = R_{i+1/2} \left(\mathbf{h}_{i+1/2}^-(\mathcal{L}^{>0}) + \mathbf{h}_{i+1/2}^+(\mathcal{L}^{<0}) \right)\quad (3.38)$$

The same process can be applied for the left cell boundary to get $\hat{\mathbf{F}}_{i-1/2}$. The final result of $\frac{\partial \mathbf{F}}{\partial x}$ can be obtained by

$$\left. \frac{\partial \mathbf{F}}{\partial x} \right|_{x=x_i} = \frac{\hat{\mathbf{F}}_{i+1/2} - \hat{\mathbf{F}}_{i-1/2}}{\Delta x}$$

For the fluxes in other directions, the same procedure is performed except that the form of the jacobian matrix has changed.

Further discussion

The 4th order central scheme is also used in this work for the evaluation of viscous terms. With a 4-cells stencil $S_1(i) = \{I_{i-1}, I_i, I_{i+1}, I_{i+2}\}$ thus 1 cell to the left of x_i and 2 cells to the right, the flux

reconstruction of 4th order central scheme reads

$$\begin{aligned} h_{i+1/2}^{4-c} &= \frac{1}{12} (-f_{i-1} + 7f_i + 7f_{i+1} - f_{i+2}) = h(x_{i+1/2}) + \mathcal{O}(\Delta x^4) \\ h_{i-1/2}^{4-c} &= \frac{1}{12} (-f_{i-2} + 7f_{i-1} + 7f_i - f_{i+1}) = h(x_{i-1/2}) + \mathcal{O}(\Delta x^4) \end{aligned} \quad (3.39)$$

This will lead to the scheme (3.3) in the previous section

$$\frac{\partial}{\partial x} f \Big|_{x=x_i}^{4-c} = \frac{1}{12\Delta x} (f_{i-2} - 8f_{i-1} + 8f_{i+1} - f_{i+2}) = \frac{\partial f}{\partial x}(x_i) + \mathcal{O}(\Delta x^4)$$

The flux splitting process will not affect the result of the central schemes as the h^+ and h^- are identical to each other so that the splitting part $\pm\alpha u$ will cancel each other during the process. Also, Taylor expansion analysis indicates that central schemes do not produce any even order derivatives errors, so no dissipation will be added to the final results when combined with the time stepping.

An interesting point here is that a linear combination of two reconstructed intercell value (3.8) and (3.39)

$$h_{i+1/2}^{\text{up-c}} \equiv \alpha h_{i+1/2}^{5\text{-up}} + (1 - \alpha) h_{i+1/2}^{4-c} \quad (3.40)$$

with $0 \leq \alpha \leq 1$ is also a valid estimation of intercell value $h(x_{i+1/2})$ with at least 4th order accuracy, thus it will lead to a 4th order differential scheme. The usage of center schemes together with upwind schemes can reduce the numerical dissipation introduced by upwind, thus is suitable for low speed applications [74]. This hybrid scheme is also used in the current work and will be further discussed in the next chapter.

3.2.2 Comparison of different schemes in the context of LES

Of primary importance for LES is the characterization of the built-in implicit filter of the numerical scheme, related to its Modified Wave Number (MWN). For a given grid size h , the numerical scheme having the lowest subfilter resolution

$$r \equiv \frac{\Delta}{h} \quad (3.41)$$

will provide the smallest resolved eddies and is the most desirable. On the other hand, given the smallest resolved scale Δ , a numerical scheme with $r \gg 1$ will need a finer grid, hence more computational resource. To quantify the subfilter resolution of a numerical scheme, two different methods can be applied: i) direct analysis in physical space, and ii) MWN analysis in Fourier space.

Subfilter resolution in physical space

According to Geurts and van der Bos [68], the built-in filter associated to a linear scheme can be expressed as a linear combination of local top-hat filters. Considering a linear FD scheme involving $n + m + 1$ cells¹

$$\frac{\delta^{(-n,m)} f(x)}{\delta x} = \frac{1}{\Delta x} \sum_{j=-n}^m a_j f(x + j\Delta x) \quad (3.42)$$

with $\sum a_j = 0$ for the consistency of the scheme. Neglecting the flux splitting, the built-in filtering process of this scheme can be defined as

$$\frac{\delta^{(-n,m)} f}{\delta x} = \frac{\partial}{\partial x} \bar{f} = \frac{\partial}{\partial x} \left[\int_{-\infty}^{+\infty} G_{-n,m}(\xi - x) f(\xi) d\xi \right] \quad (3.43)$$

where $G_{-n,m}$ is the kernel of the built-in filter.

¹Let consider a simple 1D case with constant grid $h \equiv \Delta x$

To find the expression of this implicit filter kernel, one can write (3.42) as

$$\frac{\delta^{(-n,m)} f}{\delta x}(x) = \frac{1}{\Delta x} \sum_{j=-(n-1)}^m b_j (f(x + j\Delta x) - f(x + (j-1)\Delta x)) \quad (3.44)$$

in which the coefficients b_j can be calculated from the a_j as in (3.42) as

$$b_j = \sum_{i=j}^m a_i \quad ; \quad j = -(n-1), \dots, m \quad (3.45)$$

If we consider a local top-hat filter

$$G_j^{TOP}(x) \equiv \begin{cases} 1/\Delta x & x \in [(j-1)\Delta x, j\Delta x] \\ 0 & \text{otherwise} \end{cases} \quad (3.46)$$

the filtered field by this kernel is then

$$\begin{aligned} l(f, x : (j-1)\Delta x, j\Delta x) &\equiv \int_{-\infty}^{+\infty} G_j^{TOP}(\xi - x) f(\xi) d\xi \\ &= \frac{1}{\Delta x} \int_{x+(j-1)\Delta x}^{x+j\Delta x} f(\xi) d\xi \end{aligned} \quad (3.47)$$

The derivative of this filtered function is clearly

$$\begin{aligned} \frac{\partial}{\partial x} l(f, x : (j-1)\Delta x, j\Delta x) &= \frac{1}{\Delta x} \frac{\partial}{\partial x} \left(\int_{x+(j-1)\Delta x}^{x+j\Delta x} f(\xi) d\xi \right) dx \\ &= \frac{1}{\Delta x} (f(x + j\Delta x) - f(x + (j-1)\Delta x)) \end{aligned} \quad (3.48)$$

Comparing (3.48) to (3.44), we can find that the filter kernel introduced by scheme (3.42) is

$$G_{-n,m}(x) = \sum_{j=-(n-1)}^m b_j G_j^{TOP}(x) \quad (3.49)$$

The coefficients a_j and b_j in equation (3.42) and (3.45) for 2nd order central², 4th order central (3.3) and 5th order upwind (3.10) schemes are listed in table 3.2. The built-in filter kernel of these schemes are plotted in figure 3.2.

Once the kernel of the built-in filter obtained as in (3.49), the sub-filter resolution r in (3.41) can be calculated. The effective filter width should be firstly defined as in [38, 68]:

$$\Delta = \left(\int_{-\infty}^{+\infty} G^2(x) dx \right)^{-1} \quad (3.50)$$

For linear schemes, this quantity can be integrated directly in physical space. The resulting sub-filter resolution (3.41) for the linear schemes in figure 3.2 read

$$\begin{aligned} r_{2\text{nd central}} &= 2 \\ r_{4\text{th central}} &= \frac{36}{25} = 1.44 \\ r_{5\text{th upwind}} &= \frac{15}{13} \approx 1.15 \end{aligned} \quad (3.51)$$

² $\frac{\delta^{-1,1} f(x_i)}{\delta x} \equiv \frac{1}{2\Delta x} [f_{i+1} - f_{i-1}]$

Table 3.2: Coefficients a_j and b_j in equation (3.42) and (3.45) for different schemes.

	a_j	b_j
2nd order central	$\begin{cases} a_{-1} = -1/2 \\ a_1 = 1/2 \end{cases}$	$\begin{cases} b_0 = 1/2 \\ b_1 = 1/2 \end{cases}$
4th order central	$\begin{cases} a_{-2} = 1/12 \\ a_{-1} = -2/3 \\ a_1 = 2/3 \\ a_2 = -1/12 \end{cases}$	$\begin{cases} b_{-1} = -1/12 \\ b_0 = 7/12 \\ b_1 = 7/12 \\ b_2 = -1/12 \end{cases}$
5th order upwind	$\begin{cases} a_{-3} = -1/30 \\ a_{-2} = 1/4 \\ a_{-1} = -1 \\ a_0 = 1/3 \\ a_1 = 1/2 \\ a_2 = -1/20 \end{cases}$	$\begin{cases} b_{-2} = 1/30 \\ b_{-1} = -13/60 \\ b_0 = 47/60 \\ b_1 = 9/20 \\ b_2 = -1/20 \end{cases}$

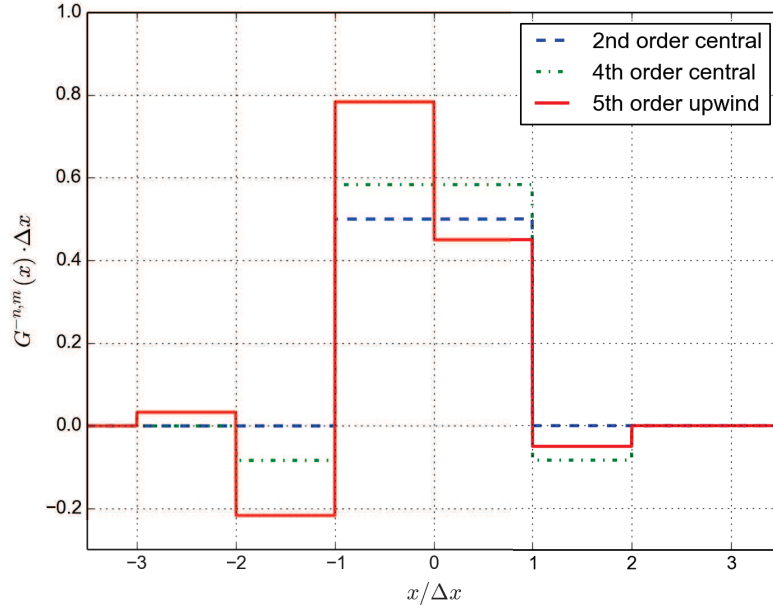


Figure 3.2: Implicit local top-hat filter induced by 2nd order central, 4th order central and 5th order upwind scheme.

Subfilter resolution in Fourier space

A more convenient way to calculate the subfilter resolution is in Fourier space using the Parseval's identity to calculate the filter width:

$$\Delta = \left(\int_{-\infty}^{+\infty} G^2(x) dx \right)^{-1} = \left(\frac{2\pi}{\Delta x} \int_{-\infty}^{+\infty} |\hat{G}(\omega)|^2 d\omega \right)^{-1} \quad (3.52)$$

in which the $\widehat{G}(\omega)$ is the built-in kernel in Fourier space that can be got from the MWN of a numerical scheme [37]. Let consider a single Fourier mode $k : f_k(x) = \widehat{f}_k e^{jkx}$. At a grid point $x_i, i = 0, \dots, N$, a linear numerical differential scheme $\frac{\delta}{\delta x}(\bullet)$ produces a derivative only at mode k

$$\left. \frac{\delta f_k}{\delta x} \right|_i^L = \frac{\widehat{\delta f_k}}{\delta x}(k) e^{jkx_i} = j_c k'(k) \widehat{f}_k e^{jkx_i} \quad (3.53)$$

where $k'(k)$ is called the modified wave number, because that the exact differential operator $\frac{\partial}{\partial x}(\bullet)$ should only give the *non-modified* wave number k instead of $k'(k)$

$$\frac{\widehat{\partial f_k}}{\partial x}(k) = j_c k \widehat{f}_k \quad (3.54)$$

This MWN is used to characterize the dissipative and dispersive errors of the spatial scheme for equation (3.4). If we write formally the equivalence between derivation and filtering expressed as a convolution with the filter kernel G as in (3.43):

$$\frac{\delta f_k}{\delta x} \equiv \frac{\partial \bar{f}_k}{\partial x} = \frac{\partial}{\partial x} \left[\int_{-\infty}^{+\infty} G(x - \xi) f_k(\xi) d\xi \right] \quad (3.55)$$

In spectral space, (3.55) is

$$j_c k'(k) \widehat{f}_k = j_c k \widehat{G}(k) \widehat{f}_k$$

With a scaling by

$$\omega'(\omega) = \Delta x k'(k \Delta x) \quad (3.56)$$

the filter kernel in Fourier space reads

$$\widehat{G}(\omega = k \Delta x) = \frac{k'(k \Delta x)}{k} = \frac{\omega'(\omega)}{\omega} \quad (3.57)$$

The standard Fourier analysis of errors for linear schemes can also be extended to non-linear schemes by considering only the linear part of the MWN [27, 22, 75]. Contrary to linear schemes, a non-linear scheme operating on a single Fourier mode $f_k(x) = \widehat{f}_k e^{jkx}$ also produces responses at other modes than k :

$$\left. \frac{\delta f_k}{\delta x} \right|_i^{NL} = \frac{\widehat{\delta f_k}}{\delta x}(k) e^{jkx_i} + \sum_{\substack{n=-N/2 \\ n \neq k}}^{N/2} \frac{\widehat{\delta f_k}}{\delta x}(n) e^{jcnx_i} \quad (3.58)$$

The response of the non-linear scheme at mode k provides, by analogy with (3.53), the linear part of MWN $k'_L(k)$:

$$k'_L(k) \equiv \frac{-j \widehat{\delta f_k}}{\widehat{f}_k} \frac{\partial}{\partial x}(k) \quad (3.59)$$

The linear part of scaled MWN of non-linear fifth order WENO-JS5 (JS), WENO-M5 (M), WENO-Z5 (Z), WENO-MZ5 (MZ), seventh order WENO-JS7 (JS7) and linear 5th order WENO-OPT (OPT) is plotted in figure 3.3 by their real and imaginary parts. The related built-in implicit filters of these schemes obtained from (3.57) are shown in 3.4 by their amplitudes $A(\omega)$ (figure 3.4(a)) and phase shifts $\phi(\omega)$ (figure 3.4(b)), which are defined as

$$\bar{f}_k(x) \equiv \int_{-\infty}^{+\infty} G(x - \xi) f_k(\xi) d\xi = \widehat{G}(\omega) \widehat{f}_k e^{jkx} = A(\omega) e^{j\phi(\omega)} \widehat{f}_k e^{jkx} \quad (3.60)$$

Using (3.52), the sub-grid resolution of different WENO schemes can be calculated numerically. For the integration in (3.52), \widehat{G} is made periodic by even symmetry around $\omega = \pi$. Hence, (3.57) has a bounded absolute value, $|\widehat{G}(\omega)|$ is square-integrable and tends rapidly to zero at infinity. So, the

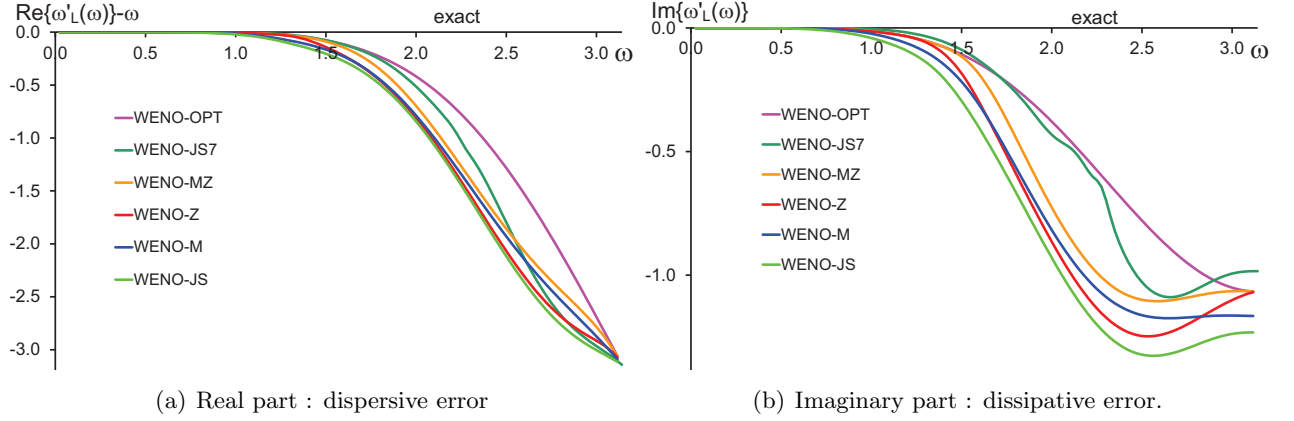


Figure 3.3: Real (a) and imaginary (b) parts of the scaled linear MWN (3.59) for different WENO schemes

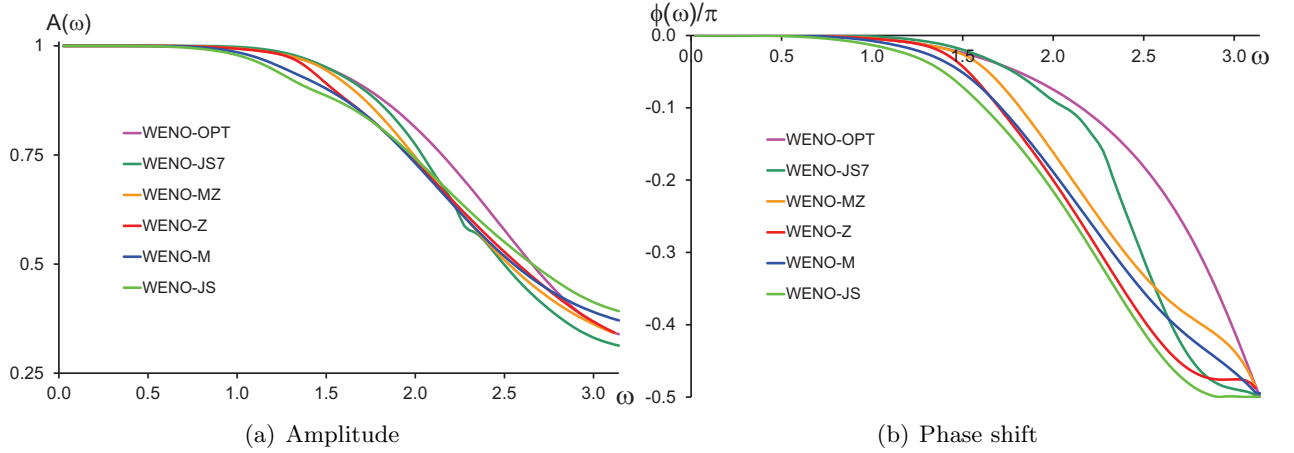


Figure 3.4: Implicit filters of different WENO schemes

integral in (3.52) converges and is estimated numerically in the interval $[0, 10^6\pi]$ by the trapezoidal method, with 4096 points in $[0, \pi]$. The computed subfilter resolutions are

$$\begin{aligned}
 r_{\text{OP}} &\approx 1.1539 \approx 15/13 & ; & & r_{\text{Z}} &\approx 1.2302 \\
 r_{\text{MZ}} &\approx 1.2213 & & & r_{\text{JS7}} &\approx 1.2368 \\
 r_{\text{JS}} &\approx 1.2277 & & & r_{\text{M}} &\approx 1.2438
 \end{aligned} \tag{3.61}$$

The value for the linear WENO-OPT scheme can also be found in (3.51) and is used to check the methodology.

The subfilter resolution of different linear and non-linear schemes as in (3.51) and (3.61) are not those expected, especially for nonlinear schemes. From this criterion, the WENO-JS subfilter resolution r_{JS} seems better than those of improved M and Z schemes, and even better than the seventh order WENO-JS7. This is not the case in most ILES applications [23, 71, 73]. We think that there are few points that one should take care of for this subfilter resolution analysis:

- The filter size Δ defined in (3.52) is used to compare different schemes but may not be a good indicator of the overall performance in actual LES applications. Using this filter width to qualify a scheme may be misleading.

- The subfilter resolution r for non-linear schemes only considers the linear part of the schemes. The contribution of the non-linear part should be further examined.
- Some processes during the flux evaluation like flux-splitting, are ignored during the analysis. These processes are usually non-linear and their impact should also be considered.

A more informative method to compare different non-linear schemes is to perform actual LES test cases. This will be shown next.

Comparison of different schemes in selected test cases

• Taylor-Green vortex

The nearly-incompressible inviscid Taylor-Green vortex flow is a very relevant test case to compare the built-in dissipation and low-pass filters of numerical schemes, since the integrated kinetic energy of the (incompressible) flow in a domain D

$$K(t) = \iiint_D k(\mathbf{x}, t) dV \quad ; \quad k(\mathbf{x}, t) = \frac{1}{2} \rho \vec{U} \cdot \vec{U} \quad (3.62)$$

should be conserved. Following the methodology and numerical setup of Shu *et al.* [76], we investigate the temporal evolution $K(t)/K(0)$ in a cubic computational domain $[0, 2\pi]^3$, on a regular 3D grid. At initial time, the calculation field is set to

$$\begin{cases} \rho(\vec{x}, 0) = 1 \\ u(\vec{x}, 0) = \sin(x) \cos(y) \cos(z) \\ v(\vec{x}, 0) = -\cos(x) \sin(y) \cos(z) \\ w(\vec{x}, 0) = 0 \\ p(\vec{x}, 0) = p_0 + \frac{\rho}{16} [(\cos(2z) + 2)(\cos(2x) + \cos(2y)) - 2] \end{cases} \quad (3.63)$$

and the calculation is performed with different schemes at CFL=0.6. The temporal evolution of the integrated kinetic energy is plotted in figure 3.5. It indicates that on a $128 \times 128 \times 128$ grid, the time needed for non-linear interactions to generate turbulent scales that are small enough (high wave-numbers) to be damped by the numerical dissipation is $t \approx 4$ for WENO-OPT, $t \approx 3$ for WENO-JS and $t \approx 3.5$ for the other non-linear schemes. The vortical structure of the flow at $t = 2$ and $t = 6.5$ can be observed in figure 3.7 using the Q-criterion[77]. The range of computed Q is $-48 \sim 84$. Iso-surface $Q = 0$ surfaces colored by the velocity magnitude are displayed in a $1/8$ sub-domain for a better readability, and the vorticity magnitude in the symmetry planes are projected on corresponding walls. The WENO-OPT solution at $t = 6.5$ reveals some details that are absent in the JS and MZ ones, although the differences are quite insignificant.

This is coherent with the amplitude of the built-in filter transfer function (figure 3.4) which departs from unity a little earlier for WENO-JS. Then, the kinetic energy decay clearly indicates that the most to the less dissipative schemes are JS > Z > M > JS7 > MZ > OPT.

• Double Mach reflection

The Double Mach reflection test case is a classical benchmark for shock-capturing schemes. The computational setup of this case and the detailed discussion of this complicated problem can be found in [78] (see also [79] for a thorough analysis of the waves pattern). A M=10 planar shock wave impinges a 30° angle reflecting wedge, creating a complicated flow field sketched in figure 3.6. As the main shock moves to the right, a reflected shock r , a Mach stem m , and a slip line s emanate from the first triple point T that characterizes the main Mach reflection. A second triple point T' is formed at the intersection of the first reflection r , the second reflection r' and the curved Mach stem m' , yielding the second Mach reflection. The fast stream to the left above s experiences the almost normal reflected shock r' and turns at 180° , to create a jet of dense fluid to the right along the wall. The shear layer s produces vertical structures via the Kelvin-Helmholtz instability, that interact with

the jet. This is the flow region of interest for the present study: the more detailed flow structures can be observed on a given grid, the less dissipative the scheme.

Figure 3.8 displays density contours at time $t = 0.25$ in the double Mach reflection region $[2.6, 3.4] \times [0, 0.6]$, for three grid resolutions, 800×200 , 1200×300 and 1600×400 . The CFL number is 1. On the coarse grid, WENO-MZ is a little more detailed than WENO-M and WENO-Z, all being better than WENO-JS. The same trend is observed on the medium grid. On the fine grid, all improved 5th order schemes are quite similar, and close to WENO-JS7. The linear WENO-OPT scheme can not pass this test case as it lacks the shock capturing feature.

Both the analysis with subfilter revolution and test cases show that the linear WENO-OPT scheme is the less dissipative. So, for a physical LES, the WENO-OPT should be most suitable among all WENO schemes. But for implicit LES, other non-linear WENO schemes might be preferable as they may model small turbulent scales better. Also, the linear WENO-OPT scheme is not capable of high speed shocky applications.

Another interesting comparison between schemes is their computational cost. The time consumption of these two test cases can be found in appendix B.4. Generally speaking, the linear WENO-OPT scheme is much faster than other non-linear shock capturing WENO schemes.

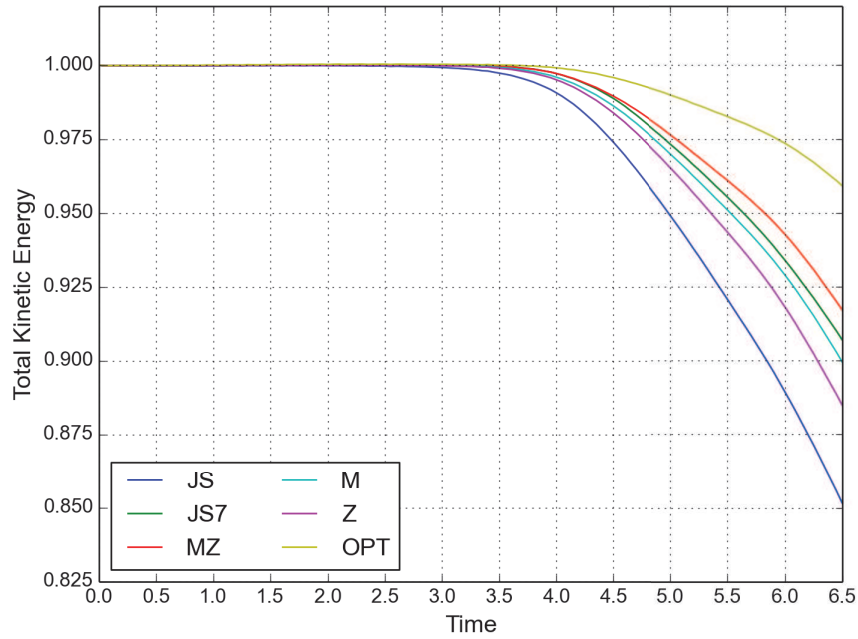


Figure 3.5: Time evolution of the integrated kinetic energy of the Taylor-Green vortex flow, resolution $128 \times 128 \times 128$.

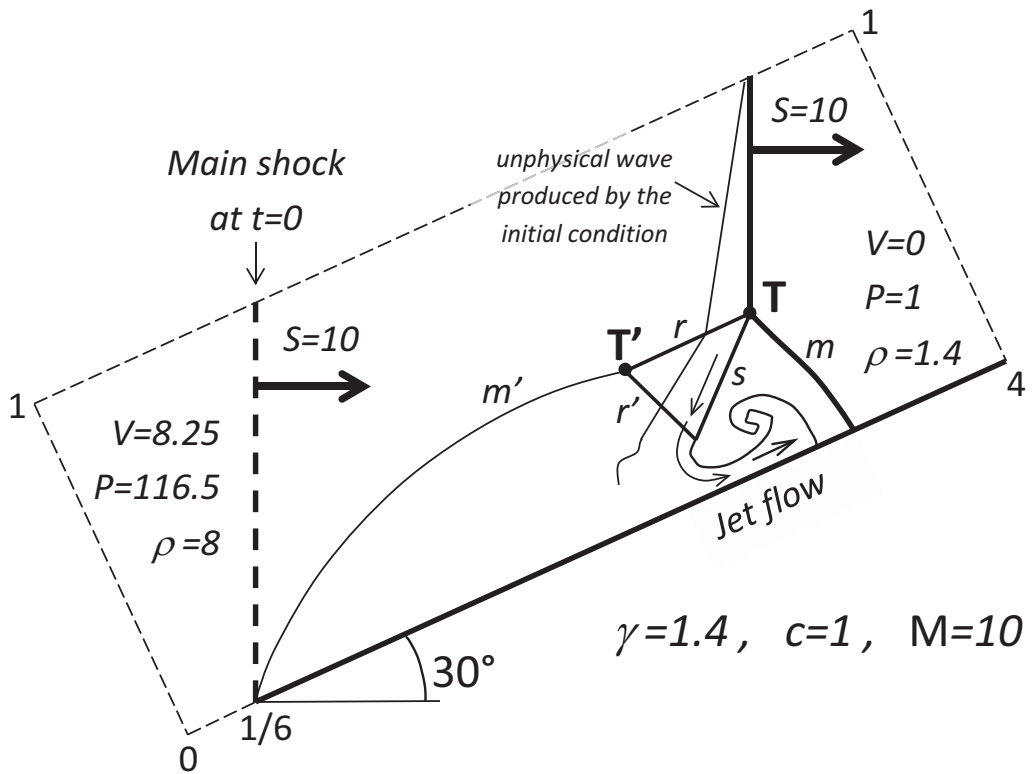


Figure 3.6: Sketch of the double-Mach reflection flow (inspired from [79]).

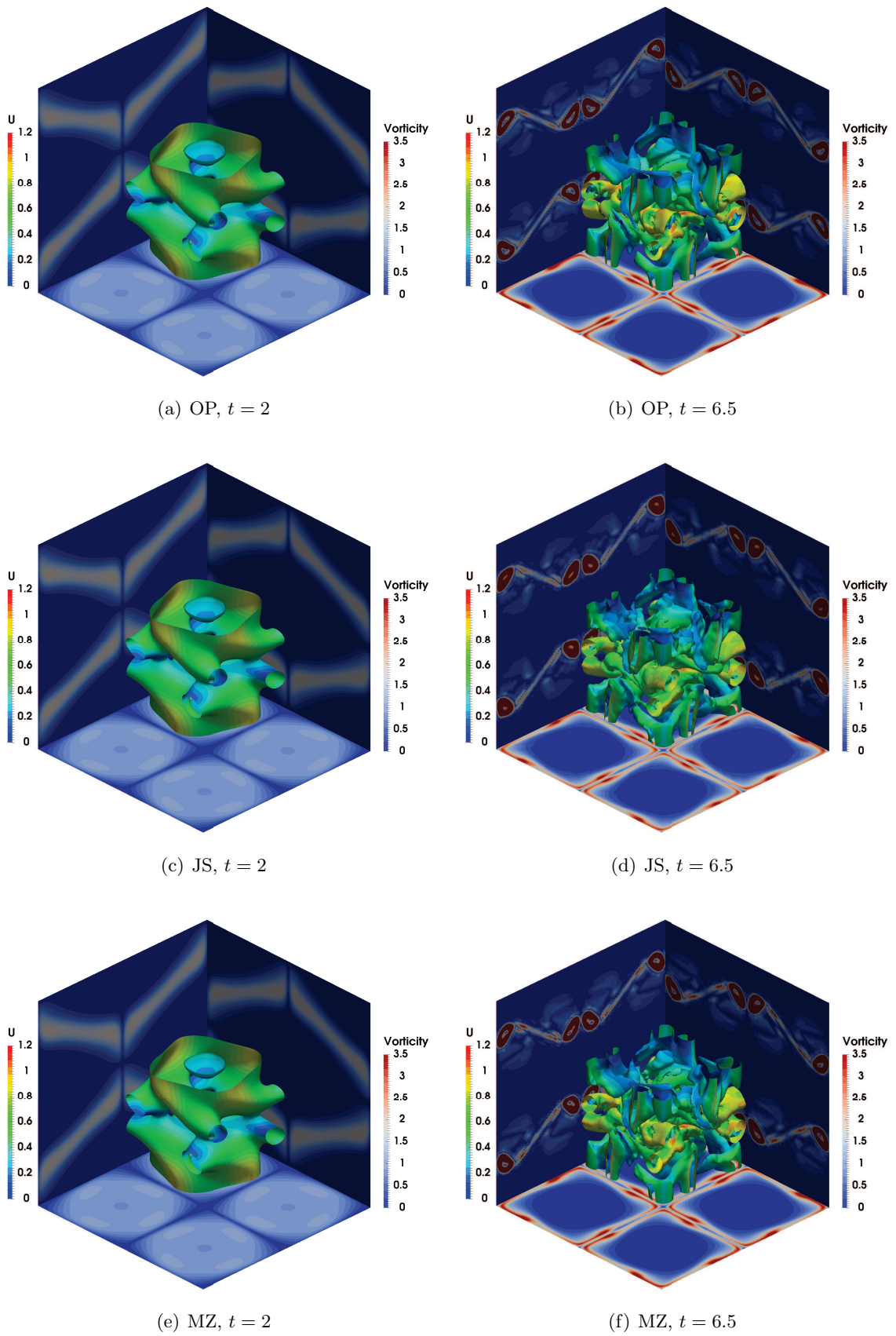


Figure 3.7: Taylor-Green vortex flow. Q -criterion ($Q = 0$) colored by velocity magnitude, and wall projections of the vorticity magnitude in the three symmetry planes.

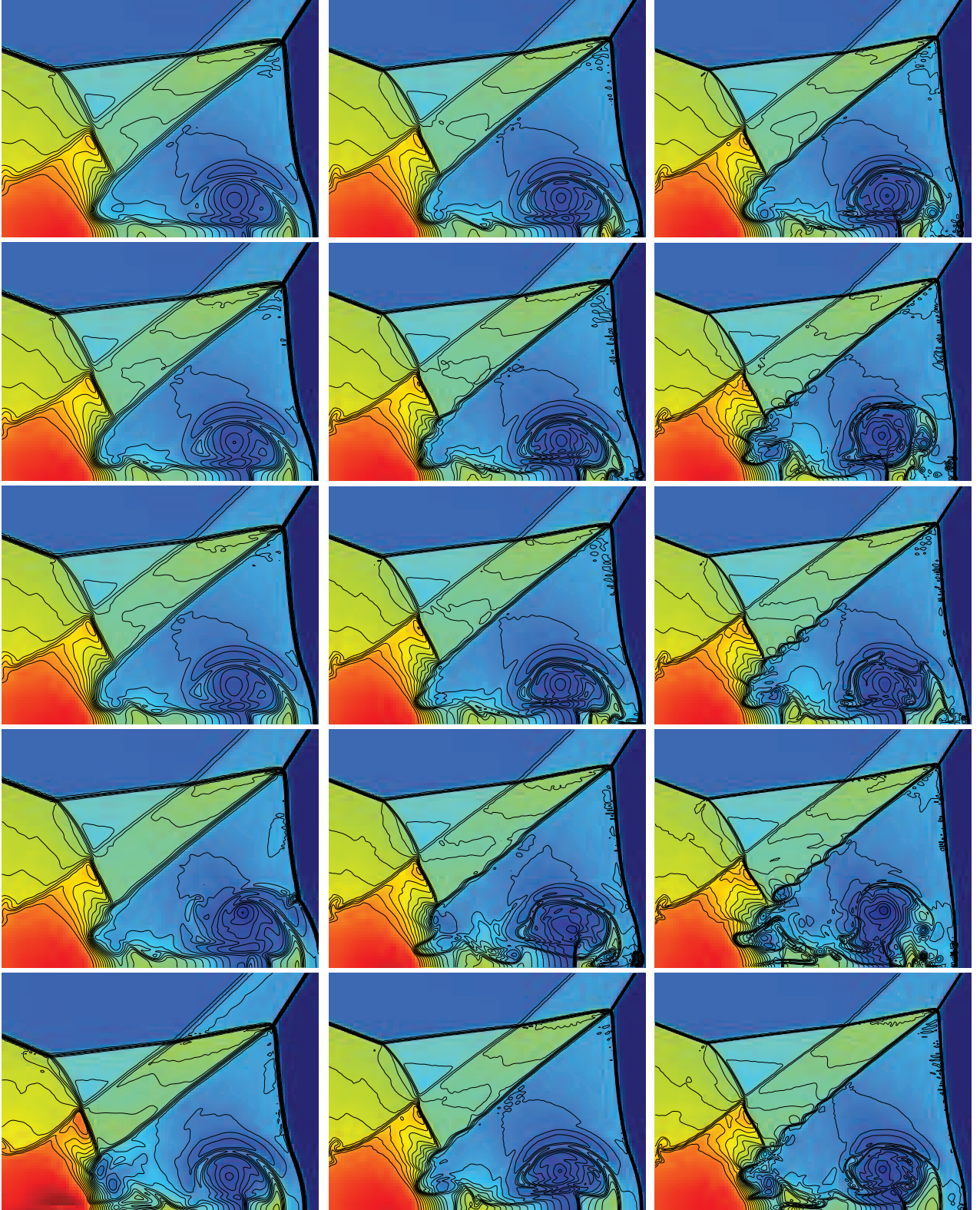


Figure 3.8: Double-Mach reflection at $t = 0.25$. Color: $\rho \in [2, 20]$, step 0.75. Left: 800×200 , middle: 1200×300 , right: 1600×400 . From top to bottom: JS, M, Z, MZ, JS7.

3.3 Low Mach modifications for time step enlarging

The explicit TVD Runge-Kutta time matching schemes for time integration are constrained by the Courant–Friedrichs–Lewy (CFL) condition, for the maximum allowed time step Δt

$$\Delta t_{max} = \mathcal{C} \min \left(\left| \frac{\Delta x}{\lambda_i} \right| \right) \quad (3.64)$$

in which, \mathcal{C} is the Courant number usually smaller than 1, Δx is the grid size and λ_i are the characteristic speeds of the hyperbolic PDEs involving the speed of sound c and the flow velocity in N-S system. This means that under low-Mach conditions when $\text{Ma} \equiv \left| \frac{u}{c} \right| \ll 1$, the time step is determined by the speed of sound c and at a scale of $\frac{\Delta x}{c}$, which is much too small when acoustics is not important.

In order to save computational time, two common solutions to increase the time step exist. The first one is to use an implicit or semi-implicit time stepping instead the explicit one; another route is to use an incompressible solver directly for low Mach flows, in which the speed of sound is infinite. Both the two routes need very deep modifications of our existing compressible LES code.

A third possibility is to artificially decrease the speed of sound as in the Artificial Acoustic Stiffness Reduction (ASR) method introduced by Wang and Trouvé [67]. In this section, this approach and our implementation will be illustrated.

3.3.1 Artificial reduction of the speed of sound

The main idea of the ASR method is to reduce the speed of sound artificially. Let consider the one dimensional, mono-species N-S equations without viscous and source terms:

$$\begin{cases} \frac{\partial \rho}{\partial t} + u \frac{\partial \rho}{\partial x} + \rho \frac{\partial u}{\partial x} = 0 \\ \frac{\partial u}{\partial t} + \frac{rT}{\rho} \frac{\partial \rho}{\partial x} + u \frac{\partial u}{\partial x} + r \frac{\partial T}{\partial x} = 0 \\ \frac{\partial T}{\partial t} + (\gamma - 1) T \frac{\partial u}{\partial x} + u \frac{\partial T}{\partial x} = 0 \end{cases} \quad (3.65)$$

This is the 1D *Euler* system for the primitive variables $\vec{V} \equiv [\rho \quad u \quad T]^T$. Equation (3.65) can be arranged in a vector form :

$$\frac{\partial \vec{V}}{\partial t} + \tilde{A} \frac{\partial \vec{V}}{\partial x} = \vec{0} \quad (3.66)$$

with

$$\tilde{A} = \begin{pmatrix} u & \rho & 0 \\ rT/\rho & u & r \\ 0 & (\gamma - 1)T & u \end{pmatrix} \quad (3.67)$$

The explicit time step constrain of system (3.66) given by the CFL condition (3.64) can be obtained by the evaluation of characteristic speeds. This can be achieved by the diagonalization of matrix \tilde{A} :

$$\tilde{A} = \tilde{R} \Lambda \tilde{L} \quad (3.68)$$

The resulting right and left eigenvector matrix of \tilde{A} (3.67) read

$$\tilde{R} = \begin{pmatrix} 1 & 1 & 1 \\ -c/\rho & 0 & c/\rho \\ (\gamma - 1)T/\rho & -T/\rho & (\gamma - 1)T/\rho \end{pmatrix} \quad (3.69)$$

$$\tilde{L} = \begin{pmatrix} 1/(2\gamma) & -\rho/(2c) & \rho/(2\gamma T) \\ (\gamma - 1)/\gamma & 0 & -\rho/(\gamma T) \\ 1/(2\gamma) & \rho/(2c) & \rho/(2\gamma T) \end{pmatrix} \quad (3.70)$$

and the eigenvalue matrix of \tilde{A} is³

$$\Lambda = \begin{pmatrix} u - c & & \\ & u & \\ & & u + c \end{pmatrix} \quad (3.71)$$

in which

$$c = \sqrt{\gamma r T} \quad (3.72)$$

The characteristic speeds of the hyperbolic system (3.65) are $|u - c|$, $|u|$ and $|u + c|$, and the CFL condition in (3.64) for (3.65) is then

$$\Delta t_{max} = C \min \left(\frac{\Delta x}{|u + c|}, \frac{\Delta x}{|u|}, \frac{\Delta x}{|u - c|} \right)$$

In order to enlarge the time step constrained by c , the ASR method modifies the speed of sound c to c/α , where $\alpha > 1$, by replacing γ by γ/α^2 in jacobian matrix \tilde{A} . The resulting jacobian matrix reads

$$\tilde{A}_{ASR} \equiv \begin{pmatrix} u & \rho & 0 \\ rT/\rho & u & r \\ 0 & (\gamma/\alpha^2 - 1)T & u \end{pmatrix} \quad (3.73)$$

And the diagonalization of this matrix gives

$$\tilde{A}_{ASR} = \tilde{R}_{ASR} \Lambda_{ASR} \tilde{L}_{ASR}$$

with

$$\tilde{R}_{ASR} = \begin{pmatrix} 1 & 1 & 1 \\ -c/\rho/\alpha & 0 & c/\rho/\alpha \\ (\gamma/\alpha^2 - 1)T/\rho & -T/\rho & (\gamma/\alpha^2 - 1)T/\rho \end{pmatrix} \quad (3.74)$$

$$\tilde{L}_{ASR} = \begin{pmatrix} \alpha^2/(2\gamma) & -\alpha\rho/(2c) & \rho\alpha^2/(2\gamma T) \\ (\gamma - \alpha^2)/\gamma & 0 & -\rho\alpha^2/(\gamma T) \\ \alpha^2/(2\gamma) & \alpha\rho/(2c) & \alpha^2\rho/(2\gamma T) \end{pmatrix} \quad (3.75)$$

$$\Lambda_{ASR} = \begin{pmatrix} u - c/\alpha & & \\ & u & \\ & & u + c/\alpha \end{pmatrix} \quad (3.76)$$

Apparently, the CFL condition after this modification is

$$\Delta t_{max} = C \min \left(\frac{\Delta x}{|u + c/\alpha|}, \frac{\Delta x}{|u|}, \frac{\Delta x}{|u - c/\alpha|} \right) \quad (3.77)$$

So, under low Mach conditions when $|u| \ll c$, this time step is almost α times larger than that for the original Euler system.

The modified 1D ASR system

$$\frac{\partial \vec{V}}{\partial t} + \tilde{A}_{ASR} \frac{\partial \vec{V}}{\partial x} = \vec{0}$$

is then

$$\left\{ \begin{array}{l} \frac{\partial \rho}{\partial t} + u \frac{\partial \rho}{\partial x} + \rho \frac{\partial u}{\partial x} = 0 \\ \frac{\partial u}{\partial t} + \frac{rT}{\rho} \frac{\partial \rho}{\partial x} + u \frac{\partial u}{\partial x} + r \frac{\partial T}{\partial x} = 0 \\ \frac{\partial T}{\partial t} + (\gamma - 1) T \frac{\partial u}{\partial x} + u \frac{\partial T}{\partial x} = \tilde{S}_{ASR} \end{array} \right. \quad (3.78)$$

³These matrix are in fact a reduction form for 1D mono-species case of \tilde{R} , \tilde{L} and Λ for 3D multi-species in equations (B.18), (B.19) and (B.17).

where

$$\tilde{S}_{ASR} \equiv \left(1 - \frac{1}{\alpha^2}\right) \gamma T \frac{\partial u}{\partial x} \quad (3.79)$$

This additional term in the temperature equation is the only difference between the ASR system (3.78) and the original Euler system (3.65). Scale analysis of this ASR system indicate that the term \tilde{S}_{ASR} is at most of order $\mathcal{O}(\text{Ma})$ thus almost no influence on the main flow properties (at order $\mathcal{O}(1)$) under low Mach conditions. More details on scale analysis and validation test cases can be found in [67, 80, 81].

3.3.2 The ASR implementation for 3D multi-species N-S equations

ASR modification on 3D Euler system

Like for the one dimensional Euler system, the ASR method can also enlarge the time step of the 3D multi-species N-S system. As a first step, the Euler part of 3D multi-species N-S equations is written using primitive variables as (B.9):

$$\frac{\partial \rho}{\partial t} + u_j \frac{\partial \rho}{\partial x_j} + \rho \frac{\partial u_j}{\partial x_j} = 0 \quad (3.80a)$$

$$\frac{\partial u_i}{\partial t} + \frac{rT}{\rho} \frac{\partial \rho}{\partial x_i} + u_j \frac{\partial u_i}{\partial x_j} + r \frac{\partial T}{\partial x_i} + T \sum_{k=1}^{N_{sp}} (r_k - r) \frac{\partial Y_k}{\partial x_i} = 0 \quad \text{for } i = 1, 2, 3 \quad (3.80b)$$

$$\frac{\partial T}{\partial t} + u_j \frac{\partial T}{\partial x_j} + (\gamma - 1) T \frac{\partial u_j}{\partial x_j} = 0 \quad (3.80c)$$

$$\frac{\partial Y_k}{\partial t} + u_j \frac{\partial Y_k}{\partial x_j} = 0 \quad \text{for } k = 1, \dots, N_{sp} \quad (3.80d)$$

Using the vector of primitive variables,

$$\mathbf{V} \equiv \begin{bmatrix} \rho \\ u \\ v \\ w \\ T \\ Y_1 \\ \vdots \\ Y_{N_{sp}} \end{bmatrix} \quad (3.81)$$

a vector form of (3.81) can be written like

$$\frac{\partial \mathbf{V}}{\partial t} + \tilde{A} \frac{\partial \mathbf{V}}{\partial x} + \tilde{B} \frac{\partial \mathbf{V}}{\partial y} + \tilde{C} \frac{\partial \mathbf{V}}{\partial z} = \mathbf{0} \quad (3.82)$$

with the matrix \tilde{A} same as (B.11) and

$$\tilde{B} = \begin{pmatrix} v & 0 & \rho & 0 & 0 & 0 & \dots & 0 \\ 0 & v & 0 & 0 & 0 & 0 & \dots & 0 \\ \frac{rT}{\rho} & 0 & v & 0 & r & T(r_1 - r) & \dots & T(r_{N_{sp}} - r) \\ 0 & 0 & 0 & v & 0 & 0 & \dots & 0 \\ 0 & 0 & (\gamma - 1)T & 0 & v & 0 & \dots & 0 \\ 0 & 0 & 0 & 0 & 0 & v & \dots & 0 \\ \vdots & \vdots & \vdots & \vdots & \vdots & \vdots(0) & \ddots & \vdots(v) \\ 0 & 0 & 0 & 0 & 0 & 0 & \dots & v \end{pmatrix} \quad (3.83)$$

$$\tilde{C} = \begin{pmatrix} w & 0 & 0 & \rho & 0 & 0 & \cdots & 0 \\ 0 & w & 0 & 0 & 0 & 0 & \cdots & 0 \\ 0 & 0 & w & 0 & 0 & 0 & \cdots & 0 \\ \frac{rT}{\rho} & 0 & 0 & w & r & T(r_1 - r) & \cdots & T(r_{N_{sp}} - r) \\ 0 & 0 & 0 & (\gamma - 1)T & w & 0 & \cdots & 0 \\ 0 & 0 & 0 & 0 & 0 & w & \cdots & 0 \\ \vdots & \vdots & \vdots & \vdots & \vdots & \vdots(0) & \ddots(w) & \vdots(0) \\ 0 & 0 & 0 & 0 & 0 & 0 & \cdots & w \end{pmatrix} \quad (3.84)$$

To artificially reduce the speed of sound in the characteristic speeds, same idea as in the 1D Euler system is applied here: replace the γ by γ/α^2 . For matrix \tilde{A} in x direction, it gives:

$$\tilde{A}_{ASR} \equiv \begin{pmatrix} u & \rho & 0 & 0 & 0 & 0 & \cdots & 0 \\ \frac{rT}{\rho} & u & 0 & 0 & r & T(r_1 - r) & \cdots & T(r_{N_{sp}} - r) \\ 0 & 0 & u & 0 & 0 & 0 & \cdots & 0 \\ 0 & 0 & 0 & u & 0 & 0 & \cdots & 0 \\ 0 & (\gamma/\alpha^2 - 1)T & 0 & 0 & u & 0 & \cdots & 0 \\ 0 & 0 & 0 & 0 & 0 & u & \cdots & 0 \\ \vdots & \vdots & \vdots & \vdots & \vdots & \vdots(0) & \ddots(u) & \vdots(0) \\ 0 & 0 & 0 & 0 & 0 & 0 & \cdots & u \end{pmatrix} \quad (3.85)$$

And the resulting diagonalization of this jacobian matrix are:

$$\tilde{L}_{ASR} = \begin{pmatrix} \frac{\alpha^2}{2\gamma} & -\frac{\rho\alpha}{2c} & 0 & 0 & \frac{\rho\alpha^2}{2\gamma T} & -\frac{\rho\alpha^2(r-r_1)}{2\gamma r} & \cdots & -\frac{\rho\alpha^2(r-r_{N_{sp}})}{2\gamma r} \\ -\frac{\alpha^2-\gamma}{\gamma} & 0 & 0 & 0 & -\frac{\rho\alpha^2}{\gamma T} & \frac{\rho\alpha^2(r-r_1)}{\gamma r} & \cdots & \frac{\rho\alpha^2(r-r_{N_{sp}})}{\gamma r} \\ 0 & 0 & 1 & 0 & 0 & 0 & \cdots & 0 \\ 0 & 0 & 0 & 1 & 0 & 0 & \cdots & 0 \\ \frac{\alpha^2}{2\gamma} & \frac{\rho\alpha}{2c} & 0 & 0 & \frac{\rho\alpha^2}{2\gamma T} & -\frac{\rho\alpha^2(r-r_1)}{2\gamma r} & \cdots & -\frac{\rho\alpha^2(r-r_{N_{sp}})}{2\gamma r} \\ 0 & 0 & 0 & 0 & 0 & 1 & \cdots(0) & 0 \\ \vdots & \vdots & \vdots & \vdots & \vdots & \vdots(0) & \ddots(1) & \vdots \\ 0 & 0 & 0 & 0 & 0 & 0 & 0 & 1 \end{pmatrix} \quad (3.86)$$

$$\tilde{R}_{ASR} = \begin{pmatrix} 1 & 1 & 0 & 0 & 1 & 0 & \cdots & 0 \\ -\frac{c}{\alpha\rho} & 0 & 0 & 0 & \frac{c}{\alpha\rho} & 0 & \cdots & 0 \\ 0 & 0 & 1 & 0 & 0 & 0 & \cdots & 0 \\ 0 & 0 & 0 & 1 & 0 & 0 & \cdots & 0 \\ -\frac{(\alpha^2-\gamma)T}{\alpha^2\rho} & -\frac{T}{\rho} & 0 & 0 & -\frac{(\alpha^2-\gamma)T}{\alpha^2\rho} & \frac{(r-r_1)T}{r} & \cdots & \frac{(r-r_{N_{sp}})T}{r} \\ 0 & 0 & 0 & 0 & 0 & 1 & \cdots(0) & 0 \\ \vdots & \vdots & \vdots & \vdots & \vdots & \cdots(0) & \ddots(1) & \cdots \\ 0 & 0 & 0 & 0 & 0 & 0 & 0 & 1 \end{pmatrix} \quad (3.87)$$

$$\Lambda_{ASR} = \begin{pmatrix} u - c/\alpha & & & & & & & \\ & u & & & & & & \\ & & u & & & & & \\ & & & u & & & & \\ & & & & u + c/\alpha & & & \\ & & & & & u & & \\ & & & & & & \ddots & \\ & & & & & & & u \end{pmatrix} \quad (3.88)$$

The characteristic speeds in the eigenvalue matrix (3.88) indicate that the time step for this ASR modified system has been enlarged α times.

Applying the same modifications to \tilde{B} and \tilde{C} , the ASR modified 3D Euler system in primitive form can be obtained. In vector form, it reads

$$\frac{\partial \mathbf{V}}{\partial t} + \tilde{A}_{ASR} \frac{\partial \mathbf{V}}{\partial x} + \tilde{B}_{ASR} \frac{\partial \mathbf{V}}{\partial y} + \tilde{C}_{ASR} \frac{\partial \mathbf{V}}{\partial z} = \mathbf{0} \quad (3.89)$$

with \tilde{A}_{ASR} given in (3.85), and \tilde{B}_{ASR} and \tilde{C}_{ASR} being the same as (3.83) and (3.84), except that γ is substituted by γ/α^2 .

The next step is then to write this modified system (3.89) in conservative form, in order to be implemented in the calculation code. The task is to use the conservative variables \mathbf{U} as defined in (2.20)

$$\mathbf{U} \equiv \begin{bmatrix} \rho \\ \rho u \\ \rho v \\ \rho w \\ \rho E \\ \rho Y_1 \\ \vdots \\ \rho Y_{N_{sp}} \end{bmatrix}$$

to write the primitive form (3.89). Firstly, the primitive form can be separated into

$$\begin{aligned} & \frac{\partial \mathbf{V}}{\partial t} + \tilde{A} \frac{\partial \mathbf{V}}{\partial x} + \tilde{B} \frac{\partial \mathbf{V}}{\partial y} + \tilde{C} \frac{\partial \mathbf{V}}{\partial z} \\ &= (\tilde{A} - \tilde{A}_{ASR}) \frac{\partial \mathbf{V}}{\partial x} + (\tilde{B} - \tilde{B}_{ASR}) \frac{\partial \mathbf{V}}{\partial y} + (\tilde{C} - \tilde{C}_{ASR}) \frac{\partial \mathbf{V}}{\partial z} \end{aligned} \quad (3.90)$$

where \tilde{A} is the original jacobian matrix (B.11), and

$$\tilde{A} - \tilde{A}_{ASR} = \begin{pmatrix} 0 & 0 & 0 & 0 & 0 & 0 & 0 & \dots & 0 \\ 0 & 0 & 0 & 0 & 0 & 0 & 0 & \dots & 0 \\ 0 & 0 & 0 & 0 & 0 & 0 & 0 & \dots & 0 \\ 0 & 0 & 0 & 0 & 0 & 0 & 0 & \dots & 0 \\ 0 & (1 - 1/\alpha^2) \gamma T & 0 & 0 & 0 & 0 & 0 & \dots & 0 \\ 0 & 0 & 0 & 0 & 0 & 0 & 0 & \dots & 0 \\ 0 & 0 & 0 & 0 & 0 & 0 & 0 & \dots & 0 \\ \vdots & \vdots & \vdots & \vdots & \vdots & \vdots & \vdots(0) & \ddots & \vdots \\ 0 & 0 & 0 & 0 & 0 & 0 & 0 & \dots & 0 \end{pmatrix} \quad (3.91)$$

Multiplying the passage matrix M

$$M \equiv \frac{d\mathbf{U}}{d\mathbf{V}} \quad (3.92)$$

to the LHS of ASR Euler system (3.90), one may have

$$\begin{aligned} & \frac{\partial \mathbf{U}}{\partial t} + \frac{\partial \mathbf{F}}{\partial x} + \frac{\partial \mathbf{G}}{\partial y} + \frac{\partial \mathbf{H}}{\partial z} \\ &= M(\tilde{A} - \tilde{A}_{ASR}) \frac{\partial \mathbf{V}}{\partial x} + M(\tilde{B} - \tilde{B}_{ASR}) \frac{\partial \mathbf{V}}{\partial y} + M(\tilde{C} - \tilde{C}_{ASR}) \frac{\partial \mathbf{V}}{\partial z} \end{aligned} \quad (3.93)$$

in which the fluxes \mathbf{F} , \mathbf{G} and \mathbf{H} can be found in equation (2.21). In scalar form, this system (3.93)

reads

$$\frac{\partial \rho}{\partial t} + \frac{\partial}{\partial x_j} (\rho u_j) = 0 \quad (3.94a)$$

$$\frac{\partial}{\partial t} (\rho u_i) + \frac{\partial}{\partial x_j} (\rho u_i u_j + p \delta_{ij}) = 0 \quad \text{for } i = 1, 2, 3 \quad (3.94b)$$

$$\frac{\partial}{\partial t} (\rho E) + \frac{\partial}{\partial x_j} (\rho E u_j + p u_j) = \left(1 - \frac{1}{\alpha^2}\right) \frac{\gamma p}{\gamma - 1} u_{j,j} \quad (3.94c)$$

$$\frac{\partial}{\partial t} (\rho Y_k) + \frac{\partial}{\partial x_j} (\rho Y_k u_j) = 0 \quad \text{for } k = 1, \dots, N_{\text{sp}} \quad (3.94d)$$

Fully conservative implementation of the 3D ASR Euler system

It is clear that this system can not be explicitly written in conservative form as the additional term

$$S_{\text{ASR}} \equiv \left(1 - \frac{1}{\alpha^2}\right) \frac{\gamma p}{\gamma - 1} \frac{\partial u_j}{\partial x_j} \quad (3.95)$$

in the energy conservation equation (3.94c) is not in conservative form. This prevents the straight forward evaluation and splitting of Euler flux. In fact, one can write this system in vector form:

$$\frac{\partial \mathbf{U}}{\partial t} + \frac{\partial \mathbf{F}_{\text{ASR}}}{\partial x} + \frac{\partial \mathbf{G}_{\text{ASR}}}{\partial y} + \frac{\partial \mathbf{H}_{\text{ASR}}}{\partial z} = \mathbf{0} \quad (3.96)$$

with, e.g. the Euler flux in x direction defined from (3.93) as

$$\frac{\partial \mathbf{F}_{\text{ASR}}}{\partial x} = \frac{\partial \mathbf{F}}{\partial x} + \begin{pmatrix} 0 \\ 0 \\ 0 \\ 0 \\ -\left(1 - \frac{1}{\alpha^2}\right) \frac{\gamma p}{\gamma - 1} \frac{\partial u}{\partial x} \\ 0 \\ \vdots \\ 0 \end{pmatrix} \quad (3.97)$$

Although \mathbf{F}_{ASR} , \mathbf{G}_{ASR} and \mathbf{H}_{ASR} are only implicitly defined, the jacobian matrix of these flux can still be obtained. If we define the jacobian for \mathbf{F}_{ASR} as

$$A_{\text{ASR}} \equiv \frac{\partial \mathbf{F}_{\text{ASR}}}{\partial \mathbf{U}} \quad (3.98)$$

it can be deduced from (3.93), as

$$A_{\text{ASR}} = M \tilde{A}_{\text{ASR}} M^{-1} \quad (3.99)$$

This matrix and it's left and right eigenvectors can be found in (B.25), (B.23) and (B.24).

A numerical treatment for ASR Euler flux reconstruction is proposed here. Let take the flux reconstruction in x direction as example. To calculate $\left. \frac{\partial \mathbf{F}_{\text{ASR}}}{\partial x} \right|_{x=x_i}$, the same process as in section 3.2.1 is applied, except that

1. The eigenvalues decomposition of the jacobian at $x = x_{i\pm 1/2}$ uses the ASR modified version as shown in (B.23) and (B.24). The eigenvalues are apparently the ASR modified reduced eigenvalues (3.88).
2. For the reconstruction of the flux splitted characteristic waves, instead of the original form (3.35) used in the original N-S system

$$\mathcal{L}_j^{>0} \equiv \frac{1}{2} (L_{i+1/2} \mathbf{F}_j + \bar{\Lambda} L_{i+1/2} \mathbf{U}_j) \quad \text{for } I_j \in S$$

the ASR system uses

$$\mathcal{L}_j^{>0} \equiv \frac{1}{2}(L_{i+1/2} \mathbf{F}_j + \begin{pmatrix} 0 \\ 0 \\ 0 \\ 0 \\ -\left(1 - \frac{1}{\alpha^2}\right) \frac{\gamma_i p_i}{\gamma_i - 1} u_j \\ 0 \\ \vdots \\ 0 \end{pmatrix}) + \bar{\Lambda} L_{i+1/2} \mathbf{U}_j \quad (3.100)$$

where the subscripts i and j indicate $x = x_i$ and $x = x_j$. In this form, the ASR term is inserted into the flux at $x = x_i$, the value of p and γ are always taken at $x = x_i$ for all the involved stencils. For example, the 5th order upwind scheme for the ASR system is then (B.26). This will give an extra non-conservative ASR term $-\left(1 - \frac{1}{\alpha^2}\right) \frac{\gamma p}{\gamma - 1} \frac{\partial u}{\partial x}$ in the energy equation compared to the original N-S energy equation.

3. With this kind of reconstruction, the value $h_{i+1/2}$ constructed for the evaluation of $\left. \frac{\partial \mathbf{F}_{ASR}}{\partial x} \right|_{x=x_i}$ can not be used as $h_{(i+1)-1/2}$ in the calculation of $\left. \frac{\partial \mathbf{F}_{ASR}}{\partial x} \right|_{x=x_{i+1}}$. The latter should be reconstructed separately. This may violate the Rankine-Hugoniot conditions for the speed of discontinuities, since this scheme is no more fully conservative (Lax-Wendroff theorem 1960). However, in low-speed flows, this is not a crucial issue.

ASR modified 3D multi-species N-S system

The ASR modified 3D multi-species N-S system can be got by adding the viscous and source terms to the ASR Euler system:

$$\begin{aligned} \frac{\partial \rho}{\partial t} + (\rho u_j)_{,j} &= 0 \\ \frac{\partial \rho u_i}{\partial t} + (\rho u_i u_j + p \delta_{ij})_{,j} &= \tau_{ij,j} \quad \text{for } i = 1, 2, 3 \\ \frac{\partial \rho E}{\partial t} + [(\rho E + p) u_j]_{,j} &= (u_i \tau_{ij})_{,j} - q_{j,j} + S_{ASR} \\ \frac{\partial \rho Y_k}{\partial t} + (\rho u_j Y_k)_{,j} &= -J_{kj,j} + \dot{\omega}_k \quad \text{for } k = 1, \dots, N_{sp} \end{aligned}$$

with the same S_{ASR} in (3.95). But following the analysis by Wang and Trouvé in [67], for the ASR N-S system, the flow dilatation $\frac{\partial u_j}{\partial x_j}$ in the additional term (3.95) should be replaced by the acoustic part of the flow dilatation. A viscous correction V_{ASR} is added to the energy equation to achieve this. The resulting ASR N-S equations read:

$$\frac{\partial \rho}{\partial t} + (\rho u_j)_{,j} = 0 \quad (3.102a)$$

$$\frac{\partial \rho u_i}{\partial t} + (\rho u_i u_j + p \delta_{ij})_{,j} = \tau_{ij,j} \quad \text{for } i = 1, 2, 3 \quad (3.102b)$$

$$\frac{\partial \rho E}{\partial t} + [(\rho E + p) u_j]_{,j} = (u_i \tau_{ij})_{,j} - q_{j,j} + S_{ASR} + V_{ASR} \quad (3.102c)$$

$$\frac{\partial \rho Y_k}{\partial t} + (\rho u_j Y_k)_{,j} = -J_{kj,j} + \dot{\omega}_k \quad \text{for } k = 1, \dots, N_{sp} \quad (3.102d)$$

with

$$S_{ASR} \equiv \left(1 - \frac{1}{\alpha^2}\right) \frac{\gamma p}{\gamma - 1} \frac{\partial u_j}{\partial x_j}$$

and

$$V_{ASR} \equiv - \left(1 - \frac{1}{\alpha^2} \right) \left[\tau_{ij} \frac{\partial u_i}{\partial x_j} - \frac{\partial q_j}{\partial x_j} - \sum_{k=1}^{N_{sp}} \left(h_k - \frac{W c_p T}{W_k} \right) \left(- \frac{\partial}{\partial x_j} (\rho Y_k V_{k,j}) + \dot{\omega}_k \right) \right] \quad (3.103)$$

in which W and W_k are the molecular weight of the mixture and species k .

3.3.3 Test-cases for ASR method

To validate our implementation of ASR method, three simple 1D test-cases are performed. The first one is Problem 1 in [67]. This is a one dimensional acoustic wave propagation problem. The calculation domain is set to be $x \in [-0.005, 0.035]$. The initial conditions are as follows: According to the linear acoustic wave approach, the flow field of a 1D acoustic wave can be separated into the mean flow (p_0, ρ_0, u_0) and the acoustic perturbation (p_1, ρ_1, u_1) ,

$$p = p_0 + p_1, \rho = \rho_0 + \rho_1, u = u_0 + u_1$$

and the perturbation should meet the condition that

$$\begin{aligned} u_1 &= \frac{p_1}{\rho_0 c_0} \\ \rho_1 &= \frac{p_1}{c_0^2} \end{aligned}$$

where c_0 is the speed of sound under mean flow conditions

$$c_0 = \sqrt{\gamma r T_0}$$

As initial conditions, the mean flow field is set to under atmospheric pressure and temperature with no mean velocity: $p_0 = 1\text{ATM} = 101325\text{Pa}$, $T_0 = 300\text{K}$, $u_0 = 0$, $\rho_0 = p_0/r/T_0$. The initial perturbation field is given as

$$p_1 = \begin{cases} p_c \left[1 + \cos \left(\frac{2\pi(x-x_0)}{L} \right) \right] & \text{if } x_0 - \frac{L}{2} \leq x \leq x_0 + \frac{L}{2} \\ 0 & \text{otherwise} \end{cases}$$

A pulse-like initial pressure field is achieved by turning p_c and L .

This test-case is calculated with $(\alpha = 10)$ and without ASR method $(\alpha = 1)$. Apparently, as an acoustic wave, the theoretical solution of this problem should be the perturbation will travel at the speed of sound c_0 following the direction of u_1 with it's original shape unchanged. And, if this problem is solved with ASR method, the perturbation should travel at a reduced speed of sound, c_0/α . The resulting pressure field of this simulation are shown in figure 3.9. The wave propagation velocity can be obtained by the traveling speed of the maximum pressure location. Using ASR with $\alpha = 10$ (Fig. 3.9(b)), the traveling speed of the wave is at $c_{\alpha=10} = 37.5\text{m/s}$, and is reduced almost α times comparing to non-ASR setup (where $c_{\alpha=1} = 377.7\text{m/s}$, Fig. 3.9(a)). However, the shapes of the perturbation under both conditions keep almost identical.

Problem 2 in [67] is a test-case to assess the ASR method with the presence of volume force, e.g. gravity. The interest of this test-case is that, some other sound speed reducing method, like PSG method introduced by Ramshaw *et al.* [82], may dramatically enforce the volume force. ASR method should not have this issue according to [67]. The calculation domain is set to $x \in [-0.005, 0.035]$, the gravity $g = 9.8\text{m/s}^2$ is set to along the x direction. Initially, the flow is set to be uniform at atmospheric condition without any velocity. The boundary at $x = 0$ is set to solid wall with ghost points method. Theoretically, after some time, when the flow becomes steady under gravity, the variation of pressure Δp at $x = \Delta x$ should be

$$\Delta p \cong \rho_0 g \Delta x$$

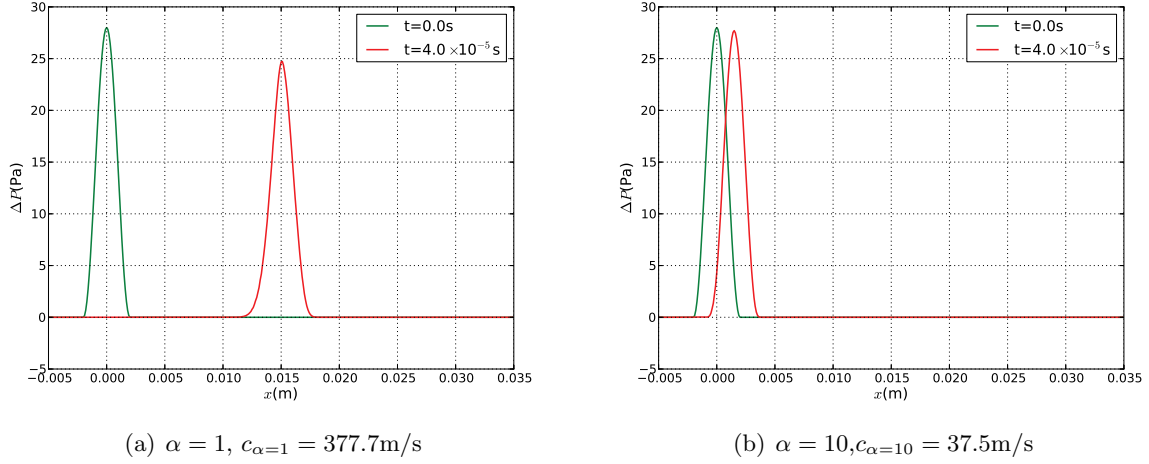


Figure 3.9: Perturbation of pressure in the Problem 1 with (a) and without (b) ASR.

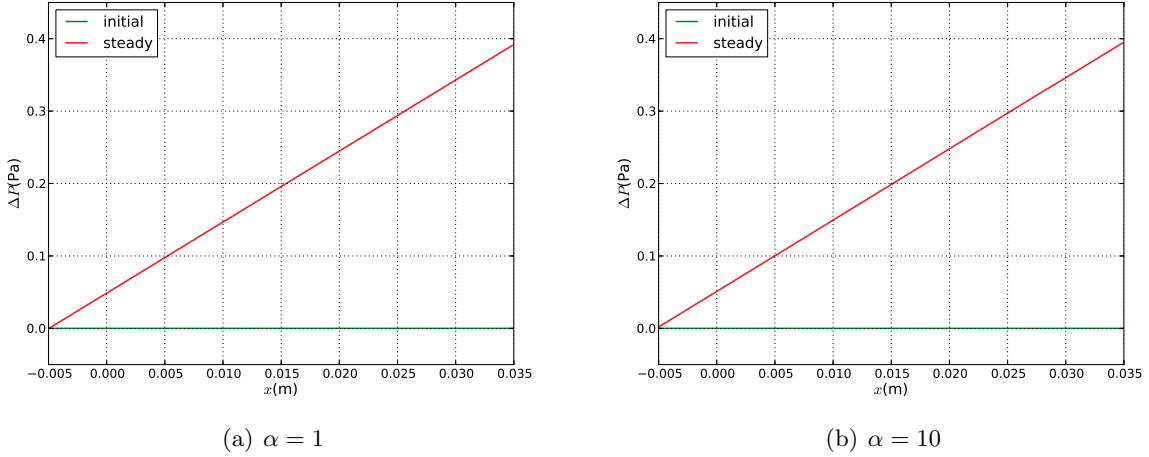


Figure 3.10: Pressure variation between the initial and the steady condition in Problem 2 of [67] with (a) and without (b) ASR.

Figure 3.10 displays the resulting pressure variation with (3.10(b)) and without (3.10(a)) ASR method. One may find that they are almost the same. ASR method can deal with problems including volume force very well.

The third test-case is performed to validate the viscous correction of ASR method. This case is set as follows: on a 1D calculation domain $[-0.02, 0.02]$, at $t = 0$ s, the initial temperature field is given as

$$T(x, 0) = \begin{cases} 300 + 100(1 + \cos(\frac{\pi x}{\delta})) & -\delta \leq x \leq \delta \\ 300 & \text{otherwise} \end{cases} \quad (3.104)$$

with $\delta = 0.008$ m. The velocity field is set to zero and the pressure is $P_0 = 1$ Atm on all the domain as plotted in figure 3.11(a). The working material in this test case is air, and the grid size is $\Delta x = 0.5$ mm. Both sides of boundary conditions are set to NSCBC perfectly non reflecting out-flow⁵. This test case is performed with ASR method at a speed-up ratio $\alpha = 10$ with a time step controlled by CFL condition (3.77) $\Delta t \approx 7 \times 10^{-6}$ s, and also without ASR method ($\alpha = 1$) with a time step $\Delta t \approx 7 \times 10^{-7}$ s. The resulting flow field is plotted in 3.11. One can see that, at the beginning of

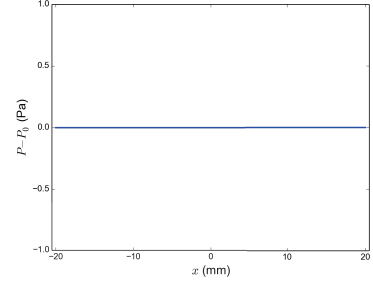
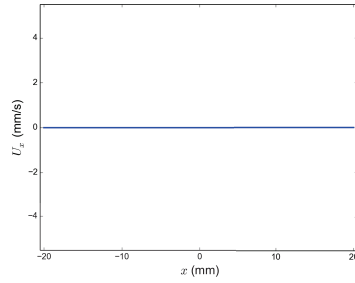
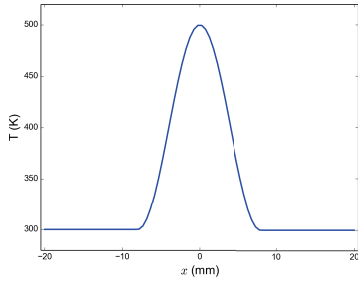
⁴All the unit system in this case is set to International System of Units (S.I)

⁵The boundary condition in low-Mach formulation will be presented in the next section.

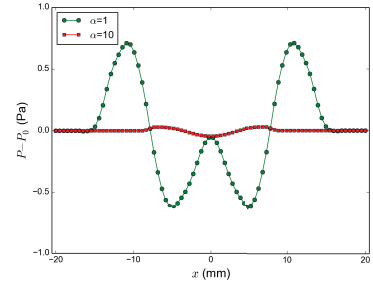
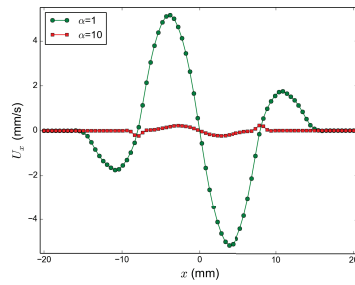
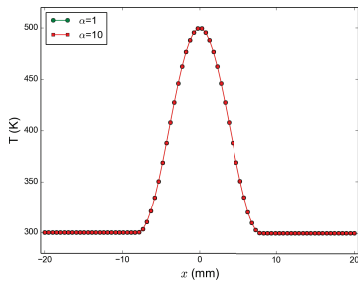
the calculation, $t = 2 \times 10^{-5}$ s as in figure 3.11(b), some acoustic waves are generated both with and without the ASR method. At $t = 2 \times 10^{-4}$ s in Fig. 3.11(c), these acoustic waves have already left the calculation domain for the calculation without ASR method, but for the calculation $\alpha = 10$, the acoustic waves are still in the domain and the velocity field is almost identical to the calculation without ASR at $t = 2 \times 10^{-5}$ s. The pressure field with $\alpha = 10$ at $t = 2 \times 10^{-4}$ s has the same shape as the pressure field without ASR at $t = 2 \times 10^{-5}$ s, but the amplitude is 10 times smaller. At $t = 0.01$ s, after the calculation is steady, the pressure, temperature and velocity fields from both $\alpha = 10$ and $\alpha = 1$ are identical to each other.

This test case shows that, even under almost zero Mach condition (maximum velocity in this test case is about 5 mm/s), the ASR method can still work well. The acoustic features will be affected by the ASR modification as the speed of sound is reduced, but the main flow field keeps identical to original N-S equation solutions.

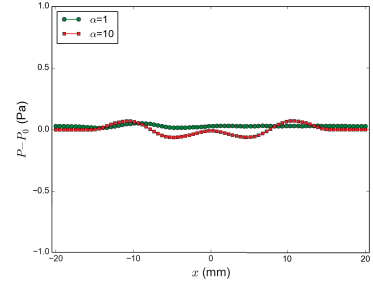
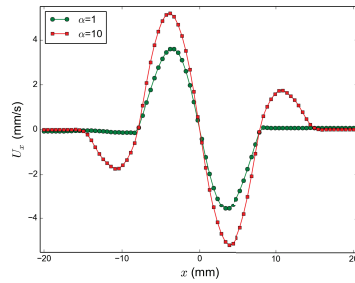
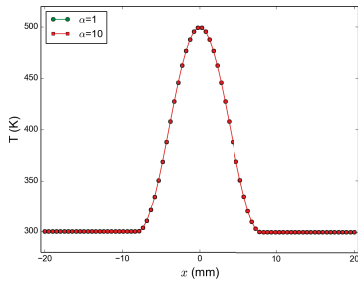
These three simple test-cases validate our implementation of ASR method in full conservative form. In the next section, the boundary conditions used in this work will be illustrated.



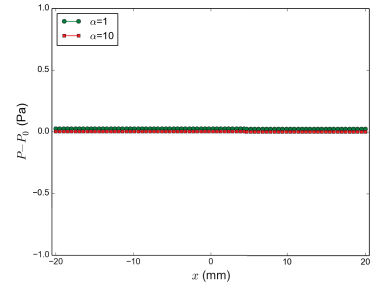
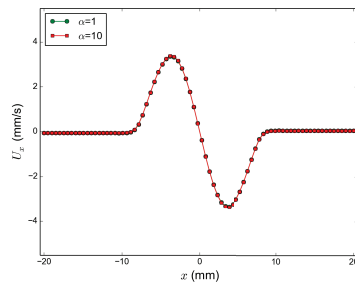
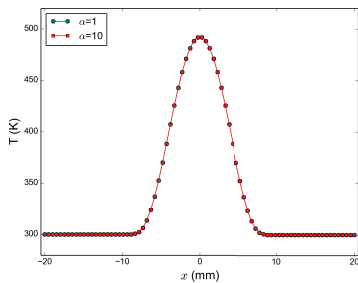
(a) Initial



(b) $t = 2 \times 10^{-5} \text{ s}$



(c) $t = 2 \times 10^{-4} \text{ s}$



(d) $t = 1 \times 10^{-2} \text{ s}$

Figure 3.11: Temperature, velocity and pressure field of the third ASR test case.

3.4 Boundary conditions for “synthetic” HIT injection

As presented in section 1.3, the multi-grid turbulence generator is very complicated. Considering the complex geometry in figure 1.1, numerical simulation of the actual flow through the multiple grids using LES is out of reach and not necessary. Our strategy to overcome this issue is to apply a *mapping or recycling method* like in [83], as follows:

1. Generate a block of “synthetic” HIT from 1D frequency spectrum using hot-wire measured velocity time series at the jet outlet in the experiment;
2. Add this HIT field to the experimental mean velocity profile of the jet;
3. Inject this field into the computational domain with a subsonic characteristic boundary.

The generation of “synthetic” turbulent field and the implementation of this subsonic characteristic boundary with low-Mach modification will be illustrated here after.

3.4.1 HIT field built from experimental measurements

Theoretically, a HIT field can be fully described by its 3D energy spectrum $E(K)$. So, to generate a HIT field from one point hot-wire experiment data, two steps are necessary: 1) obtain the 3D energy spectrum from experimental data; 2) build a corresponding velocity field.

3D energy spectrum from experimental data

The 3D energy spectrum $E(K)$ is defined as

$$E(K) \equiv \frac{1}{2} \iint_{|\vec{K}|=K} E_{ii}(\vec{K}) dA(\vec{K}) \quad (3.105)$$

where $A(\vec{K})$ is the sphere of radius $K = |\vec{K}|$, and $E_{ij}(\vec{K})$ is the 3D energy spectrum tensor, obtained from the 3D Fourier transform of space correlation tensor $Q_{ij}(\vec{\xi})$ as

$$E_{ij}(\vec{K}) \equiv \frac{1}{(2\pi)^3} \iiint Q_{ij}(\vec{\xi}) e^{-j\vec{e}\vec{K} \cdot \vec{\xi}} d^3\xi \quad (3.106)$$

where

$$Q_{ij}(\vec{\xi}) \equiv \langle u'_i(\vec{x} + \vec{\xi}) u'_j(\vec{x}) \rangle \quad (3.107)$$

In HIT, equation (3.105) leads to [33]:

$$E(K) = 2\pi K^2 E_{ii}(\vec{K}) \quad (3.108)$$

In practice, this 3D energy spectrum is obtained from the experiment as follows. The experiment provides a one-point velocity time series $u'(\vec{x}, t)$ at point \vec{x} with the hot-wire measurement [3, 4]. The one-point time correlation of velocity is calculated as

$$Q_{11}(\tau) \equiv \langle u'_1(\vec{x}, t) u'_1(\vec{x}, t + \tau) \rangle \quad (3.109)$$

for the sampling frequency

$$\omega = 2\pi f = 2\pi/\tau \quad (3.110)$$

Using local Taylor’s hypothesis, the space correlation

$$Q_{11}(\xi \vec{e}_1) \equiv \langle u'_1(\vec{x}, t) u'_1(\vec{x} + \xi \vec{e}_1, t) \rangle \quad (3.111)$$

can be calculated for the separation

$$\vec{\xi} = \xi \vec{e}_1 \quad (3.112)$$

by setting

$$\xi \equiv U_1 \tau$$

where $U_1(\vec{x})$ is the time-mean local velocity. Apparently, according to (3.110),

$$\omega = U_1 K_1$$

where K_1 is the corresponding wave number. The value of the 1D spatial spectrum $F_{11}(K_1)$ at wave number K_1 is obtained by Fourier transform [33]

$$F_{11}(K_1) \equiv \mathcal{F}(Q_{11}(\xi \vec{e}_1)) = \frac{1}{\pi} \int_{-\infty}^{\infty} Q_{11}(\xi \vec{e}_1) e^{-j_c K_1 \xi} d\xi \quad (3.113)$$

Then, the 3D energy spectrum $E(K)$ is calculated according to the HIT relation [33, 84],

$$E(K) = \frac{1}{2} K^3 \frac{d}{dK} \left(\frac{1}{K} \frac{dF_{11}(K)}{dK} \right) \quad (3.114)$$

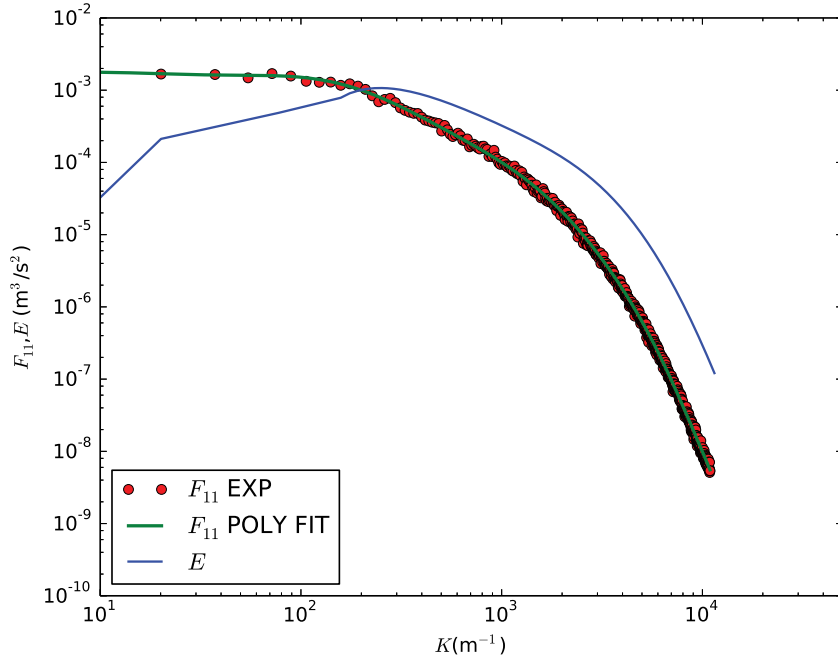


Figure 3.12: Polynomial fitting of experiment 1D energy spectrum

The experimental 1D spatial spectrum $F_{11}(K_1)$ is plotted as red dots in figure 3.12. It is clear that these data are not smooth enough to be used directly in (3.114), where the two steps of derivation may produce non-physical values of $E(K)$. A polynomial fit is applied to the experimental F_{11} curve in log-log space to overcome this un-smooth issue.

The object of polynomial fitting is to find optimal coefficients $\{a_i\}$ of a polynomial \mathcal{P} of order N

$$\mathcal{P}(x) \equiv \sum_{i=0}^N a_i x^i \quad (3.115)$$

such that the distance from this polynomial to N_p experimental 1D spectrum points⁶ has a minimum value. This least square optimization leads to the following N equations

$$\frac{\partial \left\{ \sum_{j=1}^{N_p} [f_j - \mathcal{P}(x_j)]^2 \right\}}{\partial a_m} = 0 ; \quad m = 0, \dots, N \quad (3.116)$$

⁶ $(x_j = \log(K_1), f_j = \log(F_{11}(K_1)))$

This is a linear system of the form

$$\sum_{i=1}^N a_i \sum_{j=1}^{N_p} x_j^{i+m} = \sum_{j=1}^{N_p} f_j x_j^m ; \quad m = 0, \dots, N$$

Specifically, for this 1D spectrum, as shown in [33], the first order derivative of F_{11} should be 0 at $K_1 = 0$. To achieve this feature, we impose $\frac{\partial \mathcal{P}}{\partial x} = 0$ at the first p points

$$\frac{\partial \mathcal{P}}{\partial x}(x_j) = \sum_{i=0}^N i a_i x_j^{i-1} = 0 ; \quad j = 1, 2, 3 \dots p$$

Substitute p equations in (3.116) using these new constrains, the final linear system for fitting is then:

$$\left\{ \begin{array}{l} \sum_{i=1}^N i a_i x_m^{i-1} = 0 ; \quad m = 1, 2, \dots, p \\ \sum_{i=1}^N a_i \sum_{j=1}^{N_p} x_j^{i+m} = \sum_{j=1}^{N_p} f_j x_j^m ; \quad m = p, \dots, N \end{array} \right. \quad (3.117)$$

The result of this fitting procedure is presented in the figure 3.12. The experimental 1D spectrum is plotted as red dots noted by F_{11} EXP. A 20th order fitting polynomial with $p = 3$ from (3.117) is plotted as the green line. One may find that this polynomial fits well the experiment data and is smooth enough for the 3D spectrum calculation (3.114). The resulting 3D spectrum is shown as the blue curve in figure 3.12.

Initial HIT velocity field with given 3D energy spectrum

The 3D divergence free velocity field with a given experimental 3D energy spectrum is then obtained by setting stream function $\hat{\Psi}_i$ as

$$\hat{\Psi}_i(\vec{K}) = \sqrt{\delta(\vec{0}) \frac{E(K)}{4\pi K^4}} e^{j_c \theta_i} \quad (3.118)$$

with

$$K = |\vec{K}|$$

and θ is a random angle in $(0, 2\pi)$

$$\theta_i = \text{rand}(0, 2\pi)$$

A detailed proof of equation (3.118) can be found in appendix B.5. The resulting velocity field in Fourier space reads

$$\hat{u}_i(\vec{K}) = j_c K_j \epsilon_{ijk} \hat{\Psi}_k(\vec{K}) = j_c K_j \epsilon_{ijk} \left(\delta(0) \frac{E(K)}{4\pi K^4} \right)^{\frac{1}{2}} e^{j_c \theta_i} \quad (3.119)$$

Using FFT, the velocity field in physical space can be obtained.

During the whole process of generation of the HIT field, there are some other crucial details worth to be mentioned:

1. The spectra from experiments correspond to a DNS resolution. For a LES simulation, a low-pass filter should be firstly applied in the Fourier space. In this study, a sharp cut-off filter corresponding to the LES simulation resolution is applied.
2. The size of the HIT field, L_x , should be large enough for the energy containing eddies to be presented well. In the current work, as suggested by Pope [33], the domain size is taken as

$$L_x \geq 8L_{11}$$

where L_{11} is the turbulent integral length scale.

3.4.2 Characteristic boundary conditions for HIT injection

The physical description of this inlet boundary is as follows: to inject the generated HIT field from the boundary $x = 0$, one should impose the flow density⁷ ρ and species' concentration Y_k , and set the velocity u_i varying according to the pre-generated turbulence field. Mathematically, at any given time t , on the boundary $x = 0$:

$$\left\{ \begin{array}{l} \frac{\partial \rho}{\partial t} = 0 \\ \frac{\partial Y_k}{\partial t} = 0; \quad \text{for } k = 1, \dots, N_{sp} \\ \frac{\partial u}{\partial t} = \frac{\partial u}{\partial t} \Big|_{\text{TURB}} \quad ; \quad \frac{\partial v}{\partial t} = \frac{\partial v}{\partial t} \Big|_{\text{TURB}} \quad ; \quad \frac{\partial w}{\partial t} = \frac{\partial w}{\partial t} \Big|_{\text{TURB}} \end{array} \right. \quad (3.120)$$

This boundary condition is very similar to the classic SI-2 boundary condition in [6, 85] except that the velocity varies according to the injected turbulence field ($\frac{\partial u}{\partial t} \Big|_{\text{TURB}}$, $\frac{\partial v}{\partial t} \Big|_{\text{TURB}}$ and $\frac{\partial w}{\partial t} \Big|_{\text{TURB}}$). Also, as mentioned in [6, 85], one viscous condition should be added for SI-2, which is

$$\frac{\partial \tau_{11}}{\partial x_1} = 0 \quad (3.121)$$

To adapt this to our conditions, we just simply implement

$$\frac{\partial \tau_{11}}{\partial x_1} = \frac{\partial \tau_{11}}{\partial x_1} \Big|_{\text{TURB}} \quad (3.122)$$

by forcing ghost points values.

Following the NSCBC strategy in [6], the governing equations on the boundary should be written first. At this stage, the same ASR N-S equations (3.102) inside the calculation domain are used also on the boundary. This is the MSSE (multi-species state equations) approach in [6].

Then, the amplitudes of characteristic waves \mathcal{L}_i should be evaluated. As this is a subsonic inlet condition at $x = 0$, the wave \mathcal{L}_1 is the only outgoing wave. All the other waves should be calculated using characteristic relations. To precisely control the velocity variation on the boundary, the full ASR N-S equations (3.102) are used to deduce the relationships between \mathcal{L}_i instead of LODI (Local One Dimensional Inviscid) equations. As the boundary condition described in (3.120) is in primitive variables, the connection between the characteristic form and the primitive form should be found. Following the strategy in appendix B.2, the ASR N-S equations (3.102) on the boundary can be written in conservative vector form like

$$\frac{\partial \mathbf{U}}{\partial t} + \frac{\partial \mathbf{F}_{ASR}}{\partial x} = \mathbf{S}_{xASR} \quad (3.123)$$

in which the term \mathbf{S}_{xASR} contains the flux of y and z directions, the viscous terms and the source terms. The subscript ASR will be abandoned in the following as in this section all operations are performed on the ASR equations. Multiplying equation (3.123) to the left eigenvector matrix L in (B.23), one goes to the characteristic space as in equation (B.5)

$$\frac{\partial \mathbf{W}}{\partial t} + \mathcal{L} = L \mathbf{S}_x \quad ; \quad \mathcal{L} \equiv \Lambda \frac{\partial \mathbf{W}}{\partial x}$$

where \mathcal{L} are the characteristic waves. The primitive form is obtained by multiplying (3.123) by the passage matrix M^{-1} in (B.16),

$$\frac{\partial \mathbf{V}}{\partial t} + \tilde{A} \frac{\partial \mathbf{V}}{\partial x} = M^{-1} \mathbf{S}_x \quad (3.124)$$

⁷As the injected turbulence field is divergence free

Using equation (B.10) in appendix, we can find that

$$\frac{\partial \mathbf{V}}{\partial t} + \tilde{R}\mathcal{L} = M^{-1}\mathbf{S}_x \quad (3.125)$$

Combining this equation with (3.120), a linear system for \mathcal{L} can be obtained:

$$\frac{\partial}{\partial t} \begin{bmatrix} \rho \\ u \\ v \\ w \\ Y_1 \\ \vdots \\ Y_{N_{esp}} \end{bmatrix} + \begin{bmatrix} (\tilde{R}\mathcal{L})_1 \\ (\tilde{R}\mathcal{L})_2 \\ (\tilde{R}\mathcal{L})_3 \\ (\tilde{R}\mathcal{L})_4 \\ (\tilde{R}\mathcal{L})_6 \\ \vdots \\ (\tilde{R}\mathcal{L})_{5+N_{sp}} \end{bmatrix} = \begin{bmatrix} 0 \\ \left. \frac{\partial u}{\partial t} \right|_{\text{TURB}} \\ \left. \frac{\partial v}{\partial t} \right|_{\text{TURB}} \\ \left. \frac{\partial w}{\partial t} \right|_{\text{TURB}} \\ 0 \\ \vdots \\ 0 \end{bmatrix} + \begin{bmatrix} \mathcal{L}_5 + \mathcal{L}_2 + \mathcal{L}_1 \\ \frac{c}{\alpha\rho} (\mathcal{L}_5 - \mathcal{L}_1) \\ \mathcal{L}_3 \\ \mathcal{L}_4 \\ \mathcal{L}_6 \\ \vdots \\ \mathcal{L}_{5+N_{esp}} \end{bmatrix} = \begin{bmatrix} (M^{-1}\mathbf{S}_x)_1 \\ (M^{-1}\mathbf{S}_x)_2 \\ (M^{-1}\mathbf{S}_x)_3 \\ (M^{-1}\mathbf{S}_x)_4 \\ (M^{-1}\mathbf{S}_x)_6 \\ \vdots \\ (M^{-1}\mathbf{S}_x)_{5+N_{sp}} \end{bmatrix} \quad (3.126)$$

The final characteristic wave amplitudes \mathcal{L}_i are given by solving the system (3.126):

$$\left\{ \begin{array}{l} \mathcal{L}_2 = \frac{\alpha\rho}{c} \left(\left. \frac{\partial u}{\partial t} \right|_{\text{TURB}} - (M^{-1}\mathbf{S}_x)_2 \right) + (M^{-1}\mathbf{S}_x)_1 - 2\mathcal{L}_1 \\ \mathcal{L}_3 = (M^{-1}\mathbf{S}_x)_3 - \left. \frac{\partial v}{\partial t} \right|_{\text{TURB}} \\ \mathcal{L}_4 = (M^{-1}\mathbf{S}_x)_4 - \left. \frac{\partial w}{\partial t} \right|_{\text{TURB}} \\ \mathcal{L}_5 = \frac{\alpha\rho}{c} \left((M^{-1}\mathbf{S}_x)_2 - \left. \frac{\partial u}{\partial t} \right|_{\text{TURB}} \right) + \mathcal{L}_1 \\ \mathcal{L}_{5+k} = (M^{-1}\mathbf{S}_x)_{5+k} \quad ; \quad k = 1, \dots, N_{sp} \end{array} \right. \quad (3.127)$$

The \mathcal{L}_1 wave should be evaluated with an one-sided scheme from the inner side of the calculation domain. This outgoing wave carries the temperature, hence the pressure via the equation of state, from the interior domain [6]. With these relations applied, the B.C. described in (3.120) can be achieved. The HIT generated in the last sub-section can be injected into the calculation domain using this characteristic boundary conditions (3.127).

In fact, similar boundary conditions have already been achieved by V. Moureau *et al.* where only LODI relations are used [13]. Comparing our implementation (3.127) to equation (41) to (43) in [13], one may find that the LODI parts are exactly the same when $\alpha = 1$ ⁸.

Other NSCBC boundary conditions like NSW (Isothermal no slip wall), B2 (Perfectly non reflecting outflow) and B3 (partially non reflecting outflow with P_∞ imposed) in table 9.4 of [6] are also implemented and tested during this work. Further discussion and examples of the boundary conditions can be found in chapters below.

⁸Note that the definition of characteristic waves (\mathcal{L}_i) are different in [53]

Chapter 4

Academic test-cases

Synopsis

Dans ce chapitre, on teste différentes stratégies numériques pour la simulation de la combustion turbulente prémélangée à l'aide des méthodes et modèles présentés précédemment. Ces tests sont effectués sur des cas académiques simples et peu coûteux, afin de sélectionner les approches les plus pertinentes qui seront ensuite appliquées à la simulation de l'expérience 3D en configuration non-réactive et réactive. On présente successivement :

- Une flamme prémélangée 1D, afin de quantifier l'effet de la résolution du calcul sur la vitesse et la structure de la flamme simulée, pour différents schémas numériques. Les conclusions sont les suivantes : (i) avec les schémas WENO non-linéaires, le calcul est stable quelle que soit la résolution, mais la vitesse de flamme est largement surestimée s'il y a moins de 5 mailles dans une épaisseur de flamme théorique δ_L^0 , et le profil de vitesse présente des oscillations que nous n'avons pas su expliquer. Ces oscillations ne sont pas visibles sur les profils de température et de fractions massiques. (ii) le schéma optimum décentré d'ordre 5 est instable à moins de 4 mailles dans δ_L^0 , mais produit la bonne vitesse de flamme. (iii) l'application de l'approche bas-Mach ASR conduit à une instabilité du calcul à moins de 12 mailles dans δ_L^0 . (iv) le modèle de flamme épaissie donne les résultats attendus, et peut être combiné avec la méthode ASR pour un maillage à $\Delta x \approx \delta_L^0$ et un épaississement de 12.
- L'auto-amortissement d'une turbulence homogène et isotrope, en vue de quantifier la dissipation numérique intrinsèque aux différents schémas. C'est un cas-test très classique, mais qui permet d'analyser la "survie" de la turbulence multi-échelles injectée dans le calcul. On constate que même le schéma linéaire optimum décentré d'ordre 5 est trop dissipatif pour l'application visée. Il faut l'hybrider avec un schéma centré non-dissipatif pour assurer à la fois stabilité du calcul et faible dissipation. On a testé également l'approche SGE explicite avec 2 modèles sous-maille différents et un schéma centré d'ordre 4, montrant un empilement d'énergie à la fréquence de coupure de Nyquist.
- Une représentation 2D de la flamme expérimentale, permettant de tester la résolution nécessaire aux SGE implicites et les entrées du modèle de plissement de flamme sous-maille. Ce dernier produit des résultats corrects quelle que soit le facteur d'épaississement, sur les deux maillages utilisés. On propose une méthode de pondération spatiale du facteur de plissement afin qu'il prenne toujours -au moins partiellement- en compte la turbulence dans les gaz frais.

Before going to the real world of 3D reactive applications, several academic test cases have been performed to examine our numerical strategies for turbulent premixed combustion. Three test-cases will be presented in this chapter: i) 1D premixed flame, which may provide the performance of our strategies in premixed combustion; ii) Self decaying Homogeneous Isotropic Turbulence (HIT), which focuses on turbulence modeling; iii) 2D premixed turbulent reacting jet, to tune the subgrid scale turbulent combustion models before they can be further applied to 3D applications.

4.1 One dimensional laminar premixed flame

In the current work, the LES of the species equations (2.1d) in N-S equations is either performed implicitly (ILES) or with thickened flame model (TFLES). In this section, an ILES laminar premixed flame test-case will be presented at the beginning, as it is a good benchmark to assess the impact of numerics on the physics simulated. The 1D laminar premixed flame with thickened flame model will be discussed in the second sub-section.

4.1.1 ILES of 1D laminar premixed flame

Although ILES has already been well verified for non-reacting flows [15, 41, 14], combustion simulations with ILES are still rare in the literature. In the last few years, our team has already applied the ILES approach to reacting flows [26, 27] and the comparison between implicit and physical LES has been done in [22, 23]. The results of these works have shown that ILES can be successfully applied to high-speed diffusion flames. However, in this study, a low speed premixed turbulent flame is the main topic. So the performance of ILES for premixed combustion should be examined first with great care, since the physics is totally different.

The main difficulties in applying ILES to premixed combustion is that, as the reaction source terms in species equation (2.27d) are highly non-linear, without any explicit model, ILES may lead to unstable simulations. Also, the implicit filtering introduced by numerics may fail to model the subgrid source term $C_{3\alpha}$ in (2.29j). As a first step, a one dimensional laminar premixed flame is simulated to verify the laminar flame speed and flame thickness calculated by ILES.

The setup of this test case is as follows: On a 1D domain $x \in [-L/2, L/2]$ with $L = 20$ mm, a methane/air premixed flame at equivalence ratio $\phi = 0.8$ is calculated. At $t = 0$, the flow velocity and pressure field are uniform at $u_{initial} = 0.5$ m/s, $p = 1$ Atm. Other quantities on the left ($x < 0$) and right ($x > 0$) half of the domain are set to fresh and burnt conditions with a sinus shaped profile between them to prevent sharp discontinuities. The initial conditions are shown in figure 4.1. The simulations are performed on a uniform grid, but different grid sizes are used. The left boundary condition is set to be SI-2 NSCBC in [6] where the velocity, density and chemical components are imposed constant at $x = -L/2$. The right boundary condition is set to perfectly non reflecting outflow with NSCBC strategy. The one step methane-air chemical mechanism [31] in appendix A.1 is applied for the source terms in species equations (2.27d). The third order TVD Runge-Kutta scheme [66] in equation (3.2) is used for time stepping.

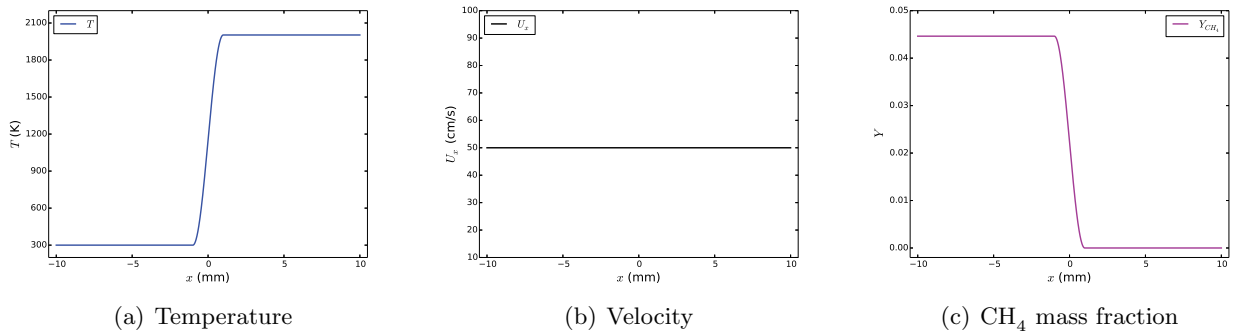


Figure 4.1: Initial temperature, velocity and methane mass fraction profiles for 1D laminar premix flame test case.

During the calculation, the velocity of the whole domain is adjusted by the difference between the push speed $u(x)|_{x=-L/2}$ and the instantaneous flame speed $S_L^0(t)$ every 0.2 ms with $S_L^0(t)$ calculated from methane burning rate as in equation (2.51). An almost steady flame structure is achieved after some times when the push speed becomes almost invariant thus equals to the calculated flame speed. Then, the calculated laminar flame speed and thickness are obtained from equations (2.51) and (2.49).

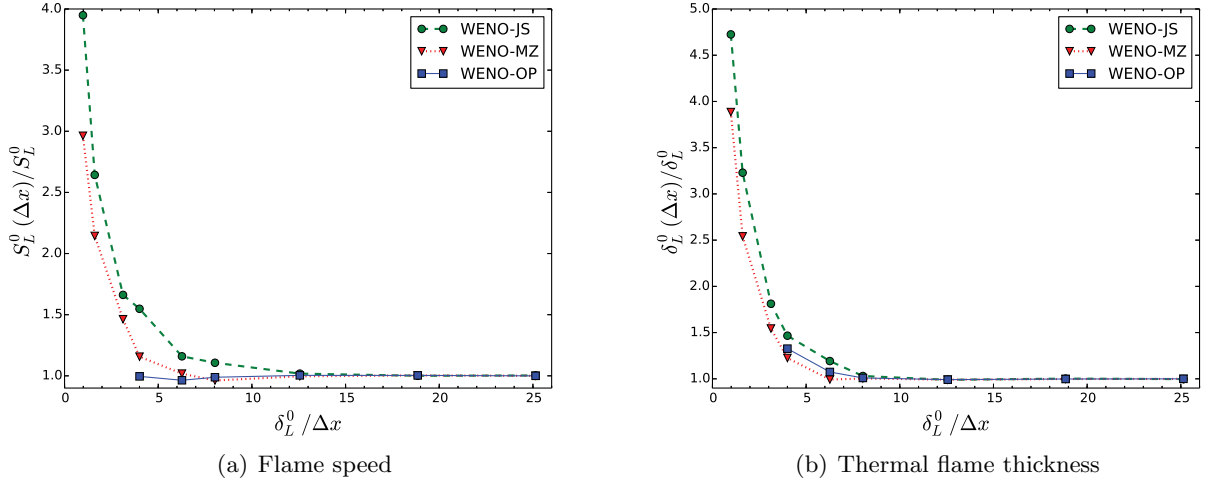


Figure 4.2: Calculated flame speed (left) and thermal flame thickness (right) with different grid size. x axis: Number of points inside one flame thickness; y axis: ratio between calculated flame speed and reference flame speed (left) and ratio between calculated flame thickness and reference flame thickness (right)

To understand the impact of the numerics and mesh resolution on the numerical premixed combustion in ILES, different numerical schemes and different grid sizes are implemented. ILES with WENO-JS5, WENO-MZ5, WENO-OP5 with quasi-laminar for chemical source terms, corresponding to JS5-QL, MZ5-QL and UP5-QL in table C.1, are tested with grid sizes from 0.02 mm to 0.5 mm. A DNS with grid size $\Delta x = 0.01$ mm using UP5-QL is performed as a reference. The thermal flame thickness and flame speed obtained from this DNS are

$$\delta_L^0 = 0.50 \text{ mm}; \quad S_L^0 = 0.286 \text{ m/s}$$

which match the results of the literature.

The flame speed and thickness obtained with different setups are plotted in figure 4.2. These figures show that the non-linear JS5-QL and MZ5-QL schemes can lead to stable simulations for 1D laminar premixed flame on a very coarse mesh, even with a grid size identical to the flame thickness, 0.5 mm. However, the resulting flame speed and thickness at this resolution are 3~5 times larger than the reference values. The linear UP5-QL setup is not stable until the grid size is smaller than one quarter of the reference flame thickness, 0.125 mm, which means that there should be at least four points inside the flame front for this linear scheme to be stable. But when the calculation is stable, the flame speed and thickness obtained by UP5-QL are very close to the reference DNS results. All simulations converge to the DNS, when there are at least 8 points in one flame thickness.

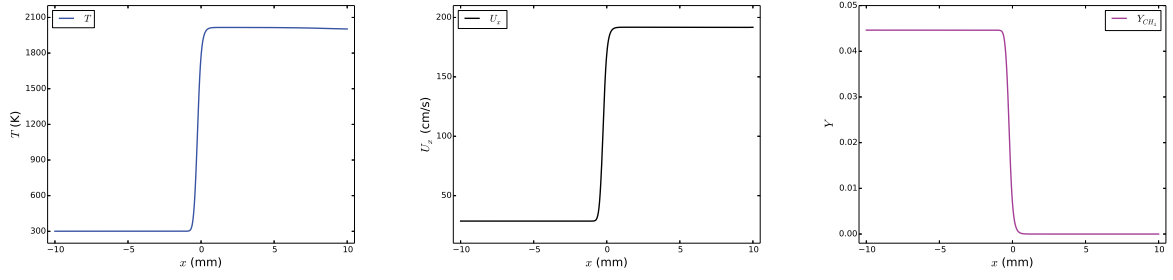
The resulting temperature, velocity and methane mass fractions profiles from different numerical setups are plotted in figure 4.3. The DNS results are in the first row 4.3(a) as references. Figure 4.3(b) shows the flame obtained by MZ5-QL on a coarse mesh when $\Delta x = \delta_L^0$. Under this resolution, the MZ5-QL gives $\delta_L^0 = 1.955\text{mm}$ and $S_L^0 = 0.848\text{m/s}$. The temperature and mass fraction profiles are quite acceptable except the flame front is much thicker than the reference. The velocity before the flame has some oscillations. Figures 4.3(c) to 4.3(e) plot the flame obtained by UP5-QL, MZ5-QL and JS5-QL at a grid when $\Delta x = 0.25\delta_L^0$. One can see that all schemes can catch the correct flame speed and thickness at this resolution, but the non-linear JS5-QL and MZ5-QL generate more oscillations in the velocity field than the linear UP5-QL calculation. When the grid resolution goes to $\delta_L^0/\Delta x = 8$, as plotted in figure 4.4, all ILES converge to DNS results.

We also tried to apply the ASR method introduced in section 3.3 on this ILES flame test case, but we found that the calculation is unstable, except at a almost DNS resolution. At $\delta_L^0/\Delta x = 12.5$,

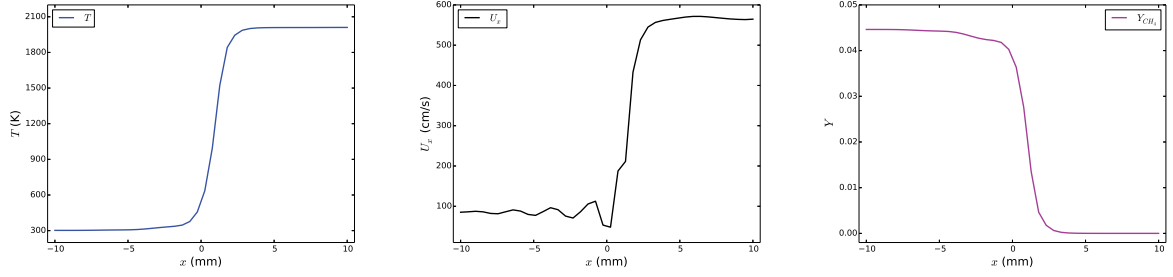
a speed up of $\alpha = 5$ can be achieved successfully, and the resulting flame structure is plotted in figure 4.5. One may find that the velocity after the flame front obtained by ASR method is lower than the calculation without ASR, but the flame speed and thickness is almost the same. This result coincides to the DNS premixed flame test case in [67].

The conclusions of this 1D premixed flame test-case are as the following:

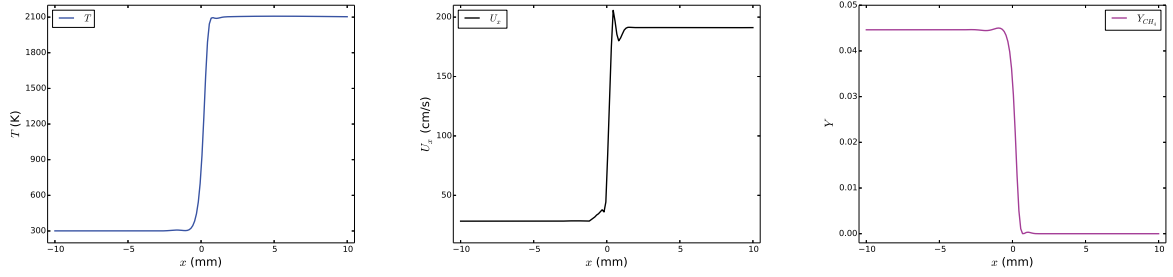
1. the non-linear MZ5-QL and JS5-QL ILES can be used in premixed combustion on a relatively coarse mesh (about one point inside one flame thickness) without numerical stability issues, but the resulting flame speed and thickness may be enlarged;
2. MZ5-QL performs better than JS5-QL for both flame speed and thickness under the same grid resolution;
3. when the flame front is well resolved (more than four points in one flame thickness), the linear UP5-QL is recommended as it generates less oscillations in the velocity field than non-linear shock capturing WENO schemes.



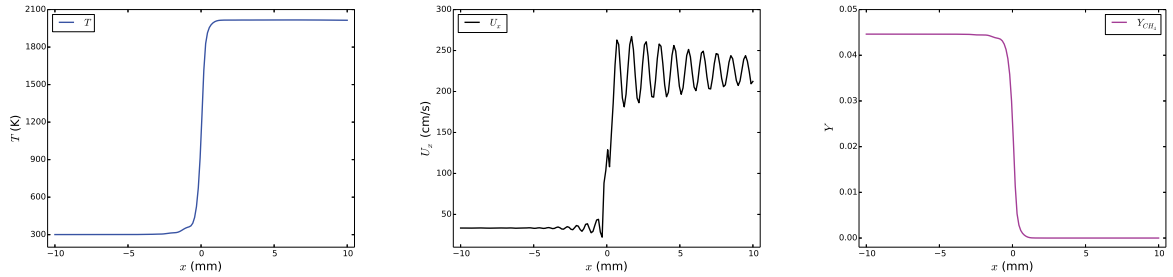
(a) Reference



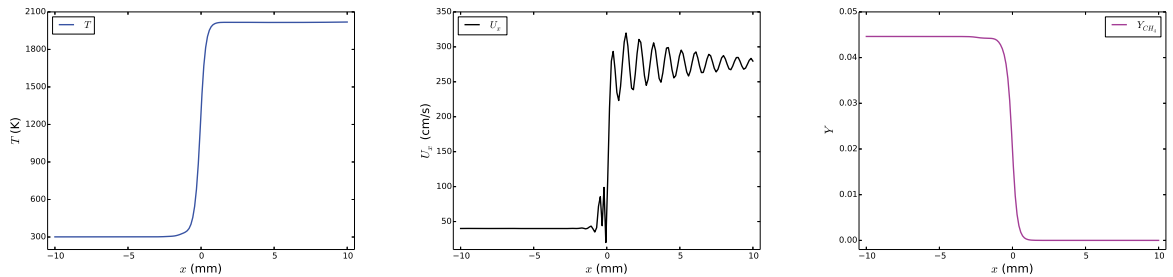
(b) MZ5-QL, $\delta_L^0/\Delta x = 1$



(c) UP5-QL, $\delta_L^0/\Delta x = 4$

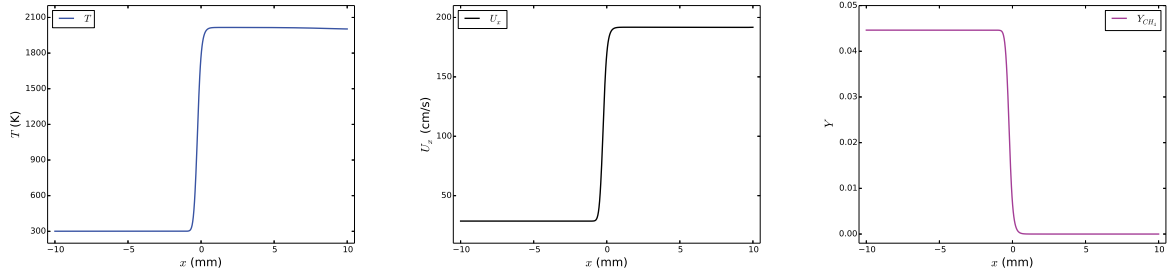


(d) MZ5-QL, $\delta_L^0/\Delta x = 4$

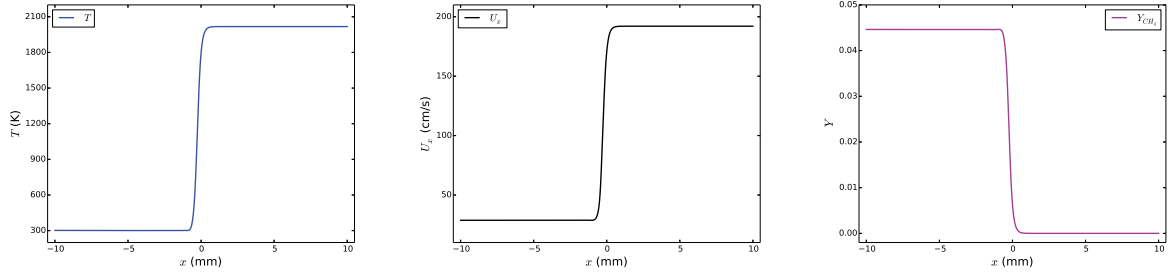


(e) JS5-QL, $\delta_L^0/\Delta x = 4$

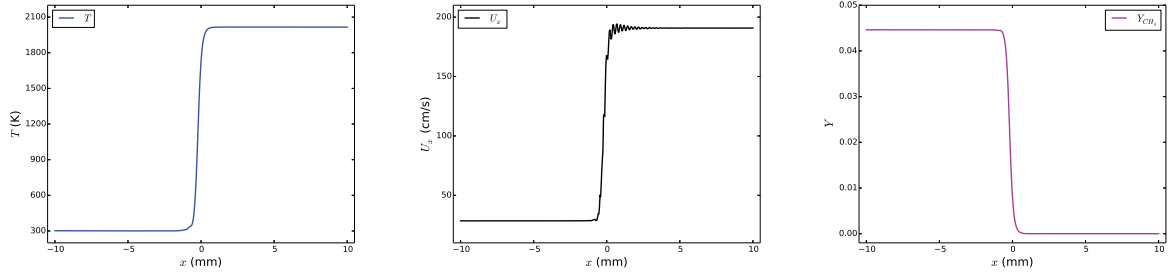
Figure 4.3: Flame structures with different numerical setups. First column: temperature, second column: flow velocity, third column: methane mass fraction.



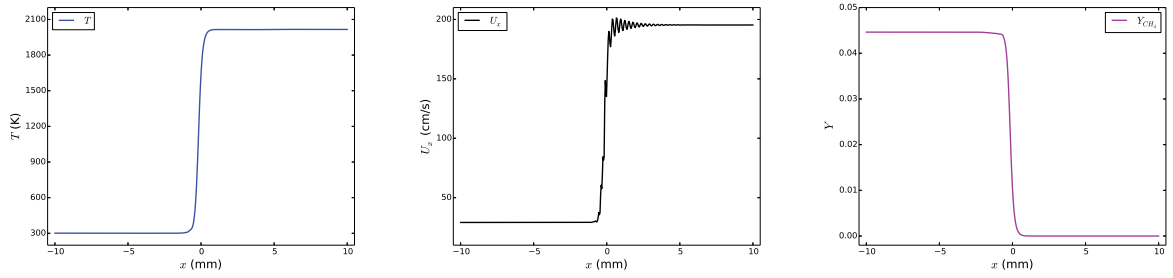
(a) Reference



(b) UP5-QL, $\delta_L^0/\Delta x = 8$



(c) MZ5-QL, $\delta_L^0/\Delta x = 8$



(d) JS5-QL, $\delta_L^0/\Delta x = 8$

Figure 4.4: Flame structures at grid resolution $\delta_L^0/\Delta x = 8$. First column: temperature, second column: flow velocity, third column: methane mass fraction.

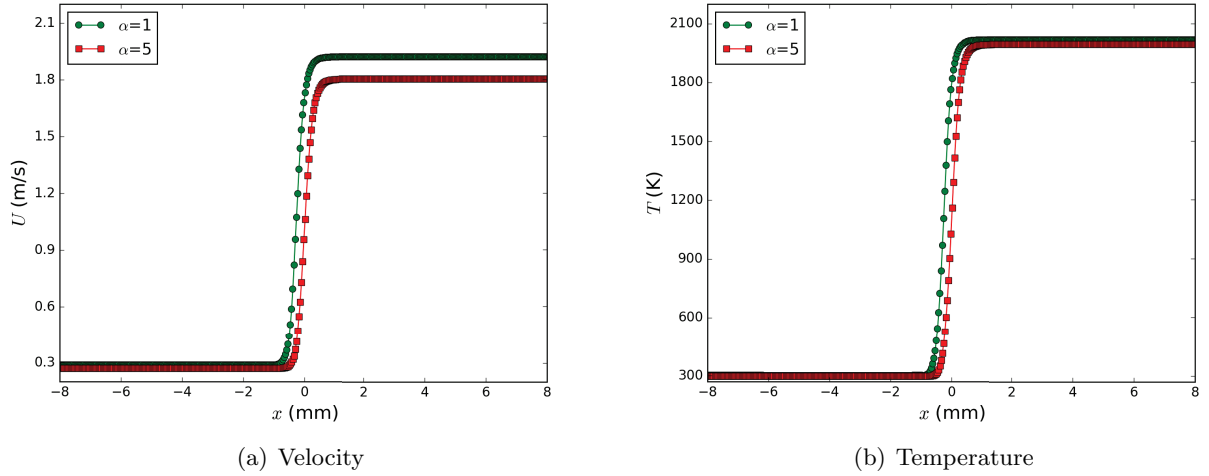


Figure 4.5: Velocity and temperature field obtained with and without ASR method. Grid size $\delta_L^0/\Delta x = 12.5$, scheme UP5-QL.

4.1.2 1D premixed laminar flame with ATF model

The artificial thickened flame model is also tested in this 1D flame test case. This group of test cases are performed on a fixed a grid size $\Delta x = \delta_L^0 = 0.5$ mm. LES strategies UP5-TF₄, UP5-TF₆, UP5-TF₈, UP5-TF₁₀ and UP5-TF₁₂ are applied. Other numerical setups are the same as the test in the last subsection. The resulting thermal flame thickness and flame speed is plotted in figure 4.6. The flame speed obtained with different thickening factors are almost the same, while the flame thickness are artificially thickened \mathcal{F} times. This can be clearly seen in the velocity and temperature field as in figure 4.7. Also, we find that at this grid resolution, the UP5-TF₄ simulation gives a oscillatory velocity field, although the resulting flame speed and flame thickness are still acceptable. The simulation with thickening factor less than 4 is not stable.

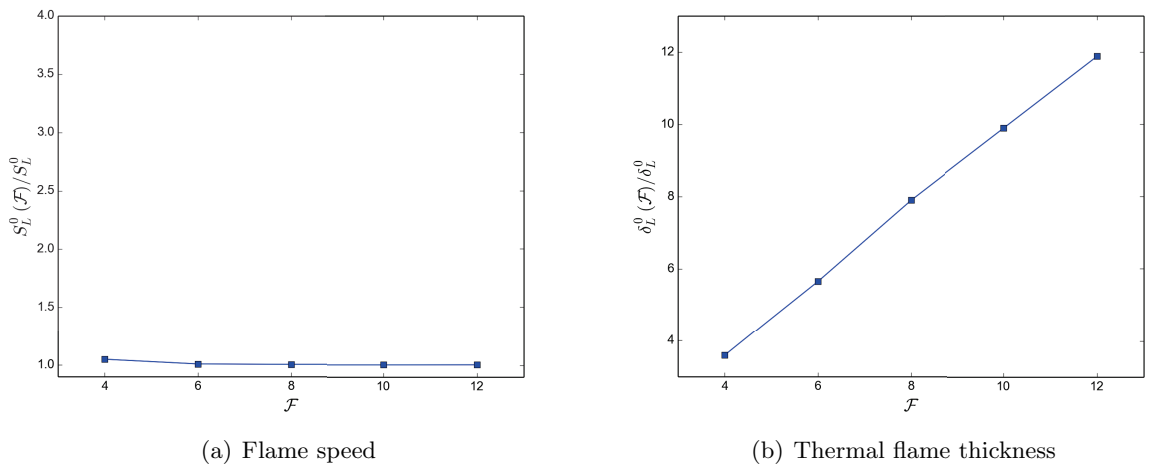


Figure 4.6: Calculated flame speed (left) and thermal flame thickness (right) with different thickening factor (\mathcal{F}). x axis: flame thickening factor; y axis: ratio between calculated flame speed and reference flame speed (left) and ratio between calculated flame thickness and reference flame thickness (right). Grid size $\Delta x = 0.5$ mm, scheme UP5-TF $_{\mathcal{F}}$

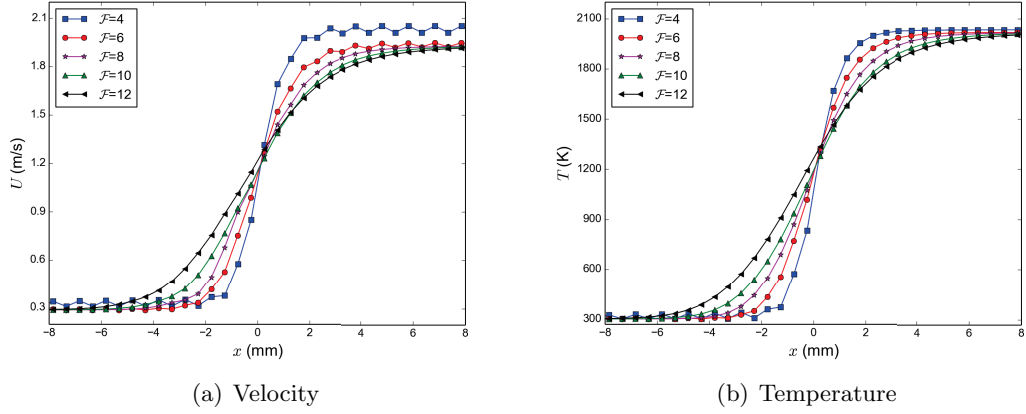


Figure 4.7: Velocity and temperature field around flame front obtained with different flame thickening factor. Grid size $\Delta x = 0.5$ mm, scheme UP5-TF \mathcal{F}

This test case is also performed with ASR method. Same as in the ILES, the simulation is not stable until a thickening factor as large as $\mathcal{F} = 12$. At this grid resolution, the time step given by CFL condition without ASR is about 7×10^{-7} s and the chemical time step is about 4×10^{-6} s. So we take a ASR speed-up ratio $\alpha = 5$ and the resulting velocity and temperature are plotted in figure 4.8. Same as DNS ASR flame in Fig. 4.5, the velocity after flame front resolved using ASR is lower than the original solution, and the flame speed and thickness are almost identical to the non-ASR calculation.

From this TFLES 1D laminar premixed flame test case, one can see that the ATF model works as expected with our numerical setups, and there need to be at least 4 points inside one thickened flame thickness to make a stable TFLES calculation; The ASR method can be applied in the TFLES, but the limitations are quite obvious: i) The chemical time step will not be affected by ASR method so that one can not speed up too much without other chemical treatment¹, like semi-implicit chemical source term integration [86] or tabular chemistry [55]. ii) The ASR calculation is only stable when a very large thickening factor is used. This may bring some inconvenience in turbulent premixed flame simulations.

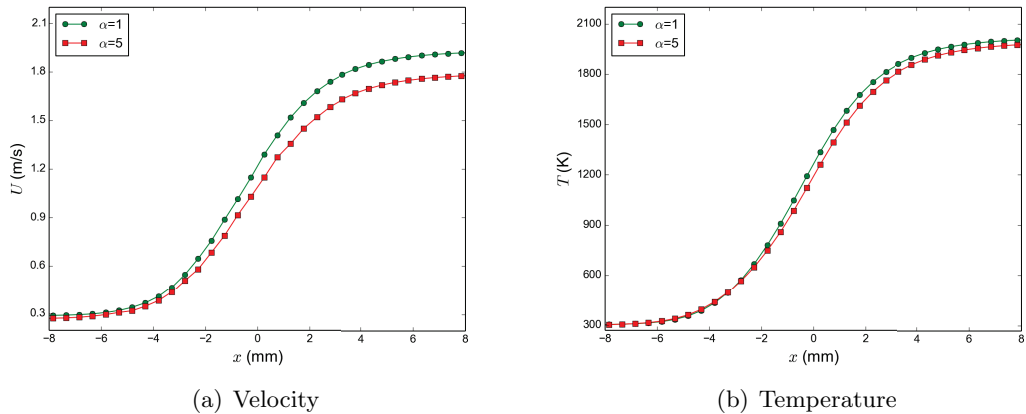


Figure 4.8: Velocity and temperature field obtained using thickened flame model with and without ASR method. Grid size $\Delta x = 0.5$ mm, scheme UP5-TF₁₂

¹In fact, in this test case, an one-step chemical scheme is used. If detailed chemistry are used, the chemical time step can be even much smaller. Thus the ASR method will be almost useless then

4.2 HIT decaying

The self-decaying HIT test case is performed to evaluate the turbulence modeling in our LES strategies. The numerical setup of this case is very classic: in a 3D calculation box $[-L_x/2, L_x/2]^3$, a HIT field is generated and used as initial condition. Periodic boundary conditions are applied on all the boundaries. Different LES strategies presented in the last two chapters are applied and the statistics of the velocity field at different times are calculated.

4.2.1 Initial field generation

Unlike most of the HIT simulations in the literature [40], in this study, a HIT velocity field directly rebuilt from experimental hot-wire data is used as initial condition. Following the procedure presented in section 3.4.1, a LES initial field is generated based on experimental data from [3, 4], in a 3D LES domain $[-30 \text{ mm}, 30 \text{ mm}]^3$ with box size $L_x = 60 \text{ mm}$. The calculation domain is discretized with $N = 120$ points in each direction such that the grid size is $\Delta x = 0.5 \text{ mm}$. The 3D spectrum recovered from the generated LES initial field using

$$E(K) = 2\pi K^2 \langle \widehat{u}_i \widehat{u}_i^*(\vec{K}) \rangle$$

is plotted as red dots in figure 4.9, together with the experimental 3D energy spectrum as the green line. One may see that the rebuilt velocity field follows the given energy spectrum well. The turbulence integral length scale obtained from the generated LES field is 4.25 mm, thus matches the experiment as in table 1.3. The size of this LES domain 60 mm is about 14 integral length scale. The grid size 0.5 mm is about 6 times of Kolmogorov scale and 10% of integral length scale. The resolved energy in this initial LES field is $k(0) = 0.594 \text{ m}^2/\text{s}^2$, i.e. 97% of the experimental data. These parameters indicate that this initial HIT field can be used for a LES simulation of the experimental field.

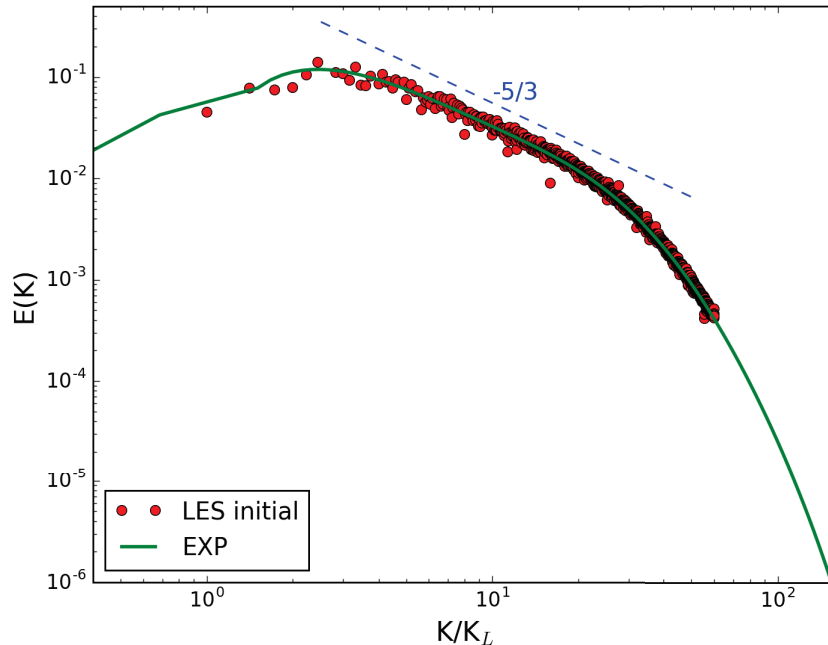


Figure 4.9: 3D energy spectrum of the LES initial velocity field rebuilt from experimental data. Red dots: spectrum of LES field; Green line: Experimental spectrum. The x axis is normalized by the wave number K_L corresponding to the simulation box size L_x : $K_L = 2\pi/L_x$. As $N = 120$, the LES spectrum stops at $K/K_L = 60$.

4.2.2 Comparison of different LES strategies

Different LES strategies are applied to the same initial condition to understand their performance in turbulence handling. These strategies are (see table C.1):

1. 4C-SM-NR. The numerical schemes for Euler flux evaluation is 4th order central scheme (3.3), and the Smagorinsky model is implemented with the parameters in section 2.2.2 (LES).
2. 4C-SSF-NR. Same numerics as the first one but the SSF model in section 2.2.2 is applied (LES).
3. UP5-NR. 5th order upwind linear scheme (WENO-OPT) (3.8) for Euler flux reconstruction, no explicit turbulence model (ILES).
4. HYB_α -NR ILES. The flux reconstruction used for Euler flux is a combination of 5th order upwind and 4th order central schemes as in (3.40)

$$h_{i+1/2}^{\text{HYB}} \equiv \alpha h_{i+1/2}^{5\text{-up}} + (1 - \alpha) h_{i+1/2}^{4\text{-c}}$$

In this test-case, $\alpha = 0.01$ and $\alpha = 0.03$ are used. No explicit turbulence model is added in this approach (ILES).

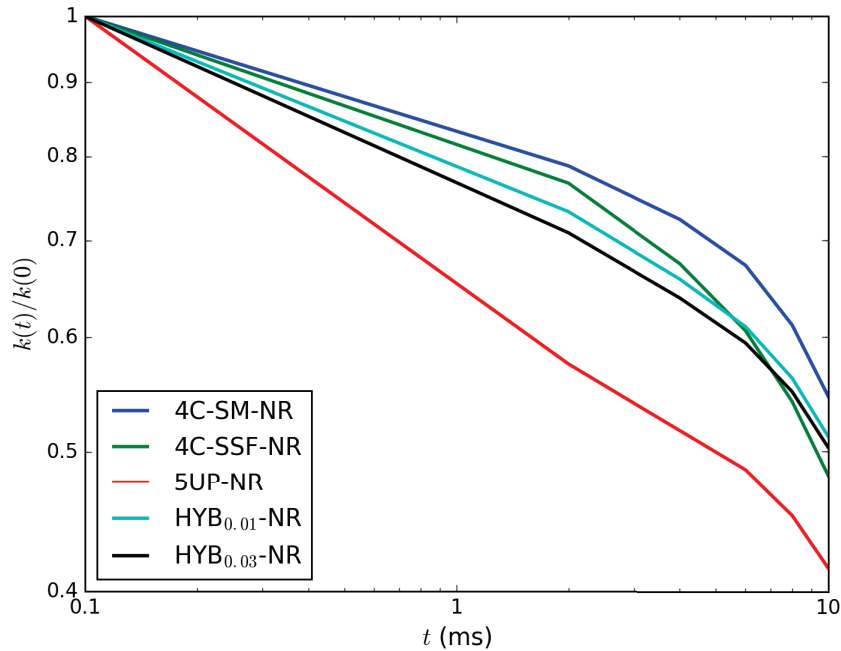


Figure 4.10: Time evolution of the turbulent kinetic energy with different LES strategies.

This simulation is performed for a physical time of 10 ms. Considering that the characteristic time scale calculated by L_{11}/\sqrt{k} of the initial field using parameters in table 1.3 is about 5 ms, this simulation time is enough to catch the differences between different strategies. The time evolution of turbulent kinetic energy

$$k(t) \equiv \frac{1}{2} \langle u_i u_i \rangle$$

from different simulations are displayed in figure 4.10, with a normalization by the initial kinetic energy for all simulations. It is clear that, on this mesh, the ILES with 5UP-NR is more dissipative than the explicit Smagorinsky and SSF models. The hybrid schemes are quite similar to explicit SSF models.

The time evolution of the 3D energy spectrum $E(K, t)$ from different simulations is displayed in figure 4.11. The first to fifth columns correspond to different LES strategies: 4C-SM-NR (Fig. 4.11(a)), 4C-SSF-NR (Fig. 4.11(b)), UP5-NR (Fig. 4.11(c)), HYB_{0.01}-NR (Fig. 4.11(d)) and HYB_{0.03}-NR (Fig. 4.11(e)). Energy spectrum from $t = 2$ ms, 4 ms, 6 ms and 8 ms are located in the first to the fourth rows as red dots. The green curves display the experimental initial spectrum as a reference. An evident difference between the energy spectrum from physical LES (4.11(a)~4.11(b)) and ILES (4.11(c)~4.11(e)) is that, the spectrum from explicit LES contains more small scales, with a piling-up of the energy at the Nyquist cut-off $K = 60K_L$; meanwhile, the small scales in ILES are damped to very small value from the very beginning of the simulation, $t = 2$ ms. In 5UP-NR simulation 4.11(c), at $t = 2$ ms, the small scales with wave numbers larger than $10K_L$, i.e. scales smaller than 12 grid size, have already been damped by the upwind scheme. The ILES HYB_{0.01}-NR 4.11(d) and HYB_{0.03}-NR 4.11(e) can keep much smaller eddies in the simulation, in the range $30K_L$ to $40K_L$, i.e. 3~4 grid size.

The same phenomenon can be observed directly on the flow field. In figure 4.12, the path lines on the boundaries LES are plotted for different, using the LIC view in PARAVIEW. The initial path lines are shown at 4.12(a). The velocity field at $t = 6$ ms from explicit LES (Fig. 4.12(b) and 4.12(c)) clearly contains more small scales than the ILES results of UP5-NR (Fig. 4.12(d)). The amount of small structures from simulations with HYB_{0.01}-NR and HYB_{0.03}-NR are in between the explicit LES and UP5-NR.

The results of this test-case can be explained by the MWN of the numerical schemes used in different simulations, especially the imaginary part in figure 3.3(b) which corresponds to the dissipative errors. For the 5th order upwind scheme, the dissipative error starts to raise from less than 1/3 of the Nyquist cut-off wave number, so that the small scales will be damped very fast by the implicit filtering provided by numerics. Meanwhile, the central schemes have no dissipative error, hence the explicit LES with central schemes can keep all the small eddies, and a hybrid central-upwind scheme can enhance the small scale resolution of ILES with upwind schemes.

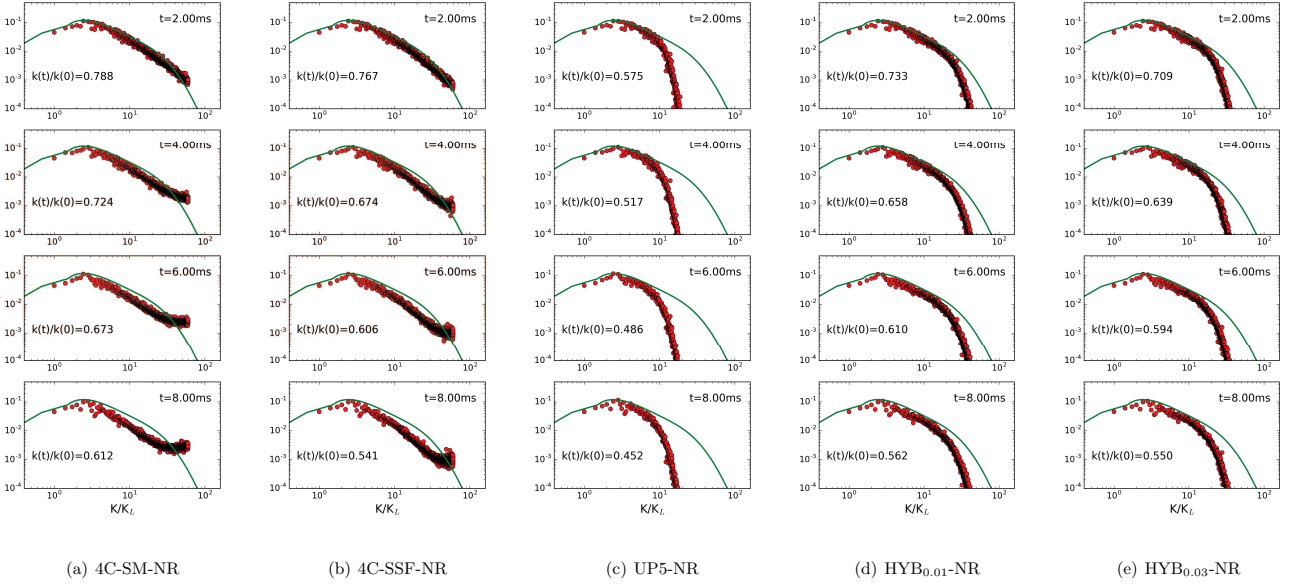
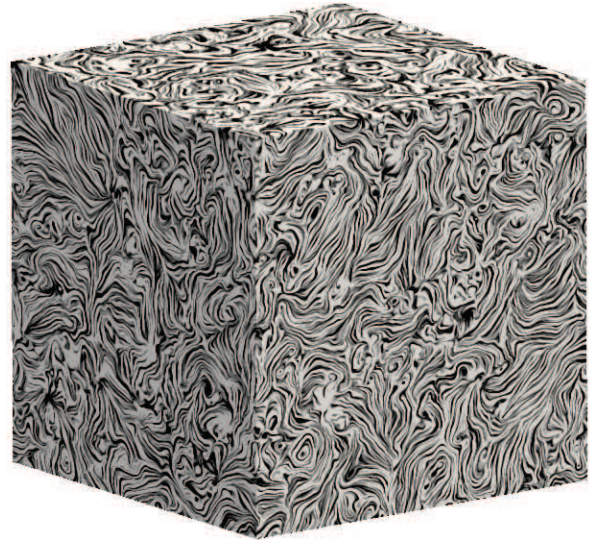


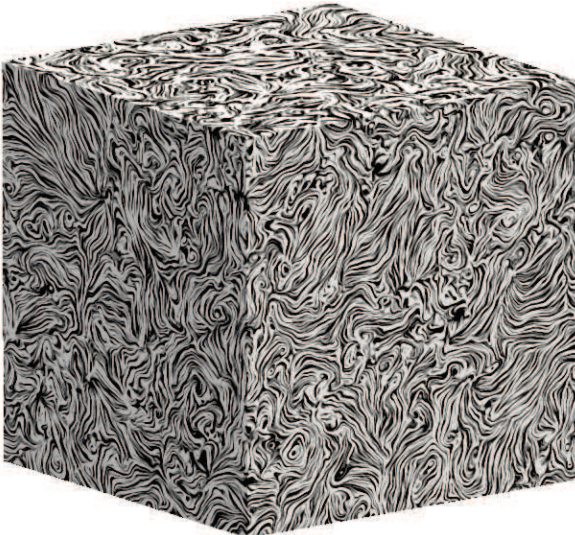
Figure 4.11: 3D Energy spectrum obtained with different LES strategies. The x axis is normalized by $K_L = 2\pi/L_x$. Nyquist cut-off for this simulation is at $K/K_L = 60$.



(a) Initial field, $t=0$



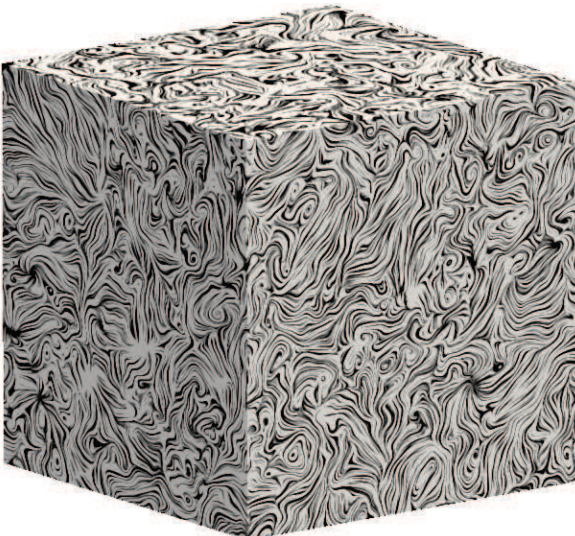
(b) 4C-SM-NR, $t=6\text{ms}$



(c) 4C-SSF-NR, $t=6\text{ms}$



(d) 5UP-NR, $t=6\text{ms}$



(e) $\text{HBY}_{0.01}\text{-NR}$, $t=6\text{ms}$



(f) $\text{HBY}_{0.03}\text{-NR}$, $t=6\text{ms}$

Figure 4.12: Path lines on the surface of velocity field from different simulation results.

4.3 Two dimensional turbulent flame

After the laminar premixed combustion and the HIT test-cases, the simulation of a two-dimensional flame will be presented in this section. A major benefit of 2D simulations is that their computational cost is much more affordable than 3D ones, so that many configurations and different LES strategies can be tested. Also, the implementation of some crucial details are verified, including boundary conditions, subgrid models for combustion and the post-treatment for reacting applications.

In this test case, a 2D methane-air premixed jet flame is simulated on a 2D domain $[0, 0.3\text{m}] \times [-0.125\text{m}, 0.125\text{m}]$. As shown in figure 4.13, a jet with diameter $D = 25\text{mm}$ is located at the center of the boundary $x = 0$. A methane-air mixture at equivalence ratio $\phi = 0.8$ is injected into the calculation domain at bulk velocity $U_D = 3.5\text{m/s}$. A pre-generated HIT field presented in the last section is added to the injected fresh gas velocity field. For this 2D case, only one slice of the 3D HIT domain is used and the velocity is enlarged by $\sqrt{3/2}$ to enforce the same turbulent kinetic energy. The grid size is constant in the flame region. Boundaries at left and right of the domain are set to slip-walls. The boundary $x = L_x$ is set to perfectly non-reflecting with NSCBC strategy [6].

The setup of boundary $x = 0$ is illustrated in figure 4.15 and in table 4.1. Boundary conditions B.C. I, B.C. II and B.C. III are implemented with NSCBC strategy as presented in section 3.4. To connect the jet region and the iso-thermal wall outside, a connection function S is used:

$$S(r, f_{in}, f_{out}) \equiv f_{out} + \frac{f_{in} - f_{out}}{2} \left[\sin \left(\frac{\pi}{d_b} (D/2 - r) \right) + 1 \right] \quad (4.1)$$

where r is the distance to the jet axis ²

$$r \equiv \sqrt{y^2 + z^2} \quad (4.2)$$

d_b is the thickness of this connection region, and f_{in} , f_{out} are the values inside and outside the jet. As initial condition, the calculation domain is filled with burnt gas. The initial condition at boundary $x = 0$ can be found in table 4.1. A 2D premixed flame will be formed during the calculation with the fresh gas continuously injected into the domain through the jet exit.

4.3.1 Comparison between different LES strategies

Two LES strategies are used in this 2D simulation:

1. ILES. The strategies UP5-QL, JS5-QL and MZ5-QL in table C.1 are applied in this category. In this approach, no explicit sub-grid term is added, neither for turbulence nor for combustion. The source terms in the species equations (2.1d) are calculated directly with Arrhenius law from the local variables, i.e. in the quasi-laminar approach.
2. Flow ILES and combustion LES. UP5-TF_n and UP5-TF_n-WF in table C.1 are implemented. The subgrid scale wrinkling model introduced by F. Thiesset in (2.59) is applied for UP5-TF_n-WF simulations, and the local Karlovitz number in (2.62) is evaluated using the subgrid eddy-viscosity calculated from the Smagorinsky model.

In the second approach, if the thickening factor and the wrinkling factor are set to 1, the simulation is identical to the first approach, i.e. the UP5-TF₁ is in fact UP5-QL.

Different grid sizes are tested to understand the grid dependency of these approaches. The grid R-2D-1 is built with 2 points in one flame thickness, $\delta_L^0/\Delta x \approx 2$. The coarse grid, R-2D-2, has less than 1 point in one flame thickness with $\delta_L^0/\Delta x \approx 0.7$. The grid size is constant inside the flame region ($4D \times 2.4D$), and is enlarged with geometric proportion outside as sketched in figure 4.14. Other parameters of the simulation grids used in this test case can be found in table 4.2. For simulations with thickened flame model, boundary conditions at $x = 0$ is also adapted by setting the connection thickness d_b in equation (4.1) to the thickened flame thickness ($\mathcal{F}\delta_L^0$), for numerical stability reasons.

² $z = 0$ for 2D cases.

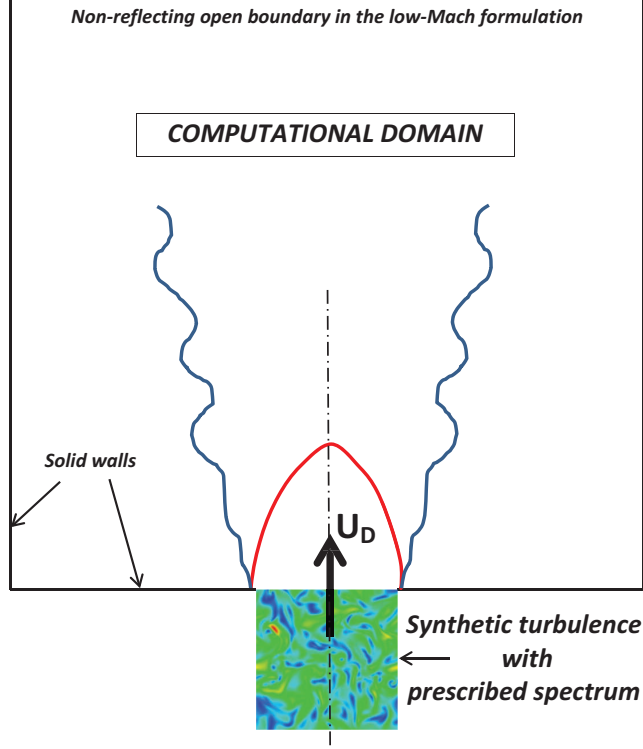


Figure 4.13: Sketch of the 2D flame setup.

Table 4.1: Boundary condition at $x = 0$ plane. The definition of function S can be found in Eq. (4.1). The subscript f and b indicate the fresh and burnt gas conditions.

	B.C. I	B.C. II	B.C. III
Location	$ r \leq (D - d_b)/2$	$ r - D/2 \leq d_b/2$	$ r \geq (D + d_b)/2$
Description	$\begin{cases} \frac{\partial \rho}{\partial t} = 0 \\ \frac{\partial Y_k}{\partial t} = 0 \\ \frac{\partial u}{\partial t} = \frac{\partial u}{\partial t} _{\text{TURB}} \\ \frac{\partial v}{\partial t} = \frac{\partial v}{\partial t} _{\text{TURB}} \\ \frac{\partial w}{\partial t} = \frac{\partial w}{\partial t} _{\text{TURB}} \end{cases}$	$\begin{cases} \frac{\partial T}{\partial t} = 0 \\ \frac{\partial Y_k}{\partial t} = 0 \\ \frac{\partial u}{\partial t} = S(r, \frac{\partial u}{\partial t} _{\text{TURB}}, 0) \\ \frac{\partial v}{\partial t} = S(r, \frac{\partial v}{\partial t} _{\text{TURB}}, 0) \\ \frac{\partial w}{\partial t} = S(r, \frac{\partial w}{\partial t} _{\text{TURB}}, 0) \end{cases}$	$\begin{cases} \frac{\partial T}{\partial t} = 0 \\ \frac{\partial u}{\partial t} = 0 \\ \frac{\partial v}{\partial t} = 0 \\ \frac{\partial w}{\partial t} = 0 \end{cases}$
Initial condition	$\begin{cases} \rho = \rho_f \\ Y_K = Y_{K,f} \\ T = T_f; \\ u = u _{\text{TURB}} + U_D \\ v = v _{\text{TURB}} \\ w = w _{\text{TURB}} \end{cases}$	$\begin{cases} \rho = S(r, \rho_f, \rho_b) \\ Y_K = S(r, Y_{K,f}, Y_{K,b}) \\ T = S(r, T_f, T_b) \\ u = S(r, u _{\text{TURB}} + U_D, 0) \\ v = S(r, v _{\text{TURB}}, 0) \\ w = S(r, w _{\text{TURB}}, 0) \end{cases}$	$\begin{cases} \rho = \rho_b \\ Y_K = Y_{K,b} \\ T = T_b \\ u = 0 \\ v = 0 \\ w = 0 \end{cases}$

The resulting instantaneous filtered progress variable

$$\tilde{c} \equiv \frac{\tilde{T} - T_f}{T_b - T_f} \quad (4.3)$$

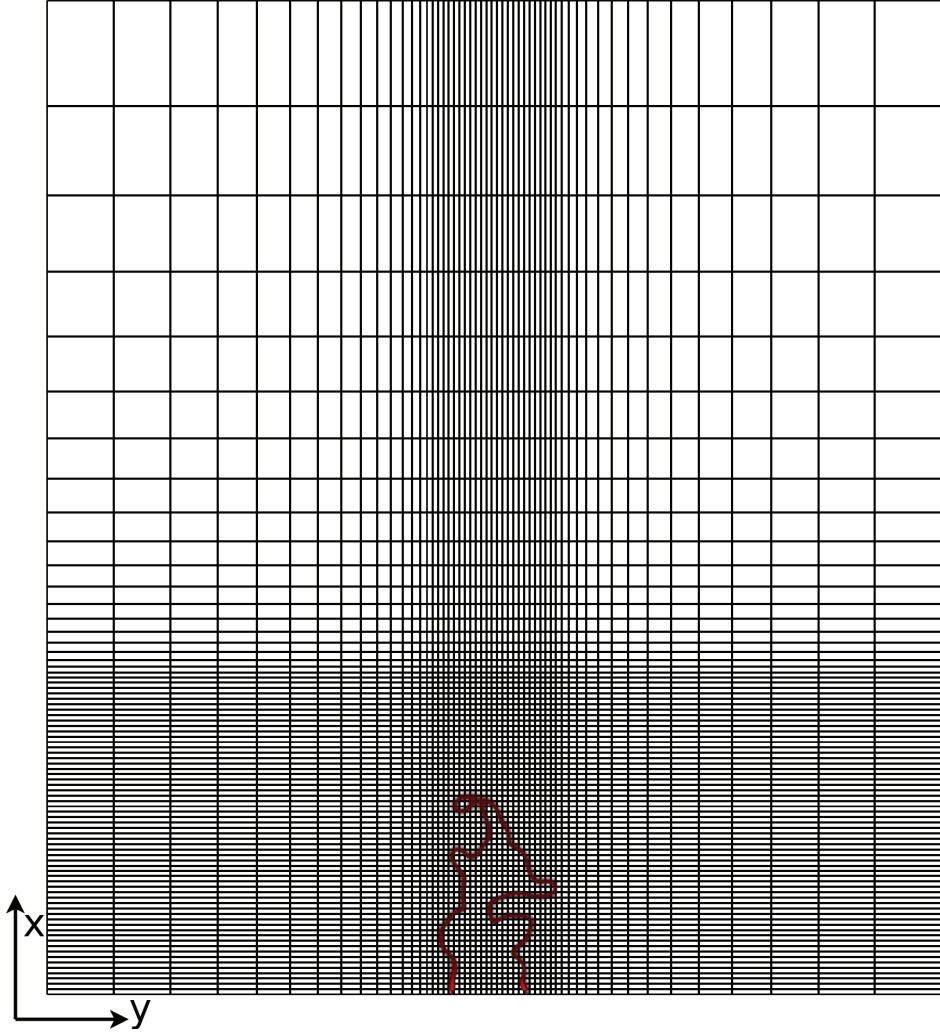


Figure 4.14: Sketch of the 2D flame grid. One third of the grid density is represented for legibility.

Table 4.2: Mesh parameters of the 2D turbulent flame test case.

	R-2D-1	R-2D-2	R-2D-3
$L_x \times L_y(\text{m})$	0.3×0.25	0.3×0.25	0.3×0.25
$N_x \times N_y$	480×384	160×128	240×192
Total grid points	184320	20480	46080
Points in jet \varnothing	107	36	50
$\Delta x_{min}/\eta$	3.1	9.3	6.7
$\Delta x_{min}/\delta_L^0$	0.47	1.4	1

where T_f and T_b are the temperature of the fresh and burnt conditions, are presented in figure 4.16 for different numerical setups. The first two rows correspond to grid R-2D-1, the third row to R-2D-2 and the last row to experimental results [4, 24]. The horizontal dashed line shows the experimental mean flame height, which is about 50 mm. In the first row, the flame length from UP5-TF $_n$ ILES gets larger with a larger thickening factor \mathcal{F} . Simulation results with the sub-grid scale wrinkling model are plotted in the first three column of the second row with thickening factor equal to 12, 6

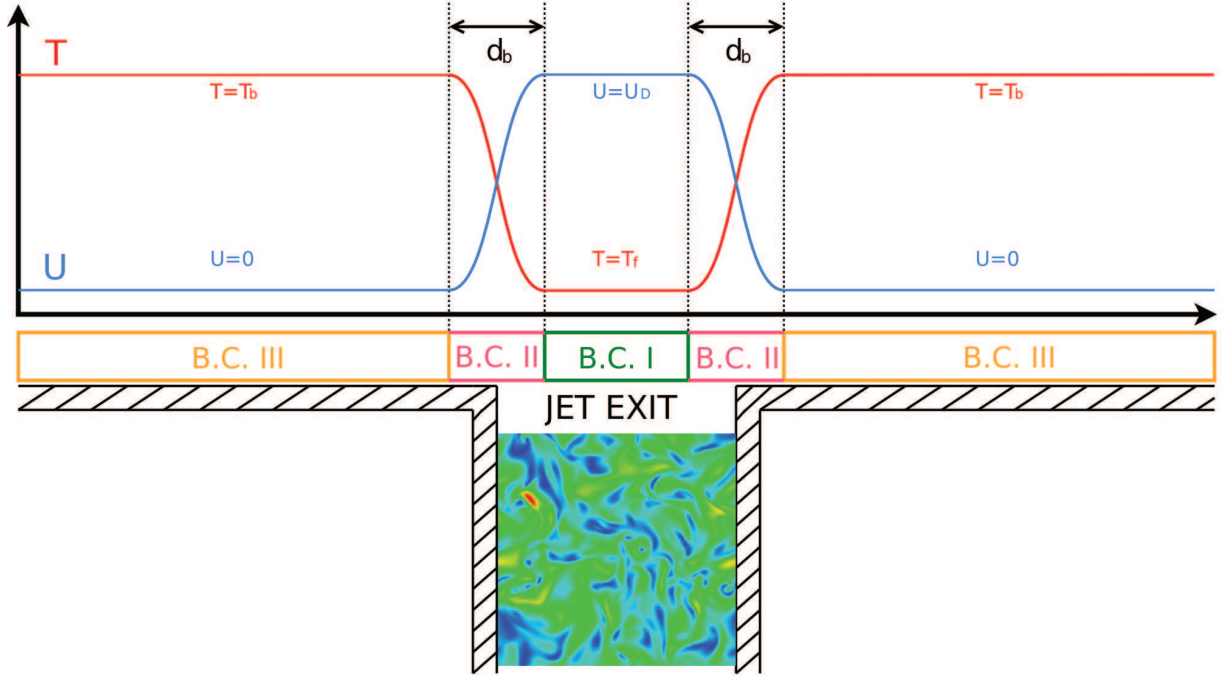


Figure 4.15: Sketch of boundary at $x = 0$

and 3. The SGS combustion model can produce similar flame length with different thickening factors. Similar results can be found on a coarser grid as plotted in first three columns of third row. The ILES with UP5-QL, MZ5-QL and JS5-QL are also shown in the last two columns. On fine mesh R-2D-1, the three ILES cases (UP5-QL, MZ5-QL and JS5-QL) produce similar flame lengths, close to the experiment. On the coarse grid R-2D-2, ILES without any explicit modeling produces a too short flame, hence a too high S_T due to excessive numerical dissipation. This is particularly obvious for JS5-QL. However, MZ5-QL is not so far from the experiment.

In summary, the full ILES approach with higher-order shock-capturing methods can lead to realistic low speed 2D premixed turbulent flame simulations with WENO schemes, provided the mesh size Δx is about 1.5 laminar flame thickness δ_L^0 . The explicit TFLES approach supplemented by the subgrid scale wrinkling model provides grid-independent results close to the experiment.

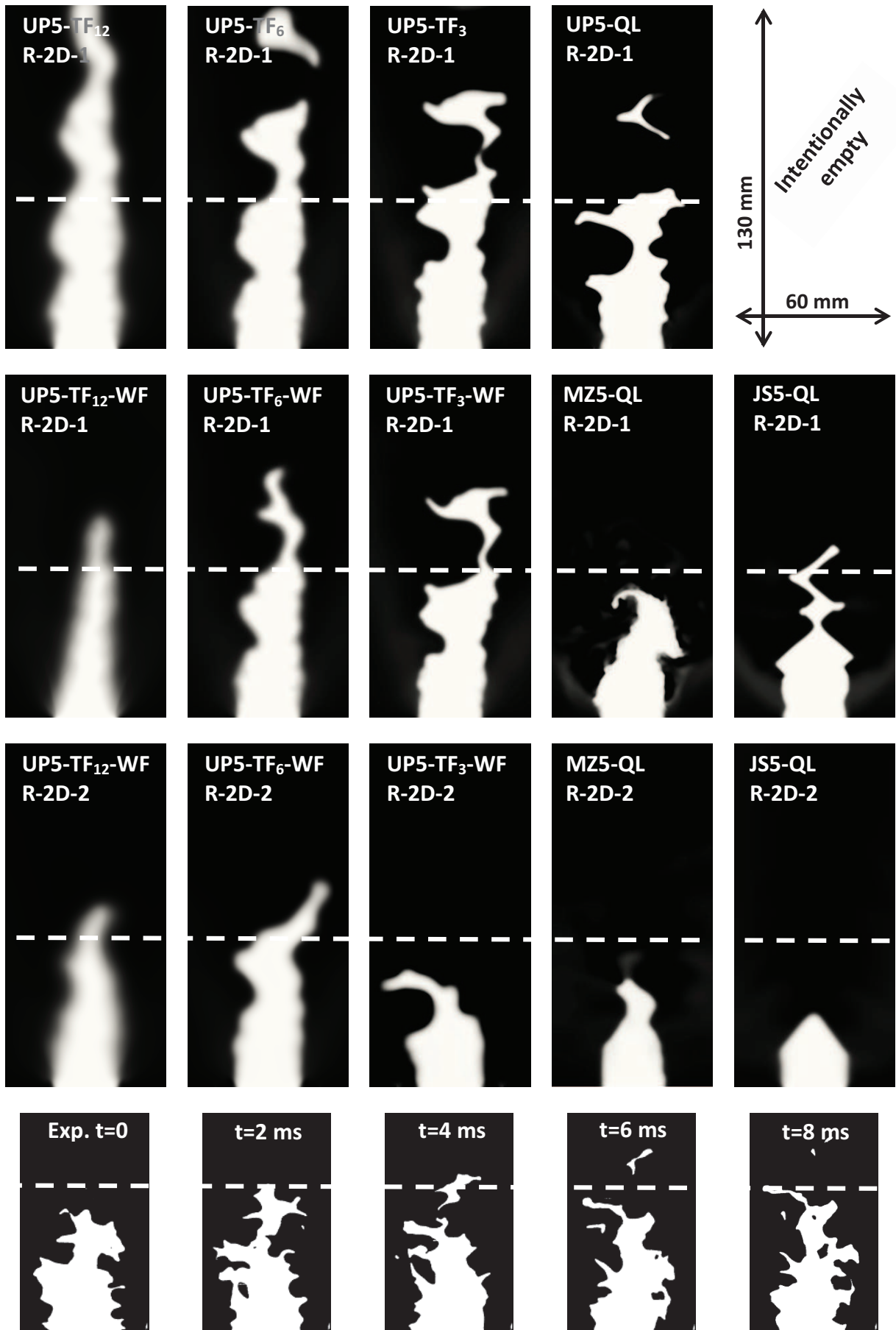


Figure 4.16: Progress variable for different 2D (I)LES strategies. Lower row: experimental flame front at 5 different times, $\phi = 0.8$, $P = 0.1\text{MPa}$.

4.3.2 Discussion and improvements

Mechanism of ILES turbulent flame

Some interesting points might be spotted by further analysis of ILES flames. The outcome of fully implicit LES simulations can show relatively good agreement with the experiment, but the reasons are not the same as the explicit LES. In figure 4.16, the progress variable contours for ILES, especially on the coarse grids R-2D-2, show that the flame surface density is not enlarged by the wrinkling of the flame front. However, the laminar flame speed obtained from ILES are notably faster than the real speed on these grid sizes with WENO schemes, as plotted in figure 4.2. Regarding these two points, we may say that, on a relatively coarse grid, the correct turbulent flame speed obtained by ILES is ensured by the filtered laminar flame speed instead of the increasing of the flame surface density.

Evaluation of SGS wrinkling factor

The explicit LES results with UP5-TF_n-WF also need further discussion. Let briefly recall some details of the process of evaluating the subgrid scale wrinkling factor, which has already been presented in section 2.3. According to Colin *et al.*[57], in TFLES, the subgrid scale wrinkling factor $\Xi \equiv S_{T\Delta}/S_L^0$ is used to model the effect of turbulence at scales roughly between δ_L^0 and $2\mathcal{F}\delta_L^0$ on the turbulent flame speed. A crucial input parameter of the SGS wrinkling factor is the local dissipation rate ε . In the simulations presented in figure 4.16, ε is estimated from SGS eddy viscosity using the Smagorinsky model as $\varepsilon = \nu_{sgs}^t{}^3 / (C_s \Delta)^4$ and $\nu_{sgs}^t = (C_s \Delta)^2 |\widetilde{S}^*|$. The drawback of using the subgrid eddy viscosity model to calculate the local dissipation rate in the combustion context is obvious: near the flame, the thermal expansion may dominate the term $|\widetilde{S}^*|$ instead of the resolved turbulent velocity fluctuations [57]. In fact, considering the results of HIT test cases in the previous section 4.2, the WENO-OPT scheme can even NOT capture any scales from δ_L^0 to $2\mathcal{F}\delta_L^0$ on the coarse grid R-2D-2 (as in figure 4.11(c)). The small structures injected into the calculation domain will be damped immediately after the jet exit. But the resulting subgrid wrinkling factor calculated from SGS eddy viscosity is still active. This is clearly due to thermal expansion only.

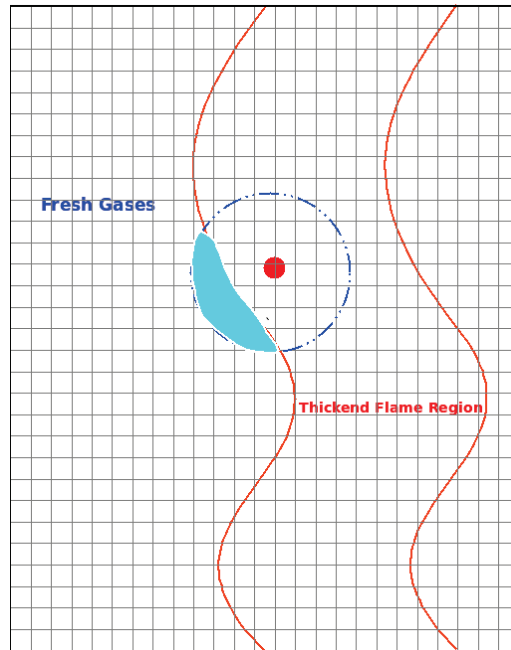


Figure 4.17: Weighted average process for SGS wrinkling factor

A better way to estimate the sub-grid turbulence velocity is to use the operator OP_2 proposed

by Colin *et al.* [57], as explained in section 2.3. This method can remove the dilatation part of the velocity field thanks to the curl operator $\nabla \times$ in (2.65), so that the thermal expansion will be eliminated from the subgrid velocity fluctuation. Also, following the results of HIT test cases, the hybrid central-upwind schemes (HYB $_{\alpha}$ -TF $_n$ -WF in table C.1) should be used in Euler flux instead of full upwind scheme, so that small turbulent scales responsible for SGS flame wrinkling can be resolved.

Another detail I would like to point out is that the SGS wrinkling factor in TFLES is calculated and applied locally, inside the reaction region. However, the turbulent level inside the reaction zone is very low due to the high viscosity introduced by the high temperature. In fact, SGS combustion models are generally designed to predict the wrinkling factor using the nearby fresh gas turbulence level (around $c = 0.05$). In the current work, a trick is proposed to overcome this issue. As shown in figure 4.17, for the evaluation of the wrinkling factor at the red dot $\vec{x} = \vec{x}_0$ inside the flame, a weighted average process is performed over a domain of radius $r = (F + 1)\delta_l^0$ surrounding \vec{x}_0

$$\Xi(\vec{x}_0) = \frac{\iiint_{\|\vec{x}-\vec{x}_0\|\leq r} \Xi(\vec{x})\omega(\vec{x})d\mathcal{V}}{\iiint_{\|\vec{x}-\vec{x}_0\|\leq r} \omega(\vec{x})d\mathcal{V}} \quad (4.4)$$

The weight ω in equation (4.4) is evaluated as

$$\omega(\vec{x}) = \begin{cases} 1 & \text{if } \tilde{c}(\vec{x}) \leq 0.05 \\ 0 & \text{otherwise} \end{cases} \quad (4.5)$$

where \tilde{c} is the local progress variable. With this treatment, the wrinkling factor at a point inside the flame region is evaluated using the surrounding fresh gas, as the blue region in figure 4.17. This is only a first proposal and some details like the radius r of the weighting should be further discussed. In fact, the same *local average on fresh gas* idea has already been successfully applied in some *a priori* tests by Veynante & Moureau [87]³.

The 2D turbulent flame test-case is then re-performed to test the improvements above. The mesh used here is the R-2D-3 grid in table 4.2, where the grid spacing is one thermal flame thickness. (I)LES strategies MZ5-QL, HYB $_{0.03}$ -TF $_6$ -WF and UP5-TF $_6$ -WF in the nomenclature C.1 is used. Firstly, the impact of different methods to calculate the SGS wrinkling factor is examined. In figure 4.18, results from different implementations of the wrinkling factor are displayed. The wrinkling factor evaluated by Smagorinsky eddy-viscosity model in Fig.4.18(a) confirms that the wrinkling factor from SGS turbulence models will be dominated by the thermal expansion inside the flame region. Wrinkling factor calculated with OP_2 for UP5-TF $_6$ -WF in figure 4.18(b) shows that, small turbulent scales responsible for SGS flame wrinkling can not be resolved on this grid using the 5th order upwind scheme. In figure 4.18(c) and 4.18(d), simulations using HYB $_{0.03}$ -TF $_6$ -WF without and with the weighting process (4.4) are plotted. The wrinkling factor is only active far from the reaction region without weighting. On the other hand, with the weighting process, as in 4.18(d), the wrinkling factor can go into the reaction region.

Simulations with MZ5-QL, UP5-TF $_6$ -WF and HYB $_{0.03}$ -TF $_6$ -WF with SGS wrinkling factor calculated by operator OP_2 and the weighting process (4.4) are displayed in figure 4.20. This figure shows that:

1. On a grid size of the order of the flame thickness, ILES can give a reasonable flame length. Meanwhile, the vorticity field in figure 4.20(d) indicates that the turbulence field on the fresh gas side of MZ5-QL simulation is badly resolved, and that the velocity field near flame front is quite oscillatory, like in 1D laminar cases as shown in figure 4.3(b).
2. The HYB $_{0.03}$ -TF $_6$ -WF can resolve far more small scale structures in the fresh gas compared to UP5-TF $_6$ -WF. Hence, the flame front is more wrinkled, and the subgrid scale wrinkling factor calculated from HYB $_{0.03}$ -TF $_6$ -WF is also larger than that from UP5-TF $_6$ -WF.

³Eq. 6 in the paper, where the turbulence intensity in fresh gas is obtained with similar method

After the improvement of the LES strategies discussed in this section, a statistical comparison between 2D simulations and experiments can be performed.

Comparison between experiments and LES

The averaged progress variable and Flame Surface Density (FSD) from 2D simulations and experiments are now compared. The comparison of averaged progress variable can be achieved in a quite straight forward manner. However, the treatment for FSD should be performed with great care, since the filtered variables obtained from TFLES can not be compared directly with experimental data.

The experimental FSD can be easily obtained as

$$\text{FSD}_E \equiv \|\nabla c_E\| \quad (4.6)$$

Meanwhile, on the numerical side, LES gives the resolved progress variable \tilde{c}_N . The resolved FSD is then

$$\text{FSD}_N \equiv \|\nabla \tilde{c}_N\| \quad (4.7)$$

Using the definition of the SGS wrinkling factor Ξ , one should have

$$\|\widetilde{\nabla c}\|_N = \Xi \|\nabla \tilde{c}_N\| = \Xi \cdot \text{FSD}_N \quad (4.8)$$

Concerning equation (4.6), the two comparable variables should be the filtered experimental flame surface density $\widetilde{\text{FSD}}_E$, and $\Xi \cdot \text{FSD}_N$ in simulations. But the LES filter is difficult to define, especially for TFLES [88]. At this stage, a gaussian filter with the same filter size as the simulation grid size Δ_x is taken to perform the filtering process for experimental results. The post treatment procedure for experimental data is described in figure 4.21. More details on the post treatment for the experimental tomographies can be found in [5].

The comparison between experiment and 2D simulations is plotted in figure 4.19. The simulation is performed with HYB_{0.03}-TF₆-WF with OP_2 and the weighting process, on grid R-2D-3 (same as in Fig. 4.20(c)). The LES results are averaged over 0.2s with 1000 time snapshots, and the experimental ones are obtained by an average of 10000 tomographic photos corresponding to a physical time of 1 s. The filtered mean progress variable from experiment and mean resolved progress variable from LES are plotted in figure 4.19(a). The filtered mean FSD from experiment $\widetilde{\text{FSD}}_E$, and $\Xi \cdot \text{FSD}_N$ from simulations are shown in figure 4.19(b). It is clear that the numerical flame is longer than the experimental one. The FSD from simulations shows that the flame flaps a lot compared to the experiment. We think that there might be two reasons for this disagreement: i) the injected 2D turbulence field has the same turbulence kinetic energy as in 3D experiment for a correct flame wrinkling factor, but this means that u' is $\sqrt{3/2}$ times larger than in experiments. ii) the 2D turbulence decays slower than the real world 3D turbulence. Hence, the simulated flame may flap more than in real experiments.

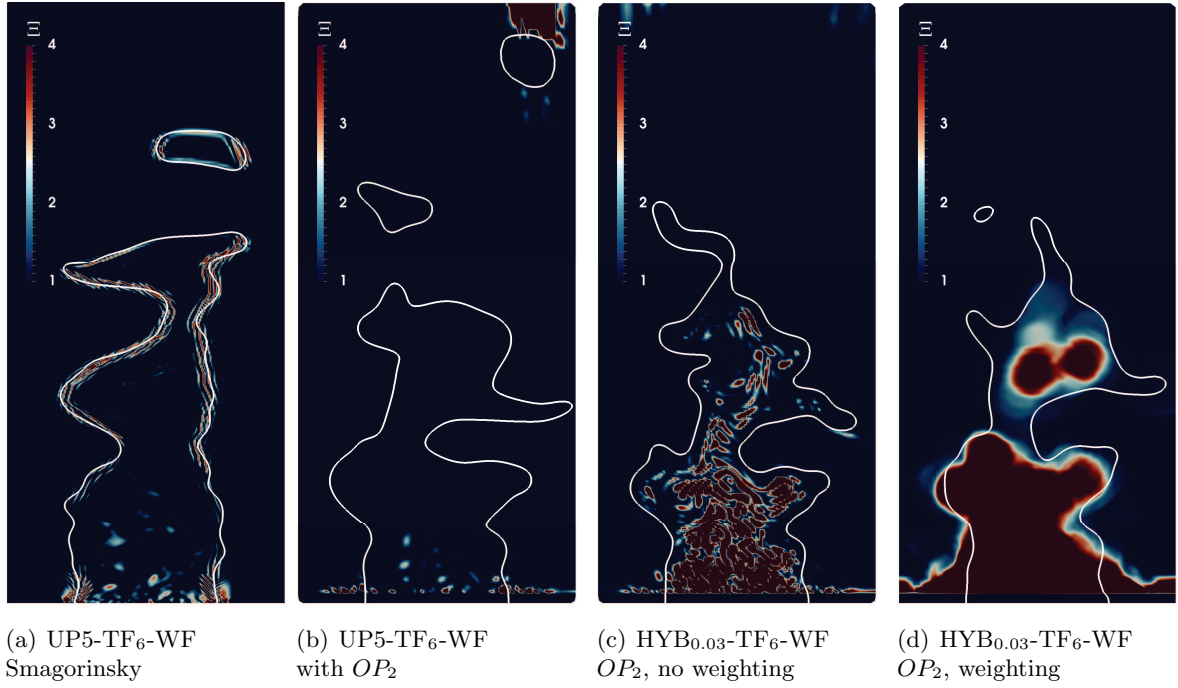


Figure 4.18: Wrinkling factor contour with different evaluation methods. The white lines are iso-value $\tilde{c} = 0.5$ which indicate the reaction zone. Grid R-2D-3 in table 4.2 ($\Delta x \approx \delta_L^0$).

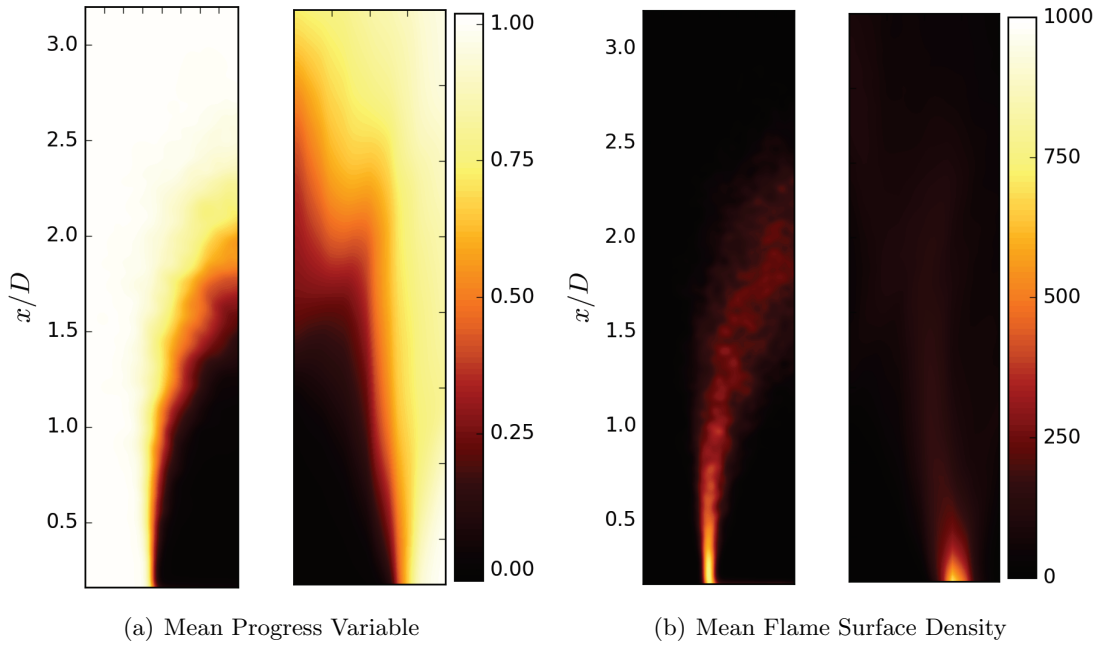
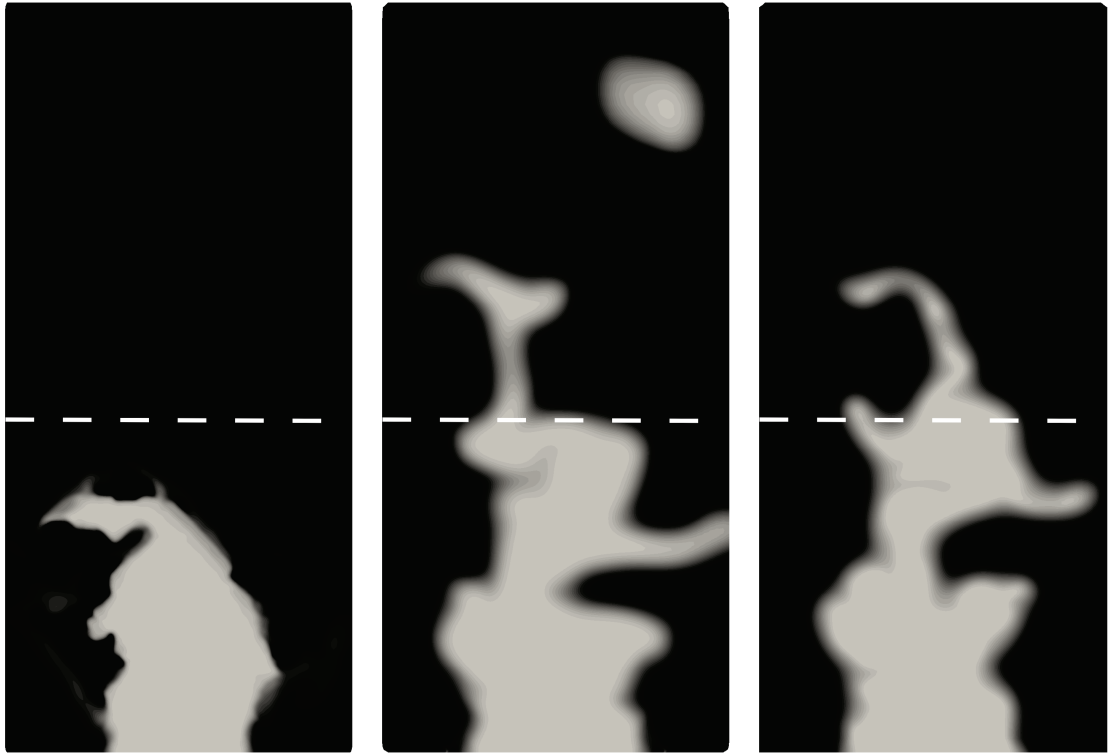


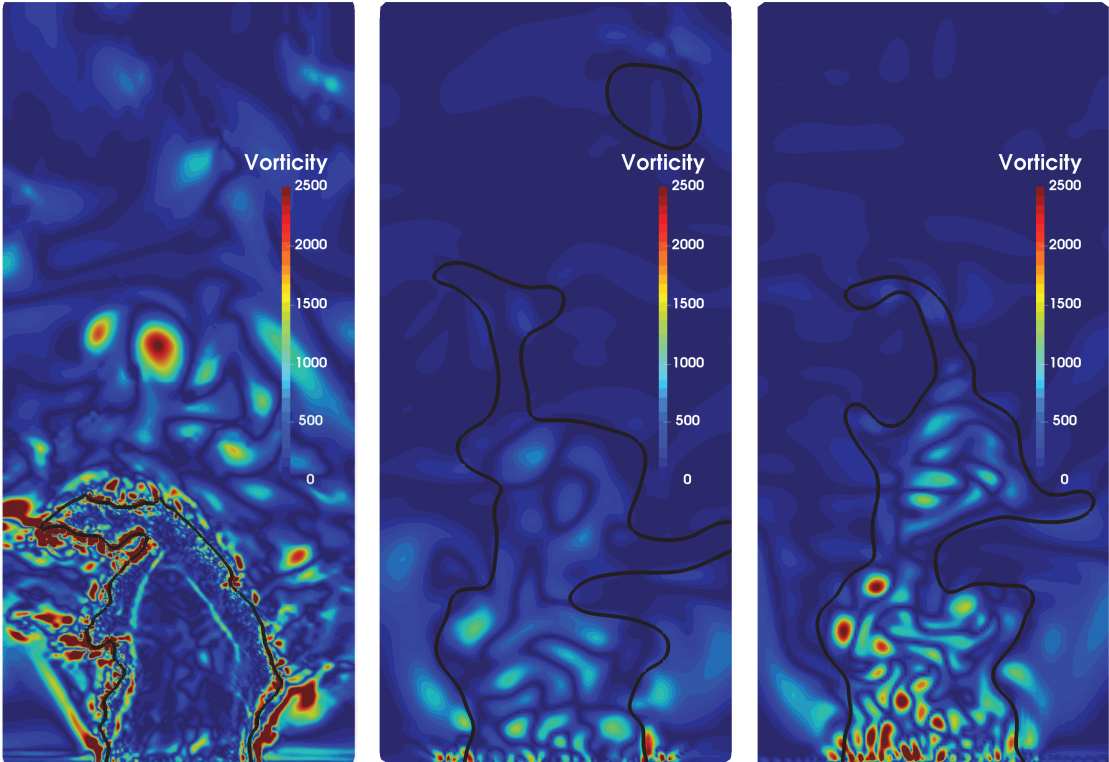
Figure 4.19: Comparison of 2D simulations and experiments. (a): Progress variable (b): Flame surface density (1/m). The experimental data and simulation results are plotted on the left and right half domains respectively.



(a) MZ5-QL, \tilde{c}

(b) UP5-TF₆-WF, \tilde{c}

(c) HYB_{0.03}-TF₆-WF, \tilde{c}



(d) MZ5-QL, vorticity

(e) UP5-TF₆-WF, vorticity

(f) HYB_{0.03}-TF₆-WF, vorticity

Figure 4.20: Progress variable and vorticity (1/s) fields for (I)LES of 2D turbulent flame test case. The black lines in the second row indicate the flame front ($\tilde{c} = 0.5$). Wrinkling factor in LES calculated with OP_2 and weighting process (4.4). Grid R-2D-3 in table 4.2.

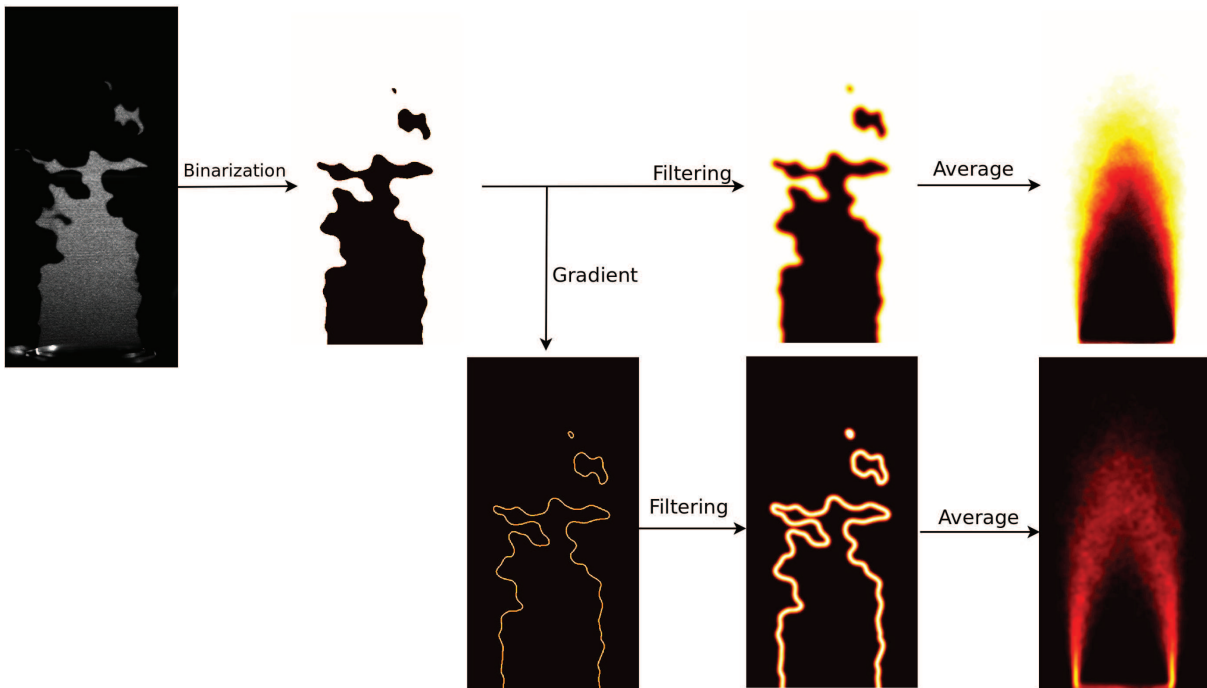


Figure 4.21: Post treatment for experimental tomographic images. First line: average progress variable. The averaged progress variable is obtained by binarization, filtering and averaging over time; Second line: average FSD. The FSD is achieved by binarization, gradient, filtering and averaging.

Chapter 5

Three dimensional multi-scale forcing turbulent premixed combustion

Synopsis

Ce dernier chapitre est consacré aux simulations 3D finales de l'expérience, en configurations non-réactive et réactive.

- Le cas non-réactif correspond à l'expérience air/air. On cherche à reproduire la longueur du cœur potentiel, la décroissance de la vitesse longitudinale et l'évolution de l'énergie cinétique turbulente sur l'axe du jet. Un premier calcul dans un domaine conforme aux dimensions de la chambre expérimentale est réalisé sur un maillage relativement grossier. Ce calcul n'est pas suffisamment résolu pour obtenir des statistiques correctes, mais permet tout de même de reproduire la structure globale du jet et de tester la méthodologie. Deux autres simulations sur des maillages raffinés et dans des domaines de calcul réduits ont permis d'obtenir des statistiques comparables à l'expérience. Ces trois simulations ont été réalisées avec le schéma WENO-JS, dit "classique". Enfin, deux autres calculs sur un domaine et un maillage identiques à celui des cas réactifs à suivre ont été réalisés en approche SGE implicite, l'un avec le schéma WENO-MZ "amélioré", l'autre avec le schéma hybride centré d'ordre 4/décentré d'ordre 5.
- Le cas réactif correspond à l'expérience CH_4/air à $p = 0.1$ Mpa et $\phi = 0.8$. On compare l'approche quasi-laminaire pour la combustion avec le schéma WENO-MZ, au calcul avec modèle de plissement sous-maille associé au schéma hybride. Ce dernier produit une longueur de flamme turbulente, une variable de progrès et une densité de surface de flamme comparables à l'expérience. L'approche ILES totale, en revanche, produit une flamme trop courte, due à un taux de consommation de méthane trop élevée.

Once the methodology verified with academic test-cases, the 3D experiment with multi-scale turbulent forcing is simulated in this chapter. (I)LES of the non-reactive air/air and reactive CH_4/air experiments will be performed, and the results will be discussed.

5.1 Non-reactive simulation

The LES for non-reactive experiments is first performed to reproduce the experimental flow field. This simulation corresponds to the multi-grid turbulent air/air experiment running at $p = 0.1$ MPa. The numerical setup for this simulation and the results will be discussed hereafter.

5.1.1 Numerical setup

In this simulation, a block of "synthetic" HIT field is generated following the procedure presented in section 3.4.1 and is injected into the calculation domain at the jet exit, as shown in figure 5.1. The

resulting HIT has the same characteristics as listed in table 1.3. The boundary condition to “inject” this HIT block is implemented using characteristic boundary conditions as in equation (3.120) and (3.127). The mean velocity profile added to this HIT field is taken from the experiments as plotted in figure 5.2(a). To simplify the process, in the simulation, inside the jet, the profile is flattened at $U/U_D = 1.05$, and a sinus like connection with a thickness $d_b = 4$ mm is used at the jet boundary, like in 2D flame test-cases in equation (4.1). The resulting profile is plotted in figure 5.2(b) and is very close to the experimental data.

The simulation domain is a parallelepiped with the jet exit located at the center of the $x = 0$ plane. As initial conditions, the whole domain is set at pressure $p = 0.1$ MPa, temperature $T = 300$ K. The velocity field is set to zero except at the jet exit. Boundaries are set as in figure 5.1: The boundary at $x = L_x$ is set to be NSCBC in-out boundary condition with a superimposed infinity pressure at $p = 0.1$ MPa (B.C. B3 in table 9.4 of [6]); Boundaries for y and z directions are set to slip-wall conditions using the symmetric ghost points method; The boundary $x = 0$ is set with the same strategy as 2D flame test-cases, as presented in figure 4.15 and table 4.1, except that here, the wall temperature at $x = 0$ is set also to $T = 300$ K.

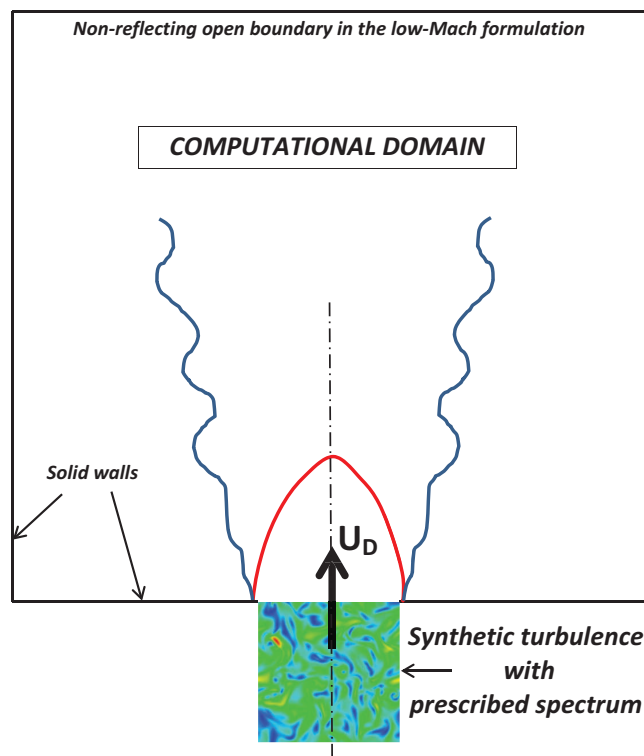


Figure 5.1: Sketch of the 3D multi-scale forcing simulation setup.

Three groups of simulations are performed for this non-reactive case. Simulation Group I (G-I) on the whole experimental domain aims to assess the simulation methodology and to obtain an overview of the flow structure; Group II (G-II-1 and G-II-2) are performed on a smaller domain with finer grids to capture the statistical results; Group III (G-III-1 and G-III-2) use the same setup as in reactive simulations¹ in order to guarantee that the flow properties in reactive case are well resolved by the numerics. Numerical parameters of these groups are given in table 5.1. The ASR low-Mach formulation [67] presented in chapter 3 is also applied with a speed-up ratio $\alpha = 10$ to all of these simulations. A sketch of the grid used in this 3D simulation can be found in figure 5.3, one third of the grid density is represented for legibility. Like 2D flame test-cases, a constant grid size is used near the jet exit.

¹The reactive case will be illustrated in the next section, Sec. 5.2.

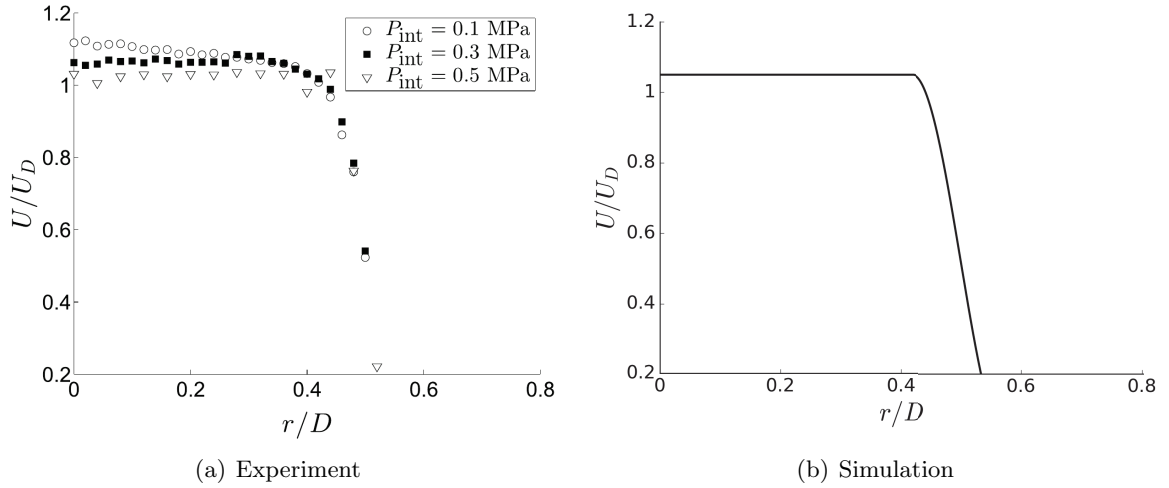


Figure 5.2: Radial mean velocity profiles at the jet exit in the experiments (a) [4] and simulations (b).

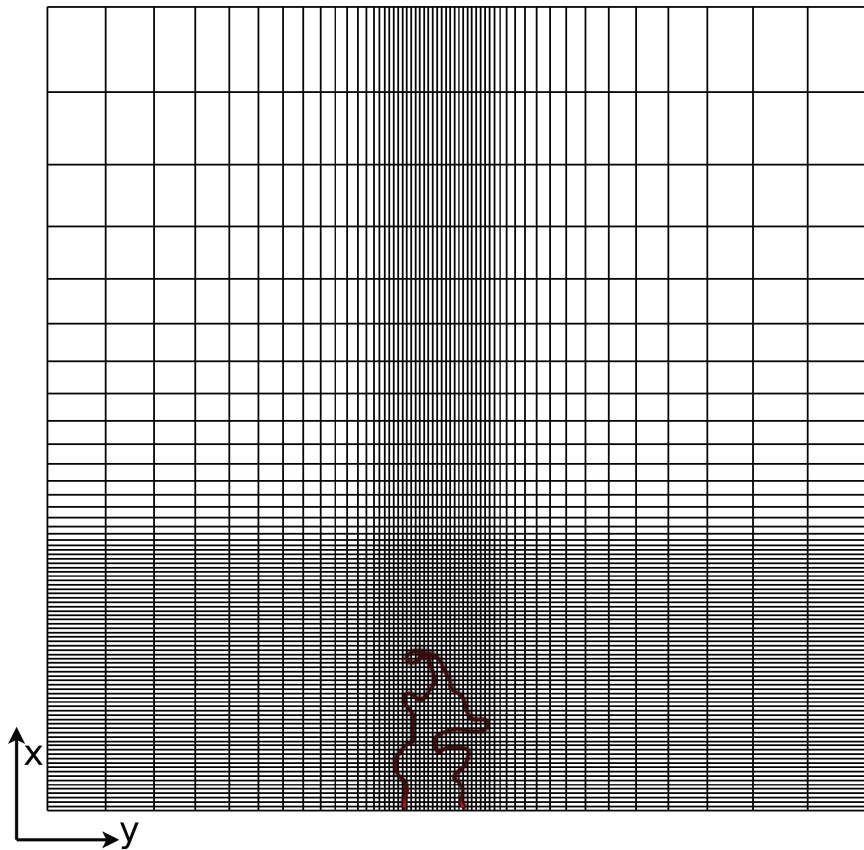


Figure 5.3: Sketch of the 3D non-reactive simulation grids (G-III) on the jet axis cut-plane. The flame front, in case of the reacting flow, is also plotted.

5.1.2 Results and discussions

The result of simulation G-I confirms that our numerical treatment can be successfully applied to this non-reactive low-speed configuration. Figure 5.4 shows the structure of the flow using the Q -

Table 5.1: Mesh and numerical parameters of the 3D non-reacting simulations.

	G-I	G-II-1	G-II-2	G-III-1	G-III-2
$L_x \times L_y \times L_z$ (m)	0.5×0.3×0.3	0.13×0.06×0.06	0.2×0.1×0.1	0.3×0.3×0.3	0.3×0.3×0.3
$N_x \times N_y \times N_z$	360×216×216	450×200×200	540×200×200	240×170×170	240×170×170
Total grid points	16.8×10^6	18.0×10^6	21.6×10^6	6.9×10^6	6.9×10^6
Points in jet \varnothing	56	100	100	50	50
$\Delta x_{min}/\eta$	6	3.3	3.3	6.7	6.7
α_{ASR} - CFL	10 - 0.8	10 - 0.8	10 - 0.8	10 - 0.8	10 - 0.8
Δt (s)	1.5×10^{-5}	0.8×10^{-5}	0.8×10^{-5}	1.33×10^{-5}	1.33×10^{-5}
Numerical scheme	JS5-NR	JS5-NR	JS5-NR	MZ5-NR	HYB _{0.03} -NR

criterion iso-surface ($Q = 1000 \text{ s}^{-2}$) colored by velocity magnitude. One can see, in the center, the injected turbulent field that evolves independently from the Kelvin-Helmholtz structures arising from the inflectional instability of the jet. The zoom in the right side of figure 5.4 indicates a fast decay of the HIT (the Taylor micro-scale increases downstream) in the potential core (length $\approx 3D$). Further downstream, the breakdown to turbulence combines with the residual HIT to create a low-speed turbulent plume.

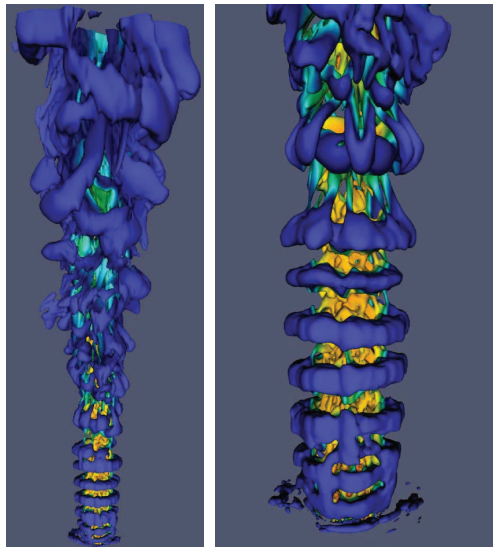


Figure 5.4: Q -criterion iso-surface $Q = 1000 \text{ s}^{-2}$ at $t = 0.8 \text{ s}$ (left), and zoom on the potential core (right) for simulation G-I. Colored by velocity magnitude.

The second group (simulations G-II-1 and G-II-2 on finer grids) is performed for statistical results. With different domain sizes in x direction (0.13 m in G-II-1 v.s. 0.2 m in G-II-2), the impact of the boundary condition at $x = L_x$ can be spotted. Figure 5.5 is a visualization of the flow in simulation G-II-1, in the injection region. Compared to G-I, more detailed structures can be observed since the grid is refined. Simulation G-II-2 gives quite similar Q -criterion iso-surface so that it is not plotted separately. The evolution of velocity and resolved turbulent kinetic energy along the jet axis in simulations G-II-1 and G-II-2 are displayed in figure 5.6(a) and 5.6(b), in comparison with experimental data from [4]. Although the axial energy decay is faster than in the experiment, the length of the potential core, where production is negligible, and the velocity profiles are both quite well predicted. Also, simulation G-II-2 on a longer domain gives better statistical results downstream, as the partially non-reflecting boundary condition at $x = L_x = 5.2D$ produces some non-physical impact on the flow field in G-II-1.

Simulations G-III-1 and G-III-2 are performed with the same numerical setup as the 3D ILES and

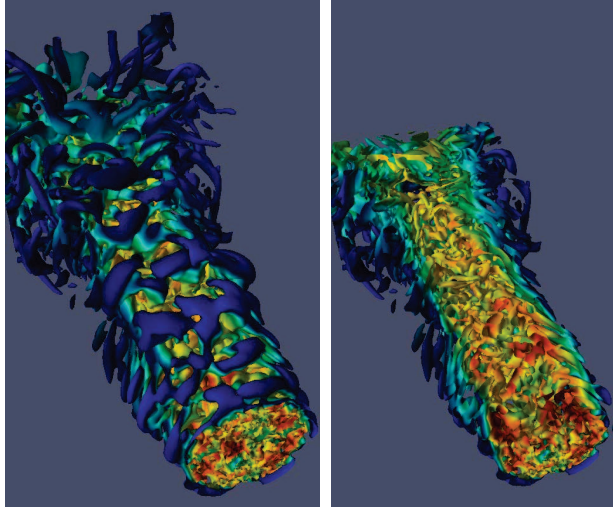


Figure 5.5: Q -criterion iso-surface $Q = 1000 \text{ s}^{-2}$ at $t = 0.14 \text{ s}$ (colored by velocity magnitude) near the injection (left), and detail of the inner structure of the jet (right) for simulation G-II-1.

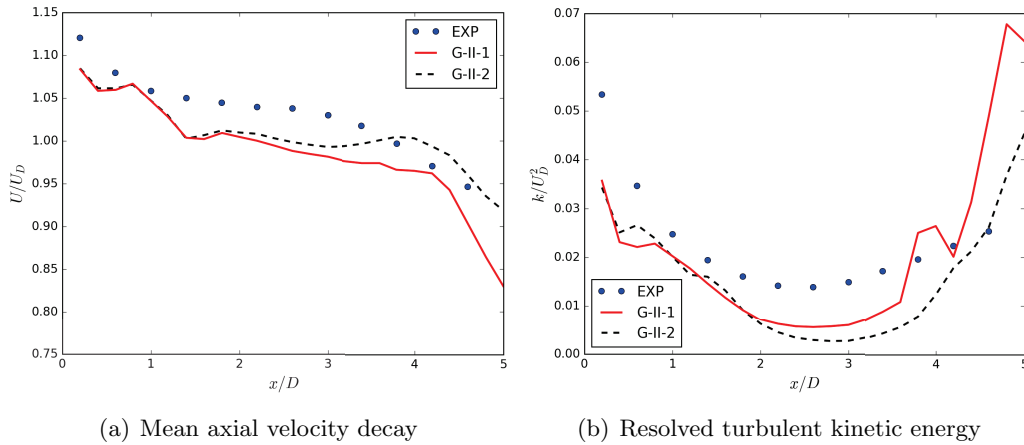


Figure 5.6: Evolution of the mean axial velocity (a) and resolved turbulent kinetic energy (b) on the jet axis for 3D non-reactive simulation Group II. The x axis is normalized by jet diameter $D = 25 \text{ mm}$ and the results are normalized with $U_D = 3.5 \text{ m/s}$.

TFLES reactive cases to validate the flow field in reactive configurations. The only difference between these two simulations is that G-III-1 is calculated with MZ5-NR while G-III-2 is with HYB_{0.03}-NR. The statistical results of velocity and resolved turbulent kinetic energy on the jet axis for Group III are plotted in figure 5.7. On this coarse mesh, the axial velocity decay after $x > 3D$ in figure 5.7(a) is not as good as in group II, where a finer mesh is used. In fact, in reactive cases, the flame length is only about 3 times of the jet diameter, so that these downstream velocity results should be acceptable for reactive case. Meanwhile, one may find in figure 5.7(b) that, the kinetic energy resolved with HYB_{0.03}-NR is even better than in the fine mesh simulations G-II with JS5-NR, and is very close to the experimental data. Q -criterion iso-surfaces of both simulations are given in figure 5.8, and the velocity and vorticity magnitude on the jet axial cut-plane are displayed in figure 5.9. These figures show that simulation G-III-2 with hybrid central-upwind scheme resolves more small scale structures than the WENO-MZ scheme does, although similar large scale structures are captured by both simulations. These results confirm our conclusions about the central-upwind scheme in the HIT decaying test-case (Sec. 4.2).

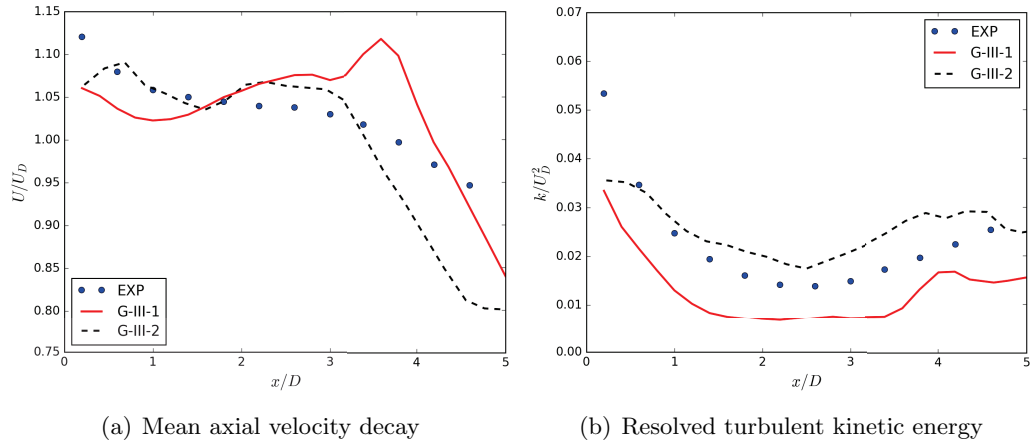
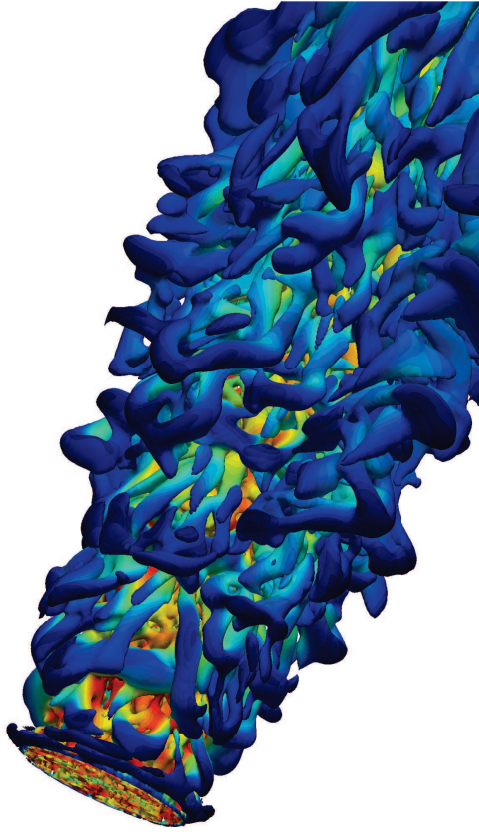
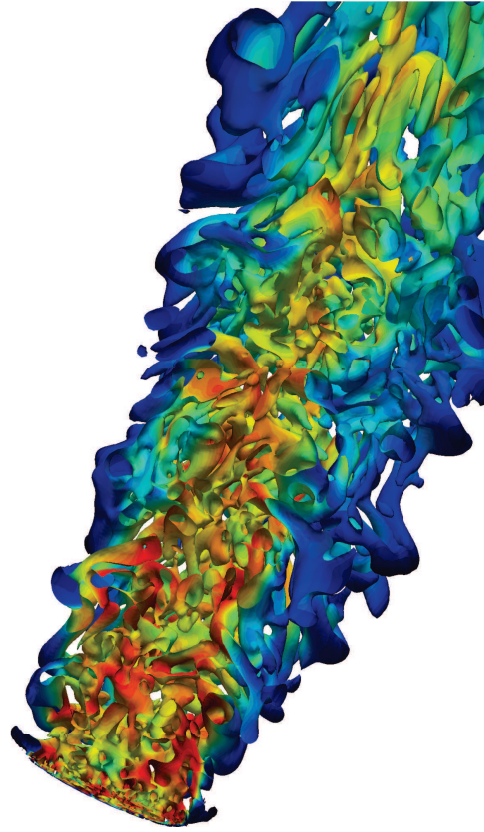


Figure 5.7: Same as figure 5.6, Group III.

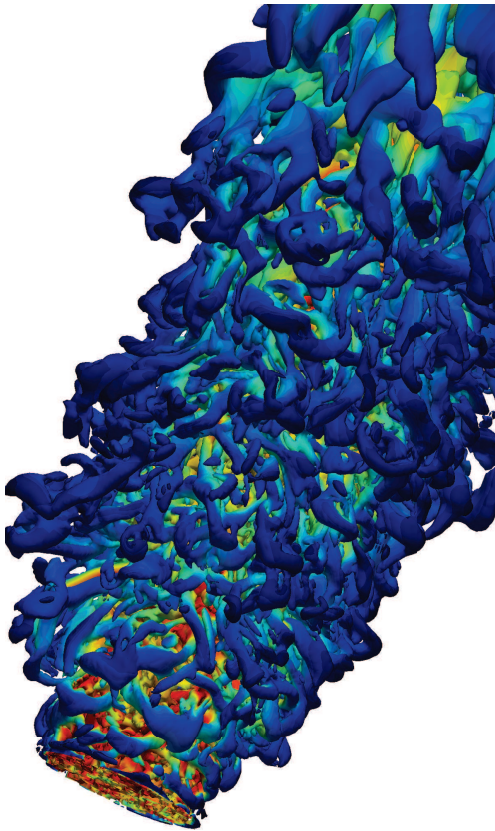
These three groups of simulations for the non-reactive configuration air/air jet show that: i) The higher-order shock-capturing methods (WENO-JS, WENO-MZ) can lead to stable and realistic ILES on relatively coarse grids; ii) ILES with HYB_α -NR schemes can capture more small scale structures than with non-linear WENO schemes, as expected from the results of the HIT test-case; iii) The numerical setup of Group III can be used in the reactive simulations.



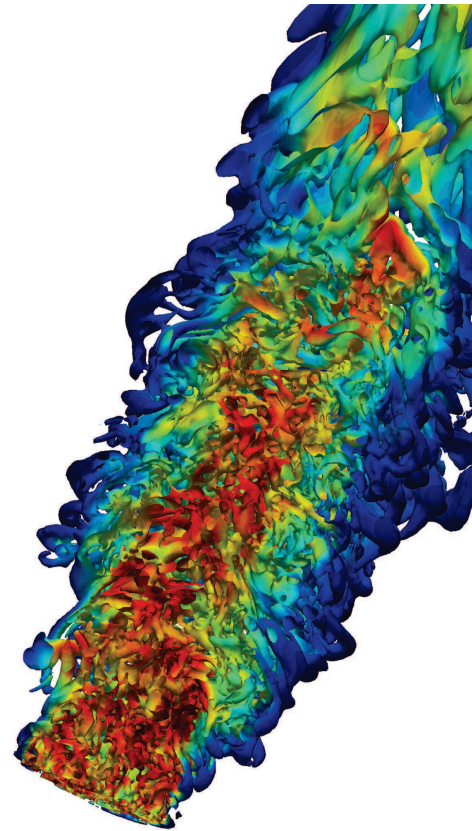
(a) G-III-1, near jet exit



(b) G-III-1, inner structures

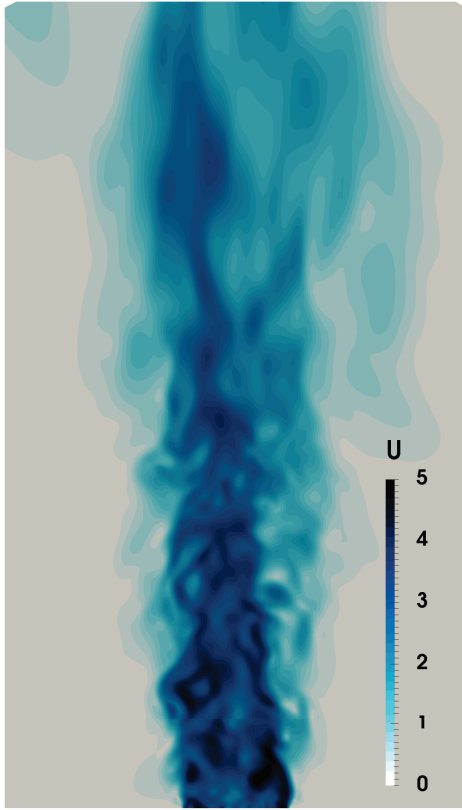


(c) G-III-2, near jet exit

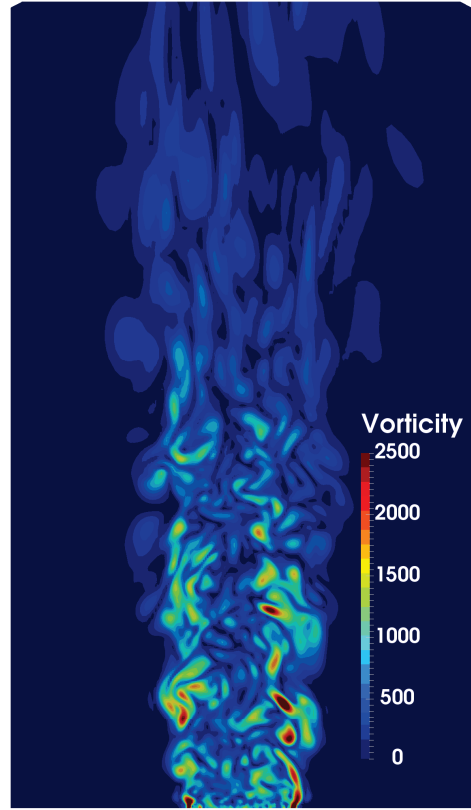


(d) G-III-2, Inner structures

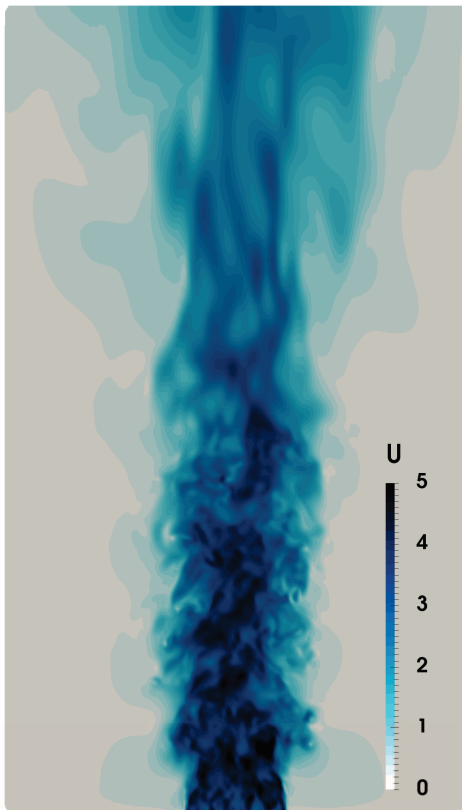
Figure 5.8: Q -criterion iso-surface $Q = 1000 \text{ s}^{-2}$ of 3D non-reactive simulations Group III at $t = 0.6 \text{ s}$ (colored by velocity magnitude).



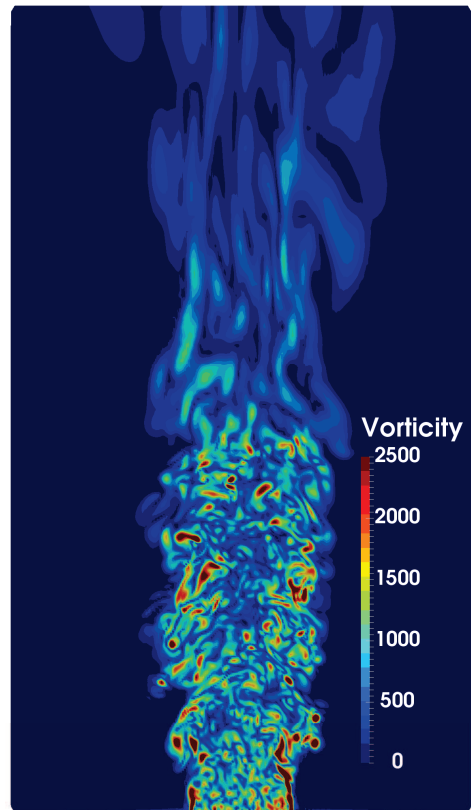
(a) Velocity, G-III-1



(b) Vorticity, G-III-1



(c) Velocity, G-III-2



(d) Vorticity, G-III-2

Figure 5.9: Velocity magnitude (m/s) and vorticity field (1/s) on the axial cut-plane of 3D non-reactive simulations Group III.

5.2 Simulations of 3D reactive cases

Three dimensional reactive cases corresponding to the reactive experiments are now simulated with both ILES and TFLES. A CH_4/air flame at equivalence ratio $\phi = 0.8$ under $p=0.1$ MPa is simulated. Detailed numerical setup and results are presented hereafter.

5.2.1 Numerical setup

Most of the numerical setup for this simulation has already been assessed in previous test-cases (HIT in section 4.2, 2D flames in section 4.3 and the 3D non-reactive simulation in the last section). Like in 2D flame test-cases, MZ5-QL (ILES) and $\text{HYB}_{0.03}\text{-TF}_8\text{-WF}$ (TFLES) are implemented and compared. The mesh setup, turbulence injection strategy and boundary conditions in this reactive simulation are identical to non-reactive simulations Group III (last two columns of table 5.1) except that, on the jet exit surface $x = 0$, the radial velocity profiles for $\text{HYB}_{0.03}\text{-TF}_8\text{-WF}$ are adjusted to match the thickened flame thickness for numerical stability, like in 2D flame test-case in Sec. 4.3. The chemical scheme used in the test case is also the CH_4/air mechanism in appendix A. The low-Mach formulation is not used in this reactive case as the time step here is mainly constrained by the chemical time step instead of CFL condition².

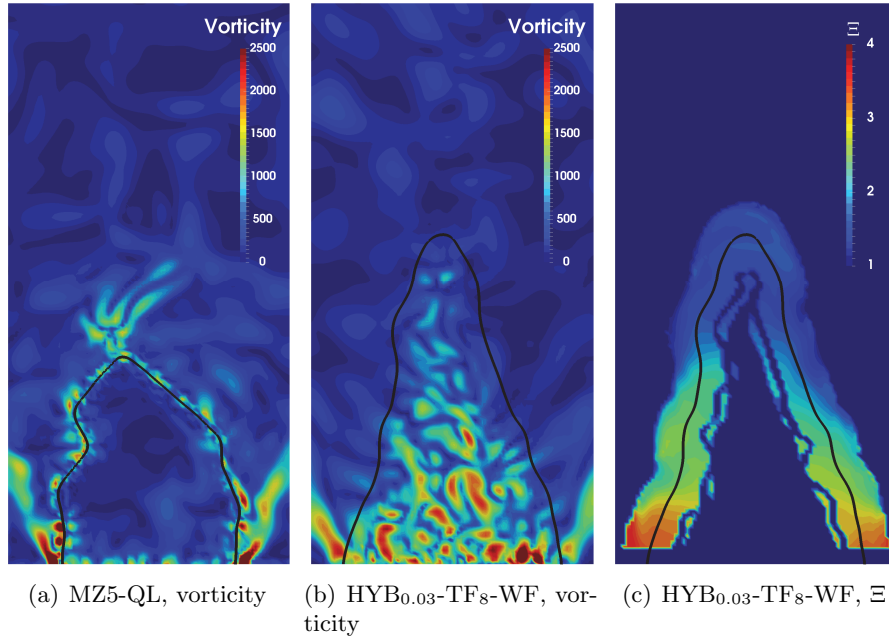


Figure 5.10: The vorticity ($1/\text{s}$) field and SGS wrinkling factor of 3D reactive simulations on the jet axis cut-plane. The black line ($\tilde{c} = 0.5$) indicates the flame front.

5.2.2 Results and discussions

Figure 5.10 shows the resolved vorticity field in the fresh gas. The fresh gas field vorticity obtained by $\text{HYB}_{0.03}\text{-TF}_8\text{-WF}$ in Fig. 5.10(b) is quite close to the non-reactive simulations $\text{HYB}_{0.03}\text{-NR}$ in Fig. 5.9(d), however, the vorticity field in the fresh gas of MZ5-QL in Fig. 5.10(a) is quite different from the non-reactive case G-III-1 (MZ5-NR) in Fig. 5.9(b). Here, the vorticity field of MZ5-QL in Fig. 5.10(a) is quite oscillatory near the flame front.

²Also, we still have some difficulties in applying the ASR to a N-S system with thickened flame model: the simulation is not stable with ASR method sometimes. We think that, for TFLES, the formulation of viscous corrections in ASR system (3.103) should be modified, as the ratio of heat diffusion to momentum viscous stress changes quite a lot when the thickened flame model is applied [67, 80].

The SGS wrinkling factor from simulation HYB_{0.03}-TF₈-WF is plotted in figure 5.10(c). During simulations, the SGS wrinkling factor is only calculated inside the flame region with OP_2 proposed in [57]. The fresh gas averaging process in equation (4.4) is also applied here. Compared with the experimental analysis in [5] and [24], the range of the SGS wrinkling factor is reasonable.

The statistical results from both (I)LES strategies are compared with experimental results. The post-treatment of the experimental tomographic photos is the same as for 2D cases, as illustrated in figure 4.21. The results of the simulation are averaged azimuthally over 35 ms, once the flame is statistically stable. In figure 5.11, the mean progress variable and FSD are plotted along the jet axis. The TFLES catches very well the flame location and structure. The FSD given by TFLES along the jet axis is higher than in experiments, whereas the MZ5-QL ILES provides the proper FSD but with too short flame. The radial profiles of progress variable and FSD are displayed in figure 5.12. Near the jet exit ($x/D = 0.5$, Fig. 5.12(a)), both MZ5-QL and HYB_{0.03}-TF₈-WF give correct radial profiles compared to the experiment. Further downstream (Fig. 5.12(b), 5.12(c) and 5.12(d)), HYB_{0.03}-TF₈-WF simulation can still provide acceptable flame locations, but this is not the case for MZ5-QL ILES, due to the too short flame compared to the experiment.

The mean progress variable and FSD on the jet axis cut-plane are also displayed in figure 5.13. Compared to the experimental results (left half of each picture), both simulations give reasonable flame length and flame surface density. However, HYB_{0.03}-TF₈-WF with subgrid scale wrinkling model from [24] shows a better agreement with the experiment.

Figure 5.14 gives the iso-surfaces of $\tilde{c} = 0.5$ from HYB_{0.03}-TF₈-WF and MZ5-QL at different times. During simulation HYB_{0.03}-TF₈-WF, the SGS flame wrinkling factor is not applied until $t = 0.35$ ms for a faster setup of the flame, as in Fig. 5.14(a), where the flame is much longer than other snapshots. One can see that CH₄ burning rate is much higher in MZ5-QL simulations, thus the resulting flame length is much smaller than the HYB_{0.03}-TF₈-WF simulations.

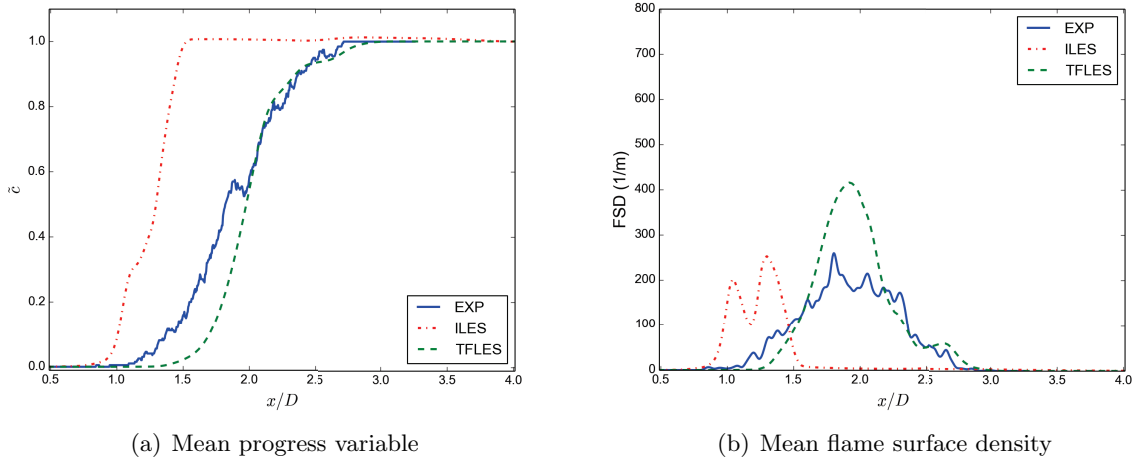
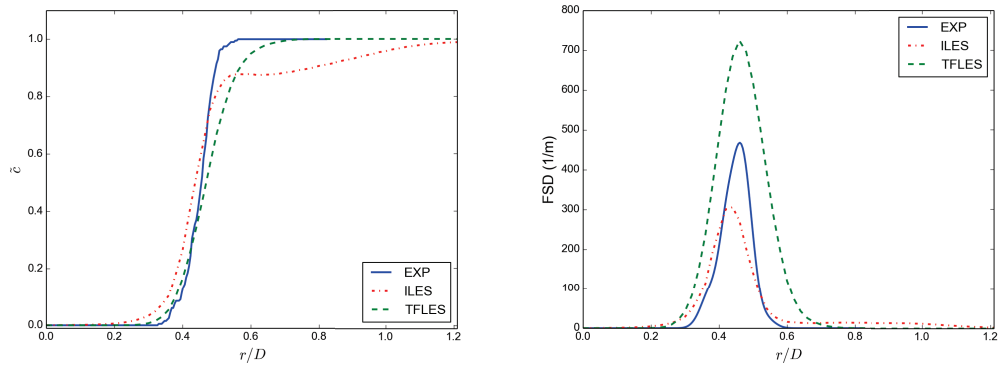
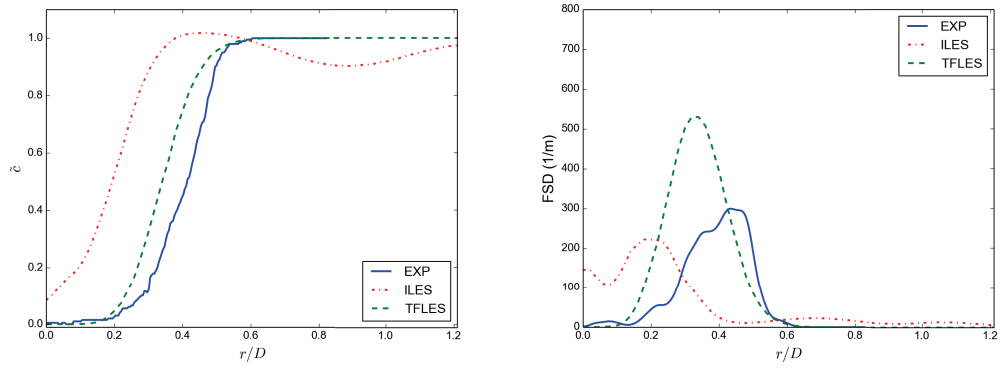


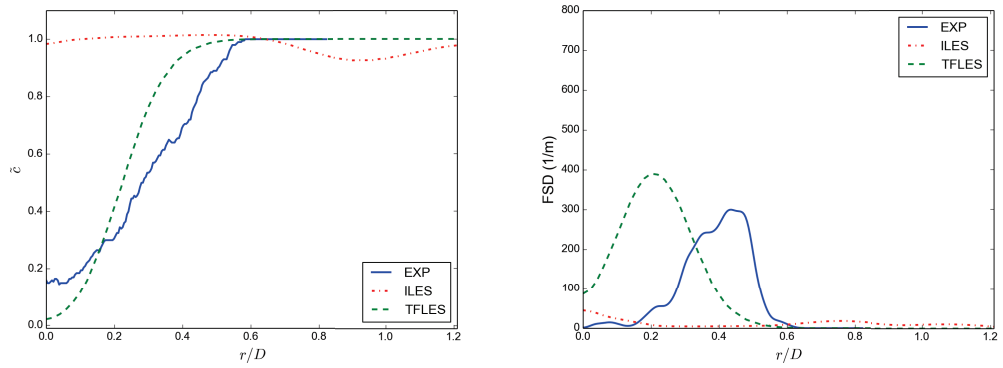
Figure 5.11: Mean Progress Variable and FSD curve along the jet axis for 3D reactive simulations



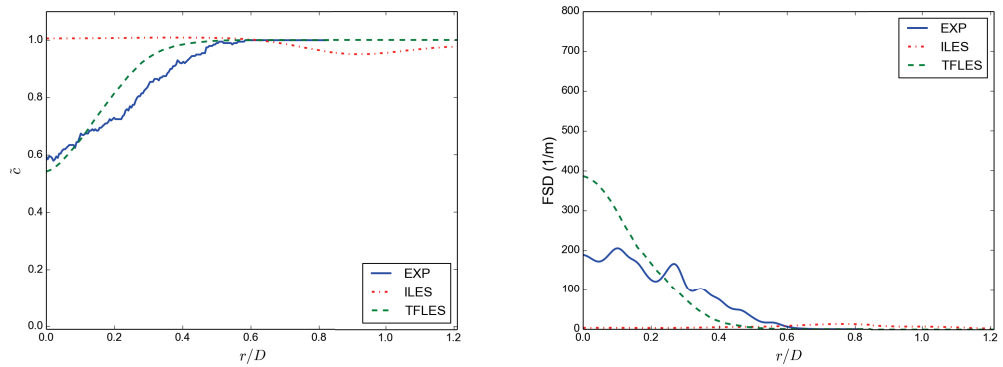
(a) $x/D=0.5$



(b) $x/D=1$



(c) $x/D=1.5$



(d) $x/D=2$

Figure 5.12: Radial profiles of mean progress variable and FSD at different locations down stream of the jet exit.

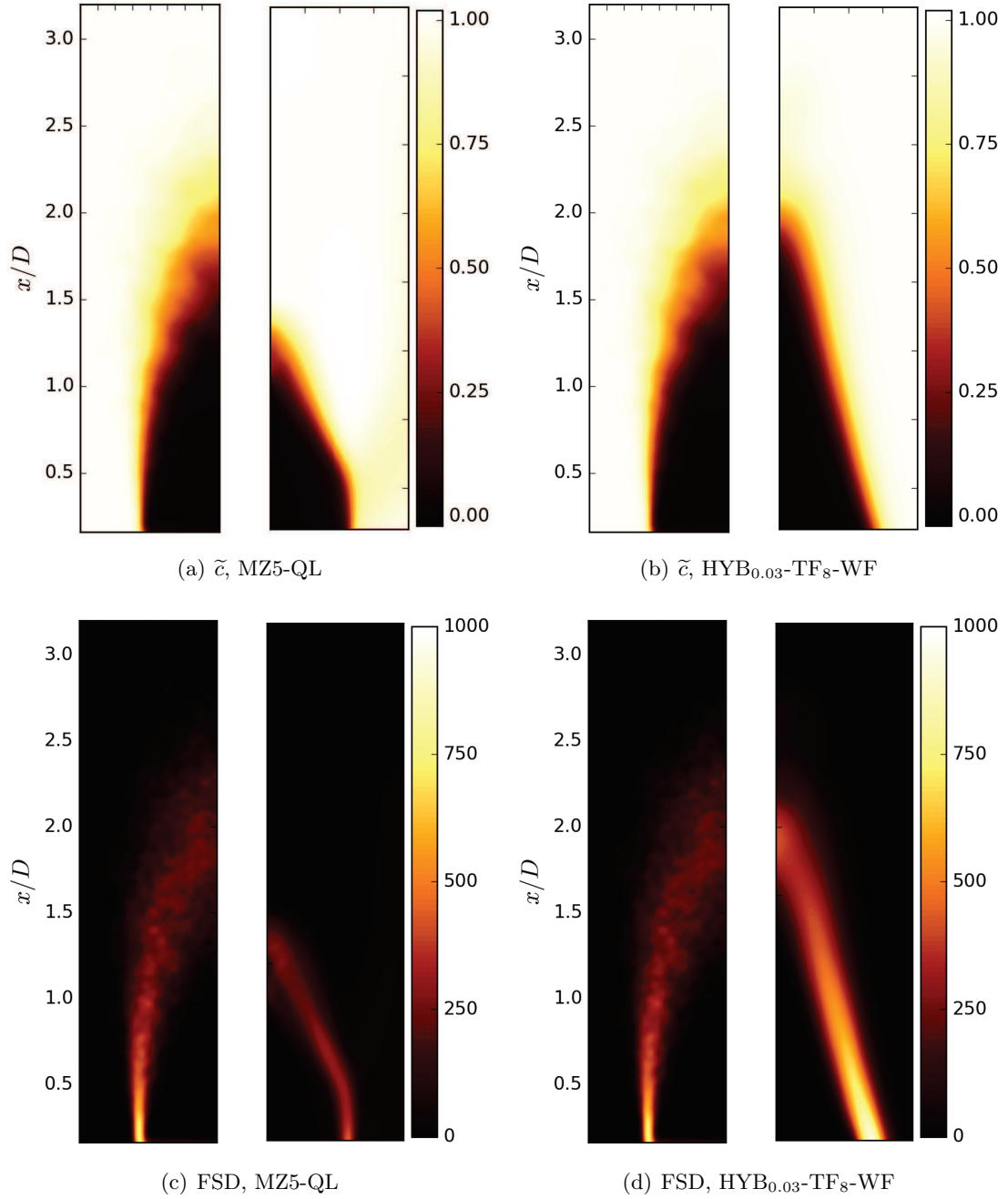


Figure 5.13: Comparison of 3D reactive simulation and experiments. (a): Mean progress variable, MZ5-QL; (b): Mean progress variable, HYB_{0.03}-TF₈-WF; (c): Mean flame surface density, MZ5-QL; (d): Mean flame surface density, HYB_{0.03}-TF₈-WF; Length unit is normalized by jet diameter $D = 25$ mm and FSD's unit is 1/m. The experimental data and simulation results are plotted on the left and on the right half of each figure, respectively.

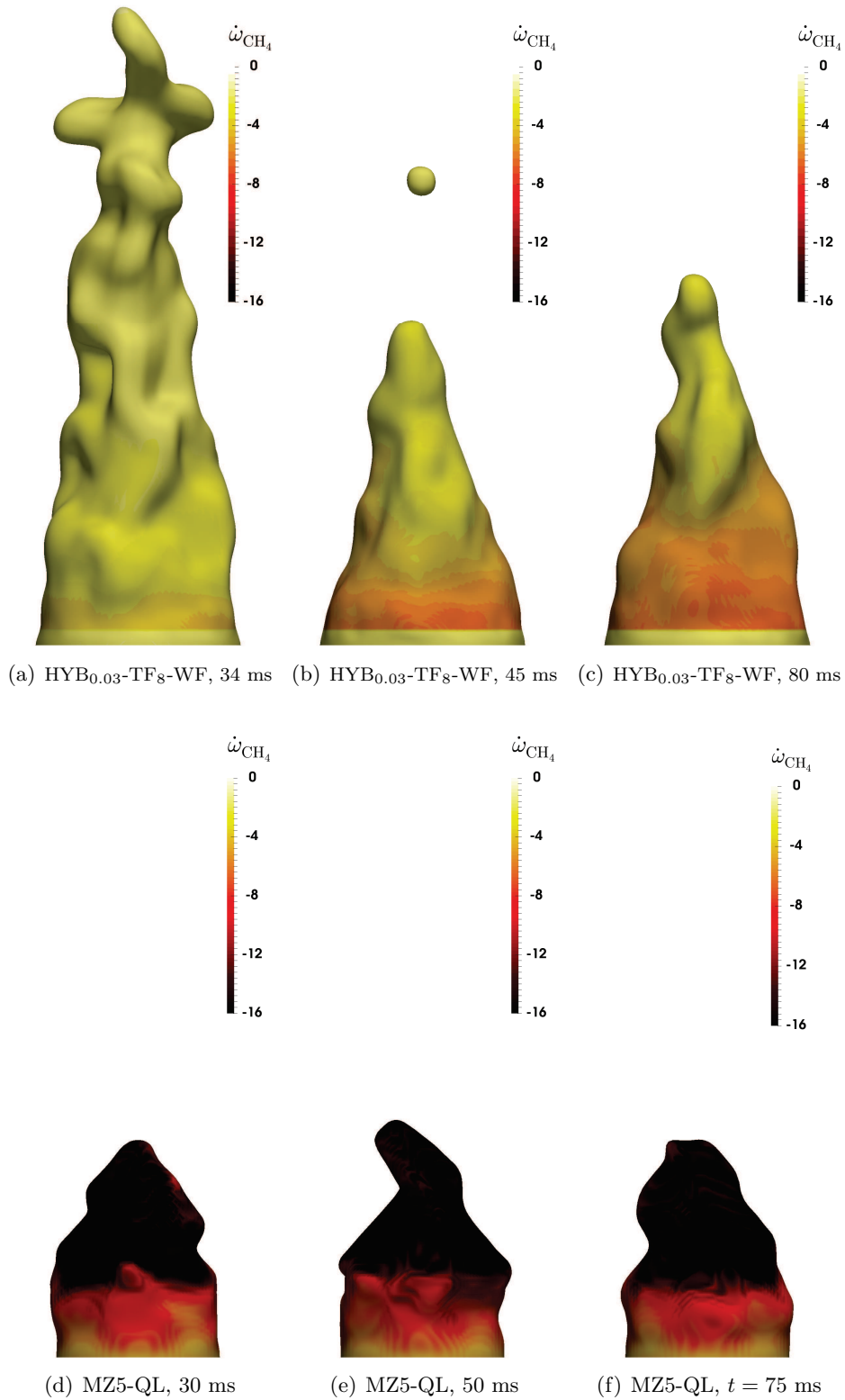


Figure 5.14: Iso-surface $\tilde{c} = 0.5$ for 3D reactive simulations at different times, colored by CH_4 consumption rate ($\text{kg}/\text{m}^3/\text{s}$). (a): HYB_{0.03}-TF₈-WF, no SGS wrinkling model, setting up the flame; (b): HYB_{0.03}-TF₈-WF, beginning of statistics; (c): HYB_{0.03}-TF₈-WF, end of statistics; (d): MZ5-QL, beginning of statistics; (e): MZ5-QL, middle of statistics; (f): MZ5-QL, end of statistics.

Chapter 6

Conclusions and perspectives

I would like now to summarize the conclusions of this work:

- A fully compressible N-S solver can be applied efficiently in low-Mach applications with some modifications using the ASR method. This pseudo-compressibility low-Mach modification keeps the benefits of compressible solvers, like characteristic boundary conditions. However, it is a hard task if the conservation form of the equations and conservative schemes are used: going to characteristic space for flux splitting implies a full rewriting and re-coding of eigen matrix. Also, a specific treatment has been mandatory to keep the full conservative form. From our knowledge, this is an original work.
- Combining explicit SGS models for combustion with implicit LES for the flow field should be achieved with great care. As pointed out by Pope [33], there is no representation or estimation of the SGS motions in a ILES resolved flow field. So a carefully examination of the explicit SGS model inputs, and of the ILES flow resolution is necessary before using this kind of implicit-explicit hybrid strategy.
- In this work, the new SGS flame wrinkling model introduced by F.Thiesset [5] has been applied for the first time. In practice, this model performs quite well, whatever the value of the thickening factor.
- Pure ILES (both flow and combustion) with non-linear WENO shock capturing schemes can provide acceptable results provided the grid size is of the order of one flame thickness. However, the mechanism for flame speed comes from an increased laminar flame speed instead of a proper turbulent flame surface density. Using a linear WENO-OPT scheme improves a little the results but lacks stability.
- The final conclusion of this study is that the best strategy is to combine ILES flow resolved by a hybrid 4th order central / linear WENO-OPT scheme, together with an explicit LES combustion model.

There are still some further work to do following the current study:

- The impact of detailed/reduced chemistry has not been studied because of a lack of time. Certainly, other chemical modeling like filtered tabulated chemistry [55] should be worth tested.
- The comparison of LES flames and experimental flames is still not clear in this work. The post-treatment of FSD both in experiments and simulations should be further discussed.
- In this work, only one operating condition of experiments (CH_4/air , $\phi = 0.8$, $p = 0.1$ MPa) is calculated. Other operating conditions should be simulated to complete our work.

Conclusions et perspectives

Je voudrais maintenant tirer les conclusions de ce travail :

- Un code Navier-Stokes compressible peut être utilisé efficacement pour des applications à bas Mach moyennant quelques modifications, à l'aide de la méthode ASR. Cette modification bas-Mach pseudo-compressible conserve les avantages du code compressible, comme par exemple la formulation caractéristique des conditions aux limites. Cependant, c'est un travail difficile si la forme conservative des équations, et l'usage de schémas conservatifs sont maintenus : le passage dans la base caractéristique pour la décomposition des flux implique une réécriture et une reprogrammation complètes des matrices des valeurs et vecteurs propres. En outre, il a fallu proposer une formulation particulière des flux numériques pour en garder la conservativité. A notre connaissance, c'est un travail original.
- La combinaison d'un modèle de combustion sous-maille explicite et de l'approche SGE implicite pour l'écoulement doit se faire avec précaution. Comme souligné par Pope [33], il n'y a ni représentation ni même estimation des fluctuations sous-maille dans les champs simulés en ILES. Les entrées du modèle de combustion sous-maille explicite, et la résolution adéquate de l'écoulement doivent donc être étudiées avec soin avant d'appliquer ce type de stratégie hybride "implicite-explicite".
- Lors de ce travail, le nouveau modèle de plissement de flamme sous-maille introduit par F.Thiesset [5] a été appliqué pour la première fois. En pratique, ce modèle se comporte bien quelle que soit la valeur du facteur d'épaississement de la flamme.
- La SGE totale (écoulement et combustion) au moyen de schémas WENO non-linéaires à capture de choc peut produire des résultats acceptables à condition que la taille des mailles soit de l'ordre d'une épaisseur de flamme laminaire. Cependant, le mécanisme produisant une vitesse de flamme turbulente réaliste provient d'une vitesse de flamme laminaire augmentée plutôt que d'une densité de surface de flamme turbulente correcte. L'emploi d'un schéma WENO linéaire optimum améliore légèrement les résultats, mais au détriment de la stabilité du calcul.
- La conclusion finale de cette étude est que la meilleure stratégie consiste à combiner la SGE implicite de l'écoulement à l'aide d'un schéma centré d'ordre 4 hybridé avec un schéma WENO linéaire optimum, avec un modèle explicite de combustion sous-maille.

Il y a encore du travail à réaliser à la suite de cette étude :

- L'impact d'un schéma de cinétique chimique détaillé ou réduit n'a pas été étudié par manque de temps. Certainement, d'autres modélisations comme la chimie filtrée tabulée [55] mériteraient d'être testées.
- La comparaison des flammes simulées en SGE et des flammes expérimentales n'est toujours pas évidente dans ce travail. La procédure de post-traitement de la densité de surface de flamme dans les expériences et dans les simulations doit être davantage approfondie.
- Dans ce travail, une seule condition expérimentale (CH_4/air , $\phi = 0.8$, $p = 0.1$ MPa) a été simulée. Il faudrait simuler d'autres conditions pour compléter notre travail.

Appendices

Appendix A

Chemical Schemes

A.1 One step CH₄/Air chemical schemes

```
! 1 step methane chemkin
```

```
ELEMENTS
```

```
O H C N
```

```
END
```

```
SPECIES
```

```
CH4 O2 H2O CO2 N2
```

```
END
```

```
REACTIONS
```

```
! All coefs are in CGS unit
```

```
CH4 + 2O2 => 2H2O + CO2 1.1E10 0.0 20000.0 !REF Wang et al. C&F 2011
```

```
FORD / CH4 1.0 /
```

```
FORD / O2 0.5 /
```

```
END
```

A.2 9 species 28 reactions H₂-Air chemical schemes

```

ELEMENTS
H O N
END
SPECIES
H2      O2      H O OH H2O      HO2 H2O2 N2
END

REACTIONS
! All coefs are in CGS unit
H2+M <=> H+H+M          4.57E+019      -1.4  104380.00
  H2 /2.5/   H2O /12/
! 1      Tsang & Hampson, J. Phys. Chem. Ref. Data, 15, 1986.
H2+O2 <=> OH+OH          2.5E+012      0    39000.00
! 3      Konnov
H+H+H <=> H2+H          3.2E+015      0    0.00
! 4      Konnov
H+HO2 <=> H2O+O          3E+013      0    1720.00
! 5      Konnov
O+H2 <=> H+OH           50800      2.67  6290.00
! 6      Sutherland et. al., 21st Symp. on Comb., p929, 1986.
O+O+M <=> O2+M          6.16E+015     -0.5   0.00
  H2 /2.5/   H2O /12/
! 7      Tsang & Hampson, J. Phys. Chem. Ref. Data, 15, 1986.
H+O2 <=> O+OH           1.91E+014     0    16439.00
! 9      Pirraglia et. al. (TJK)###
H+O2(+M) <=> HO2(+M)    1.48E+012     0.6   0.00
  LOW /3.482E+016 -0.411 -1115/
  TROE /0.5 1E-030 1E+030/
  H2 /2.5/   H2O /12/
! 10     Mueller et al Proc. Comb. Ins. 27, (1998)
H+O+M <=> OH+M          4.71E+018     -1    0.00
  H2 /2.5/   H2O /12/
! 12     Tsang & Hampson, J. Phys. Chem. Ref. Data, 15, 1986
OH+H2 <=> H2O+H          2.16E+008     1.51  3430.00
! 13     Michael & Sutherland, J. Phys. Chem., 92, 3853, 1988
H2O+O <=> OH+OH          2.97E+006     2.02  13400.00
! 14     Sutherland et. al. Proc Comb. Ins., 28 51 (1990)
H2O2(+M) <=> OH+OH(+M)  2.95E+014     0    48430.00
  LOW /1.2E+017 0 45500/
  TROE /0.5 1E-090 1E+090/
  H2 /2.5/   H2O /12/
! 15     Brower, Cobos, Troe, Duba, & Crim, J. Chem. Phys. 86, 6171, 1987.
OH+H+M <=> H2O+M        2.21E+022     -2    0.00
  H2 /2.5/   H2O /12/
! 17     Tsang & Hampson, J. Phys. Chem. Ref. Data, 15, 1986
HO2+O <=> O2+OH          3.3E+013     0    0.00
! 19     Baulch et al., JPC Ref Data, 21:411 (1992)
HO2+H <=> H2+O2          1.66E+013     0    823.00
! 20     Mueller et al. IJCK 31, 113 (1995)
HO2+H <=> OH+OH          7.08E+013     0    295.00
! 21     Mueller et al. IJCK 31, 113 (1995)
HO2+OH <=> H2O+O2        2.89E+013     0   -497.00
! 22     Keyser, L.F., J. Phys. Chem. 92, 1193, 1988
HO2+HO2 <=> H2O2+O2      4.2E+014     0   11982.00
  DUP
! 23     Hippler, Troe, Willner, J. Chem. Phys. 93, 1755, 1990
HO2+HO2 <=> H2O2+O2      1.3E+011     0  -1629.00
  DUP
! 24     Hippler, Troe, Willner, J. Chem. Phys. 93, 1755, 1990
H2O2+O <=> OH+HO2        9.55E+006     2    3970.00
! 25     Tsang & Hampson, J. Phys. Chem. Ref. Data, 15, 1986
H2O2+H <=> H2O+OH        2.4E+013     0    3970.00
! 26     Tsang and Hampson, JPC Ref. Data, 15:1087 (1986)
H2O2+H <=> HO2+H2        4.82E+013     0    7950.00
! 27     Tsang & Hampson, J. Phys. Chem. Ref. Data, 15, 1986
H2O2+OH <=> H2O+HO2      1E+012     0    0.00
  DUP
! 28     Hippler et. al. Double Exponential fit by(TJK)###
H2O2+OH <=> H2O+HO2      5.8E+014     0    9557.00
  DUP
! 29     Hippler et. al. Double Exponential fit by(TJK)###
END

```


Appendix B

Numerical Details

B.1 The WENO coefficients

k	r	$j = 0$	$j = 1$	$j = 2$	$j = 3$	$j = 4$	$j = 5$
1	0	1					
2	0	1/2	1/2				
	1	-1/2	3/2				
3	0	1/3	5/6	-1/6			
	1	-1/6	5/6	1/3			
	2	1/3	-7/6	11/6			
4	0	1/4	13/12	-5/12	1/12		
	1	-1/12	7/12	7/12	-1/12		
	2	1/12	-5/12	13/12	1/4		
	3	-1/4	13/12	-23/12	25/12		
5	0	1/5	77/60	-43/60	17/60	-1/20	
	1	-1/20	9/20	47/60	-13/60	1/30	
	2	1/30	-13/60	47/60	9/20	-1/20	
	3	-1/20	17/60	-43/60	77/60	1/5	
	4	1/5	-21/20	137/60	-163/60	137/60	
6	0	1/6	29/20	-21/20	37/60	-13/60	1/30
	1	-1/30	11/30	19/20	-23/60	7/60	-1/60
	2	1/60	-2/15	37/60	37/60	-2/15	1/60
	3	-1/60	7/60	-23/60	19/20	11/30	-1/30
	4	1/30	-13/60	37/60	-21/20	29/20	1/6
	5	-1/6	31/30	-163/60	79/20	-71/20	49/20

Table B.1: Coefficients c_{rj} for $k=1$ to 6.

k	$r = 0$	$r = 1$	$r = 2$	$r = 3$	$r = 4$	$r = 5$
1	1					
2	2/3	1/3				
3	3/10	3/5	1/10			
4	4/35	18/35	12/35	1/35		
5	5/126	40/126	60/126	20/126	1/126	
6	1/77	25/154	100/231	25/77	5/77	1/462

Table B.2: Coefficients d_r for $k=1$ to 6.

The coefficients β necessary for computation of the smoothness indicators β_r , for different stencils presented for reconstruction for $k = 1$ to 6.

$k = 1$

There exist single stencil for reconstruction : $S_0 = (i)$.

$$\beta_0 = f_i f_i$$

$k = 2$

There exist two stencils for reconstruction : $S_0 = (i, i + 1)$ $S_1 = (i - 1, i)$.

$$\begin{aligned}\beta_0 &= (f_{i+1} - f_i)^2 \\ \beta_1 &= (f_i - f_{i-1})^2\end{aligned}$$

$k = 3$

There exist three stencils for reconstruction : $S_0 = (i, i + 1, i + 2)$ $S_1 = (i - 1, i, i + 1)$ $S_2 = (i - 2, i - 1, i)$.

$$\begin{aligned}\beta_0 &= \frac{13}{12}(f_i - 2f_{i+1} + f_{i+2})^2 + \frac{1}{4}(3f_i - 4f_{i+1} + f_{i+2})^2 \\ \beta_1 &= \frac{13}{12}(f_{i-1} - 2f_i + f_{i+1})^2 + \frac{1}{4}(f_{i-1} - f_{i+1})^2 \\ \beta_2 &= \frac{13}{12}(f_{i-2} - 2f_{i-1} + f_i)^2 + \frac{1}{4}(f_{i-2} - 4f_{i-1} + 3f_i)^2\end{aligned}$$

$k = 4$

There exist four stencils for reconstruction : $S_0 = (i, i + 1, i + 2, i + 3)$ $S_1 = (i - 1, i, i + 1, i + 2)$ $S_2 = (i - 2, i - 1, i, i + 1)$ $S_3 = (i - 3, i - 2, i - 1, i)$.

$$\begin{aligned}\beta_0 &= 2107f_i^2 - 9402f_{i+1}f_i + 7042f_{i+2}f_i - 1854f_{i+3}f_i + 11003f_{i+1}^2 - 17246f_{i+2}f_{i+1} \\ &+ 4642f_{i+3}f_{i+1} + 7043f_{i+2}^2 - 3882f_{i+3}f_{i+2} + 547f_{i+3}^2 \\ \beta_1 &= 547f_{i-1}^2 - 2522f_i f_{i-1} + 1922f_{i+1}f_{i-1} - 494f_{i+2}f_{i-1} + 3443f_i^2 - 5966f_{i+1}f_i \\ &+ 1602f_{i+2}f_i + 2843f_{i+1}^2 - 1642f_{i+2}f_{i+1} + 267f_{i+2}^2 \\ \beta_2 &= 267f_{i-2}^2 - 1642f_{i-1}f_{i-2} + 1602f_i f_{i-2} - 494f_{i+1}f_{i-2} + 2843f_{i-1}^2 - 5966f_i f_{i-1} \\ &+ 1922f_{i+1}f_{i-1} + 3443f_i^2 - 2522f_{i+1}f_i + 547f_{i+1}^2 \\ \beta_3 &= 547f_{i-3}^2 - 3882f_{i-2}f_{i-3} + 4642f_{i-1}f_{i-3} - 1854f_i f_{i-3} + 7043f_{i-2}^2 - 17246f_{i-1}f_{i-2} \\ &+ 7042f_i f_{i-2} + 11003f_{i-1}^2 - 9402f_i f_{i-1} + 2107f_i^2\end{aligned}$$

$k = 5$

There exist five stencils for reconstruction : $S_0 = (i, i + 1, i + 2, i + 3, i + 4)$ $S_1 = (i - 1, i, i + 1, i + 2, i + 3)$ $S_2 = (i - 2, i - 1, i, i + 1, i + 2)$ $S_3 = (i - 3, i - 2, i - 1, i, i + 1)$ $S_4 = (i - 4, i - 3, i - 2, i - 1, i)$.

$$\begin{aligned}\beta_0 &= 107918f_i^2 - 649501f_{i+1}f_i + 758823f_{i+2}f_i - 411487f_{i+3}f_i + 86329f_{i+4}f_i \\ &+ 1020563f_{i+1}^2 - 2462076f_{i+2}f_{i+1} + 1358458f_{i+3}f_{i+1} - 288007f_{i+4}f_{i+1} + 1521393f_{i+2}^2 \\ &- 1704396f_{i+3}f_{i+2} + 364863f_{i+4}f_{i+2} + 482963f_{i+3}^2 - 208501f_{i+4}f_{i+3} + 22658f_{i+4}^2 \\ \beta_1 &= 22658f_{i-1}^2 - 140251f_i f_{i-1} + 165153f_{i+1}f_{i-1} - 88297f_{i+2}f_{i-1} + 18079f_{i+3}f_{i-1} \\ &+ 242723f_i^2 - 611976f_{i+1}f_i + 337018f_{i+2}f_i - 70237f_{i+3}f_i + 406293f_{i+1}^2 \\ &- 464976f_{i+2}f_{i+1} + 99213f_{i+3}f_{i+1} + 138563f_{i+2}^2 - 60871f_{i+2}f_{i+3} + 6908f_{i+3}^2 \\ \beta_2 &= 6908f_{i-2}^2 - 51001f_{i-1}f_{i-2} + 67923f_i f_{i-2} - 38947f_{i+1}f_{i-2} + 8209f_{i+2}f_{i-2} \\ &+ 104963f_{i-1}^2 - 299076f_i f_{i-1} + 179098f_{i+1}f_{i-1} - 38947f_{i+2}f_{i-1} + 231153f_i^2 \\ &- 299076f_{i+1}f_i + 67923f_{i+2}f_i + 104963f_{i+1}^2 - 51001f_{i+2}f_{i+1} + 6908f_{i+2}^2\end{aligned}\tag{B.1}$$

$$\begin{aligned}
\beta_3 &= 6908f_{i-3}^2 - 60871f_{i-2}f_{i-3} + 99213f_{i-1}f_{i-3} - 70237f_i f_{i-3} + 18079f_{i+1}f_{i-3} \\
&+ 138563f_{i-2}^2 - 464976f_{i-1}f_{i-2} + 337018f_i f_{i-2} - 88297f_{i+1}f_{i-2} + 406293f_{i-1}^2 \\
&- 611976f_i f_{i-1} + 165153f_{i+1}f_{i-1} + 242723f_i^2 - 140251f_{i+1}f_i + 22658f_{i+1}^2 \\
\beta_4 &= 22658f_{i-4}^2 - 208501f_{i-3}f_{i-4} + 364863f_{i-2}f_{i-4} - 288007f_{i-1}f_{i-4} + 86329f_i f_{i-4} \\
&+ 482963f_{i-3}^2 - 1704396f_{i-2}f_{i-3} + 1358458f_{i-1}f_{i-3} - 411487f_i f_{i-3} + 1521393f_{i-2}^2 \\
&- 2462076f_{i-1}f_{i-2} + 758823f_i f_{i-2} + 1020563f_{i-1}^2 - 649501f_{i-1}f_i + 107918f_i^2
\end{aligned}$$

$k = 6$

There exist six stencils for reconstruction : $S_0 = (i, i + 1, i + 2, i + 3, i + 4, i + 5)$ $S_1 = (i - 1, i, i + 1, i + 2, i + 3, i + 4)$ $S_2 = (i - 2, i - 1, i, i + 1, i + 2, i + 3)$ $S_3 = (i - 3, i - 2, i - 1, i, i + 1, i + 2)$ $S_4 = (i - 5, i - 4, i - 3, i - 2, i - 1, i)$ $S_5 = (i - 4, i - 3, i - 2, i - 1, i)$.

$$\begin{aligned}
\beta_0 &= 6150211f_i^2 - 47460464f_{i+1}f_i + 76206736f_{i+2}f_i - 63394124f_{i+3}f_i + 27060170f_{i+4}f_i \\
&- 4712740f_{i+5}f_i + 94851237f_{i+1}^2 - 311771244f_{i+2}f_{i+1} + 262901672f_{i+3}f_{i+1} - 113206788f_{i+4}f_{i+1} \\
&+ 19834350f_{i+5}f_{i+1} + 260445372f_{i+2}^2 - 444003904f_{i+3}f_{i+2} + 192596472f_{i+4}f_{i+2} \\
&- 33918804f_{i+5}f_{i+2} + 190757572f_{i+3}^2 - 166461044f_{i+4}f_{i+3} + 29442256f_{i+5}f_{i+3} \\
&+ 36480687f_{i+4}^2 - 12950184f_{i+5}f_{i+4} + 1152561f_{i+5}^2 \\
\beta_1 &= 1152561f_{i-1}^2 - 9117992f_i f_{i-1} + 14742480f_{i+1}f_{i-1} - 12183636f_{i+2}f_{i-1} + 5134574f_{i+3}f_{i-1} \\
&- 880548f_{i+4}f_{i-1} + 19365967f_i^2 - 65224244f_{i+1}f_i + 55053752f_{i+2}f_i - 23510468f_{i+3}f_i \\
&+ 4067018f_{i+4}f_i + 56662212f_{i+1}^2 - 97838784f_{i+2}f_{i+1} + 42405032f_{i+3}f_{i+1} - 7408908f_{i+4}f_{i+1} \\
&+ 43093692f_{i+2}^2 - 37913324f_{i+3}f_{i+2} + 6694608f_{i+4}f_{i+2} + 8449957f_{i+3}^2 - 3015728f_{i+4}f_{i+3} \\
&+ 271779f_{i+4}^2 \\
\beta_2 &= 271779f_{i-2}^2 - 2380800f_{i-1}f_{i-2} + 4086352f_i f_{i-2} - 3462252f_{i+1}f_{i-2} + 1458762f_{i+2}f_{i-2} \\
&- 245620f_{i+3}f_{i-2} + 5653317f_{i-1}^2 - 20427884f_i f_{i-1} + 17905032f_{i+1}f_{i-1} - 7727988f_{i+2}f_{i-1} \\
&+ 1325006f_{i+3}f_{i-1} + 19510972f_i^2 - 35817664f_{i+1}f_i + 15929912f_{i+2}f_i - 2792660f_{i+3}f_i \\
&+ 17195652f_{i+1}^2 - 15880404f_{i+2}f_{i+1} + 2863984f_{i+3}f_{i+1} + 3824847f_{i+2}^2 - 1429976f_{i+3}f_{i+2} \\
&+ 139633f_{i+3}^2 \\
\beta_3 &= 139633f_{i-3}^2 - 1429976f_{i-2}f_{i-3} + 2863984f_{i-1}f_{i-3} - 2792660f_i f_{i-3} + 1325006f_{i+1}f_{i-3} \\
&- 245620f_{i+2}f_{i-3} + 3824847f_{i-2}^2 - 15880404f_{i-1}f_{i-2} + 15929912f_i f_{i-2} - 7727988f_{i+1}f_{i-2} \\
&+ 1458762f_{i+2}f_{i-2} + 17195652f_{i-1}^2 - 35817664f_i f_{i-1} + 17905032f_{i+1}f_{i-1} - 3462252f_{i+2}f_{i-1} \\
&+ 19510972f_i^2 - 20427884f_{i+1}f_i + 4086352f_{i+2}f_i + 5653317f_{i+1}^2 - 2380800f_{i+2}f_{i+1} \\
&+ 271779f_{i+2}^2 \\
\beta_4 &= 271779f_{i-4}^2 - 3015728f_{i-3}f_{i-4} + 6694608f_{i-2}f_{i-4} - 7408908f_{i-1}f_{i-4} + 4067018f_i f_{i-4} \\
&- 880548f_{i+1}f_{i-4} + 8449957f_{i-3}^2 - 37913324f_{i-2}f_{i-3} + 42405032f_{i-1}f_{i-3} - 23510468f_i f_{i-3} \\
&+ 5134574f_{i+1}f_{i-3} + 43093692f_{i-2}^2 - 97838784f_{i-1}f_{i-2} + 55053752f_i f_{i-2} - 12183636f_{i+1}f_{i-2} \\
&+ 56662212f_{i-1}^2 - 65224244f_i f_{i-1} + 14742480f_{i+1}f_{i-1} + 19365967f_i^2 - 9117992f_{i+1}f_i \\
&+ 1152561f_{i+1}^2 \\
\beta_5 &= 1152561f_{i-5}^2 - 12950184f_{i-4}f_{i-5} + 29442256f_{i-3}f_{i-5} - 33918804f_{i-2}f_{i-5} \\
&+ 19834350f_{i-1}f_{i-5} - 4712740f_i f_{i-5} + 36480687f_{i-4}^2 - 166461044f_{i-3}f_{i-4} \\
&+ 192596472f_{i-2}f_{i-4} - 113206788f_{i-1}f_{i-4} + 27060170f_i f_{i-4} + 190757572f_{i-3}^2 \\
&- 444003904f_{i-2}f_{i-3} + 262901672f_{i-1}f_{i-3} - 63394124f_i f_{i-3} + 260445372f_{i-2}^2 \\
&- 311771244f_{i-1}f_{i-2} + 76206736f_i f_{i-2} + 94851237f_{i-1}^2 - 47460464f_i f_i + 6150211f_i^2
\end{aligned}$$

B.2 Diagonalization of Jacobian Matrix

The diagonalization of the Jacobian matrix brings the hyperbolic part of N-S equations to the characteristic space. This process may i) decouple the N-S equations to a set of independent equations in characteristic space to use the scalar PDE numerical methods; ii) provide us the ability to analyze the numerical stability, like CFL conditions; iii) be used for boundary conditions.

For the diagonalization of N-S equations in the x direction, the vector form of N-S equations (2.19) can be written as

$$\frac{\partial \mathbf{U}}{\partial t} + \frac{\partial \mathbf{F}}{\partial x} = \mathbf{S}_x \quad (\text{B.2})$$

in which

$$\mathbf{S}_x \equiv \mathbf{V} + \mathbf{S} - \frac{\partial \mathbf{G}}{\partial y} - \frac{\partial \mathbf{H}}{\partial z}$$

with Jacobian matrix A defined as

$$A \equiv \frac{\partial \mathbf{F}}{\partial \mathbf{U}} \quad (\text{B.3})$$

An eigenvalue decomposition of the Jacobian matrix A is then performed. If we denote the left and right eigenvectors as L and R^1 , and the eigenvalues matrix as Λ , the decomposition of A is then

$$A = R\Lambda L \quad (\text{B.4})$$

Equation (B.2) is then

$$\frac{\partial \mathbf{U}}{\partial t} + R\Lambda L \frac{\partial \mathbf{U}}{\partial x} = \mathbf{S}_x$$

As $RL = LR = I$, if we multiply matrix L on both sides of this equation, we have

$$\frac{\partial \mathbf{W}}{\partial t} + \Lambda \frac{\partial \mathbf{W}}{\partial x} = L\mathbf{S}_x \quad (\text{B.5})$$

with the *characteristic variables* \mathbf{W}

$$d\mathbf{W} \equiv Ld\mathbf{U} \quad (\text{B.6})$$

The eigenvalue matrix Λ in (B.5) is a diagonal matrix composed by all the eigenvalues λ_i of A .

$$\Lambda \equiv \begin{pmatrix} \lambda_1 & & & & \\ & \lambda_2 & & & \\ & & \lambda_3 & & \\ & & & \ddots & \\ & & & & \lambda_{N_{sp}+5} \end{pmatrix} \quad (\text{B.7})$$

The N-S equations in characteristic space (B.5) can be written in the form of a set of independent scalar hyperbolic PDEs in *characteristic space*.

$$\left\{ \begin{array}{l} \frac{\partial w_1}{\partial t} + \lambda_1 \frac{\partial w_1}{\partial x} = (L\mathbf{S}_x)_1 \\ \frac{\partial w_2}{\partial t} + \lambda_2 \frac{\partial w_2}{\partial x} = (L\mathbf{S}_x)_2 \\ \vdots \\ \frac{\partial w_{N_{sp}+5}}{\partial t} + \lambda_{N_{sp}+5} \frac{\partial w_{N_{sp}+5}}{\partial x} = (L\mathbf{S}_x)_{N_{sp}+5} \end{array} \right.$$

The numerical methods for scalar PDEs then can be applied to this system.

¹In fact, L and R are matrix whose lines (resp. columns) are the left (resp. right) eigenvectors of A .

This strategy of direct diagonalization of the jacobian matrix in conservative form seems to be simple. But in practice, this procedure is not easy to achieve. The primitive variables can be used as a bridge for an easier calculation thanks to the chain rule. The primitive variables can be chosen as

$$\mathbf{V} \equiv \begin{bmatrix} \rho \\ u \\ v \\ w \\ T \\ Y_1 \\ \vdots \\ Y_{N_{sp}} \end{bmatrix} \quad (\text{B.8})$$

The hyperbolic part of N-S equations using this set of variables reads

$$\left\{ \begin{array}{l} \frac{\partial \rho}{\partial t} + u_j \frac{\partial \rho}{\partial x_j} + \rho \frac{\partial u_j}{\partial x_j} = 0 \\ \frac{\partial u_i}{\partial t} + \frac{rT}{\rho} \frac{\partial \rho}{\partial x_i} + u_j \frac{\partial u_i}{\partial x_j} + r \frac{\partial T}{\partial x_i} + T \sum_{\alpha=1}^{N_{sp}} r_\alpha \frac{\partial Y_\alpha}{\partial x_i} = 0 \\ \frac{\partial T}{\partial t} + u_j \frac{\partial T}{\partial x_j} + (\gamma - 1) T \frac{\partial u_j}{\partial x_j} = 0 \\ \frac{\partial Y_\alpha}{\partial t} + u_j \frac{\partial Y_\alpha}{\partial x_j} = 0 \end{array} \right. \quad \text{for } \alpha = 1, \dots, N_{sp} \quad (\text{B.9})$$

In vector form, the N-S equations with primitive variables read

$$\frac{\partial \mathbf{V}}{\partial t} + \tilde{A} \frac{\partial \mathbf{V}}{\partial x} = \tilde{\mathbf{S}}_x \quad (\text{B.10})$$

with the matrix \tilde{A} in primitive form obtained straightforwardly from equation (B.9):

$$\tilde{A} = \begin{pmatrix} u & \rho & 0 & 0 & 0 & 0 & \dots & 0 \\ \frac{rT}{\rho} & u & 0 & 0 & r & (r_1 - r)T & \dots & (r_{N_{sp}} - r)T \\ 0 & 0 & u & 0 & 0 & 0 & \dots & 0 \\ 0 & 0 & 0 & u & 0 & 0 & \dots & 0 \\ 0 & (\gamma - 1)T & 0 & 0 & u & 0 & \dots & 0 \\ 0 & 0 & 0 & 0 & 0 & u & \dots(0) & 0 \\ \vdots & \vdots & \vdots & \vdots & \vdots & \vdots(0) & \ddots(u) & \vdots \\ 0 & 0 & 0 & 0 & 0 & 0 & \dots & u \end{pmatrix} \quad (\text{B.11})$$

The diagonalization can be done on this matrix as

$$\tilde{A} = \tilde{R} \Lambda \tilde{L} \quad (\text{B.12})$$

with the help of the software MAXIMA. The passage matrix M between conservative and primitive variables is defined as

$$\begin{aligned} d\mathbf{U} &\equiv M d\mathbf{V} \\ d\mathbf{V} &\equiv M^{-1} d\mathbf{U} \end{aligned} \quad (\text{B.13})$$

This passage matrix M is the connection between the primitive form (B.10) and the conservative form (B.2):

$$\begin{aligned} \tilde{A} &= M^{-1} A M & A &= M \tilde{A} M^{-1} \\ \tilde{L} &= L M & L &= \tilde{L} M^{-1} \\ \tilde{R} &= M^{-1} R & R &= M \tilde{R} \\ \mathbf{S}_x &= M \tilde{\mathbf{S}}_x & \tilde{\mathbf{S}}_x &= M^{-1} \mathbf{S}_x \end{aligned} \quad (\text{B.14})$$

For multi-species N-S equations, the passage matrix is

$$M \equiv \frac{\partial \mathbf{U}}{\partial \mathbf{V}} = \begin{pmatrix} 1 & 0 & 0 & 0 & 0 & 0 & \dots & 0 \\ u & \rho & 0 & 0 & 0 & 0 & \dots & 0 \\ v & 0 & \rho & 0 & 0 & 0 & \dots & 0 \\ w & 0 & 0 & \rho & 0 & 0 & \dots & 0 \\ (e + \kappa) & \rho u & \rho v & \rho w & \rho C_v & \rho(e_1 - e) & \dots & \rho(e_{N_{sp}} - e) \\ Y_1 & 0 & 0 & 0 & 0 & \rho & \dots(0) & 0 \\ \vdots & 0 & 0 & 0 & 0 & \vdots(0) & \ddots(\rho) & 0 \\ Y_{N_{sp}} & 0 & 0 & 0 & 0 & 0 & \dots & \rho \end{pmatrix} \quad (\text{B.15})$$

in which κ is the kinetic energy

$$\kappa \equiv \frac{u^2 + v^2 + w^2}{2}$$

and e_α is the internal energy of species α

$$e_\alpha \equiv h_\alpha - r_\alpha T = \Delta h_\alpha^0 + \int_{T_0}^T C_{p\alpha}(\theta) d\theta - r_\alpha T$$

and

$$e = \sum_{\alpha=1}^{N_{sp}} e_\alpha Y_\alpha$$

The inverse passage matrix is

$$M^{-1} \equiv \frac{\partial \mathbf{V}}{\partial \mathbf{U}} = \frac{1}{\rho} \begin{pmatrix} \rho & 0 & 0 & 0 & 0 & 0 & \dots & 0 \\ -u & 1 & 0 & 0 & 0 & 0 & \dots & 0 \\ -v & 0 & 1 & 0 & 0 & 0 & \dots & 0 \\ -w & 0 & 0 & 1 & 0 & 0 & \dots & 0 \\ (\kappa - e)/C_v & -u/C_v & -v/C_v & -w/C_v & 1/C_v & -(e_1 - e)/C_v & \dots & -(e_{N_{sp}} - e)/C_v \\ -Y_1 & 0 & 0 & 0 & 0 & 1 & \dots(0) & 0 \\ \vdots & 0 & 0 & 0 & 0 & \vdots(0) & \ddots(1) & 0 \\ -Y_{N_{sp}} & 0 & 0 & 0 & 0 & 0 & \dots & 1 \end{pmatrix} \quad (\text{B.16})$$

The eigenvalue matrix Λ is

$$\Lambda = \begin{pmatrix} u - c & & & & & & & \\ & u & & & & & & \\ & & u & & & & & \\ & & & u & & & & \\ & & & & u + c & & & \\ & & & & & u & & \\ & & & & & & \ddots & \\ & & & & & & & u \end{pmatrix} \quad (\text{B.17})$$

where

$$c \equiv \sqrt{\gamma r T}$$

is the local speed of sound. One should notice that as multiple eigenvalues can be found in matrix (B.17), the left and right eigenvector matrix is not unique. Normally, we choose the form the least expensive to compute (like having more terms in common). We tested different forms of these matrix with classical 1D and 2D test cases and very little difference can be spotted. Both the primitive and conservative left and right eigenvector matrix used in our simulations can be found in (B.18) to

(B.21):

$$\tilde{R} = \begin{pmatrix} 1 & 1 & 0 & 0 & 1 & 0 & \cdots & 0 \\ -\frac{c}{\rho} & 0 & 0 & 0 & \frac{c}{\rho} & 0 & \cdots & 0 \\ 0 & 0 & 1 & 0 & 0 & 0 & \cdots & 0 \\ 0 & 0 & 0 & 1 & 0 & 0 & \cdots & 0 \\ \frac{(\gamma-1)T}{\rho} & -\frac{T}{\rho} & 0 & 0 & \frac{(\gamma-1)T}{\rho} & \frac{(r-r_1)T}{r} & \cdots & \frac{(r-r_{N_{sp}})T}{r} \\ 0 & 0 & 0 & 0 & 0 & 1 & \cdots(0) & 0 \\ \vdots & \vdots & \vdots & \vdots & \vdots & \vdots(0) & \ddots(1) & \vdots \\ 0 & 0 & 0 & 0 & 0 & 0 & 0 & 1 \end{pmatrix} \quad (\text{B.18})$$

$$\tilde{L} = \tilde{R}^{-1} = \begin{pmatrix} \frac{1}{2\gamma} & -\frac{\rho}{2c} & 0 & 0 & \frac{\rho}{2\gamma T} & -\frac{(r-r_1)\rho}{2\gamma r} & \cdots & -\frac{(r-r_{N_{sp}})\rho}{2\gamma r} \\ \frac{\gamma-1}{\gamma} & 0 & 0 & 0 & -\frac{\rho}{\gamma T} & \frac{(r-r_1)\rho}{\gamma r} & \cdots & \frac{(r-r_{N_{sp}})\rho}{\gamma r} \\ 0 & 0 & 1 & 0 & 0 & 0 & \cdots & 0 \\ 0 & 0 & 0 & 1 & 0 & 0 & \cdots & 0 \\ \frac{1}{2\gamma} & \frac{\rho}{2c} & 0 & 0 & \frac{\rho}{2\gamma T} & -\frac{(r-r_1)\rho}{2\gamma r} & \cdots & -\frac{(r-r_{N_{sp}})\rho}{2\gamma r} \\ 0 & 0 & 0 & 0 & 0 & 1 & \cdots(0) & 0 \\ \vdots & \vdots & \vdots & \vdots & \vdots & \vdots(0) & \ddots(1) & \vdots \\ 0 & 0 & 0 & 0 & 0 & 0 & \cdots & 1 \end{pmatrix} \quad (\text{B.19})$$

$$R = \begin{pmatrix} 1 & 1 & 0 & 0 & 1 & 0 & 0 & 0 \\ u-c & u & 0 & 0 & u+c & 0 & 0 & 0 \\ v & v & \rho & 0 & v & 0 & 0 & 0 \\ w & w & 0 & \rho & w & 0 & 0 & 0 \\ \kappa+h-cu & \kappa+h-C_vT & \rho v & \rho w & \kappa+h+cu & R_{51} & \cdots & R_{5N_{sp}} \\ Y_1 & Y_1 & 0 & 0 & Y_1 & \rho & \cdots(0) & 0 \\ \vdots & \vdots & \vdots & \vdots & \vdots & \vdots(0) & \ddots(\rho) & \vdots \\ Y_{N_{sp}} & Y_{N_{sp}} & 0 & 0 & Y_{N_{sp}} & 0 & \cdots & \rho \end{pmatrix} \quad (\text{B.20})$$

with

$$R_{5\alpha} = \rho \left[(e_\alpha - e) - C_v T \left(\frac{r_\alpha - r}{r} \right) \right]$$

$$L = \begin{pmatrix} \frac{cu+(\gamma-1)\kappa+(1-\gamma)h+c^2}{2c^2} & -\frac{(\gamma-1)u+c}{2c^2} & -\frac{(\gamma-1)v}{2c^2} & -\frac{(\gamma-1)w}{2c^2} & \frac{\gamma-1}{2c^2} & L_{11} & \cdots & L_{1N_{sp}} \\ -\frac{(\gamma-1)\kappa+(1-\gamma)h}{c^2} & \frac{(\gamma-1)u}{c^2} & \frac{(\gamma-1)v}{c^2} & \frac{(\gamma-1)w}{c^2} & -\frac{\gamma-1}{c^2} & -2L_{11} & \cdots & -2L_{1N_{sp}} \\ -v/\rho & 0 & 1/\rho & 0 & 0 & 0 & \cdots & 0 \\ -w/\rho & 0 & 0 & 1/\rho & 0 & 0 & \cdots & 0 \\ -\frac{cu+(1-\gamma)\kappa+(\gamma-1)h-c^2}{2c^2} & -\frac{(\gamma-1)u-c}{2c^2} & -\frac{(\gamma-1)v}{2c^2} & -\frac{(\gamma-1)w}{2c^2} & \frac{\gamma-1}{2c^2} & L_{11} & \cdots & L_{1N_{sp}} \\ -Y_1/\rho & 0 & 0 & 0 & 0 & \frac{1}{\rho} & \cdots(0) & 0 \\ \vdots & \vdots & \vdots & \vdots & \vdots & \vdots(0) & \ddots(\frac{1}{\rho}) & \vdots \\ -Y_{N_{sp}}/\rho & 0 & 0 & 0 & 0 & 0 & 0 & \frac{1}{\rho} \end{pmatrix} \quad (\text{B.21})$$

with

$$L_{1\alpha} = \frac{1}{2c^2} [(\gamma-1)(e - e_\alpha) - (r - r_\alpha)T]$$

The Jacobian matrix A in conservative form can be calculated by equation (B.4):

$$A = \begin{pmatrix} 0 & 1 & 0 & 0 & 0 & 0 & 0 & 0 \\ -u^2 + (\gamma-1)(\kappa-h) + c^2 & (3-\gamma)u & (1-\gamma)v & (1-\gamma)w & \gamma-1 & A_{21} & \cdots & A_{2N_{sp}} \\ -uv & v & u & 0 & 0 & 0 & \cdots & 0 \\ -uw & w & 0 & u & 0 & 0 & \cdots & 0 \\ ((\gamma-2)\kappa - \gamma h + c^2)u & (1-\gamma)u^2 + \kappa + h & (1-\gamma)uv & (1-\gamma)uw & \gamma u & A_{51} & \cdots & A_{5N_{sp}} \\ -Y_1 u & Y_1 & 0 & 0 & 0 & u & \cdots(0) & 0 \\ \vdots & \vdots & \vdots & \vdots & \vdots & \vdots(0) & \ddots(u) & 0 \\ -Y_{N_{sp}} u & Y_{N_{sp}} & 0 & 0 & 0 & 0 & \cdots & u \end{pmatrix} \quad (\text{B.22})$$

with

$$A_{2\alpha} = (h_\alpha - h) - \gamma(e_\alpha - e)$$
$$A_{5\alpha} = uA_{2\alpha}$$

$$L = \begin{pmatrix} \frac{\alpha c u + (\gamma-1)\alpha^2 \kappa + (1-\gamma)\alpha^2 h + \alpha^2 c^2}{2c^2} & -\frac{(\gamma-1)\alpha^2 u + \alpha c}{2c^2} & -\frac{(\gamma-1)\alpha^2 v}{2c^2} & -\frac{(\gamma-1)\alpha^2 w}{2c^2} & \frac{(\gamma-1)\alpha^2}{2c^2} & L_{11} & \cdots & L_{1N_{sp}} \\ -\frac{(\gamma-1)\alpha^2 \kappa + (1-\gamma)\alpha^2 h + (\alpha^2-1)c^2}{c^2} & \frac{(\gamma-1)\alpha^2 u}{c^2} & \frac{(\gamma-1)\alpha^2 v}{c^2} & \frac{(\gamma-1)\alpha^2 w}{c^2} & -\frac{(\gamma-1)\alpha^2}{c^2} & -2L_{11} & \cdots & -2L_{1N_{sp}} \\ -\frac{v}{\rho} & 0 & \frac{1}{\rho} & 0 & 0 & 0 & \cdots & 0 \\ -\frac{w}{\rho} & 0 & 0 & \frac{1}{\rho} & 0 & 0 & \cdots & 0 \\ -\frac{\alpha c u + (1-\gamma)\alpha^2 \kappa + (\gamma-1)\alpha^2 h - \alpha^2 c^2}{2c^2} & -\frac{(\gamma-1)\alpha^2 u - \alpha c}{2c^2} & -\frac{(\gamma-1)\alpha^2 v}{2c^2} & -\frac{(\gamma-1)\alpha^2 w}{2c^2} & \frac{(\gamma-1)\alpha^2}{2c^2} & L_{11} & \cdots & L_{1N_{sp}} \\ -\frac{1}{\rho} & 0 & 0 & 0 & 0 & \frac{1}{\rho} & \cdots (0) & 0 \\ \vdots & \vdots & \vdots & \vdots & \vdots & 0 & \ddots & \vdots \\ -\frac{Y_{N_{sp}}}{\rho} & 0 & 0 & 0 & 0 & 0 & \cdots & \frac{1}{\rho} \end{pmatrix} \quad (\text{B.23})$$

with

$$\begin{aligned} \kappa &\equiv \frac{u^2 + v^2 + w^2}{2} \\ L_{1k} &= \frac{\gamma r_k \alpha^2 T + (\gamma-1)\alpha^2 h - \alpha^2 c^2 + (1-\gamma)h_k \alpha^2}{2c^2} \\ R &= \begin{pmatrix} 1 & 1 & 0 & 0 & 1 & 0 & \cdots & 0 \\ u - \frac{c}{\alpha} & u & 0 & 0 & u + \frac{c}{\alpha} & 0 & \cdots & 0 \\ v & v & \rho & 0 & v & 0 & \cdots & 0 \\ w & w & 0 & \rho & w & 0 & \cdots & 0 \\ \kappa + h - u\frac{c}{\alpha} + \frac{(1-\alpha^2)c^2}{(\gamma-1)\alpha^2} & \kappa + h - \frac{c^2}{\gamma-1} & \rho v & \rho w & \kappa + h + u\frac{c}{\alpha} + \frac{(1-\alpha^2)c^2}{(\gamma-1)\alpha^2} & R_{51} & \cdots & R_{5N_{sp}} \\ Y_1 & Y_1 & 0 & 0 & Y_1 & \rho & \cdots (0) & 0 \\ \vdots & \vdots & 0 & 0 & \vdots & \vdots (0) & \ddots & \vdots \\ Y_{N_{sp}} & Y_{N_{sp}} & 0 & 0 & Y_{N_{sp}} & 0 & \cdots & \rho \end{pmatrix} \quad (\text{B.24}) \end{aligned}$$

with

$$R_{5k} \equiv -\frac{\gamma r_k \rho T + ((\gamma-1)h - c^2 + (1-\gamma)h_k)\rho}{\gamma-1}$$

$$A = \begin{pmatrix} 0 & 1 & 0 & 0 & 0 & 0 & \cdots & 0 \\ -u^2 + (\gamma - 1)\kappa + (1 - \gamma)h + c^2 & (3 - \gamma)u & (1 - \gamma)v & (1 - \gamma)w & \gamma - 1 & A_{21} & \cdots & A_{2N_{\text{sp}}} \\ -uw & v & u & 0 & 0 & 0 & \cdots & 0 \\ -uw & w & 0 & u & 0 & 0 & \cdots & 0 \\ (\gamma - 2)\kappa u - \gamma hu + \frac{(\gamma\alpha^2 - 1)c^2 u}{(\gamma - 1)\alpha^2} & (1 - \gamma)u^2 + \kappa + h - \frac{(\alpha^2 - 1)c^2}{(\gamma - 1)\alpha^2} & (1 - \gamma)uv & (1 - \gamma)uw & \gamma u & uA_{21} & \cdots & uA_{2N_{\text{sp}}} \\ -Y_1 u & Y_1 & 0 & 0 & 0 & u & \cdots (0) & 0 \\ \vdots & \vdots & \vdots & \vdots & \vdots & \vdots (0) & \ddots & \vdots \\ -Y_{N_{\text{sp}}} u & Y_{N_{\text{sp}}} & 0 & 0 & 0 & 0 & 0 & u \end{pmatrix} \quad (\text{B.25})$$

with

$$A_{2k} = \gamma r_k T + (\gamma - 1)h - c^2 + (1 - \gamma)h_k$$

$$h_{i+1/2}^{5\text{-up-}} = \frac{1}{60} \left(2 \left(\frac{1}{2} (L_{i+1/2} \mathbf{F}_{i-2} + \begin{pmatrix} 0 \\ 0 \\ 0 \\ 0 \\ -\left(1 - \frac{1}{\alpha^2}\right) \frac{\gamma_i p_i}{\gamma_i - 1} u_{i-2} \\ \vdots \\ 0 \end{pmatrix} + \bar{\Lambda} L_{i+1/2} \mathbf{U}_{i-2} \right) - 13 \left(\frac{1}{2} (L_{i+1/2} \mathbf{F}_{i-1} + \begin{pmatrix} 0 \\ 0 \\ 0 \\ 0 \\ -\left(1 - \frac{1}{\alpha^2}\right) \frac{\gamma_i p_i}{\gamma_i - 1} u_{i-1} \\ \vdots \\ 0 \end{pmatrix} + \bar{\Lambda} L_{i+1/2} \mathbf{U}_{i-1} \right) \right. \\ \left. + 47 \left(\frac{1}{2} (L_{i+1/2} \mathbf{F}_i + \begin{pmatrix} 0 \\ 0 \\ 0 \\ 0 \\ -\left(1 - \frac{1}{\alpha^2}\right) \frac{\gamma_i p_i}{\gamma_i - 1} u_i \\ \vdots \\ 0 \end{pmatrix} + \bar{\Lambda} L_{i+1/2} \mathbf{U}_i \right) + 27 \left(\frac{1}{2} (L_{i+1/2} \mathbf{F}_{i+1} + \begin{pmatrix} 0 \\ 0 \\ 0 \\ 0 \\ -\left(1 - \frac{1}{\alpha^2}\right) \frac{\gamma_i p_i}{\gamma_i - 1} u_{i+1} \\ \vdots \\ 0 \end{pmatrix} + \bar{\Lambda} L_{i+1/2} \mathbf{U}_{i+1} \right) \right. \\ \left. - 3 \left(\frac{1}{2} (L_{i+1/2} \mathbf{F}_{i+2} + \begin{pmatrix} 0 \\ 0 \\ 0 \\ 0 \\ -\left(1 - \frac{1}{\alpha^2}\right) \frac{\gamma_i p_i}{\gamma_i - 1} u_{i+2} \\ \vdots \\ 0 \end{pmatrix} + \bar{\Lambda} L_{i+1/2} \mathbf{U}_{i+2} \right) \right) \quad (\text{B.26})$$

B.3 MAXIMA code for diagonalization and NSCBC

(%i1) kill(all)

$$(\%i1) \text{ At : } \begin{pmatrix} u & \rho & 0 & 0 & 0 & 0 & 0 & 0 \\ \frac{rT}{\rho} & u & 0 & 0 & r & (r_1 - r)T & (r_2 - r)T & (r_3 - r)T \\ 0 & 0 & u & 0 & 0 & 0 & 0 & 0 \\ 0 & 0 & 0 & u & 0 & 0 & 0 & 0 \\ 0 & (\gamma/\alpha - 1)T & 0 & 0 & u & 0 & 0 & 0 \\ 0 & 0 & 0 & 0 & 0 & u & 0 & 0 \\ 0 & 0 & 0 & 0 & 0 & 0 & u & 0 \\ 0 & 0 & 0 & 0 & 0 & 0 & 0 & u \end{pmatrix}$$

(%i2) load("eigen")\$ assume($p > 0, \rho > 0, \gamma > 0, r > 0, T > 0, \alpha > 0, c > 0, r_1 > 0, r_2 > 0, r_3 > 0$)

(%i4) [val, vecs] : eigenvectors(At)

(%i5) (vect : $\frac{r-r_3}{r}T$ vecs[3][4], Rt : transpose(matrix(vecs[1][1], vecs[3][1] - $\frac{r}{(r-r_3)\rho}$ vect, vecs[3][2], vecs[3][3], vecs[2][1], vecs[3][5] + $\frac{r-r_1}{r-r_3}$ vect, vecs[3][6] + $\frac{r-r_2}{r-r_3}$ vect, vect)))

(%i6) Lt : ev(invert(Rt), fullratsimp)

$$(\%i7) \Lambda : \begin{pmatrix} u - \sqrt{r}\sqrt{\gamma}\sqrt{T}/\alpha & 0 & 0 & 0 & 0 & 0 & 0 & 0 \\ 0 & u & 0 & 0 & 0 & 0 & 0 & 0 \\ 0 & 0 & u & 0 & 0 & 0 & 0 & 0 \\ 0 & 0 & 0 & u & 0 & 0 & 0 & 0 \\ 0 & 0 & 0 & 0 & u + \sqrt{r\gamma T}/\alpha & 0 & 0 & 0 \\ 0 & 0 & 0 & 0 & 0 & u & 0 & 0 \\ 0 & 0 & 0 & 0 & 0 & 0 & u & 0 \\ 0 & 0 & 0 & 0 & 0 & 0 & 0 & u \end{pmatrix}$$

$$(\%i8) M : \begin{pmatrix} 1 & 0 & 0 & 0 & 0 & 0 & 0 & 0 \\ u & \rho & 0 & 0 & 0 & 0 & 0 & 0 \\ v & 0 & \rho & 0 & 0 & 0 & 0 & 0 \\ w & 0 & 0 & \rho & 0 & 0 & 0 & 0 \\ \left(h - rT + \frac{u^2 + v^2 + w^2}{2}\right) & \rho u & \rho v & \rho w & \rho C_p - \rho r & \rho(h_1 - r_1 T - h + rT) & \rho(h_2 - r_2 T - h + rT) & \rho(h_3 - r_3 T - h + rT) \\ Y_1 & 0 & 0 & 0 & 0 & \rho & 0 & 0 \\ Y_2 & 0 & 0 & 0 & 0 & 0 & \rho & 0 \\ Y_3 & 0 & 0 & 0 & 0 & 0 & 0 & \rho \end{pmatrix}$$

(%i9) (R : ev(M, Rt, fullratsimp))

(%i10) $L : \text{ev}(\text{Lt.invert}(M), \text{fullratsimp})$

(%i11) $(A : \text{ev}(M, \text{At.invert}(M), \text{fullratsimp}))$

$$(\%i12) \quad U : \left(\begin{array}{c} \rho \\ \rho u \\ \rho v \\ \rho w \\ \rho \left(h - rT + \frac{u^2 + v^2 + w^2}{2} \right) \\ \rho Y_1 \\ \rho Y_2 \\ \rho Y_3 \end{array} \right), \text{Fp} : \text{ev}(A.U, \text{fullratsimp})$$

(%i13) $(L : \text{Lt.invert}(M), L : \text{ratsubst}(-2r, -2r_3Y_3 - 2r_2Y_2 - 2r_1Y_1, L), L : \text{ratsubst}(2h, 2h_3Y_3 + 2h_2Y_2 + 2h_1Y_1, L),$

$L : \text{ratsubst}\left(\frac{\gamma r}{\gamma - 1}, C_p, L\right), L : \text{ev}(L, \text{fullexapnd}), L : \text{ratsubst}\left(c, \sqrt{\gamma}\sqrt{r}\sqrt{T}, L\right), L : \text{ratsubst}(c^2, \gamma rT, L),$

$L : \text{ratsubst}(2\kappa - u^2 - w^2, v^2, L), L : \text{ratsubst}(Y_3, 1 - Y_2 - Y_1, L), L : \text{ratsubst}(Y_3, 1 - Y_2 - Y_1, L), L : \text{ev}(L, \text{radcan}, \text{fullratsimp}))$

(%i14) $A : \text{ev}(M, \text{At.invert}(M), \text{fullratsimp})$

(%i15) $(A : \text{ratsubst}(-2r, -2r_3Y_3 - 2r_2Y_2 - 2r_1Y_1, A), A : \text{ratsubst}(2h, 2h_3Y_3 + 2h_2Y_2 + 2h_1Y_1, A),$

$A : \text{ratsubst}\left(\frac{\gamma r}{\gamma - 1}, C_p, A\right), A : \text{ev}(A, \text{fullexapnd}), A : \text{ratsubst}\left(c, \sqrt{\gamma}\sqrt{r}\sqrt{T}, A\right), A : \text{ratsubst}(c^2, \gamma rT, A),$

$A : \text{ratsubst}(2\kappa - u^2 - w^2, v^2, A), A : \text{ratsubst}(Y_1, 1 - Y_2 - Y_3, A), A : \text{ratsubst}(Y_1, 1 - Y_2 - Y_3, A), A : \text{ev}(A, \text{radcan}, \text{fullratsimp}))$

(%i16) $(R : \text{ev}(M, \text{Rt}, \text{fullratsimp}), R : \text{ratsubst}\left(\frac{\gamma r}{\gamma - 1}, C_p, R\right), R : \text{ev}(R, \text{fullexapnd}), R : \text{ratsubst}\left(c, \sqrt{\gamma}\sqrt{r}\sqrt{T}, R\right),$

$R : \text{ratsubst}(c^2, \gamma rT, R), R : \text{ratsubst}(2\kappa - u^2 - w^2, v^2, R), R : \text{ev}(R, \text{radcan}, \text{fullratsimp}))$

(%i17) $(\text{Fp} : \text{ev}(A.U, \text{fullratsimp}), \text{Fp} : \text{ratsubst}(-2r, -2r_3Y_3 - 2r_2Y_2 - 2r_1Y_1, \text{Fp}),$

$\text{Fp} : \text{ratsubst}(2h, 2h_3Y_3 + 2h_2Y_2 + 2h_1Y_1, \text{Fp}), \text{Fp} : \text{ratsubst}(Y_1, 1 - Y_2 - Y_3, \text{Fp}), \text{Fp} : \text{ratsubst}(Y_1, 1 - Y_2 - Y_3, \text{Fp}),$

$\text{Fp} : \text{ratsubst}\left(\frac{u^2 + v^2 + w^2}{2}, \kappa, \text{Fp}\right))$

(%i18) $R1 : \text{ev}(\text{ratsubst}(1, \alpha, R), \text{fullratsimp})$

(%i19) $L1 : \text{ev}(\text{ratsubst}(1, \alpha, L), \text{fullratsimp})$

(%i20) $A1 : \text{ev}(\text{ratsubst}(1, \alpha, A), \text{fullratsimp})$

(%i21) $L1.A1.R1, \text{fullratsimp}$

$$(\%i22) \quad \left(\text{Lc} : \begin{pmatrix} \text{Lc } 1 \\ \text{Lc } 2 \\ \text{Lc } 3 \\ \text{Lc } 4 \\ \text{Lc } 5 \\ \text{Lc } 6 \\ \text{Lc } 7 \\ \text{Lc } 8 \end{pmatrix}, \text{Sc} : \begin{pmatrix} \text{Sc } 1 \\ \text{Sc } 2 \\ \text{Sc } 3 \\ \text{Sc } 4 \\ \text{Sc } 5 \\ \text{Sc } 6 \\ \text{Sc } 7 \\ \text{Sc } 8 \end{pmatrix} \right)$$

(%i23) $(\text{Rt} : \text{ratsubst}(c, \sqrt{\gamma}\sqrt{r}\sqrt{T}, \text{Rt}), d : \text{Rt} . \text{Lc})$

(%i24) $\text{LODITconst} : \text{algsys}(\text{append}(d[5], d[2] + \text{dudt}, d[3] + \text{dvdt}, d[4] + \text{dwdt}, d[6], d[7], d[8]), [\text{Lc } 1, \text{Lc } 2, \text{Lc } 3, \text{Lc } 4, \text{Lc } 5, \text{Lc } 6, \text{Lc } 7, \text{Lc } 8])$

(%i25) $\text{LODITconst} : \text{subst}(\text{Lc } 1, \text{last}(\% \text{rnum_list}), \text{LODITconst}[1])$

(%i26) $\text{LODIRhconst} : \text{algsys}(\text{append}(d[1], d[2] + \text{dudt}, d[3] + \text{dvdt}, d[4] + \text{dwdt}, d[6], d[7], d[8]), [\text{Lc } 1, \text{Lc } 2, \text{Lc } 3, \text{Lc } 4, \text{Lc } 5, \text{Lc } 6, \text{Lc } 7, \text{Lc } 8])$

(%i27) $\text{LODIRhconst} : \text{subst}(\text{Lc } 1, \text{last}(\% \text{rnum_list}), \text{LODIRhconst}[1])$

(%i28) $\text{NSCBCRhoconst} : \text{algsys}(\text{append}(d[1] - \text{Sc } 1, d[2] + \text{dudt} - \text{Sc } 2, d[3] + \text{dvdt} - \text{Sc } 3, d[4] + \text{dwdt} - \text{Sc } 4, d[6] - \text{Sc } 6, d[7] - \text{Sc } 7, d[8] - \text{Sc } 8), [\text{Lc } 1, \text{Lc } 2, \text{Lc } 3, \text{Lc } 4, \text{Lc } 5, \text{Lc } 6, \text{Lc } 7, \text{Lc } 8])$

(%i29) $\text{NSCBCRhoconst} : \text{subst}(\text{Lc } 1, \text{last}(\% \text{rnum_list}), \text{NSCBCRhoconst}[1])$

(%i30) $\text{NSCBCTwall} : \text{algsys}(\text{append}(d[2] - \text{Sc } 2, d[3] - \text{Sc } 3, d[4] - \text{Sc } 4, d[5] - \text{Sc } 5), [\text{Lc } 1, \text{Lc } 6, \text{Lc } 7, \text{Lc } 8, \text{Lc } 2, \text{Lc } 3, \text{Lc } 4, \text{Lc } 5])$

(%i31) $(\text{NSCBCTwall} : (\text{subst}(\text{Lc } 8, \text{last}(\% \text{rnum_list}), \text{NSCBCTwall}[1])), \text{NSCBCTwall} : \text{subst}(\text{Lc } 7, \% \text{rnum_list}[3], \text{NSCBCTwall}), \text{NSCBCTwall} : \text{subst}(\text{Lc } 6, \% \text{rnum_list}[2], \text{NSCBCTwall}), \text{NSCBCTwall} : \text{subst}(\text{Lc } 1, \% \text{rnum_list}[1], \text{NSCBCTwall})), \text{expand}$

(%i32) $\text{Lc } 2 = -\frac{\rho \text{Sc } 5}{T} + \frac{\alpha \rho \text{Sc } 2}{c} - \frac{\gamma \rho \text{Sc } 2}{\alpha c} - \frac{r_3 \text{Lc } 8 \rho}{r} - \frac{r_2 \text{Lc } 7 \rho}{r} - \frac{r_1 \text{Lc } 6 \rho}{r} + \text{Lc } 8 \rho + \text{Lc } 7 \rho + \text{Lc } 6 \rho + \frac{2r_1 \text{Lc } 5}{\alpha^2} - 2\text{Lc } 5$

(%i33) $\text{NSCBCTconst} : \text{algsys}(\text{append}(d[5] - \text{Sc } 5, d[2] + \text{dudt} - \text{Sc } 2, d[3] + \text{dvdt} - \text{Sc } 3, d[4] + \text{dwdt} - \text{Sc } 4, d[6] - \text{Sc } 6, d[7] - \text{Sc } 7, d[8] - \text{Sc } 8), [\text{Lc } 1, \text{Lc } 2, \text{Lc } 3, \text{Lc } 4, \text{Lc } 5, \text{Lc } 6, \text{Lc } 7, \text{Lc } 8])$

(%i34) $\text{NSCBCTconst} : \text{subst}(\text{Lc } 1, \text{last}(\% \text{rnum_list}), \text{NSCBCTconst}[1]), \text{expand}$

(%i35) $(\text{Mm } 1 : \text{ratsubst}(-2r, -2r_3 Y_3 - 2r_2 Y_2 - 2r_1 Y_1, \text{Mm } 1), \text{Mm } 1 : \text{ratsubst}(2h, 2h_3 Y_3 + 2h_2 Y_2 + 2h_1 Y_1, \text{Mm } 1),$

$\text{Mm } 1 : \text{ratsubst}(2\kappa - u^2 - w^2, v^2, \text{Mm } 1), \text{Mm } 1 : \text{ratsubst}(Y_1, 1 - Y_2 - Y_3, \text{Mm } 1),$

$\text{Mm } 1 : \text{ratsubst}(Y_1, 1 - Y_2 - Y_3, \text{Mm } 1), \text{Mm } 1 : \text{ev}(\text{Mm } 1, \text{radcan}, \text{fullratsimp}))$

(%i36) M

(%i37) $\text{ratsubst}(1, \alpha, d), \text{fullratsimp}$

B.4 Computational cost for Taylor-Green and Double-Mach test cases

Table B.3: Computational cost of the Taylor-Green vortex flow for different WENO schemes on a $128 \times 128 \times 128$ grid, 16 Intel[®] Xeon[®] E5430 4-cores@2.66GHZ (64 cores).

	JS	OP	M	Z	MZ	JS7
Time steps	8415	8450	8431	8429	8438	8428
CPU/step/node ($\times 10^{-5}$ s)	5.406	1.118	5.329	5.426	5.481	5.506
CPU/step/node ratio	1	0.216	0.986	1.004	1.014	1.018
Wall-time (s)	14904	3260	14722	14982	15152	15206
Wall-time ratio	1	0.218	0.988	1.005	1.017	1.020

Table B.4: Computational cost of the double Mach reflection for different WENO schemes on the 300×1200 grid, 4 Intel[®] Sandy Bridge[®] E5-4650 procs (32 cores).

	JS	M	Z	MZ	JS7
Time steps	4491	4520	4509	4597	4539
CPU/step/node ($\times 10^{-5}$ s)	1.132	1.315	1.089	1.274	1.439
CPU/step/node ratio	1	1.162	0.962	1.126	1.272
Wall-time (s)	610	713	589	703	784
Wall-time ratio	1	1.169	0.966	1.152	1.285

B.5 Stream function with a given spectrum

The task is to find a stream function $\hat{\Psi}_i(\vec{K})$, such that the velocity field

$$\hat{u}_i(\vec{K}) = j_c K_j \epsilon_{ijk} \hat{\Psi}_k(\vec{K}) \quad (\text{B.27})$$

follows a given 3D energy spectrum $E(K)$.

Firstly, the stream function can be written as

$$\hat{\Psi}_i(\vec{K}) = \Psi(K) e^{j_c \theta_i(\vec{K})}$$

with

$$K = |\vec{K}|$$

and θ is a random angle in $(0, 2\pi)$.

Then, one has

$$\begin{aligned} \hat{u}_i \hat{u}_i^*(\vec{K}) &= \epsilon_{ijk} \epsilon_{ilm} K_j K_l \hat{\Psi}_k(\vec{K}) \hat{\Psi}_m^*(\vec{K}) \\ &= (\delta_{jl} \delta_{km} - \delta_{jm} \delta_{kl}) K_j K_l \hat{\Psi}_k(\vec{K}) \hat{\Psi}_m^*(\vec{K}) \\ &= K_j K_j \hat{\Psi}_k(\vec{K}) \hat{\Psi}_k^*(\vec{K}) - K_j K_k \hat{\Psi}_k(\vec{K}) \hat{\Psi}_j^*(\vec{K}) \\ &= 3K^2 \Psi^2(K) - \frac{1}{2} \left[K_j K_k \hat{\Psi}_k(\vec{K}) \hat{\Psi}_j^*(\vec{K}) + K_j K_k \hat{\Psi}_j(\vec{K}) \hat{\Psi}_k^*(\vec{K}) \right] \\ &= 3K^2 \Psi^2(K) - K_j K_k \Psi^2(K) \cos(\theta_k - \theta_j) \\ &= 3K^2 \Psi^2(K) - \Psi^2(K) \left[K^2 + 2K_1 K_2 \cos(\theta_2 - \theta_1) + 2K_2 K_3 \cos(\theta_3 - \theta_2) + 2K_1 K_3 \cos(\theta_3 - \theta_1) \right] \\ &= 2K^2 \Psi^2(K) - 2K_1 K_2 \cos(\theta_2 - \theta_1) - 2K_2 K_3 \cos(\theta_3 - \theta_2) - 2K_1 K_3 \cos(\theta_3 - \theta_1) \end{aligned} \quad (\text{B.28})$$

So that,

$$E_{ii}(\vec{K}) = \frac{1}{\delta(\vec{0})} \langle \hat{u}_i \hat{u}_i^*(\vec{K}) \rangle = \frac{1}{\delta(\vec{0})} 2K^2 \Psi^2(K) \quad (\text{B.29})$$

Using equation (3.108), the 3D spectrum is then

$$E(K) = 2\pi K^2 E_{ii}(\vec{K}) = \frac{1}{\delta(\vec{0})} 4\pi K^4 \Psi^2(K) \quad (\text{B.30})$$

\Rightarrow

$$\Psi(K) = \sqrt{\delta(\vec{0}) \frac{E(K)}{4\pi K^4}} \quad (\text{B.31})$$

So that a velocity field with a stream function

$$\hat{\Psi}_i(\vec{K}) = \sqrt{\delta(\vec{0}) \frac{E(K)}{4\pi K^4}} e^{j_c \theta_i} \quad (\text{B.32})$$

and θ is a random angle in $(0, 2\pi)$

$$\theta_i = \text{rand}(0, 2\pi)$$

has a 3D spectrum $E(K)$.

Appendix C

(I)LES nomenclature

Table C.1: (I)LES nomenclature

Flow		Combustion	Non-reacting	Combustion ILES (Quasi-Laminar)	Combustion LES	
					Thickened flame ($\mathcal{F} = n$)	Thickened Flame +SGS Wrinkling
Flow LES	4th Central+SM	4C-SM-NR				
	4th Central+SSF	4C-SSF-NR				
Flow ILES	(1 - α) 4th Central + α 5th Upwind	HYB$_{\alpha}$-NR				HYB$_{\alpha}$-TF$_n$-WF
	5th Upwind	UP5-NR	UP5-QL	UP5-TF$_n$	UP5-TF$_n$-WF	
	WENO-JS5	JS5-NR	JS5-QL			
	WENO-M5	M5-NR				
	WENO-Z5	Z5-NR				
	WENO-MZ5	MZ5-NR	MZ5-QL			
WENO-JS7	JS7-NR					

List of Figures

1.1	Schematic of the turbulent Bunsen burner with multi-scale forcing.	15
1.2	Photos of the pressurized combustion chamber (left) and the burner (right).	16
1.3	(a) Variation of U/U_D along the burner axis (hot-wire measurements); (b) Evolution of the turbulent kinetic energy along the burner axis (LDV measurements) [4].	16
1.4	High-pressure Bunsen burner with multi-grid injection system used in the experiment [5]	17
1.5	Example tomographic photos from reacting experiment. CH_4/Air flame at $\phi = 0.8$, $p = 0.1$ MPa.	18
1.6	The experimental condition overlaid on the turbulent premixed combustion regime diagram [5].	18
2.1	Laminar premixed flame structure.	32
2.2	Laminar premixed flame structure with thickened flame model at $\mathcal{F} = 2$	34
3.1	Illustration of the WENO method.	40
3.2	Implicit local top-hat filter induced by 2nd order central, 4th order central and 5th order upwind scheme.	46
3.3	Real (a) and imaginary (b) parts of the scaled linear MWN (3.59) for different WENO schemes	48
3.4	Implicit filters of different WENO schemes	48
3.5	Time evolution of the integrated kinetic energy of the Taylor-Green vortex flow, resolution $128 \times 128 \times 128$	51
3.6	Sketch of the double-Mach reflection flow (inspired from [79]).	51
3.7	Taylor-Green vortex flow. Q -criterion ($Q = 0$) colored by velocity magnitude, and wall projections of the vorticity magnitude in the three symmetry planes.	52
3.8	Double-Mach reflection at $t = 0.25$. Color: $\rho \in [2, 20]$, step 0.75. Left: 800×200 , middle: 1200×300 , right: 1600×400 . From top to bottom: JS, M, Z, MZ, JS7.	53
3.9	Perturbation of pressure in the Problem 1 with (a) and without (b) ASR.	62
3.10	Pressure variation between the initial and the steady condition in Problem 2 of [67] with (a) and without (b) ASR.	62
3.11	Temperature, velocity and pressure field of the third ASR test case.	64
3.12	Polynomial fitting of experiment 1D energy spectrum	66
4.1	Initial temperature, velocity and methane mass fraction profiles for 1D laminar premix flame test case.	71
4.2	Calculated flame speed (left) and thermal flame thickness (right) with different grid size. x axis: Number of points inside one flame thickness; y axis: ratio between calculated flame speed and reference flame speed (left) and ratio between calculated flame thickness and reference flame thickness (right)	72
4.3	Flame structures with different numerical setups. First column: temperature, second column: flow velocity, third column: methane mass fraction.	74
4.4	Flame structures at grid resolution $\delta_L^0/\Delta x = 8$. First column: temperature, second column: flow velocity, third column: methane mass fraction.	75

4.5	Velocity and temperature field obtained with and without ASR method. Grid size $\delta_L^0/\Delta x = 12.5$, scheme UP5-QL.	76
4.6	Calculated flame speed (left) and thermal flame thickness (right) with different thickening factor (\mathcal{F}). x axis: flame thickening factor; y axis: ratio between calculated flame speed and reference flame speed (left) and ratio between calculated flame thickness and reference flame thickness (right). Grid size $\Delta x = 0.5$ mm, scheme UP5-TF \mathcal{F}	76
4.7	Velocity and temperature field around flame front obtained with different flame thickening factor. Grid size $\Delta x = 0.5$ mm, scheme UP5-TF \mathcal{F}	77
4.8	Velocity and temperature field obtained using thickened flame model with and without ASR method. Grid size $\Delta x = 0.5$ mm, scheme UP5-TF $_{12}$	77
4.9	3D energy spectrum of the LES initial velocity field rebuilt from experimental data.	78
4.10	Time evolution of the turbulent kinetic energy with different LES strategies.	79
4.11	3D Energy spectrum obtained with different LES strategies. The x axis is normalized by $K_L = 2\pi/L_x$. Nyquist cut-off for this simulation is at $K/K_L = 60$	81
4.12	Path lines on the surface of velocity field from different simulation results.	82
4.13	Sketch of the 2D flame setup.	84
4.14	Sketch of the 2D flame grid.	85
4.15	Sketch of boundary at $x = 0$	86
4.16	Progress variable for different 2D (I)LES strategies. Lower row: experimental flame front at 5 different times, $\phi = 0.8$, $P = 0.1$ MPa.	87
4.17	Weighted average process for SGS wrinkling factor	88
4.18	Wrinkling factor contour with different evaluation methods.	91
4.19	Comparison of 2D simulations and experiments. (a): Progress variable (b): Flame surface density (1/m). The experimental data and simulation results are plotted on the left and right half domains respectively.	91
4.20	Progress variable and vorticity fields for (I)LES of 2D turbulent flame test case.	92
4.21	Post treatment for experimental tomographic images.	93
5.1	Sketch of the 3D multi-scale forcing simulation setup.	95
5.2	Radial mean velocity profiles at the jet exit in the experiments (a) [4] and simulations (b).	96
5.3	Sketch of the 3D non-reactive simulation grids (G-III) on the jet axis cut-plane. The flame front, in case of the reacting flow, is also plotted.	96
5.4	Q -criterion iso-surface $Q = 1000$ s $^{-2}$ at $t = 0.8$ s (left), and zoom on the potential core (right) for simulation G-I. Colored by velocity magnitude.	97
5.5	Q -criterion iso-surface $Q = 1000$ s $^{-2}$ at $t = 0.14$ s (colored by velocity magnitude) near the injection (left), and detail of the inner structure of the jet (right) for simulation G-II-1.	98
5.6	Evolution of the mean axial velocity (a) and resolved turbulent kinetic energy (b) on the jet axis for 3D non-reactive simulation Group II.	98
5.7	Same as figure 5.6, Group III.	99
5.8	Q -criterion iso-surface $Q = 1000$ s $^{-2}$ of 3D non-reactive simulation Group III.	100
5.9	Velocity magnitude (m/s) and vorticity field (1/s) on the axial cut-plane of 3D non-reactive simulations Group III.	101
5.10	The vorticity (1/s) field and SGS wrinkling factor of 3D reactive simulations on the jet axis cut-plane. The black line ($\tilde{c} = 0.5$) indicates the flame front.	102
5.11	Mean Progress Variable and FSD curve along the jet axis for 3D reactive simulations	103
5.12	Radial profiles of mean progress variable and FSD at different locations down stream of the jet exit.	104
5.13	Comparison of 3D reactive simulation and experiments.	105
5.14	Iso-surface $\tilde{c} = 0.5$ for 3D reactive simulations at different times.	106

List of Tables

1.1	Nomenclature of different flow and combustion (I)LES strategies.	14
1.2	Geometrical characteristics of the multi-scale grid where d_j , M_j , σ_j and K_j stand for the hole diameter, the mesh size, the blockage ratio and the pressure drop coefficient of the j -th perforated plate [4].	15
1.3	Turbulence parameters at the jet exit from non-reactive experiment results [4].	17
2.1	Classical regimes of turbulent premixed combustion [6].	33
3.1	Butcher array for the optimal third order TVD Runge-Kutta scheme	37
3.2	Coefficients a_j and b_j in equation (3.42) and (3.45) for different schemes.	46
4.1	Boundary condition at $x = 0$ plane. The definition of function S can be found in Eq. (4.1). The subscript f and b indicate the fresh and burnt gas conditions.	84
4.2	Mesh parameters of the 2D turbulent flame test case.	85
5.1	Mesh and numerical parameters of the 3D non-reacting simulations.	97
B.1	Coefficients c_{rj} for $k=1$ to 6.	112
B.2	Coefficients d_r for $k=1$ to 6.	112
B.3	Computational cost of the Taylor-Green vortex flow for different WENO schemes on a $128 \times 128 \times 128$ grid, 16 Intel [®] Xeon [®] E5430 4-cores@2.66GHZ (64 cores).	125
B.4	Computational cost of the double Mach reflection for different WENO schemes on the 300×1200 grid, 4 Intel [®] Sandy Bridge [®] E5-4650 procs (32 cores).	125
C.1	(I)LES nomenclature	127

Bibliography

- [1] F.T.C. Yuen and Ö.L. Gülder. Turbulent premixed flame front dynamics and implications for limits of flamelet hypothesis. *Proceedings of the Combustion Institute*, 34:1393–1400, 2013.
- [2] N. Mazellier, B. Danaila, and B. Renou. Multi-scale injection: a new tool to generate intense homogeneous and isotropic turbulence for premixed combustion. *Journal of Turbulence*, 11(43):1–30, 2010.
- [3] R. Fragner, F. Halter, N. Mazellier, C. Chauveau, and I. Gökalp. Investigation of pressure effects on the small scale wrinkling of turbulent premixed bunsen flames. *Proceedings of the Combustion Institute*, 35(2):1527–1535, 2015.
- [4] R. Fragner, N. Mazellier, F. Halter, C. Chauveau, and I. Gökalp. Multi-scale high intensity turbulence generator applied to a high pressure turbulent burner. *Flow, Turbulence and Combustion*, 94(1):263–283, 2015.
- [5] F. Thiesset, G. Maurice, F. Halter, N. Mazellier, C. Chauveau, and I. Gökalp. Geometrical properties of turbulent premixed flames and other corrugated interfaces. *Phys. Rev. E*, 93:013116, Jan 2016.
- [6] T. Poinso and D. Veynante. *Theoretical and Numerical Combustion*. 2nd edition. Edwards, 2005.
- [7] E.R. Hawkes, O. Chatakonda, H. Kolla, A.R. Kerstein, and J.H. Chen. A petascale direct numerical simulation study of the modelling of flame wrinkling for large-eddy simulations in intense turbulence. *Combustion and flame*, 159:2690–2703, 2012.
- [8] D. B. Spalding. Development of the eddy-break-up model of turbulent combustion. In *Symposium (International) on Combustion*, volume 16, pages 1657–1663. Elsevier, 1977.
- [9] N. Peters. *Turbulent Combustion*. Cambridge university press, 2000.
- [10] B. Fiorina, R. Mercier, G. Kuenne, A. Ketelheun, A. Avdic, J. Janicka, D. Geyer, A. Dreizler, E. Alenius, C. Duwig, P. Trisjono, K. Kleinheinz, S. Kang, H. Pitsch, F. Proch, F. Cavallo Marincola, and A. Kempf. Challenging modeling strategies for LES of non-adiabatic turbulent stratified combustion. *Combustion and Flame*, 162(11):4264–4282, NOV 2015.
- [11] H. Pitsch. Large-eddy simulation of turbulent combustion. *Annual Review of Fluid Mechanics*, 38:453–482, 2006.
- [12] B. Fiorina, D. Veynante, and S. Candel. Modeling combustion chemistry in large eddy simulation of turbulent flames. *Flow, Turbulence and Combustion*, 94(1):3–42, 2015.
- [13] V. Moureau, G. Lartigue, Y. Sommerer, C. Angelberger, O. Colin, and T. Poinso. Numerical methods for unsteady compressible multi-component reacting flows on fixed and moving grids. *Journal of Computational Physics*, 202(2):710–736, 2005.
- [14] L.G. Margolin, W.J. Rider, and F.F. Grinstein. Modeling turbulent flows with implicit LES. *Journal of Turbulence*, 7(15):1–27, 2006.

- [15] F.F. Grinstein, L.G. Margolin, and W.J. Rider. *Implicit Large Eddy Simulation : computing turbulent fluid dynamics*. Cambridge University Press, 2007.
- [16] S.B. Pope. Ten questions concerning the large-eddy simulation of turbulent flows. *New Journal of Physics*, 6(35):1–24, 2004.
- [17] C. Duwig, K.-J. Nogenmyr, C. Chan, and M.J. Dunn. Large eddy simulations of a piloted lean premix jet flame using finite-rate chemistry. *Combustion Theory and Modelling*, 15(4):537–568, 2011.
- [18] C. Duwig and M.J. Dunn. Large eddy simulation of a premixed jet flame stabilized by a vitiated co-flow: Evaluation of auto-ignition tabulated chemistry. *Combustion and Flame*, 160:2879–2895, 2013.
- [19] C. Duwig and L. Fuchs. Large eddy simulation of a H₂/N₂ lifted flame in a vitiated co-flow. *Combustion Science and Technology*, 180:453–480, 2008.
- [20] E. George, Ph. Magre, and V. Sabelnikov. Numerical simulations of self-ignition of hydrogen-hydrocarbons mixtures in a hot supersonic air flow. In *AIAA paper 2006-4611, 42nd AIAA/ASME/SAE/ASEE Joint Propulsion Conference & Exhibit*, Sacramento, California, 9–12 July, 2006.
- [21] M. Karaca. *Contribution to the Development of Implicit Large Eddy Simulation methods for compressible and reacting turbulent flows*. PhD thesis, Université d’Orléans, France., 2011.
- [22] M. Karaca, N. Lardjane, and I. Fedioun. Implicit large eddy simulation of high-speed non-reacting and reacting air/h₂ jets with a 5th order weno scheme. *Computers & Fluids*, 62:25–44, 2012.
- [23] S. Zhao, N. Lardjane, and I. Fedioun. Comparison of improved finite-difference WENO schemes for the implicit large eddy simulation of turbulent non-reacting and reacting high-speed shear flows. *Computers & Fluids*, 95:74–87, 2014.
- [24] F. Thiesset, G. Maurice, F. Halter, N. Mazellier, C. Chauveau, and I. Gökalp. Modeling of the subgrid scale wrinkling factor for large-eddy simulation of turbulent premixed combustion. *Combustion Theory and Modelling*, 2016.
- [25] F.A. Williams. *Combustion Theory: The Fundamental Theory of Chemically Reacting Flow Systems*. Combustion science and engineering series. The Benjamin/Cummings Publishing Company, Inc, 1985.
- [26] L. Gougeon. *Comparaison de schémas numériques pour la simulation d’écoulements turbulents réactifs*. PhD thesis, Université d’Orléans, France. Available online : http://tel.archives-ouvertes.fr/docs/00/28/22/42/PDF/these_LudivineGougeon.pdf, 2007.
- [27] N. Lardjane. *Etude théorique et numérique des écoulements cisailés libres à masse volumique fortement variable*. PhD thesis, Université d’Orléans, France. Available online : <http://tel.archives-ouvertes.fr/docs/00/04/69/65/PDF/tel-00006483.pdf>, 2002.
- [28] A. Ern and V. Giovangigli. Fast and accurate multicomponent transport property evaluation. *Journal of Computational Physics*, 120(1):105 – 116, 1995.
- [29] A. Ern and V. Giovangigli. Eglib: A general-purpose fortran library for multicomponent transport property evaluation. *Manual of EGlIb*, (3):12, 2004.
- [30] A. Ern and V. Giovangigli. *Multicomponent transport algorithms*, volume 24. Springer, 1994.

- [31] G. Wang, M. Boileau, and D. Veynante. Implementation of a dynamic thickened flame model for large eddy simulations of turbulent premixed combustion. *Combustion and Flame*, 158:2199–2213, 2011.
- [32] R.J. Kee, F.M. Rupley, J.A. Miller, M.E. Coltrin, J.F. Grcar, E. Meeks, H.K. Moffat, A.E. Lutz, G. Dixon-Lewis, M.D. Smooke, J. Warnatz, G.H. Evans, R.S. Larson, R.E. Mitchell, L.R. Petzold, W.C. Reynolds, M. Caracotsios, W.E. Stewart, and P. Glarborg. *CHEMKIN collection*. release 3.5. Reaction Design, Inc., San Diego, CA, 1999.
- [33] S. B. Pope. *Turbulent flows*. Cambridge university press, 2000.
- [34] C.R. Wilke. A viscosity equation for gas mixture. *Chemical Physics*, 18:517–19, 1950.
- [35] A. Burcat and B. Ruscic. Ideal gas thermodynamic data in polynomial form for combustion and air pollution use, December 2006. Third Millennium Ideal Gas and Condensed Phase Thermochemical Database for Combustion [on line database].
- [36] E. Garnier, N. Adams, and P. Sagaut. *Large Eddy Simulation for Compressible Flows*. Scientific Computations. Springer, 2009.
- [37] P. Sagaut. *Large-Eddy Simulation for Incompressible Flows*. 3rd edition. Springer, Berlin, 2006.
- [38] F. van der Bos and B. J. Geurts. Commutator errors in the filtering approach to large-eddy simulation. *Physics of Fluids*, 17(2005):0–20, 2005.
- [39] S.K. Lele. Compact finite difference schemes with spectral-like resolution. *Journal of Computational Physics*, 103:16–42, 1992.
- [40] E. Garnier, M. Mossi, P. Sagaut, P. Comte, and M. Deville. On the use of shock-capturing schemes for large-eddy simulation. *Journal of Computational Physics*, 153:273–311, 1999.
- [41] S. Hickel, N. A. Adams, and J. A. Domaradzki. An adaptive local deconvolution method for implicit LES. *Journal of Computational Physics*, 213(1):413–436, March 2006.
- [42] J. Smagorinsky. General circulation experiments with the primitive equations i. the basic experiment. *Monthly Weather Review*, 91(3):99–164, 1963.
- [43] M. Germano. Turbulence: the filtering approach. *Journal of Fluid Mechanics*, 238:325–336, 1992.
- [44] G. Erlebacher, M.Y. Hussaini, C.G. Speziale, and T.A. Zang. Toward the large eddy simulation of compressible turbulent flows. *Journal of Fluid Mechanics*, 238:155–185, 1992.
- [45] E. Garnier, P. Sagaut, and M. Deville. Large-eddy simulation of shock/turbulence interaction. *Computers and Fluids*, 31:245–268, 2002.
- [46] A. Yoshizawa. Statistical theory for compressible turbulent shear flows, with the application to subgrid modeling. *Physics of Fluids*, 29(7):2152–2164, 1986.
- [47] J. Meyer, B.J. Geurts, and P. Sagaut. A computational error-assessment of central finite-volume discretizations in large-eddy simulation using a smagorinsky model. *Journal of Computational Physics*, 227:156–173, 2007.
- [48] M. Lesieur. *Turbulence in Fluids, Fourth edition*. Fluid mechanics and its applications, Vol. 84. Springer, 2008.
- [49] D. Carati, G.S. Winckelmans, and H. Jeanmart. On the modelling of the subgrid-scale and subfilter-scale stress tensors in large-eddy simulation. *Journal of Fluid Mechanics*, 441:119–138, 2001.

- [50] P. J. Martínez Ferrer, R. Buttay, G. Lehnasch, and A. Mura. A detailed verification procedure for compressible reactive multicomponent Navier–Stokes solvers. *Computers & Fluids*, 89:88–110, January 2014.
- [51] B. Thornber, R.W. Bilger, A.R. Masri, and E.R. Hawkes. An algorithm for LES of premixed compressible flow using the Conditional Moment Closure model. *Journal of Computational Physics*, 230:7687–7705, 2011.
- [52] H. Pitsch and L. D. De La Geneste. Large-eddy simulation of premixed turbulent combustion using a level-set approach. *Proceedings of the Combustion Institute*, 29:2001–2008, 2002.
- [53] V. Moureau, B. Fiorina, and H. Pitsch. A level set formulation for premixed combustion LES considering the turbulent flame structure. *Combustion and Flame*, 156(4):801–812, 2009.
- [54] E. Knudsen and H. Pitsch. A dynamic model for the turbulent burning velocity for large eddy simulation of premixed combustion. *Combustion and flame*, 154:740–760, 2008.
- [55] B. Fiorina, R. Vicquelin, P. Auzillon, N. Darabiha, O. Gicquel, and D. Veynante. A filtered tabulated chemistry model for LES of premixed combustion. *Combustion and Flame*, 157(3):465–475, 2010.
- [56] P.J. O’Rourke and F.V. Bracco. Two scaling transformations for the numerical computation of multidimensional unsteady laminar flames. *Journal of Computational Physics*, 33(2):185–203, 1979.
- [57] O. Colin, F. Ducros, D. Veynante, and T. Poinso. A thickened flame model for large eddy simulations of turbulent premixed combustion. *Physics of Fluids*, 12(7):1668–1693, 2000.
- [58] F. Charlette, C. Meneveau, and D. Veynante. A power-law flame wrinkling model for LES of premixed turbulent combustion. Part I. *Combustion and Flame*, 131:159–180, 2002.
- [59] F. Charlette, C. Meneveau, and D. Veynante. A power-law flame wrinkling model for LES of premixed turbulent combustion. Part II. *Combustion and Flame*, 131:181–197, 2002.
- [60] M. Boileau. *Simulation aux grandes échelles de l’allumage diphasique des foyers aéronautiques*. PhD thesis, Institut National Polytechnique de Toulouse, France, 2007.
- [61] G. Kuenne, A. Ketelheun, and J. Janicka. LES modeling of premixed combustion using a thickened flame approach coupled with FGM tabulated chemistry. *Combustion and Flame*, 158(9):1750–1767, September 2011.
- [62] C. Fureby. A fractal flame-wrinkling large eddy model for premixed turbulent simulation combustion. *Proceedings of the Combustion Institute*, 30(1):593–601, 2005. 30th International Symposium on Combustion, Univ Illinois Chicago, Chicago, IL, JUL 25-30, 2004.
- [63] N. Chakraborty and M. Klein. A priori direct numerical simulation assessment of algebraic flame surface density models for turbulent premixed flames in the context of large eddy simulation. *Physics of Fluids*, 20(8), 2008.
- [64] M. Katragadda, N. Chakraborty, and R.S. Cant. A priori assessment of algebraic flame surface density models in the context of large eddy simulation for nonunity lewis number flames in the thin reaction zones regime. *Journal of Combustion*, 2012, 2012.
- [65] F. Thiesset, G. Maurice, F. Halter, N. Mazellier, C. Chauveau, and I. Gökalp. Modelling of the subgrid scale wrinkling factor for large-eddy simulation of turbulent premixed combustion. In *15th International Conference on Numerical Combustion*, Avignon, France, 19-22 April 2015, 2015.

- [66] C.W. Shu. Essentially non-oscillatory and weighted essentially non-oscillatory schemes for hyperbolic conservation laws. Technical Report NASA/CR-97-206253, ICASE report No.97-65, Langley Research Center, November 1997.
- [67] Y. Wang and A. Trouvé. Artificial Acoustic Stiffness Reduction in Fully Compressible, Direct Numerical Simulation of Combustion. *Combustion Theory and Modelling*, 8(3), 2004.
- [68] B.J. Geurts and F. van der Bos. Numerically induced high-pass dynamics in large-eddy simulation. *Physics of Fluids*, 17(12):125103, 2005.
- [69] C.W. Shu. High order weighted essentially non-oscillatory schemes for convection dominated problems. *SIAM Review*, 51(1):82–126, 2009.
- [70] G.S. Jiang and C.W. Shu. Efficient implementation of weighted ENO schemes. *Journal of Computational Physics*, 126:202–228, 1996.
- [71] A.K. Henrick, T.D. Aslam, and J.M. Powers. Mapped weighted essentially non-oscillatory schemes: Achieving optimal order near critical points. *Journal of Computational Physics*, 207:542–567, 2005.
- [72] R. Borges, M. Carmona, B. Costa, and W.S. Don. An improved weighted essentially non-oscillatory scheme for hyperbolic conservation laws. *Journal of Computational Physics*, 227:3191–3211, 2008.
- [73] M. Castro, B. Costa, and W.S. Don. Higher order weighted essentially non-oscillatory weno-z schemes for hyperbolic conservation laws. *Journal of Computational Physics*, 230:1766–1792, 2011.
- [74] L. Zhao, Y. Zhang, and C. Haixin. A low dissipation numerical scheme for Implicit Large Eddy Simulation. *Computers & Fluids*, 117:233–246, 2015.
- [75] S. Pirozzoli. On the spectral properties of shock-capturing schemes. *Journal of Computational Physics*, 219:489–497, 2006.
- [76] C.W. Shu, W.S. Don, D. Gottlieb, O. Schilling, and L. Jameson. Numerical Convergence Study of Nearly Incompressible, Inviscid Taylor-Green Vortex Flow. *Journal of Scientific Computing*, 24(1):1–27, 2005.
- [77] Y. Dubief and F. Delcayre. On coherent-vortex identification in turbulence. *Journal of Turbulence*, 1(011):1–22, 2000.
- [78] P. Woodard and P. Colella. The numerical simulation of two-dimensional fluid flow with strong shocks. *Journal of Computational Physics*, 54(1):115 – 173, 1984.
- [79] H. Li and G. Ben-Dor. Analysis of double-Mach reflection wave configurations with convexly curved Mach stems. *Shock Waves*, 9:319–326, 1999.
- [80] G. P. Zank and W. H. Matthaeus. The equations of nearly incompressible fluids I. Hydrodynamics Turbulence and Waves. *Physics of Fluids*, 3(1), 1991.
- [81] T. MA. *Large-eddy simulation of variable density flows*. PhD thesis, University of Maryland, 2006.
- [82] J.D. Ramshaw, P.J. O’Rourke, and L.R. Stein. Pressure gradient scaling method for fluid flow with nearly uniform pressure. *Journal of Computational Physics*, 58(3):361–376, May 1985.
- [83] J. M. Vedovoto, A. da Silveira Neto, L. F. Figueira da Silva, and A. Mura. Influence of synthetic inlet turbulence on the prediction of low Mach number flows. *Computers & Fluids*, 106:135–153, jan 2015.

- [84] J.O. Hinze. *Turbulence, 2nd edition*. Mc Graw Hill, 1975.
- [85] Prvir D. Stable boundary conditions and difference schemes for navier–stokes equations. *SIAM Journal on Numerical Analysis*, 25(2):245–267, 1988.
- [86] X. Zhong. Additive semi implicit Runge Kutta methods for computing high speed nonequilibrium reactive flows. *Journal of Computational Physics*, 31:19–31, 1996.
- [87] D. Veynante and V. Moureau. Analysis of dynamic models for large eddy simulations of turbulent premixed combustion. *Combustion and Flame*, 162(12):4622–4642, 2015.
- [88] R. Mercier, V. Moureau, D. Veynante, and B. Fiorina. LES of turbulent combustion: On the consistency between flame and flow filter scales. *Proceedings of the Combustion Institute*, 35(2):1359–1366, 2015.

Song ZHAO

Simulation des grandes échelles explicite et implicite de la combustion turbulente avec forçage multi-échelles

Résumé:

Le contexte de cette étude est l'optimisation de la combustion turbulente prémélangée de syngaz pour la production propre d'énergie. Un brûleur CH_4/air de type bec Bunsen avec forçage turbulent multi-échelles produit par un système de trois grilles, est simulé numériquement par différentes techniques de simulation des grandes échelles (SGE), et les résultats sont comparés à l'expérience. On a développé et appliqué une formulation bas-Mach du solveur Navier-Stokes basé sur différents schémas numériques, allant des différences finies centrées d'ordre 4 à des versions avancées des schémas WENO d'ordre 5. La méthodologie est évaluée sur une série de cas-tests classiques (flamme laminaire 1D prémélangée, turbulence homogène et isotrope en auto-amortissement), et sur des simulations 2D de la flamme turbulente prémélangée expérimentale. Les SGE implicites (ILES), i.e. sans aucune modélisation sous-maille, et explicites avec le modèle de flamme épaissie et un modèle de plissement sous-maille nouvellement élaboré (TFLES), sont appliquées à la simulation 3D du brûleur expérimental. Les résultats montrent que l'approche TFLES avec un schéma d'ordre élevé à faible dissipation numérique prédit correctement la longueur de la flamme et la densité de surface de flamme. La SGE implicite avec un schéma WENO avancé produit une flamme trop courte mais réaliste à condition que la taille de la maille soit de l'ordre de l'épaisseur de flamme laminaire. La représentation des interactions flamme/turbulence est néanmoins très différente entre TFLES et ILES.

Mots clés: Combustion turbulente prémélangée, Simulation des grandes échelles, formulation bas-Mach, schémas WENO

Explicit and Implicit Large Eddy Simulation of Turbulent Combustion with Multi-Scale Forcing

Abstract:

The context of this study is the optimization of premixed turbulent combustion of syngas for clean energy production. A Bunsen-type CH_4/air turbulent premixed burner with a multi-scale grid generator is simulated with different Large Eddy Simulation (LES) strategies and compared to experimental results. A low-Mach formulation of a compressible Navier-Stokes solver based on different numerical methods, ranging from 4th order central finite difference to 5th order advanced WENO schemes, is developed and applied. Classical test cases (1D laminar premixed flame, decaying HIT), and 2D simulations of the turbulent premixed flame are performed to assess the numerical methodology. Implicit LES (ILES), i.e. LES without any explicit subgrid modeling, and explicit LES with the Thickened Flame model and subgrid scale flame wrinkling modelling (TFLES) are applied to simulate numerically the 3D experimental burner. Results show that TFLES with a high-order low dissipation scheme predicts quite well the experimental flame length and flame surface density. ILES with advanced WENO schemes produces a slightly shorter although realistic flame provided the grid spacing is of order of the laminar flame thickness. The representation of flame/turbulence interactions in TFLES and ILES are however quite different.

Keywords: Turbulent premixed combustion, Large Eddy Simulation, low-Mach formulation, WENO schemes



Institut de Combustion Aérodynamique Réactivité
et Environnement, CNRS Orléans
1C, avenue de la Recherche Scientifique, 45071
Orléans cedex 2, France

